Tectonic Geomorphology of the San Gabriel Mountains, CA

by

Roman Alexander DiBiase

A Dissertation Presented in Partial Fulfillment
of the Requirements for the Degree
Doctor of Philosophy

Approved September 2011 by the
Graduate Supervisory Committee:

Kelin X Whipple, Co-chair
Arjun M. Heimsath, Co-chair
J Ramón Arrowsmith
Edward J. Garnero
Kip V. Hodges

ARIZONA STATE UNIVERSITY

December 2011

ABSTRACT

The San Gabriel Mountains (SGM) of southern California provide the opportunity to study the topographic controls on erosion rate in a mountain range where climate and lithology are relatively constant. I use a combination of digital elevation model data, detailed channel survey data, decadal climate records, and catchment-averaged erosion rates quantified from ^{10}Be concentrations in stream sands to investigate the style and rates of hillslope and channel processes across the transition from soil-mantled to rocky landscapes in the SGM. Specifically, I investigate (1) the interrelations among different topographic metrics and their variation with erosion rate, (2) how hillslopes respond to tectonic forcing in "threshold" landscapes, (3) the role of discharge variability and erosion thresholds in controlling the relationship between relief and erosion rate, and (4) the style and pace of transient adjustment in the western SGM to a recent increase in uplift rate.

Millennial erosion rates in the SGM range from 0.03-1.1 mm/a, generally increasing from west to east. For low erosion rates (< 0.3 mm/a), hillslopes tend to be soil-mantled, and catchment-averaged erosion rates are positively correlated with catchment-averaged slope, channel steepness, and local relief. For erosion rates greater than 0.3 mm/a, hillslopes become increasingly rocky, catchment-mean hillslope angle becomes much less sensitive to erosion rate, and channels continue to steepen. I find that a non-linear relationship observed between channel steepness and erosion rate can be explained by a simple bedrock incision model that combines a threshold for erosion with a probability distribution of discharge events where large floods follow an inverse power-law. I also find that the timing of a two-staged increase in uplift rate in the western SGM based on stream profile analysis agrees with independent estimates. Field observations in the same region suggest that the relict topography that allows for this calculation has persisted for more than 7 Ma due to the stalling of migrating knickpoints by locally stronger bedrock and a lack of coarse sediment cover.

ACKNOWLEDGMENTS

This dissertation represents the culmination of five years of research in collaboration with a group of professors, post-docs, and graduate students who I have been extraordinarily lucky to work with. There is certainly not enough room to properly acknowledge everyone who has helped me along this path, but I wish to point out a handful of people in particular. First off, I would like to thank my advisors, Kelin Whipple and Arjun Heimsath. I look up to both of you, and I am grateful for the ideal balance of support and independence given to me during my time at ASU.

Field work for this dissertation involved 3 more-or-less full summers in the San Gabriel Mountains, a land of steep hillslopes, yucca, poison oak, and few trails. I owe sincerest thanks (and perhaps apologies in some cases!) to all those who have helped me collect samples, survey channels, bushwhack, and explore this rugged, yet strangely metropolitan mountain range: Byron Adams, Erin DiMaggio, Nicole Gasparini, Benny Guralnik, Matt Jungers, Jeni McDermott, Matt Rossi, Melinda Shimizu, Drew Stolar, and Joe Walsh.

I have been fortunate to have consistent funding for this project throughout my stay at ASU. The Geomorphology and Land Use Dynamics program of the National Science Foundation (NSF) provided the bulk of funding for this work via two awards (EAR-0724194 to Kelin Whipple and EAR-0518998 to Arjun Heimsath). The NSF-sponsored National Center for Airborne Laser Mapping (NCALM) provided me with 40 km^2 of LiDAR data as part of a seed grant awarded in 2007. The remainder of the LiDAR coverage (for a total of nearly 500 km^2) was also flown and processed by NCALM as part of a joint effort with Caltech following the devastating Station Fire of 2009. I would also like to thank the ARCS Foundation for their support during my final year here.

I would like to thank my parents Tony and Deb DiBiase for impressing upon me the value (and providing me the opportunity) of choosing a career based on my passions and not the expectations of others. I thank my sister Olivia, for never letting me fake it and calling me out on every slip. And finally, I would like to especially thank Erin DiMaggio. Not only did you teach me the fundamentals of making pretty figures, but your unfailing support and understanding has made this process infinitely more enjoyable.

TABLE OF CONTENTS

CHAPTER Page

CHAPTER Page

CHAPTER Page

APPENDIX

LIST OF TABLES

Table Page

LIST OF FIGURES

Figure Page

PREFACE

“This range, containing most of the characteristic features of the other ranges just mentioned, overlooks the Los Angeles vineyards and orange groves from the north, and is more rigidly inaccessible in the ordinary meaning of the word than any other that I ever attempted to penetrate. The slopes are exceptionally steep and insecure to the foot, and they are covered with thorny bushes from five to ten feet high. With the exception of little spots not visible in general views, the entire surface is covered with them, massed in close hedge growth, sweeping gracefully down into every gorge and hollow, and swelling over every ridge and summit in shaggy, ungovernable exuberance.”

-John Muir, *The Mountains of California* (1894)

CHAPTER 1

INTRODUCTION

MOTIVATION

Earth's surface topography encodes the rich story of the competition between uplift and erosion. Fundamental to the job of geomorphologists is the task of identifying the processes acting to shape the landscape and quantifying their rates. *Gilbert* [1877] was perhaps the first to systematically analyze a landscape in terms of discrete processes. Indeed, many of the original hypotheses Gilbert developed in the Henry Mountains of Utah are still topics of active debate today. For example, the interpretation that convex hilltops arise as a result of slope-dependent soil transport dates to the early work of *Davis* [1892] and *Gilbert* [1909]. Later workers formalized analytical approaches to predicting hillslope form [e.g., *Culling*, 1963; *Kirkby*, 1971], and only recently have the predictions of such models been explicitly field tested [e.g., *Heimsath et al.*, 1997].

The fact that these topics continue to garner interest in the geomorphology community can best be ascribed to the initial difficulties and subsequent advances in both quantifying long-term erosion rates and characterizing and manipulating topographic data. Traditionally, erosion rates were estimated by measuring either suspended sediment loads directly, or integrating rates over decadal timescales using reservoir infilling rates [e.g., *Schumm*, 1963]. Classical studies of the influence of climate [*Langbein and Schumm*, 1958] and relief [*Ahnert*, 1970] on erosion rate were based on these short-term sediment yield data. However, these methods had significant limitations; short-term erosion rates do not adequately capture the influence of low recurrence, high magnitude events, and are sensitive to anthropogenic influences or the fire cycle [e.g., *Kirchner et al.*, 2001; *Lavé and Burbank*, 2004].

In the past few decades, the advent of cosmogenic radionuclide (CRN) exposure dating has enabled the measurement of erosion rates over much longer timescales (10^2-10^5 years) [*Granger and Riebe*, 2007]. Cosmogenic isotopes such as ^{10}Be are created through the interaction of high-energy cosmic rays with the uppermost meters of Earth's surface. Thus, CRN concentrations of rock (and soil) samples are inversely proportional to the time spent near the surface, and can be used to infer exposure ages or erosion rates. We focus here on one application in particular that forms the backbone for much of this dissertation. *Bierman and Steig* [1996] proposed that the CRN concentrations in alluvial sediments should reflect the average exposure history of each grain and allow for the determination of a catchment-averaged erosion rate. *Granger et al.* [1996] tested this method using catchments where erosion rates were independently known from the measured volume of dated alluvial fan deposits. Since then, this method has been successfully applied in numerous studies of upland landscapes [e.g., *von Blanckenburg*, 2005 and references within].

The availability of digital elevation models (DEMs) and increasing computing power has similarly rejuvenated methods of quantitative landscape analysis. For example, the pioneering studies of scaling in fluvial systems were painstakingly conducted using field surveys and paper topographic maps [e.g., *Flint*, 1974; *Hack*, 1957]. Today, the proliferation of high quality DEMs and consumer GIS software makes such calculations trivial, and enables a more sophisticated analysis of topographic metrics. Specifically, the topographic variables of local slope, curvature, and contributing drainage area are routinely used to identify slope stability thresholds [e.g., *Dietrich et al.*, 1995], highlight transitions in dominant erosion process [e.g., *Montgomery and Foufoula-Georgiou*, 1993], and discriminate among predictions from different landscape evolution models [e.g., *Dietrich et al.*, 2003].

Bedrock rivers define the relief structure of unglaciated mountain ranges, set the local baselevel for hillslopes, and transmit signals of climatic and tectonic forcing throughout the landscape [*Whipple*, 2004]. Because of this, much of the work presented in this dissertation focuses on understanding the controls on bedrock river incision. I use a combination of DEM analysis, detrital CRN erosion rates, and detailed field surveys to investigate the controls on erosion rate in the San Gabriel Mountains of California, where a gradient in uplift rate allows for the study of channel and hillslope processes across the transition from low-slope, soil mantled regions to rugged, rocky terrain.

A summary of the chapters is provided below. Chapters 2-5 were prepared independently for publication as stand-alone journal articles, so there is a certain unavoidable overlap in background material.

OUTLINE OF CHAPTERS 2-6

Chapter 2 sets the stage (both location-wise and methods-wise) for the remainder of the dissertation. In this paper, we use ^{10}Be concentrations in stream sediments to quantify catchment-averaged erosion rates across a gradient in topographic relief in the San Gabriel Mountains. We use a 10 m resolution DEM to calculate a range of topographic metrics for each of our sample catchments, including mean hillslope angle, channel steepness index, and local relief measured over different length scales. We show that mean hillslope angle increases with erosion rate until it reaches a maximum value of ~37 degrees at erosion rates of ≥ 0.3 mm/a. In contrast, the channel steepness index increases monotonically with erosion rate (for $E = 0.03 - 1.1$ mm/a), and emerges as a robust metric of erosion rate in steep landscapes.

In Chapter 3, we use a LiDAR-derived 1 m DEM covering 500 km^2 in the San Gabriel Mountains to explore how hillslope form and texture vary with erosion rate in a steep landscape (mean slopes > 30°). We also use high-resolution panoramic photographs to calibrate a new slope-based metric of hillslope rock exposure determined from the LiDAR DEM. We study in detail 20 small (2-3 km^2) catchments that span a wide range of erosion rates (0.04-1.0 mm/a), mean slope (16-43°), and texture (soil mantled to rocky). In contrast to previous work based on coarser topographic data, we find that mean slopes increase with erosion rate up to 1 mm/a. Exposed rock is rare in catchments with mean slope lower than 30°. For steeper catchments, rock exposure increases steadily with mean slope and erosion rate, and a positive relationship between slope distribution skewness and mean slope emerges as the prevalence of angle-of-repose debris wedges keeps modal slopes near 37°. Finally, as erosion rates increase, the extent of the fluvial network decreases, while colluvial channels extend downstream, keeping the total drainage density, and thus mean hillslope length, similar across the range.

In Chapter 4, we use a 1-D river incision model to explore how climate variability and the magnitude of erosion thresholds influence the relationship between relief (quantified by the channel steepness index) and erosion rate shown in Chapter 2. We calibrate this model using field observations, discharge records, and catchment-averaged erosion rate data from the San Gabriel Mountains. The non-linear relationship between channel steepness index and erosion rate observed in the San Gabriel Mountains can be explained by this simple bedrock incision model that includes both a threshold for erosion and a probability distribution function of discharge events where large floods follow a power-law scaling. Starting from this case, we explore the implications of an empirical relationship between mean runoff and variability to test whether dry, variable climates can erode more efficiently than wet, stable climates. For channels with high thresholds or low steepness, modeled erosion rate reaches a maximum at a mean runoff of 200-400 mm/a. In general, erosion rates are predicted to become less sensitive to increases in runoff above 500 mm/a, with important implications for the hypothesized influence of climate on tectonics.

In Chapter 5, we focus on Big Tujunga Creek, a 300 km^2 catchment that drains much of the western San Gabriel Mountains. A hypothesized two-stage increase in uplift rate has resulted in three physiographic regions in Big Tujunga Creek separated by two knickpoints. We use a combination of DEM analysis, detailed field surveys, and detrital CRN erosion rates to (1) study the style and pace of knickpoint retreat and (2) interpret the tectonic history of the western SGM. We find that knickpoint migration in Big Tujunga Creek and its tributaries does not scale directly with drainage area, as predicted by simple stream power models. Rather, small-scale heterogeneities in rock strength stall the upward migration of knickpoints through the generation oversteepened reaches consisting of large bedrock steps. We find that this effect is enhanced in catchments with low coarse sediment supply. By reconstructing relict stream profiles and using detrital CRN erosion rates, we interpret a two-phase increase in baselevel fall along the Sierra Madre Fault Zone. The first increase, estimated at 7-9 Ma, corresponds with independent estimates of the initial uplift phase of the SGM. The second increase appears to occur ca. 1.5 Ma, though there is little independent information constraining uplift rates during this time. We hypothesize that this latter increase corresponds to the initiation of the San Jacinto Fault, whose age of initiation is similar.

Chapter 6 presents a synthesis of the preceding chapters, and provides insight into future directions.

Since chapters 2-5 have been published elsewhere, please cite them appropriately as indicated below:

Chapter 2: DiBiase, R.A., K.X. Whipple, A.M. Heimsath, and W.B. Ouimet (2010), Landscape form and millennial erosion rates in the San Gabriel Mountains, CA, *Earth and Planetary Science Letters*, 289(1-2), 134-144

Chapter 3: DiBiase, R.A., A.M. Heimsath, and K.X. Whipple (2011), Hillslope response to tectonic forcing in threshold landscapes, in review at *Earth Surface Processes and Landforms*

Chapter 4: DiBiase, R.A., and K.X. Whipple, (2011), The influence of erosion thresholds and runoff variability on the relationships among topography, climate, and erosion rate, in review at *Journal of Geophysical Research - Earth Surface*

Chapter 5: DiBiase, R.A., K.X. Whipple, and A.M. Heimsath (2011), Investigation of a transient landscape in the western San Gabriel Mountains, California: Implications for knickpoint migration and tectonic history, in preparation for submission to *GSA Bulletin*

REFERENCES

Ahnert, F. (1970), Functional relationships between denudation, relief, and uplift in large mid-latitude drainage basins, *American Journal of Science*, *268*, 243-263.

Bierman, P., and E. J. Steig (1996), Estimating rates of denudation using cosmogenic isotope abundances in sediment, *Earth Surface Processes and Landforms*, *21*, 125-139.

Culling, W. E. H. (1963), Soil creep and the development of hillside slopes, *The Journal of Geology*, *71*(2), 127-161.

Davis, W. M. (1892), The convex profile of badland divides, *Science*, *20*, 245.

Dietrich, W. E., R. Reiss, M. Hsu, and D. Montgomery (1995), A process-based model for colluvial soil depth and shallow landsliding using digital elevation data, *Hydrological Processes*, *9*, 383-400.

Dietrich, W. E., D. G. Bellugi, L. S. Sklar, J. D. Stock, A. M. Heimsath, and J. J. Roering (2003), Geomorphic transport laws for predicting landscape form and dynamics, *Prediction in Geomorphology Geophysical Monograph 135*.

Flint, J. J. (1974), Stream gradient as a function of order, magnitude, and discharge, *Water Resources Research*, *10*(5), 969-973.

Gilbert, G. K. (1877), Geology of the Henry Mountains, (Utah), 160 pp, Geographical and geological survey of the Rocky Mountains Region, U.S., Government printing office, Washington, D.C., U.S.

Gilbert, G. K. (1909), The Convexity of Hilltops, *The Journal of Geology*, *17*(4), 344-350.

Granger, D. E., and C. S. Riebe (2007), Cosmogenic nuclides in weathering and erosion, in *Treatise on Geochemistry, Volume 5: Surface and Ground Water, Weathering, and Soils*, edited by J. I. Drever, Elsevier, London.

Granger, D. E., J. W. Kirchner, and R. C. Finkel (1996), Spatially averaged long-term erosion rates measured from in situ-produced cosmogenic nuclides in alluvial sediment, *The Journal of Geology*, *104*(3), 249-257.

Hack, J. T. (1957), Studies of longitudinal stream profiles in Virginia and Maryland, 97 pp.

Heimsath, A. M., W. E. Dietrich, K. Nishiizumi, and R. C. Finkel (1997), The soil production function and landscape equilibrium, *Nature*, *388*, 358-361.

Kirchner, J. W., R. C. Finkel, C. S. Riebe, D. E. Granger, J. L. Clayton, J. G. King, and W. F. Megahan (2001), Mountain erosion over 10 yr, 10 k.y., and 10 m.y. time scales, *Geology*, *29*(7), 591-594.

Kirkby, M. J. (1971), Hillslope process-response models based on the continuity equation, *Institute of British Geographers Special Publication*, *3*, 15-30.

Langbein, W. B., and S. A. Schumm (1958), Yield of sediment in relation to mean annual precipitation, *EOS, American Geophys. Union Transactions*, *39*(6), 1076-1084.

Lavé, J., and D. W. Burbank (2004), Denudation processes and rates in the Transverse Ranges, southern California: Erosional response of a transitional landscape to external and anthropogenic forcing, *Journal of Geophysical Research*, *109*.

Montgomery, D. R., and E. Foufoula-Georgiou (1993), Channel Network Source Representation Using Digital Elevation Models, *Water Resources Research*, *29*(12), 3925-3934.

Schumm, S. A. (1963), The disparity between present rates of denudation and orogeny, *United States Geological Survey Professional Paper*, *454-H*.

von Blanckenburg, F. (2005), The control mechanisms of erosion and weathering at basin scale from cosmogenic nuclides in river sediment, *Earth and Planetary Science Letters*, *237*(3-4), 462-479.

Whipple, K. X. (2004), Bedrock rivers and the geomorphology of active orogens, *Annual Review of Earth and Planetary Sciences*, *32*, 151-185.

CHAPTER 2

LANDSCAPE FORM AND MILLENNIAL EROSION RATES IN THE SAN GABRIEL MOUNTAINS, CA

ABSTRACT

It has been long hypothesized that topography, as well as climate and rock strength, exert first order controls on erosion rates. Here we use detrital cosmogenic ^{10}Be from 50 basins, ranging in size from 1-150 km^2, to measure millennial erosion rates across the San Gabriel Mountains in southern California, where a strong E-W gradient in relief compared to weak variation in precipitation and lithology allow us to isolate the relationship between topographic form and erosion rate. Our erosion rates range from 30-1000 m/Ma, and generally agree with both decadal sediment fluxes and long term exhumation rates inferred from low temperature thermochronometry. Catchment-mean hillslope angle increases with erosion rate until ~300 m/Ma, at which point slopes become invariant with erosion rate. Although this sort of relation has been offered as support for non-linear models of soil transport, we use 1-D analytical hillslope profiles derived from existing soil transport laws to show that a model with soil flux linear in slope, but including a slope stability threshold, is indistinguishable from a non-linear law within the scatter of our data. Catchment-mean normalized channel steepness index increases monotonically, though non-linearly, with erosion rate throughout the San Gabriel Mountains, even where catchment-mean hillslope angles have reached a threshold. This non-linearity can be mostly accounted for by a stochastic threshold incision model, though additional factors likely contribute to the observed relationship between channel steepness and erosion rate. These findings substantiate the claim that the normalized channel steepness index is an important topographic metric in active ranges.

INTRODUCTION

Modern surface topography reflects the competition and interaction between climatic and tectonic forcing. Whereas climatic and tectonic variables are often difficult to quantify, surface topography can be readily obtained for much of the Earth's land surface from spaceborne sensors and aerial photography. However, extracting quantitative understanding of the interactions among climate, topography, and tectonics requires the unraveling of the relative contributions of a complicated suite of surface processes. Consequently, a central theme in modern geomorphology involves linking surface processes and their rates to observed landforms [e.g., *Dietrich et al.*, 2003]. Such quantitative knowledge is required before we can fully exploit the archive of climatic and tectonic history that is encoded in landforms.

The importance of probing current topography for clues to process rates and mechanics is well recognized, and many have proposed that erosion rate increases with hillslope angle and local relief [e.g., *Ahnert*, 1970; *Gilbert*, 1877; *Montgomery and Brandon*, 2002]. Basic observations support this, and the concept of slope-dependent soil flux on hillslopes has been around for over 100 years [*Davis*, 1892]. Similarly, decadal sediment yield measurements were widely used to infer quantitative relationships between erosion rate and precipitation, uplift, and relief [e.g., *Ahnert*, 1970; *Judson and Ritter*, 1964; *Langbein and Schumm*, 1958; *Schumm*, 1963]. Much uncertainty remains, however, regarding interrelationships among channel steepness, hillslope gradients, relief measured at various scales, and erosion rate even within a single climate zone. In addition, data of sufficient quality and distribution to allow rigorous testing of existing theory are sparse. Cosmogenic radionuclide (CRN) dating of surfaces and inference of erosion rates, in conjunction with the widespread availability of digital elevation models, affords an opportunity to make significant progress on this problem.

Beginning with *Granger et al.* [1996], there have been a number of comparisons of hillslope gradients with millennial erosion rates determined with CRN [e.g., *Binnie et al.*, 2007; *Ouimet et al.*, 2009; *Safran et al.*, 2005; *Stock et al.*, 2008; *Vanacker et al.*, 2007], as well as studies comparing erosion rates with various measures of local relief [e.g., *Burbank et al.*, 1996; *Montgomery and Brandon*, 2002; *Schaller et al.*, 2001; *Wittmann et al.*, 2007]. As initially noted by *Penck* [1953] and *Strahler* [1950], and later recast by *Burbank et al.* [1996], *Schmidt and Montgomery* [1995], and *Montgomery and Brandon* [2002], meso-scale rock strength limitations result in hillslopes reaching threshold angles wherever erosion rate exceeds a critical value. Above this rate, hillslopes are thought to respond to further increases in base level lowering rate via increasing landslide frequency [*Hovius et al.*, 1997] and possibly slope length [*Howard*, 1994; *Tucker and Bras*, 1998]. Recent studies corroborated these thoughts on the transition to threshold hillslopes and provided the first quantification of this critical erosion rate. In the semi-arid, granitic San Bernardino Mountains, *Binnie et al.* [2007] found that above erosion rates of ~250 m/Ma, catchment-averaged hillslope angle remains constant, consistent with field observations of landslide-dominated terrain. *Ouimet et al.* [2009] found similar results for semi-arid catchments in both granitic rocks and highly deformed Triassic flysch on the eastern margin of the Tibetan Plateau.

Comparison of erosion rates with channel form garnered considerably less attention, with only a few studies addressing the problem using cosmogenic radionuclides [e.g., *Ouimet et al.*, 2009; *Safran et al.*, 2005]. Other workers [e.g., *Duvall et al.*, 2004; *Kirby and Whipple*, 2001; *Lague and Davy*, 2003; *Snyder et al.*, 2003] used independent measures of rock uplift rate to calibrate models of river long profile evolution. Nonetheless, there is a dearth of data suitable for quantifying many basic relationships (influence of sediment supply, climate, lithology, channel width, etc.) and for testing models of river incision into bedrock [e.g., *Whipple*, 2004].

In this contribution, we quantify and use CRN (^{10}Be) based erosion rates in the San Gabriel Mountains, southern California, and use a 10 m digital elevation model (DEM), to: (1) evaluate in detail different topographic metrics; (2) test the application of detrital CRN techniques to landslide dominated catchments and across catchment sizes; (3) quantify the relationship between erosion rate and average hillslope gradient, expanding available data and evaluating existing hillslope transport models; and (4) quantify the relation between erosion rate and channel steepness and discuss implications for theory.

STUDY AREA

The San Gabriel Mountains (SGM) provide an excellent field setting for studying the relationship between topographic form and erosion rate. The range lies along a large restraining bend in the San Andreas Fault in southern California (Figure 2.1), where active thrusting along the Sierra Madre and Cucamonga fault zones at the southern range front maintained Holocene vertical slip rate components of 0.5-0.9 mm/a [*Lindvall and Rubin*, 2008; *Peterson and Wesnousky*, 1994]. Uplift of the SGM began with the switch of activity from the San Gabriel Fault to the current trace of the San Andreas Fault, ca. 5-7 Ma [*Matti and Morton*, 1993]. A progressive increase of dip-slip fault motion from west to east creates a strong gradient of relief, short term sediment flux (decadal reservoir fills) and long term (Ma) exhumation rates (inferred from apatite fission track and (U-

Th)/He thermochronology), all increasing to the east [*Blythe et al.*, 2000; *Lavé and Burbank*, 2004; *Spotila et al.*, 2002].

Mean annual precipitation rates (MAP) vary south to north, from 0.5 m/a in the Los Angeles basin, increasing to 1.3 m/a over the range crest, and decreasing to 0.2 m/a in the southern Mojave Desert (PRISM – www.prism.oregonstate.edu). We focused on mainly south-draining basins with MAP ranging from 0.6-1.0 m/a with elevation. The impact of this gradient on runoff is potentially mediated by a transition from rain to snow above 2000 m elevation. While detailed long-term climate is poorly constrained, there is no evidence for glaciation in the SGM.

The geology of the SGM consists primarily of Precambrian and Mesozoic granitic and metamorphic rocks. Lithological variation has two potential impacts on our analysis. First, uneven quartz distribution within basins can bias calculated basin-wide erosion rates [*Bierman and Steig*, 1996; *Small et al.*, 1999]. The only basin that fits this criterion, Falls Creek (SG0730), is characterized by low relief headwaters cut on a quartz-poor syenite-anorthosite complex above a major knickpoint at the lower end of the basin below which a deep gorge is cut into granite. Guided by available geologic maps [*Morton and Miller*, 2006; *Yerkes and Campbell*, 2005], all other catchments samples were carefully selected to avoid such complications. Second, material strength differences between lithologies may influence slope stability thresholds and thus catchment mean slopes, drainage density, and relief. Similarly subtle lithologic differences could influence the fraction of sediment delivered to channels as bed-load and its grain size distribution, both of which could affect the relationship between channel steepness and erosion rate. Such variations do not appear to be strong, but likely contribute to scatter in our data.

The strong E-W gradient in relief, in comparison to a weak variation in precipitation and relatively spatially homogenous lithology optimizes our ability to isolate the topographic controls on erosion. In addition, the drainage networks in the SGM are nearly fully integrated, allowing for appropriate comparisons between low and high relief landscapes across basin sizes.

We also compare our results in the SGM to a similar data set in the San Bernardino Mountains (SBM), which lie just to the east across the San Andreas Fault [*Binnie et al.*, 2007]. Lithology and climate in the SBM are similar to that of the SGM, but the topography and relief structure is strikingly different. The Big Bear Plateau dominates the central SBM, and represents an uplifted low relief surface that has yet to adjust to the regional base level [*Spotila et al.*, 1998]. Additionally, rapidly uplifting regions determined from CRN [*Binnie et al.*, 2007] and low-temperature thermochronometry [*Blythe et al.*, 2000; *Spotila et al.*, 1998], are isolated and lack drainage basins larger than 10 km^2.

METHODS

Cosmogenic Erosion Rates

Traditionally, erosion rates were estimated by measuring suspended sediment loads or sediment accumulation behind dams over years to decades. These methods are subject to important weaknesses; they fail to capture the role of large events, and are sensitive to anthropogenic impacts and the fire cycle [e.g., *Kirchner et al.*, 2001; *Lavé and Burbank*, 2004]. Catchment averaged CRN methods, in contrast, are relatively insensitive to short term perturbations and provide geomorphically pertinent erosion rates [*Bierman and Nichols*, 2004; *von Blanckenburg*, 2005].

We measured ^{10}Be concentrations in quartz-rich sediments for 50 basins ranging in size from 1-150 km^2 across the region (Figure 2.1) to determine catchment averaged erosion rates [*Bierman and Steig*, 1996; *Brown et al.*, 1995; *Granger et al.*, 1996]. This method has been successfully applied in numerous studies of upland landscapes [e.g., *von Blanckenburg*, 2005 and references within]. The timescale over which the erosion rates integrate can be estimated by dividing the cosmic ray penetration depth (~0.6 m in rock) by the calculated erosion rate (for our case 0.1 – 1 m/ka). For the SGM, this implies timescales ranging from ~1-50 ka. Application of detrital CRN methods to landscapes dominated by mass wasting was evaluated numerically by *Niemi et al.* [2005] and *Yanites et al.* [2009], both of whom suggest that at high erosion rates, larger basins must be sampled to better integrate stochastic landslide inputs and to ensure adequate fluvial mixing. Field testing in the slowly-eroding Great Smoky Mountains by *Matmon et al.* [2003] also shows that larger basins provide more accurate measures of erosion rate. However, a recent study in the neighboring San Bernardino Mountains suggests that accurate erosion rate measurements in threshold landscapes are possible in basins as small as 1-3 km^2 [*Binnie et al.*, 2007].

With this in mind, our sampling scheme in the SGM focused primarily on basins draining areas greater than 1 km^2 in soil-mantled catchments, and greater than 20 km^2 in bedrock dominated catchments. Large basins (>100 km^2) in both the low and high uplift regions were sampled, and we avoided catchments exhibiting strongly transient behavior (containing major knickpoints). With one exception (Cucamonga Canyon, SG162, SG163), we also avoided catchments with clear evidence of recent floods or large landslides.

For each catchment, we separated quartz using standard techniques [*Kohl and Nishiizumi*, 1992] while PrimeLab (Purdue University) performed the ^{10}Be isolation and measurement. We calculated ^{10}Be production rates for each catchment, correcting for elevation and latitude on a pixel by pixel basis using the 10 m DEM for the catchment [*Dunai*, 2000]. Topographic shielding, snow cover, and muogenic production were not accounted for, and contribute to an estimated 5% uncertainty in production rates that is added to the 1σ analytical error. Although we lacked data to precisely quantify possible variability in quartz content, we do not expect significant variation as nearly all of the basins sample quartz-rich basement rocks or granitic intrusions. Comparing our data with that of *Binnie et al.* [2007] in the SBM (Figure 2.1) enables an excellent test of the reproducibility and reliability of the detrital CRN method in rapidly eroding mountainous topography; catchments span similar ranges of topographic metrics in very similar settings, but different researchers selected sampling locations, different laboratories prepared targets, different facilities measured ^{10}Be, and our combined data encompass a wide range of catchment size across the full spectrum of erosion rates. The range of catchment sizes and the development of relations between erosion rate and topographic metrics also begin to test the model predictions that the detrital CRN method will typically underestimate erosion rates where landsliding is a common process, and that this underestimation increases with decreasing catchment size [*Niemi et al.*, 2005; *Yanites et al.*, 2009].

Catchment-Mean Hillslope Angle

We used a 10 m digital elevation model to extract a catchment-mean hillslope angle for each sample basin. Local slope for each pixel in the DEM is the dip of a plane fit to a 3 x 3 array of pixels centered on the pixel of interest, and we averaged individual pixel slopes for each catchment. To focus our attention on the hillslopes, we selectively excluded valley fill from our calculation, though few of our sample basins are significantly aggraded. As our sampling strategy excluded transient basins characterized by prominent knickpoints, inner gorges, and remnant patches of low-relief landscapes at high elevation, calculating catchment mean hillslope angle for SGM sample basins is straightforward.

Evaluating a representative hillslope from transient basins, in which there is a bimodal hillslope distribution is more complicated, and seven catchments used by *Binnie et al.* [2007] are affected. These catchments primarily lie along the southern front of the Big Bear Plateau, with this relict, low relief surface contributing significantly (20-30%) to their catchment areas. A minimum value for the representative catchment mean hillslope angle is simply the mean slope in the entire catchment, as reported by *Binnie et al.* [2007]. However, as the CRN-derived erosion rate will be strongly weighted to the steep, incised lower portions of these catchments, the catchment mean hillslope angle associated with this erosion rate is probably closer to the mean hillslope angle downstream of the plateau edge (which provides a maximum estimate of the representative catchment mean hillslope angle). We use these minimum and maximum bounds to define error bars on catchment mean slope and take a weighted average of these slopes as a best estimate. The mean slopes of the part of the catchment on the plateau and that below the plateau were weighted by their predicted fractional contribution to the total sediment flux out of the basin, based on the relationship between erosion rate and mean slope defined by our data in the SGM. Generally this flux-weighted mean slope is close to the maximum estimate given by the mean slope of the steep, incised lower portions of these disequilibrium catchments. We show both minimum and maximum representative catchment mean slope in plots and stress that these points are included for visual comparison only. The complexity of these seven basins does highlight the importance of selecting well-adjusted catchments with uniform topographic characteristics to most clearly define the relationships among topographic metrics and erosion rate.

Catchment-Mean Channel Steepness Index

Graded fluvial channels tend to follow a power law relationship between local slope (S) and upstream drainage area (A) commonly referred to as Flint's law [*Flint*, 1974; *Hack*, 1957]:

$$S = k_s A^{-\theta}, \tag{2.1}$$

where k_s is the channel steepness index and θ is the concavity index. Models of fluvial incision ranging from detachment-limited to transport-limited end-members all predict a monotonic relation between channel slope and rock uplift rate at steady state (when erosion rate = rock uplift rate), generally well approximated as a power-law relation [*Lague et al.*, 2005; *Sklar and Dietrich*, 2004; *Snyder et al.*, 2003]:

$$S \propto U^p \propto k_s. \tag{2.2}$$

The predicted relation between k_s and U varies between models and depends on climate, rock strength, and dominant incision process (e.g., plucking, bed-load abrasion). For the well known end-member stream power models of detachment-limited and transport-limited incision, channel steepness index k_s is given by, respectively:

$$k_s = (U / K_d)^{1/n}, \tag{2.3a}$$

$$k_s = (\beta U / K_t)^{1/n_t}, \tag{2.3b}$$

where U is rock uplift rate, n and n_t are the stream power slope exponents, such that $p = 1/n$ or $1/n_t$, for detachment- and transport-limited cases, respectively, K_d and K_t are the coefficients of erosional efficiency (function of climate, lithology, etc.) for detachment- and transport-limited cases, respectively, and β is the fraction of total load delivered to channels as bedload. These and most other models predict that channel concavity is independent of rock uplift rate at steady state [e.g., *Whipple and Tucker*, 1999], an expectation borne out by field observations in many landscapes, including the SGM [*Tucker and Whipple*, 2002; *Wobus et al.*, 2006]. In analyses of topographic data using equation (2.1), a complication arises in that slight variations in best-fit concavity index (θ) exist in every landscape and estimates of k_s are strongly correlated to the fit concavity index [e.g., *Sklar and Dietrich*, 1998]. This can be resolved by evaluating a normalized channel steepness index using a fixed reference concavity, θ_{ref} [e.g., *Wobus et al.*, 2006]:

$$S = k_{sn} A^{-\theta_{ref}} \quad . \tag{2.4}$$

By fixing $\theta = \theta_{ref}$, and making the assumption that K_d and n do not vary systematically across the landscape, k_{sn} (normalized channel steepness index) proves to be a useful metric for studying the relations between topography and rock uplift or erosion [e.g. *Hilley and Arrowsmith*, 2008; *Kirby and Whipple*, 2001; *Kobor and Roering*, 2004; *Snyder et al.*, 2000]. *Wobus et al.* [2006] provide additional examples and detailed methodology concerning the extraction of river profile topography from DEMs and the fitting of k_{sn} to individual channel segments.

For this study, we determined a representative k_{sn} for each of our sample basins in the SGM, and also where possible (i.e., for catchments of sufficient size) for the basins sampled in the SBM by *Binnie et al.* [2007]. We followed a methodology similar to that used by *Ouimet et al.* [2009]. Using a fixed reference concavity index of 0.45, we used a freely available set of Matlab and ArcMap scripts (http://www.geomorphtools.org) to automate profile fits for all channel reaches (500 m segments) draining >2 km^2 from the 10 m resolution USGS NED DEM (Figure 2.2). We report the catchment average k_{sn} for each sample basin as the mean k_{sn} of all individual reaches, with an uncertainty of 2 standard errors about this mean. Errors associated with individual reach fits (2 standard deviations) are much less than intra-basin variability of k_{sn}. We did not assign a channel steepness index to small (<2 km^2), steep, rocky catchments (especially those in the SBM), as the slope-area data for these basins do not conform to Flint's law, showing little or no variation of slope with drainage area.

Catchment-Mean Local Relief

Studies of the controls on denudation rate often use various measures of topographic relief as their primary topographic metric [e.g., *Aalto et al.*, 2006; *Ahnert*, 1970; *Montgomery and Brandon*, 2002]. Relief is by definition a scale-dependent measurement, and how the scale of analysis affects what aspect of topographic form (hillslope relief, colluvial channel relief, fluvial tributary relief, main stem relief, and combinations thereof) is measured has never been systematically evaluated. Here we quantify the relations among mean hillslope angle, mean channel steepness index, and mean local relief measured over a wide range of length scales for all the catchments sampled within the SGM. Following *Ahnert* [1970] and *Montgomery and Brandon* [2002], for each pixel in the SGM DEM we measured local relief within a circular window with radius ranging from 100 m to 5 km. Catchment mean local relief is simply the average of all values within a catchment. It should be noted that for small catchments and large relief windows, local relief calculations may incorporate topography outside of the basin. For convenience we plot these data as normalized mean local relief, where normalized local relief is defined as elevation range divided by window diameter.

RESULTS

Interrelations Among Topographic Metrics

Catchment-mean hillslope angle increases with increasing channel steepness index until k_{sn}~100 $m^{0.9}$, above which hillslope angles become invariant (Figure 2.3). The form of this relationship supports the hypothesis that channel steepness reflects erosion rates, thus retaining a tectonic signature, in landscapes where hillslopes have achieved threshold gradients, and corroborates the similar relationship found by *Ouimet et al.* [2009].

Figure 2.4 highlights the complex relationships among the various topographic metrics (e.g., slope angle, relief, k_{sn}), and the significant influence of the measurement scale of relief. At the smallest scales (10's to 100's of m) local relief is simply a proxy for hillslope angle. Indeed, hillslope gradient can be thought of as fine scale relief normalized for the length scale over which it is measured. Relief measured with a 100 m radius window is tightly correlated to mean basin gradient (Figure 2.4a), while at progressively larger scales (1-5 km), tributary channel relief begins to dwarf hillslope relief [*Whipple et al.*, 1999], and local relief begins to be a measure of tributary channel steepness. At still larger scales (>10 km) trunk channel relief is incorporated, and eventually relief becomes solely a measure of range height. In the SGM, relief measured with a 2.5 km radius window tracks linearly with channel steepness index (Figure 2.4b). In addition, the spatial pattern of 2.5 km-scale local relief maps directly with the spatial pattern of channel steepness index values (Figure 2.2). This optimal relief scale is not universal and can be expected to vary with catchment size, relief magnitude, and drainage density.

Though these two metrics are strongly correlated, there are important advantages to using k_{sn} rather than relief. First, not all of the spatial variation in channel steepness is captured by km-scale relief; lithologic controls on channel steepness, uplift patterns associated with active structures, and knickpoints associated with accelerated incision are much more finely resolved using k_{sn}. Additionally, k_{sn} can be derived from specific, process-based models of river incision and is scale independent, while local relief always measures a combination of landscape elements (e.g., hillslope relief, colluvial and fluvial channel steepness, channel length) governed by distinct processes and involves additional uncertainty in determining an appropriate measurement scale. Relief is however, easier and quicker to calculate than channel steepness, and can yield information in preliminary landscape analysis to help direct further, more detailed topographic examination.

Spatial Distribution of Topographic Metrics

Catchment-mean hillslope angle in the SGM varies from 10 to 38 degrees, generally increasing from west to east until hillslopes attain threshold values. No clear dependence of catchment-mean slope on drainage area is seen. Basin slope distributions are predominantly normally distributed; skewed or bimodal distributions are either attributable to large areas of low slope such as wide valley bottoms and terraces or reflect potential disequilibrium conditions with low relief surfaces perched above significant knickpoints in channel profiles.

Local channel steepness values range from below 20 to over 500 $m^{0.9}$ (Figure 2.2). However, the highest values are confined primarily to immediately below significant knickpoints. Catchment mean k_{sn} in the SGM ranges from 20-200 $m^{0.9}$, covering much of the known worldwide variation in k_{sn} [*Wobus et al.*, 2006]. Similar to hillslope angle, channel steepness index increases generally from west to east, with no dependence on drainage area. Basins from the SBM sampled by *Binnie et al.* [2007] for detrital CRN were also analyzed for comparison. In the SBM, channel steepness index averaged over the basin has a smaller range than in the SGM. This likely reflects the fact that all of the rapidly eroding (>0.7 mm/a) SBM sample basins are less than 2 km^2. These channels likely are entirely dominated by debris flows [e.g., *Montgomery and Foufoula-Georgiou*, 1993; *Stock and Dietrich*, 2003], making determination of channel steepness values inappropriate.

Erosion Rates and Topography

Catchment averaged erosion rates, inferred from ^{10}Be concentrations in alluvial sands, range from 30 to 1000 m/Ma in the SGM (Table 2.1), and are in general agreement with both long-term (Ma) estimates from low-temperature thermochronometry work [*Blythe et al.*, 2000; *Spotila et al.*, 2002] and decadal sediment yield data compiled by *Lavé and Burbank* [2004]. For catchments sampled in the SGM, we do not expect the actual erosion rates to have any dependence on drainage area. However, for reasons discussed earlier, we expect that the CRN derived erosion rates may systematically underestimate the actual erosion rates for landslide-dominated catchments, with the effect being strongest for small catchments (<10 km^2) [*Niemi et al.*, 2005; *Yanites et al.*, 2009]. Although we introduced a slight sampling bias towards larger basins in areas of high relief to account for this effect, our measured erosion rates in the SGM show little dependence on drainage area across a wide range of both basin size (0.1 – 100 km^2) and erosion rate (10 – 1000 m/Ma, Figure 2.5). In addition, in the SBM, rapid uplift is constrained to narrow ridges between faults that preclude sampling large, high relief basins. As a result, there is a sampling bias towards smaller basins at high erosion rates [*Binnie et al.*, 2007]. Taken together, there appears to be no dependence of CRN derived erosion rate on drainage area, though it should be noted that neither of these two datasets were collected with the explicit intention of testing this hypothesis. The data suggest that models of the impact of stochastic sediment delivery on erosion rates estimated from detrital CRN concentrations may exaggerate the influence of large landslides, a tentative conclusion that warrants caution applying these models for data interpretation and merits further investigation.

Catchment-mean hillslope angle increases with erosion rate until ~300 m/Ma (Figure 2.6). At erosion rates higher than ~300 m/Ma, catchment-averaged slopes are invariant at a threshold value of ~35 degrees. Detrital CRN data from the SBM [*Binnie et al.*, 2007] are also plotted here and follow the same trend, particularly after correcting mean slope estimates for SBM basins with headwater reaches on the Big Bear plateau surface.

Channel steepness index increases non-linearly but monotonically with erosion rate throughout the range of observed erosion rates, with some scatter (Figure 2.7). The channel steepness index therefore records erosion rate information in threshold landscapes, where hillslope form is no longer sensitive to erosion rate, and thus serves as a key metric for interpreting rapidly eroding landscapes in tectonically active settings [see also *Ouimet et al.*, 2009]. Comparison with channel profile analysis of the SBM dataset shows a very similar trend for erosion rates below 500 m/Ma. As noted earlier, more rapidly eroding basins in the SBM are almost all too small to allow meaningful assessment of the normalized channel steepness index.

ANALYSIS

Catchment Mean Slope and Erosion Rate

To model the morphological transition from slope-dependent to threshold hillslopes, soil transport laws that account for both creep-related and landslide processes must be used [e.g., *Anderson*, 1994; *Howard*, 1994; *Roering et al.*, 1999]. Two end-member approaches allow for analytical 1-D profile analysis:

$$q_s = \frac{-KS}{1-\left({}^{S}\!/_{S_c} \right)^2} \tag{2.5a}$$

$$\begin{aligned} q_s &= -KS; \quad |S| < S_c \\ q_s &= \infty; \qquad |S| \geq S_c \end{aligned} \tag{2.5b}$$

where q_s is the volumetric soil flux (m^2/yr), K is the transport coefficient (m^2/yr), S is local slope ($\mathrm{d}z/\mathrm{d}x$), and S_c is a critical slope at which soil flux approaches infinity. Equation (5a) is a non-linear transport law [*Roering et al.*, 1999] supported by field [e.g., *Pelletier and Cline*, 2007] and experimental [e.g., *Gabet*, 2003] studies, while equation (5b) represents a simple, linear slope-dependent flux at slopes less than critical, with a transition to infinite potential soil transport capacity above a threshold slope. Both of these models can be combined with a statement of mass conservation to derive one-dimensional steady-state characteristic forms [e.g., *Kirkby*, 1971; *Roering et al.*, 2007]:

$$z(x) = \frac{KS_c^2}{2(\rho_r/\rho_s)E} \left[\begin{matrix} \ln\left(\frac{1}{2}\left(\sqrt{1+\left(\frac{2(\rho_r/\rho_s)Ex}{KS_c} \right)^2} + 1 \right) \right) - \\ \sqrt{1+\left(\frac{2(\rho_r/\rho_s)Ex}{KS_c} \right)^2} + 1 \end{matrix} \right] \tag{2.6a}$$

$$z(x) = \frac{-(\rho_r/\rho_s)Ex^2}{2K} \qquad x < x_t$$

$$z(x) = -S_c x + \frac{1}{2} S_c x_t \qquad x \geq x_t \tag{2.6b}$$

$$x_t = \frac{KS_c}{(\rho_r/\rho_s)E}$$

where $z(x)$ is the surface elevation, E is erosion rate, and x_t is the transition point from convex to planar hillslopes for the linear with threshold model (for full derivations of equations (6a) and (7a), see *Roering et al.* [2007]). Taking the derivative of equation (6) with respect to x and averaging slope over the horizontal hillslope length L_H, steady state relationships between profile-averaged hillslope gradient, S_{ave}, and the variables E, S_c, K, and L_H can be derived:

$$S_{ave} = S_c \frac{1}{E^*}\left(\sqrt{1+(E^*)^2} - \ln\left(\frac{1}{2}\left(1+\sqrt{1+(E^*)^2}\right)\right) - 1\right) \tag{2.7a}$$

$$S_{ave} = S_c\left(1-\frac{1}{E^*}\right) \qquad E^* \geq 2$$

$$S_{ave} = \frac{E^* S_c}{4} \qquad E^* < 2 \tag{2.7b}$$

$$E^* = \frac{2E(\rho_r/\rho_s)L_H}{KS_c}$$

where E^* is a dimensionless erosion rate [*Roering et al.*, 2007]. Thus for each model the average slope of a 1-D hillslope varies with K/L_H – any change to this ratio has an equivalent effect on mean slope. Note that the linear transport law with a threshold predicts a distinctly non-linear relationship between mean slope and erosion rate. Thus an observation of such a non-linear relation does not necessarily support a non-linear diffusion model. The relations between mean slope and erosion rate derived above are distinct from that proposed by *Montgomery and Brandon* [2002]. They predict similar non-linear forms, but make explicit how measurable hillslope transport coefficients (K), hillslope length (L_H), and soil density (ρ_r/ρ_s) influence the erosion coefficient in the *Montgomery and Brandon* [2002] relationship.

Modeling one-dimensional hillslope profiles using the above framework is straightforward, though extending known controls on mean slope of these "characteristic forms" to full landscapes is not. Local variables that govern sediment transport (i.e., slope) must be related to basin-averaged measurements to make comparisons with catchment-averaged cosmogenic erosion rates. *Roering et al.* [2007] have shown that, to first order, this can be done by calculating the average slope over a representative (average length, L_H) 1-D hillslope profile and equating this to the catchment mean hillslope angle. Because this approach allows only a first order comparison, we do not attempt to use our data to constrain statistical best-fit model parameters. Instead, we aim to evaluate whether realistic values of model parameters reasonably predict observed relations between topography and erosion rates and to determine whether the two models can be distinguished based on these types of data.

Reasonable estimates of all parameter values for these hillslope soil transport models can be readily determined. Our DEM analysis suggests that $S_c \geq 35^{\circ}$, consistent with estimates elsewhere [e.g., *Roering et al.*, 2007]. DEM analysis and aerial photograph interpretation suggest $L_H = 75$m is reasonable for the SGM, but is variable within catchments and may vary with erosion rate – a complication that merits further investigation. A value of 2 is taken as the typical density ratio for granitic soils. Given these constraints, and the scatter in our data, we find that reasonable values of K (0.008 and 0.015 m^2/yr for 7A and 7B, respectively) and S_c (39º and 37º for equations (7a) and

(7b), respectively) provide visually satisfying fits to our data using both models (solid lines in Figure 2.6). In addition to inherent uncertainty in erosion rate estimates from detrital CRN concentrations, scatter in our data is likely due to variability in lithology, hillslope length, and aspect within our sample basins, and should be expected with such a crude mapping of the local, process-controlling slope to a variable such as catchment-mean hillslope angle.

Catchment Mean Channel Steepness Index and Erosion Rate

As noted earlier, channel steepness index increases non-linearly with erosion rate in the SGM, and approximately follows the power-law relation described by equation (2) where $p \sim ½$. Other researchers have found this relationship to be approximately described by $p = 1$ [*Kirby and Whipple*, 2001; *Lague and Davy*, 2003], $p = 1/2$ [*Ouimet et al.*, 2009], and $p = 1/4$ [*Snyder et al.*, 2003]. The stream power model of detachment-limited bedrock incision is consistent with a range of non-linear behaviors ($3/5 \leq p \leq 3/2$), depending on process mechanics [*Hancock et al.*, 1998; *Whipple et al.*, 2000]. However, for $p < 1$ channels are predicted to become buried in sediment as erosion rates and sediment fluxes increase such that they are forced to maintain a slope sufficient to transport the full sediment load [*Tucker and Whipple*, 2002]. Consistent with this, the majority of channels in the SGM, including those in high-relief, rapidly eroding areas, show little bedrock exposure in their beds and are likely transporting sediment near capacity. Simple models (e.g., equation (3b)) for this transport-limited condition predict $p = 1$ (bedload transport capacity is linear in slope), implying $p \geq 1$ across the SGM.

In light of the expectation that a transition to transport-limited conditions will preclude a sub-linear relationship between channel steepness and erosion rate, why our data suggest $p = ½$ becomes an important question. To account for the observed non-linear relationship between channel steepness and erosion rate ($p < 1$), transport as well as detachment processes must be affected. We use here the stochastic threshold model of *Tucker and Bras* [2000] and *Tucker* [2004], which combines a threshold shear stress for motion or detachment with variable discharge via an exponential probability distribution of rainfall in a stream-power type incision model.

In its simplest form, the stochastic threshold model expands the coefficient of erosional efficiency, K_d in equation (3a), into three terms, such that:

$$E = K_R K_C K_{\tau c} A^m S^n , \tag{2.8}$$

where K_R encompasses the physical parameters of channel geometry, hydraulic roughness, and substrate resistance to erosion, K_C is a function of stochastic climate parameters, and $K_{\tau c}$ is a threshold term set by the critical shear stress and local channel slope that varies between 0 and 1 [*Tucker*, 2004; *Whipple*, 2004]. To illustrate the implications of this model for the SGM data, we used channel geometry and hydraulic roughness constants consistent with *Snyder et al.* [2003] and *Tucker* [2004]. Climate parameters were estimated from rainfall records at Mt. Baldy (National Climatic Data Center – http://www.ncdc.noaa.gov), and kept constant for all basins. We then adjusted the critical shear stress (controls height of rollover) and substrate resistance to erosion (controls slope of curve at high erosion rate) to fit our data by eye in Figure 2.7. We find that the stochastic threshold model can explain much of the variance in our data using reasonable parameter estimates (Figure 2.7).

DISCUSSION

Implications for Channel Incision Theory

Our analysis demonstrates that much of the non-linearity of the relation between channel steepness index and erosion rate ($p < 1$) can be explained by the combined effects of a critical threshold for bedload entrainment or bedrock detachment and a stochastic distribution of floods (Figure 2.7). This is, however, a non-unique finding. There are numerous alternate mechanisms for generating $p < 1$. Two frequently discussed factors include orographic precipitation effects [*Roe et al.*, 2002], and a narrowing of channel width with erosion rate [*Finnegan et al.*, 2005], but neither appear to play an important role in the SGM. We purposefully selected catchments with only weak orographic effects (mean annual rainfall increases from ~0.6 to ~0.9 m/a from low to high relief catchments). Also, field observations do not support significant channel narrowing with increased erosion rate in well-adjusted, quasi-equilibrium catchments [*DiBiase et al.*, 2007]. In addition, systematic changes in the caliber, durability, and fraction of bedload sediment (β) with erosion rate, as well as an increase in debris flow activity with increasing erosion rate, may influence the relationship between k_{sn} and erosion rate [e.g., *Sklar and Dietrich*, 2006; *Stock and Dietrich*, 2003]. Additional field measurements are necessary to evaluate how important these factors may be in this, and other, landscapes.

What is most satisfying about the simple stochastic threshold model illustrated in Figure 2.7 is that it incorporates only effects that we know with certainty must operate in all landscapes (thresholds of motion and/or detachment and stochastic floods). Much of the non-linearity in the relation between channel steepness index and erosion rate seen in our data can be explained by these effects alone, suggesting that, in aggregate, other factors exert only a secondary influence. Additional erosion rate and topography data from a range of landscapes in different geologic, tectonic, and climatic settings will be required to fully evaluate this tentative conclusion.

Implications for Hillslope Transport Theory

A non-linear relation between catchment-mean hillslope angle and erosion rate is used [e.g., *Montgomery and Brandon*, 2002; *Roering et al.*, 2007] to support the non-linear transport model of *Roering et al.* [1999]. Whereas available data is consistent with this model, our analysis demonstrates that the simpler linear-threshold model (equation (7b)) fits the data from the SGM and SBM equally well. Indeed, predictions of the two models are so similar that they will likely remain indistinguishable on the basis of the relation between mean slope and erosion rate, though experimental studies of granular creep [*Roering et al.*, 2001] and dry ravel [*Gabet*, 2003] clearly distinguish and support the non-linear model. Ouimet et al. [2009] reached a similar conclusion based on their data from catchments on the eastern margin of the Tibetan Plateau (ETP).

Interestingly, very similar values of the hillslope transport coefficient (*K*) provide the visually most satisfying fit to data from SGM/SBM (~-0.008 m^2/a) and the ETP (~0.006 m^2/a) [*Ouimet et al.*, 2009], consistent with more direct estimates of *K* in many semi-arid to temperate landscapes [e.g., *Hanks et al.*, 1984]. Moreover, although the SGM/SBM data require a higher threshold slope (S_c ~38º vs. ~32º for the ETP dataset), this merely reflects the difference in DEM resolution available in the two regions (10 m in SGM/SBM vs. 90 m in the ETP) [*Ouimet et al.*, 2009]. It is tempting to speculate that these hillslope transport model parameters may be insensitive to geologic and climatic conditions. However, both field sites are semi-arid, and the ETP data includes a significant fraction of catchments underlain by granitic rocks. Similar field data is needed from field sites spanning a range of geologic and climatic conditions before any firm conclusions can be drawn. Nonetheless, it is remarkable that no distinction can be made either between the SGM/SBM and the ETP datasets nor between catchments underlain by granitic rocks and highly deformed Triassic flysch within the ETP dataset [*Ouimet et al.*, 2009].

The transition to slope-invariant erosion rates above ~300 m/Ma is interpreted to represent a change from steady, creep-related processes (e.g. tree throw, burrowing) to mass wasting and the achievement of threshold slopes [e.g., *Binnie et al.*, 2007; *Montgomery and Brandon*, 2002; *Ouimet et al.*, 2009]. Field observations in the SGM are consistent with this interpretation. At low erosion rates (< 150 m/Ma), basins are nearly entirely mantled by a thin (<1 m) layer of mobile, well-mixed soil and hilltops are smoothly convex up. In rapidly eroding basins (>400 m/Ma), the soil mantle has been mostly replaced with a patchwork of talus, bare bedrock, and landslide scarps and deposits on roughly planar slopes with rugged ridgelines.

Cosmogenically determined soil production rates typically show an inverse exponential relationship with soil depth [e.g., 2005; *Heimsath et al.*, 1997]. In these studies, the maximum surface soil production rates range from ~50-250 m/Ma, and the transition to threshold slopes is thought to correspond to erosion exceeding these rates. Soil production rates measured in the SGM reach a maximum of either 100 or 300 m/Ma, depending on locality, closely matching the erosion rate responsible for the development of threshold hillslopes [*DiBiase et al.*, 2008; *Heimsath*, 1999]. This represents the first quantitative test of the hypothesis that the transition to threshold hillslopes corresponds to erosion exceeding the ‘speed limit’ set by the conversion of bedrock to soil. Further work is needed to test whether this speed limit varies with uplift rate; the coupling of chemical weathering with physical erosion rate may complicate this first cut interpretation.

CONCLUSIONS

The location of the San Gabriel Mountains along a restraining bend in the San Andreas Fault sets up a strong gradient of tectonic forcing (and relief) over a relatively small (100 x 30 km) region with minimally varying climate and lithology. Catchment-mean hillslope angle, channel steepness index, and local relief measured at various scales all increase from west to east. We measured ^{10}Be concentrations in 50 alluvial sand samples to determine catchment-averaged, millennial scale erosion rates across the range. These rates show little dependence on drainage area (which ranges from 0.1 to 100 km^2 in our dataset), in contrast to expectations from numerical experiments [*Niemi et al.*, 2005; *Yanites et al.*, 2009], suggesting that steep basins as small as 1-3 km^2 yield accurate detrital CRN erosion rates. Catchment-mean hillslope angle increases with erosion rate until ~300m/Ma, above which slopes become invariant with erosion rate. This transition in form is seen both in the field, as a switch from soil-mantled to bedrock landscapes, and in local soil production rates, which suggest a maximum bedrock weathering rate of 100-300m/Ma [*DiBiase et al.*, 2008; *Heimsath*, 1999]. Similar data has supported a non-linear soil transport law [e.g., *Montgomery and Brandon*, 2002], but we show that a simpler linear with threshold hillslope transport law fits our data equally well. Normalized channel steepness index tracks monotonically, though non-linearly, with erosion rate throughout the SGM. Much of this non-linearity can be ascribed to the addition of a threshold shear stress and variable discharge to the stream power models of either detachment- or transport-limited river incision. Normalized channel steepness thus serves as a reliable topographic metric of erosion rate in actively deforming orogens where threshold hillslopes fail to retain a tectonic signature.

ACKNOWLEDGEMENTS

Many thanks are due to those involved with collecting samples and assisting with field work, especially the MIT field classes led by KXW in 2002 and KXW and AMH in 2006. Two anonymous reviewers helped improve the manuscript. This work was supported by funding from the Geomorphology and Landuse Dynamics Program at NSF (EAR-0724194 to KXW, EAR-0518998 to AMH).

REFERENCES

Aalto, R., T. Dunne, and J. L. Guyot (2006), Geomorphic controls on Andean denudation rates, *J. Geol.*, *114*, 85-99.

Ahnert, F. (1970), Functional relationships between denudation, relief, and uplift in large mid-latitude drainage basins, *Am. J. Sci.*, *268*, 243-263.

Anderson, R. S. (1994), Evolution of the Santa Cruz Mountains, California, through tectonic growth and geomorphic decay, *J. Geophys. Res.*, *99*(B10), 20161 - 20179.

Bierman, P., and E. J. Steig (1996), Estimating rates of denudation using cosmogenic isotope abundances in sediment, *Earth Surf. Processes Landforms*, *21*, 125-139.

Bierman, P. R., and K. K. Nichols (2004), Rock to sediment - slope to sea with 10Be - rates of landscape change, *Ann. Rev. Earth Planet. Sci.*, *32*, 215-255.

Binnie, S. A., W. M. Phillips, M. A. Summerfield, and L. K. Fifield (2007), Tectonic uplift, threshold hillslopes, and denudation rates in a developing mountain range, *Geology*, *35*(8), 743.

Blythe, A. E., D. W. Burbank, K. A. Farley, and E. J. Fielding (2000), Structural and topographic evolution of the central Transverse Ranges, California, from apatite fission-track, (U-Th)/He and digital elevation model analyses, *Basin Research*, *12*, 97-114.

Brown, E. T., R. F. Stallard, M. C. Larsen, G. M. Raisbeck, and F. Yiou (1995), Denudation rates determined from the accumulation of in situ-produced ^{10}Be in the Luquillo Experimental Forest, Puerto Rico, *Earth Planet. Sci. Lett.*, *129*, 193-202.

Burbank, D. W., J. Leland, E. Fielding, R. S. Anderson, N. Brozovic, M. R. Reid, and C. Duncan (1996), Bedrock incision, rock uplift and threshold hillslopes in the northwestern Himalayas, *Nature*, *379*, 505-510.

Davis, W. M. (1892), The convex profile of badland divides, *Science*, *20*, 245.

DiBiase, R. A., K. X. Whipple, and A. M. Heimsath (2007), Channel morphology response to differential rock uplift rates in the San Gabriel Mountains, CA, *EOS, American Geophysical Union Transactions*, *88*(52), Abstract H41D-0760.

DiBiase, R. A., A. M. Heimsath, and K. X. Whipple (2008), Hillslope angle, channel steepness, and millenial erosion rates in the San Gabriel Mountains, CA, *EOS, American Geophysical Union Transactions*, *89*(53), Abstract H43F-1080.

Dietrich, W. E., D. G. Bellugi, L. S. Sklar, J. D. Stock, A. M. Heimsath, and J. J. Roering (2003), Geomorphic transport laws for predicting landscape form and dynamics, *Prediction in Geomorphology Geophysical Monograph 135*.

Dunai, T. J. (2000), Scaling factors for production rates of in situ produced cosmogenic nuclides: a critical reevaluation, *Earth Planet. Sci. Lett.*, *176*, 157-169.

Duvall, A., E. Kirby, and D. Burbank (2004), Tectonic and lithologic controls on bedrock channel profiles and processes in coastal California, *J. Geophys. Res.*, *109*(F03002), doi:10.1029/2003JF000086.

Finnegan, N. J., G. Roe, D. R. Montgomery, and B. Hallet (2005), Controls on the channel width of rivers: Implications for modeling fluvial incision of bedrock, *Geology*, *33*(3), 229-232, doi:10.1130/g21171.1.

Flint, J. J. (1974), Stream gradient as a function of order, magnitude, and discharge, *Water Resour. Res.*, *10*(5), 969-973.

Gabet, E. J. (2003), Sediment transport by dry ravel, *J. Geophys. Res.*, *108*, doi:10.1029/2001JB001686.

Gilbert, G. K. (1877), Geology of the Henry Mountains, 160 pp, U.S. Geographical and geological survey of the Rocky Mountains Region, Washington, D.C.

Granger, D. E., J. W. Kirchner, and R. C. Finkel (1996), Spatially averaged long-term erosion rates measured from in situ-produced cosmogenic nuclides in alluvial sediment, *J. Geol.*, *104*(3), 249-257.

Hack, J. T. (1957), Studies of longitudinal stream profiles in Virginia and Maryland, 97 pp.

Hancock, G. S., R. S. Anderson, and K. X. Whipple (1998), Beyond power; bedrock river incision process and form, in *Rivers over Rock: Fluvial Processes in Bedrock Channels*, edited by K. J. Tinkler and E. E. Wohl, pp. 35-60, American Geophysical Union, Washington, D.C.

Hanks, T. C., R. C. Bucknam, K. R. Lajoie, and R. E. Wallace (1984), Modification of wave-cut and faulting-controlled landforms, *J. Geophys. Res.*, *89*(B7), 5771-5790.

Heimsath, A. M. (1999), The Soil Production Function, *PhD thesis, University of California, Berkeley, 324pp.*

Heimsath, A. M., D. J. Furbish, and W. E. Dietrich (2005), The illusion of diffusion: Field evidence for depth-dependent sediment transport, *Geology*, *33*(12), 949-952.

Heimsath, A. M., W. E. Dietrich, K. Nishiizumi, and R. C. Finkel (1997), The soil production function and landscape equilibrium, *Nature*, *388*, 358-361.

Hilley, G. E., and J. R. Arrowsmith (2008), Geomorphic response to uplift along the Dragon's Back pressure ridge, Carrizo Plain, California, *Geology*, *36*(5), 367-370, doi:10.1130/g24517a.1.

Hovius, N., C. P. Stark, and P. A. Allen (1997), Sediment flux from a mountain belt derived by landslide mapping, *Geology*, *25*(3), 231-234.

Howard, A. (1994), A detachment-limited model of drainage basin evolution, *Water Resour. Res.*, *30*(7), 2261-2285.

Judson, S., and D. F. Ritter (1964), Rates of regional denudation in the United States, *J. Geophys. Res.*, *69*(16), 3395-3401.

Kirby, E., and K. X. Whipple (2001), Quantifying differential rock-uplift rates via stream profile analysis, *Geology*, *29*(5), 415-418.

Kirchner, J. W., R. C. Finkel, C. S. Riebe, D. E. Granger, J. L. Clayton, J. G. King, and W. F. Megahan (2001), Mountain erosion over 10 yr, 10 k.y., and 10 m.y. time scales, *Geology*, *29*(7), 591-594.

Kirkby, M. J. (1971), Hillslope process-response models based on the continuity equation, *Institute of British Geographers Special Publication*, *3*, 15-30.

Kobor, J. S., and J. J. Roering (2004), Systematic variation of bedrock channel gradients in the central Oregon Coast Range: implications for rock uplift and shallow landsliding, *Geomorphology*, *62*(3-4), 239-256, doi:10.1016/j.geomorph.2004.02.013.

Kohl, C. P., and K. Nishiizumi (1992), Chemical isolation of quartz for measurement of *in-situ*-produced cosmogenic nuclides, *Geochim. Cosmochim. Acta*, *56*, 3583-3587.

Lague, D., and P. Davy (2003), Constraints on the long-term colluvial erosion law by analyzing slope-area relationships at various tectonic uplift rates in the Siwaliks Hills (Nepal), *J. Geophys. Res.*, *108*(B2), doi:10.1029/2002JB001893.

Lague, D., N. Hovius, and P. Davy (2005), Discharge, discharge variability, and the bedrock channel profile, *J. Geophys. Res.*, *110*(F04006), doi:10.1029/2004JF000259.

Langbein, W. B., and S. A. Schumm (1958), Yield of sediment in relation to mean annual precipitation, *EOS, American Geophysical Union Transactions*, *39*(6), 1076-1084.

Lavé, J., and D. W. Burbank (2004), Denudation processes and rates in the Transverse Ranges, southern California: Erosional response of a transitional landscape to external and anthropogenic forcing, *J. Geophys. Res.*, *109*.

Lindvall, S. C., and C. M. Rubin (2008), Slip rate studies along the Sierra Madre-Cucamonga fault system using geomorphic and cosmogenic surface exposure age constraints, US Geological Survey final report 03HQGR0084.

Matmon, A., P. R. Bierman, J. Larsen, S. Southworth, M. Pavich, and M. Caffee (2003), Temporally and spatially uniform rates of erosion in the southern Appalachian Great Smoky Mountains, *Geology*, *31*(2), 155–158.

Matti, J. C., and D. M. Morton (1993), Paleogeographic evolution of the San Andreas fault in southern California: A reconstruction based on a new cross-fault correlation, *Geological Society of America Memoir 178*, 107-159.

Montgomery, D. R., and E. Foufoula-Georgiou (1993), Channel Network Source Representation Using Digital Elevation Models, *Water Resour. Res.*, *29*(12), 3925-3934.

Montgomery, D. R., and M. T. Brandon (2002), Topographic controls on erosion rates in tectonically active mountain ranges, *Earth Planet. Sci. Lett.*, *201*(3-4), 481-489.

Morton, D. M., and F. K. Miller (2006), Geologic map of the San Bernardino and Santa Ana 30' x 60' quadrangles, California, U.S. Geological Survey Open-File Report 2006-1217.

Niemi, N. A., M. Oskin, D. W. Burbank, A. J. M. Heimsath, and E. J. Gabet (2005), Effects of bedrock landslides on cosmogenically determined erosion rates, *Earth Planet. Sci. Lett.*, *237*(3), 480-498.

Ouimet, W. B., K. X. Whipple, and D. E. Granger (2009), Beyond threshold hillslopes: Channel adjustment to base-level fall in tectonically active mountain ranges, *Geology*, *37*(7), 579-582.

Pelletier, J. D., and M. L. Cline (2007), Nonlinear slope-dependent sediment transport in cinder cone evolution, *Geology*, *35*(12), 1067-1070.

Penck, W. (1953), *Morphological Analysis of Landforms: a contribution to physical geology*, English translation ed., Macmillan and Co., London.

Peterson, M. D., and S. G. Wesnousky (1994), Fault slip rates and earthquake histories for active faults in Southern California, *Bulletin of the Seismological Society of America*, *84*(5), 1608-1649.

Roe, G. H., D. R. Montgomery, and B. Hallet (2002), Effects of orographic precipitation variations on the concavity of steady-state river profiles, *Geology*, *30*(2), 143-146.

Roering, J. J., J. W. Kirchner, and W. E. Dietrich (1999), Evidence for nonlinear, diffusive sediment transport on hillslopes and implications for landscape morphology, *Water Resour. Res.*, *35*(3), 853-870.

Roering, J. J., J. T. Perron, and J. W. Kirchner (2007), Functional relationships between denudation and hillslope form and relief, *Earth Planet. Sci. Lett.*, *264*, 245-258.

Roering, J. J., J. W. Kirchner, L. S. Sklar, and W. E. Dietrich (2001), Hillslope evolution by nonlinear creep and landsliding: An experimental study, *Geology*, *29*(2), 143-146.

Safran, E. B., P. R. Bierman, R. Aalto, T. Dunne, K. X. Whipple, and M. Caffee (2005), Erosion rates driven by channel network incision in the Bolivian Andes, *Earth Surf. Processes Landforms*, *30*(8), 1007-1024.

Schaller, M., F. von Blanckenburg, N. Hovius, and P. W. Kubik (2001), Large-scale erosion rates from in situ-produced cosmogenic nuclides in European river sediments, *Earth Planet. Sci. Lett.*, *188*(3-4), 441-458.

Schmidt, K. M., and D. R. Montgomery (1995), Limits to relief, *Science*, *270*(5236), 617-620.

Schumm, S. A. (1963), The disparity between present rates of denudation and orogeny, *U.S. Geol. Surv. Prof. Pap.*, *454-H*.

Sklar, L., and W. E. Dietrich (1998), River longitudinal profiles and bedrock incision models: Stream power and the influence of sediment supply, in *Rivers Over Rock: Fluvial Processes in Bedrock Channels*, edited by K. J. Tinkler and E. E. Wohl, pp. 237-260, American Geophysical Union, Washington, D.C.

Sklar, L. S., and W. E. Dietrich (2004), A mechanistic model for river incision into bedrock by saltating bed load, *Water Resour. Res.*, *40*(6), W06301, doi:10.1029/2003WR002496.

Sklar, L. S., and W. E. Dietrich (2006), The role of sediment in controlling steady-state bedrock channel slope: Implications of the saltation-abrasion incision model, *Geomorphology*, *82*(1-2), 58-83, doi:10.1016/j.geomorph.2005.08.019.

Small, E. E., R. S. Anderson, and G. S. Hancock (1999), Estimates of the rate of regolith production using ^{10}Be and ^{26}Al from an alpine hillslope, *Geomorphology*, *27*(1-2), 131-150.

Snyder, N. P., K. X. Whipple, G. E. Tucker, and D. J. Merritts (2000), Landscape response to tectonic forcing: Digital elevation model analysis of stream profiles in the Mendocino triple junction region, northern California, *Geol. Soc. Am. Bull.*, *112*(8), 1250-1263.

Snyder, N. P., K. X. Whipple, G. E. Tucker, and D. J. Merritts (2003), Importance of a stochastic distribution of floods and erosion thresholds in the bedrock river incision problem, *J. Geophys. Res.*, *108*(B2), 2117.

Spotila, J. A., K. A. Farley, and K. Sieh (1998), Uplift and erosion of the San Bernardino Mountains associated with transpression along the San Andreas fault, California, as constrained by radiogenic helium thermochronometry, *Tectonics*, *17*(3), 360-378.

Spotila, J. A., M. A. House, A. E. Blythe, N. A. Niemi, and G. C. Bank (2002), Controls on the erosion and geomorphic evolution of the San Bernardino and San Gabriel Mountains, southern California, *Geological Society of America Special Paper 365*, 205-230.

Stock, G. M., K. L. Frankel, T. A. Ehlers, M. Schaller, S. M. Briggs, and R. C. Finkel (2008), Spatial and temporal variations in denudation of the Wasatch Mountains, Utah, USA, *Lithosphere*, *1*(1), 34-40.

Stock, J., and W. E. Dietrich (2003), Valley incision by debris flows: Evidence of a topographic signature, *Water Resour. Res.*, *39*(4), 1089, doi:10.1029/2001wr001057.

Strahler, A. N. (1950), Equilibrium theory of erosional slopes approached by frequency distribution analysis, *Am. J. Sci.*, *248*, 673-696.

Tucker, G. E. (2004), Drainage basin sensitivity to tectonic and climatic forcing: Implications of a stochastic model for the role of entrainment and erosion thresholds, *Earth Surf. Processes Landforms*, *29*, 185-205.

Tucker, G. E., and R. L. Bras (1998), Hillslope processes, drainage density, and landscape morphology, *Water Resour. Res.*, *34*(10), 2751-2764.

Tucker, G. E., and R. L. Bras (2000), A stochastic approach to modeling the role of rainfall variability in drainage basin evolution, *Water Resour. Res.*, *36*(7), 1953-1964.

Tucker, G. E., and K. X. Whipple (2002), Topographic outcomes predicted by stream erosion models: Sensitivity analysis and intermodel comparison, *J. Geophys. Res.*, *107*(B9), doi:10.1029/2001JB000162.

Vanacker, V., F. von Blanckenburg, T. Hewawasam, and P. W. Kubik (2007), Constraining landscape development of the Sri Lankan escarpment with cosmogenic nuclides in river sediment, *Earth Planet. Sci. Lett.*, *253*(3-4), 402-414, doi:10.1016/j.epsl.2006.11.003.

von Blanckenburg, F. (2005), The control mechanisms of erosion and weathering at basin scale from cosmogenic nuclides in river sediment, *Earth Planet. Sci. Lett.*, *237*(3-4), 462-479.

Whipple, K. X. (2004), Bedrock rivers and the geomorphology of active orogens, *Ann. Rev. Earth Planet. Sci.*, *32*, 151-185.

Whipple, K. X., and G. E. Tucker (1999), Dynamics of the stream-power river incision model: implications for height limits of mountain ranges, landscape response timescales, and research needs, *J. Geophys. Res.*, *104*(B8), 17661-17674.

Whipple, K. X., E. Kirby, and S. H. Brocklehurst (1999), Geomorphic limits to climate-induced increases in topographic relief, *Nature*, *401*(6748), 39-43.

Whipple, K. X., G. S. Hancock, and R. S. Anderson (2000), River incision into bedrock: Mechanics and relative efficacy of plucking, abrasion, and cavitation, *Geol. Soc. Am. Bull.*, *112*(3), 490-503.

Wittmann, H., F. von Blanckenburg, T. Kruesmann, K. P. Norton, and P. W. Kubik (2007), Relation between rock uplift and denudation from cosmogenic nuclides in river sediment in the Central Alps of Switzerland, *Journal of Geophysical Research-Earth Surface*, *112*(F4), doi:10.1029/2006jf000729.

Wobus, C., K. X. Whipple, E. Kirby, N. Snyder, J. Johnson, K. Spyropolou, B. Crosby, and D. Sheehan (2006), Tectonics from topography: Procedures, promise, and pitfalls, *Geological Society of America Special Paper 398*, 55-74.

Yanites, B. J., G. E. Tucker, and R. S. Anderson (2009), Numerical and analytical models of cosmogenic radionuclide dynamics in landslide-dominated drainage basins, *Journal of Geophysical Research-Earth Surface*, *114*(F01007), doi:10.1029/2008JF001088.

Yerkes, R. F., and R. H. Campbell (2005), Preliminary Geologic Map of the Los Angeles 30' x 60' Quadrangle, Southern California, U.S. Geological Survey Open-File Report 2005-1019.

FIGURE CAPTIONS

Figure 2.1. (a) Overview map of central transverse ranges, CA, showing topography (0-3500m) and quaternary faults (black lines, thickness corresponds to activity (http//earthquakes.usgs.gov/regional/qfaults/)). SGM = San Gabriel Mountains, SBM = San Bernardino Mountains, SAFZ = San Andreas Fault Zone, SMFZ = Sierra Madre Fault Zone, CFZ = Cucamonga Fault Zone. Dashed grey box indicates extent of (b), location map for basins sampled for detrital CRN (black points, polygons) in the San Gabriel Mountains. Basin color corresponds to catchment averaged erosion rate.

Figure 2.2. Map of normalized channel steepness index (k_{sn}) draped on top of 2.5 km relief in the San Gabriel Mountains. Although there is a direct correlation between the two, channel profiles contain additional high resolution information about both spatial and temporal patterns of uplift.

Figure 2.3. Catchment averaged slope (S_{ave}) vs. normalized channel steepness index (k_{sn}) for SGM sample basins.

Figure 2.4. (a) Measured at 100 m scale, local relief is nearly identical to hillslope angle, but as the scale of relief measurement increases, both the scatter and non-linearity of the relief-hillslope angle relationship increase. (**b**) At a radius of 2.5 km, relief increases linearly with channel steepness. Measured at 1 km scale or less, relief values reach a threshold similar to that shown in figure 2.3. Large scales of relief smooth out the variability that we are interested in from the landscape.

Figure 2.5. CRN derived erosion rate vs. catchment area for SGM data (black diamonds) and SBM data [*Binnie et al,* 2007, grey diamonds]. SGM error bars include 1σ analytical error as well as an additional 5% uncertainty in ^{10}Be production rate calculation. White diamonds indicate SGM samples that are either repeats of or nested within catchments showing erosion rates less than 110 m/Ma. White squares represent Cucamonga Canyon (CC; SG162, SG163).

Figure 2.6. Catchment average hillslope angle (S_{ave}) vs. CRN-derived erosion rate (symbols as in figure 2.5). Inset plot shows full range of SBM data. Non-linear model shown with S_c = 39 degrees, K = 0.008 m^2/yr, L_H = 75 m. Linear with threshold model shown with S_c = 37 degrees, K = 0.015 m^2/yr, and L_H = 75 m. Dashed grey line indicates maximum surface soil production rate measured in the SGM from *Heimsath* [1999].

Figure 2.7. Catchment mean normalized channel steepness index vs. CRN-derived erosion rate (symbols as in figure 2.5). Data shown only for basins draining >2 km^2 (47 out of 70 basins). Grey line shows result of stochastic threshold model with the following parameters: mean rainfall intensity = 3 mm/h, mean storm duration = 7 h, mean interstorm period = 238 h, threshold shear stress τ_c = 55 Pa (equivalent to movement of 11 cm cobbles), and erosional efficiency k_e = 0.0003 (see *Tucker* [2004] for full explanations of variables). Dashed grey line indicates maximum surface soil production rate measured in the SGM from *Heimsath* [1999].

Table 2.1. Detrital CRN sample basin location, morphometry and erosion rate data

Sample ID	Easting[a]	Northing[a]	Area (km^2)	mean elevation (m)	basin relief (m)	S_{ave} (deg)	k_{sn}	$^{10}Be/SiO_2$ (x 10^3 atoms/g)	N(z,I)[b]	Erosion rate (m/Ma)[c]
SGB1	393590	3796490	174.70	1401	1438	25.9	62 ± 6	73.21 ± 14.6	2.46	109 ± 27
SGB2	398070	3796470	102.00	1448	1200	24.2	63 ± 6	69.03 ± 17.25	2.54	119 ± 36
SGB3	396850	3797050	106.90	1437	1268	24.0	63 ± 6	96.74 ± 13.99	2.52	84 ± 16
SGB4	405576	3793270	6.00	1528	489	21.3	43 ± 1	244.33 ± 243.44	2.67	35 ± 37
SGB5	396964	3799133	9.91	1358	817	27.2	60 ± 1	56.53 ± 10.86	2.37	135 ± 33
SGB6	385052	3799080	9.68	1286	875	33.0	115 ± 4	29.39 ± 12.46	2.23	246 ± 117
SGB7	394360	3795594	3.18	1311	770	34.4	106 ± 8	29.16 ± 4.74	2.27	253 ± 54
SGB9	384501	3796261	17.33	1139	1189	33.6	118 ± 3	15.33 ± 0.56	2.01	424 ± 37
SGB10	389930	3793860	7.48	1107	1042	32.1	105 ± 5	22.56 ± 0.76	1.94	279 ± 23
SGB11	431950	3795090	82.45	1953	2131	34.9	157 ± 3	14.82 ± 0.67	3.78	826 ± 79
SGB12	429900	3789052	148.38	1803	2463	35.3	163 ± 2	11.07 ± 0.63	3.45	1010 ± 108
SGB13	431750	3795109	35.03	1959	1921	35.2	178 ± 4	28.22 ± 1.84	3.80	436 ± 50
SG116	406050	3793401	1.11	1511	400	22.5	N/A	27.15 ± 2.54	2.64	314 ± 45
SG118	405531	3793280	6.03	1527	494	21.2	43 ± 1	2.57 ± 2.25	2.67	265 ± 32
SG123	403550	3801480	3.19	1731	838	28.4	66 ± 2	93.68 ± 3.95	3.14	108 ± 10
SG124	403580	3800022	0.35	1409	445	24.2	70 ± 7	52.55 ± 3.06	2.44	151 ± 16
SG125	400471	3785950	1.96	1336	858	33.6	N/A	16.14 ± 1.32	2.32	465 ± 61
SG126	400230	3786700	2.30	1361	801	36.4	N/A	12.94 ± 0.9	2.36	591 ± 71
SG127	400100	3786719	2.60	1344	934	39.1	N/A	10.26 ± 0.87	2.33	736 ± 99
SG128	407130	3799908	2.13	1790	182	12.9	29 ± 8	250.69 ± 20.68	3.25	42 ± 6
SG129	406977	3800170	0.14	1788	149	16.0	29 ± 4	213.83 ± 57.3	3.24	49 ± 16
SG130	408940	3804594	0.29	1734	230	25.5	27 ± 3	138.47 ± 9.04	3.12	73 ± 8
SG131	408762	3802978	2.30	1738	250	14.9	29 ± 3	102.88 ± 12.7	3.13	98 ± 17
SG132	409009	3802950	1.13	1728	257	16.8	35 ± 4	94.48 ± 4.54	3.10	106 ± 10
SG136	427489	3798670	0.11	2275	203	24.4	N/A	103.09 ± 4.45	4.60	144 ± 13
SG137	418150	3792511	46.84	1524	1863	34.6	154 ± 3	15.05 ± 1.4	2.75	591 ± 84
SG138	417980	3792440	17.88	1383	1699	35.7	131 ± 3	18.65 ± 2.75	2.47	428 ± 85
SG140	412561	3789280	7.71	1071	1044	29.9	93 ± 6	32.49 ± 1.99	1.89	189 ± 21
SG141	410390	3790543	43.06	1526	1696	30.2	126 ± 4	30.45 ± 2.38	2.74	292 ± 37
SG150	405510	3793789	0.02	1378	56	13.3	N/A	23.82 ± 2.57	2.38	323 ± 51
SG151	426461	3797780	3.53	2290	813	31.2	146 ± 17	34.82 ± 10.27	4.67	434 ± 150
SG152	426300	3798089	2.10	2343	738	31.4	N/A	199.29 ± 9.52	4.85	79 ± 8
SG157	432789	3796090	25.39	2019	2046	35.0	173 ± 5	11.68 ± 1.57	3.99	1106 ± 204
SG158	432614	3796111	53.21	1949	1922	34.4	145 ± 3	11.68 ± 1.39	3.75	1039 ± 175
SG159	431831	3795020	35.03	1958	1929	35.2	178 ± 4	17.15 ± 1.67	3.80	717 ± 106
SG161	429939	3795791	11.55	1954	1550	36.0	164 ± 7	12.03 ± 1.69	3.74	1006 ± 191
SG162	441441	3780431	27.99	1570	2036	35.9	172 ± 6	33.69 ± 4.63	2.91	279 ± 52
SG163	441440	3780432	27.99	1570	2036	35.9	172 ± 6	43.13 ± 2.83	2.91	218 ± 25
SG204	408889	3802380	0.08	1706	73	10.2	N/A	16 ± 2.18	3.05	617 ± 115
SG205	408780	3802535	0.12	1697	90	10.6	N/A	89.34 ± 5.77	3.03	110 ± 13
SG206	427120	3787967	5.39	862	632	32.2	81 ± 12	18.56 ± 5.21	1.59	277 ± 91
SG207	425810	3788950	6.52	1053	1254	35.1	89 ± 3	23.04 ± 2.33	1.89	265 ± 40
SG0701	408768	3802844	0.19	1680	113	10.3	N/A	81.27 ± 3.49	2.99	119 ± 11
SG0702	405524	3804763	0.18	2087	179	20.8	N/A	167.58 ± 8.31	4.03	78 ± 8
SG0703	398617	3796775	9.89	1349	880	30.1	66 ± 3	12.54 ± 0.83	2.34	605 ± 70
SG0728	417222	3802455	9.07	2088	734	24.6	95 ± 15	110.91 ± 6.08	4.05	118 ± 12
SG0729	416848	3802226	5.34	2127	685	23.9	94 ± 24	155.05 ± 7.65	4.16	87 ± 9
SG0730	393010	3706541	5.69	1174	904	31.5	131 ± 13	11.55 ± 2.64	1.76	492 ± 137
SG0740	411172	3798020	2.09	1916	907	24.4	N/A	78.64 ± 4.28	3.58	147 ± 15
SG0743	409731	3796134	21.96	1725	1291	27.8	113 ± 5	42.7 ± 2.89	3.16	239 ± 28

[a] UTM coordinates (NAD 27 Datum)

[b] Production rate latitude/elevation scaling factor (Dunai, 2000)

[c] Erosion rates calculated using density of 2.6 g/cm3 , attenuation length of 165 g/cm2, and high latitude production rate of 5.1 atoms/g/yr

Figure 2.1

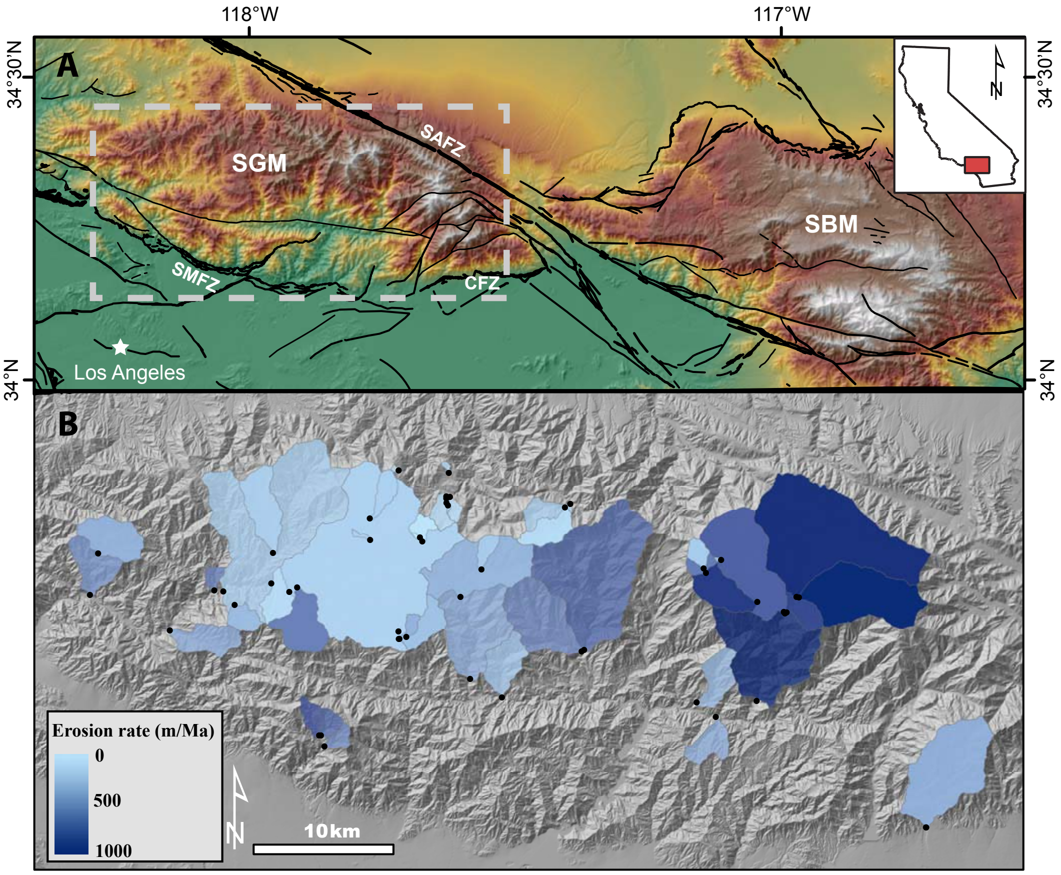
118°W
117°W
34°30'N
34°N
A
SGM
SAFZ
SBM
SMFZ
CFZ
Los Angeles
N
B
Erosion rate (m/Ma)
0
500
1000
N
10km

Figure 2.2

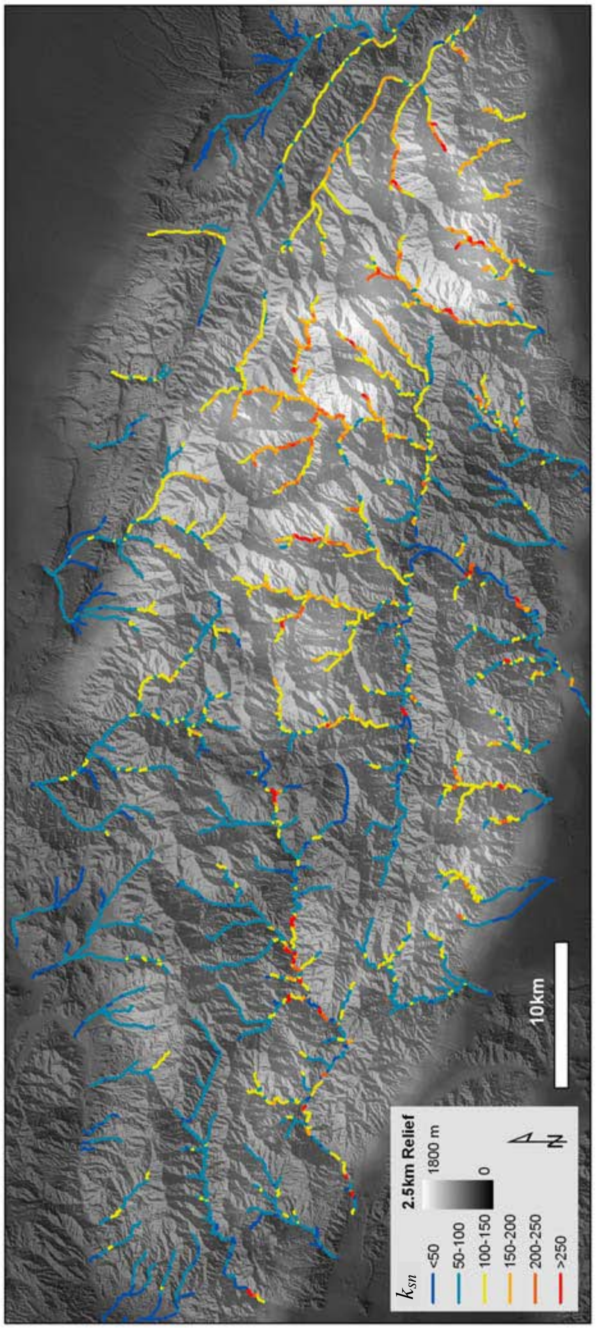
k_{sn}
<50
50-100
100-150
150-200
200-250
>250
2.5km Relief
1800 m
0
N
10km

Figure 2.3

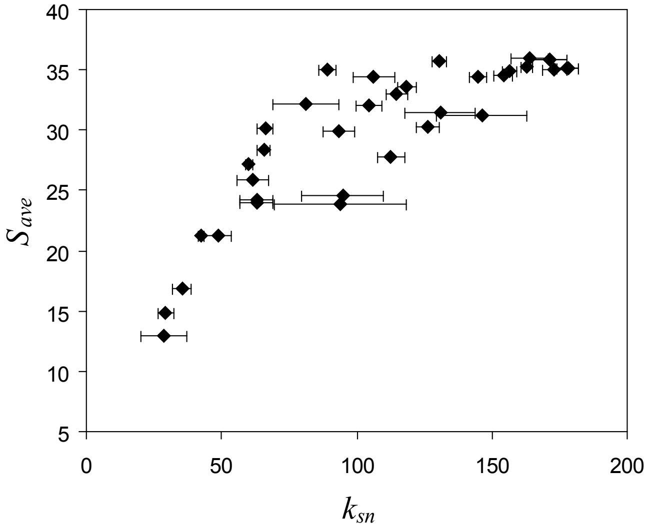

Figure 2.4

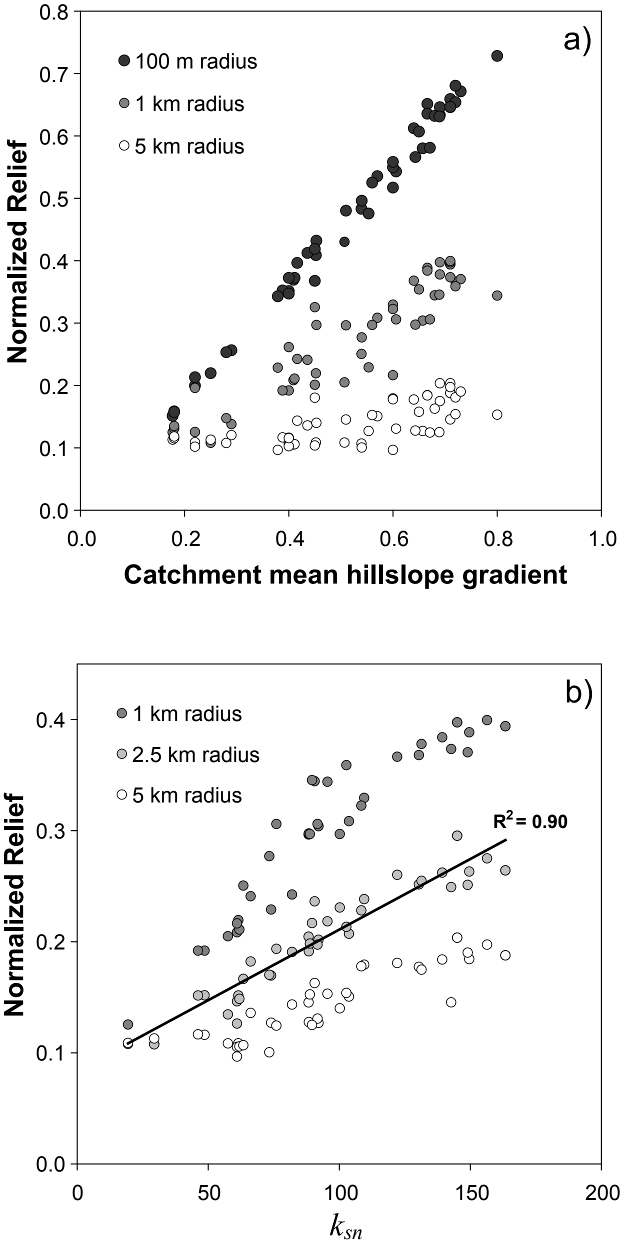
a)
● 100 m radius
● 1 km radius
○ 5 km radius
Normalized Relief
0.0
0.1
0.2
0.3
0.4
0.5
0.6
0.7
0.8
0.0
0.2
0.4
0.6
0.8
1.0
Catchment mean hillslope gradient
b)
● 1 km radius
● 2.5 km radius
○ 5 km radius
$R^2 = 0.90$
Normalized Relief
0.0
0.1
0.2
0.3
0.4
0
50
100
150
200
k_{sn}

Figure 2.5

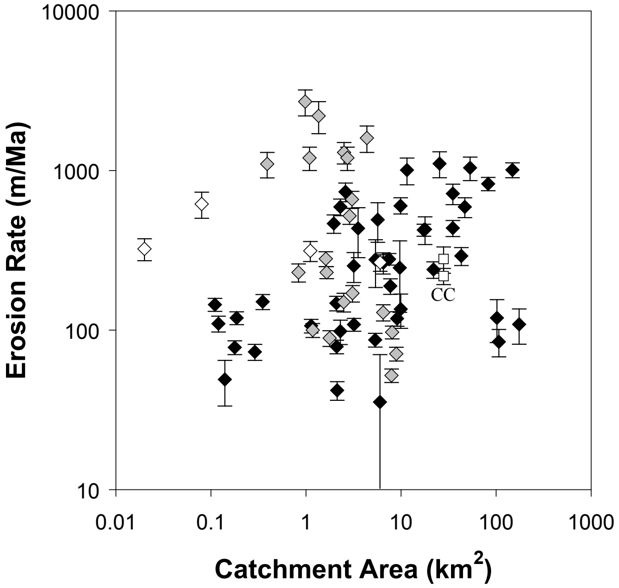

10000
1000
100
10
0.01
0.1
1
10
100
1000
Erosion Rate (m/Ma)
Catchment Area (km^2)
CC

Figure 2.6

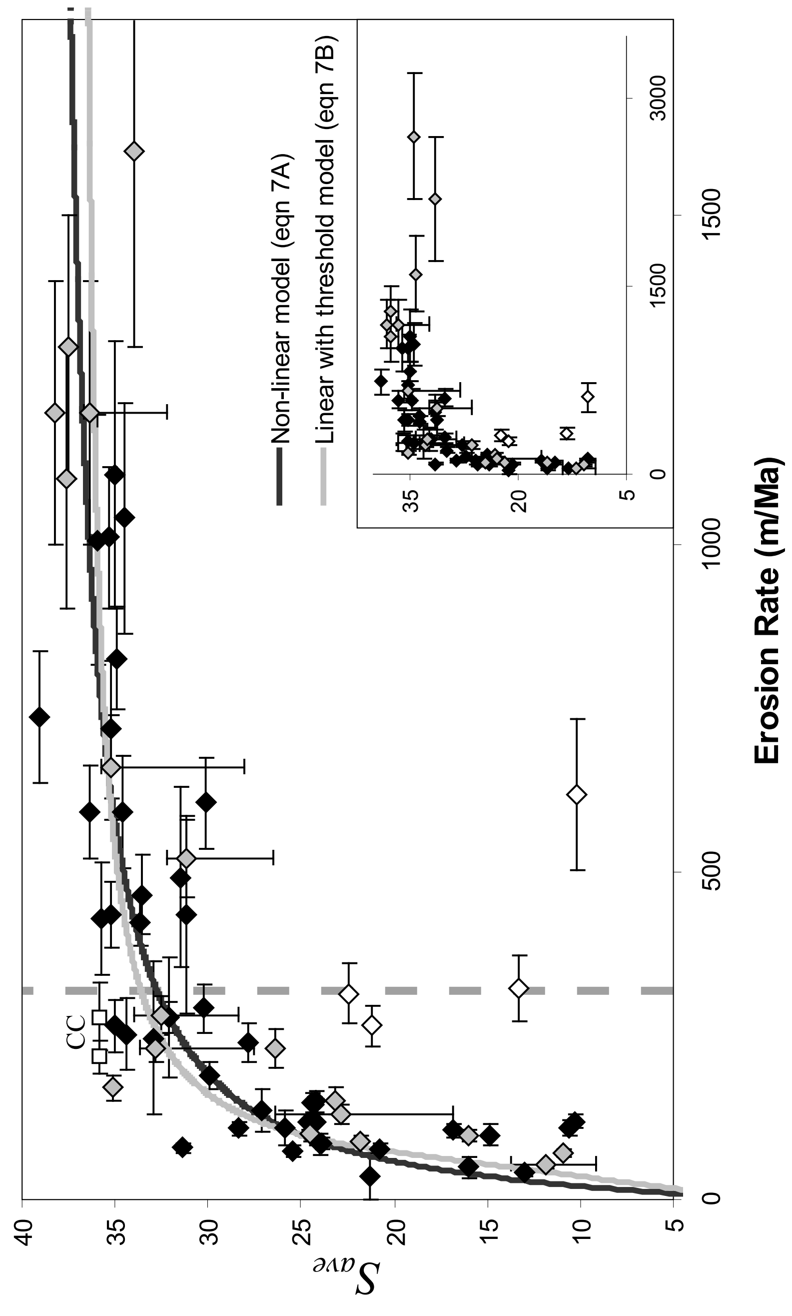
S_{ave}
40
35
30
25
20
15
10
5
0
500
1000
1500
Erosion Rate (m/Ma)
CC
Non-linear model (eqn 7A)
Linear with threshold model (eqn 7B)
35
20
5
0
1500
3000

Figure 2.7

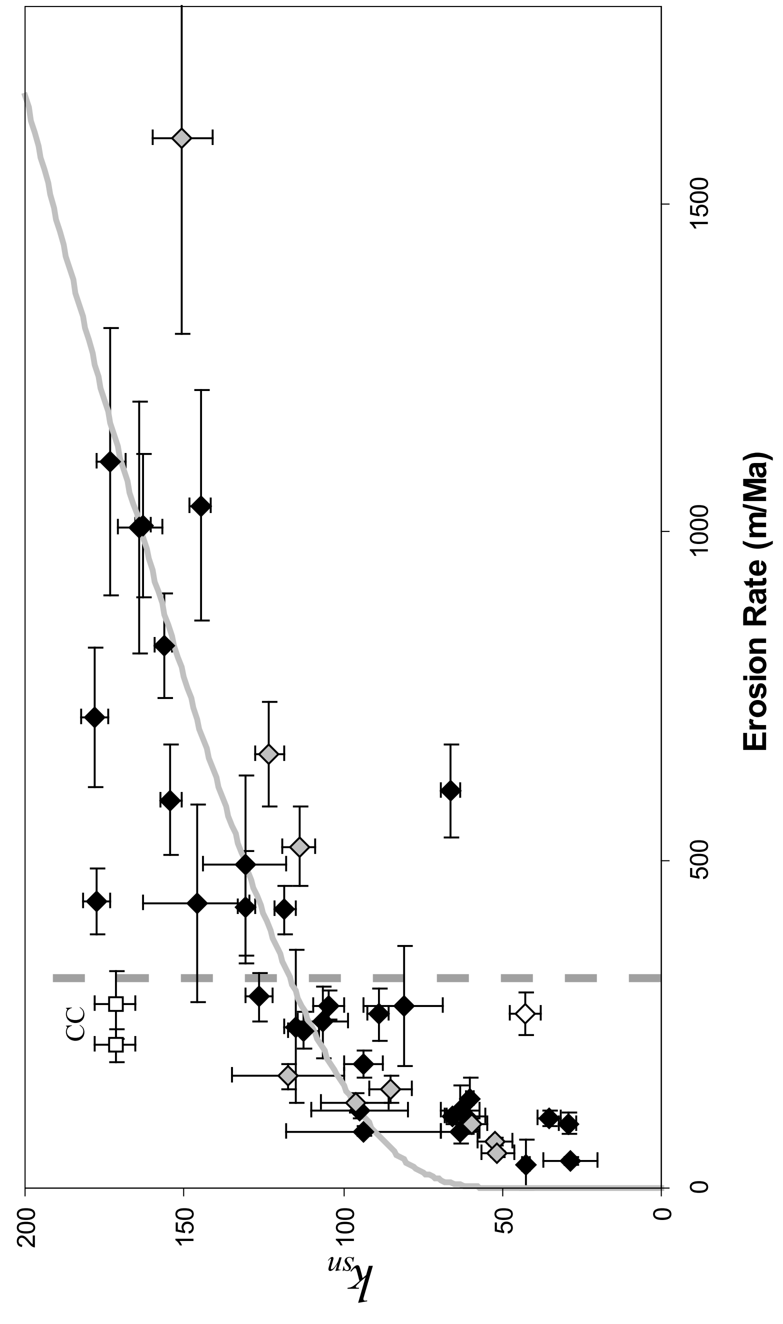

CHAPTER 3

HILLSLOPE RESPONSE TO TECTONIC FORCING IN THRESHOLD LANDSCAPES

ABSTRACT

Hillslopes are thought to poorly record tectonic signals in threshold landscapes. Numerous previous studies of steep landscapes suggest that large changes in long-term erosion rate lead to small changes in mean hillslope angle, measured at coarse resolution. New LiDAR-derived topography data enables a finer examination of threshold hillslopes. Here we quantify hillslope response to tectonic forcing in a threshold landscape. To do so, we use a gradient of tectonic forcing and topographic relief in the San Gabriel Mountains, California, with extensive cosmogenic ^{10}Be-based averaged erosion rates, and a 500 km^2 LiDAR-derived 1 m digital elevation model. We also calibrate a new method of quantifying rock exposure from LiDAR-derived slope measurements using high-resolution panoramic photographs. Two distinct trends in hillslope behavior emerge: below catchment-mean slopes of 30º, modal slopes increase with mean slopes, slope distribution skewness decreases with increasing mean slope, and bedrock exposure is limited; above mean slopes of 30º, rock exposure index increases strongly with mean slope, and the prevalence of angle-of-repose debris wedges keeps modal slopes near 37º, resulting in a positive relationship between slope distribution skewness and mean slope. We find that both mean slope and rock exposure increase with erosion rate up to 1 mm/a, in contrast to previous work based on coarser topographic data. We also find that as erosion rates increase, the extent of the fluvial network decreases, while colluvial channels extend downstream, keeping the total drainage density similar across the range. Our results reveal important textural details lost in 10 or 30 m resolution digital elevation

models of steep landscapes, and highlight the need for process-based studies of threshold hillslopes and colluvial channels.

INTRODUCTION

Steep, tectonically active landscapes provoke broad interest, both for geoscientists interested in interactions among climate, uplift, and erosion, and for an increasing global population that is encroaching deeper into landscapes exposed to landslides, floods, and earthquakes. Such regions are typically interpreted to be threshold landscapes – where rock strength limitations decouple mean hillslope angle from erosion rate, and prevent hillslopes from sustaining mean gradients steeper than 35-40 degrees [*Burbank et al.*, 1996; *Carson and Petley*, 1970; *Montgomery and Brandon*, 2002; *Schmidt and Montgomery*, 1995]. Mean slope is, therefore, a poor measure of landscape-averaged erosion rate in steep mountain ranges [*DiBiase et al.*, 2010; *Ouimet et al.*, 2009]. However, even casual observation suggests that the fraction of exposed bedrock varies significantly in these "threshold" landscapes and that local slopes can become extreme where rock is outcropping. The fact that much of the work pertaining to threshold hillslope morphology has been based on either detailed but spatially limited field measurements [e.g., *Strahler*, 1950] or coarse resolution topographic analyses (local slopes measured over 300-30 meters) using digital elevation models (DEMs) [*Binnie et al.*, 2007; *Burbank et al.*, 1996; *DiBiase et al.*, 2010; *Korup*, 2008; *Montgomery*, 2001] raises the question of whether the observed constancy of mean slope is either an artifact of data resolution or the scale of analysis. Moreover, little is known about how hillslope form, texture, and length vary with erosion rate in steep landscapes. Key first-order questions remain unanswered for steep landscapes: How does rock exposure vary with erosion rate? How does the distribution of local slopes reflect changes in rock exposure? What sets drainage density and the balance between hillslope relief and that of fluvial and colluvial channels? In short, do hillslopes in "threshold" landscapes in fact record tectonic information?

The availability of high-resolution DEMs derived from airborne LiDAR surveys enables a detailed examination of the response of steep landscapes to tectonic-driven erosion rate at the process (and outcrop) scale. The transformative potential of this increase in observation scale from ~30 m to ~1 m in soil-mantled landscapes has been well appreciated by geomorphologists [e.g., National Research Council, 2010]. For example, *Roering* [2008] used high-resolution topography to discriminate among hillslope soil transport laws whose differences in topographic expression cannot be captured by coarser elevation data. Similarly, *Hilley and Arrowsmith* [2008] used a 1 m LiDAR DEM to quantify hillslope and channel response to time-varying rock uplift in weak sedimentary rocks along the San Andreas Fault, highlighting the potential to extract tectonic information from erosional landscapes given sufficiently detailed topographic data. We collected ~500 km^2 of high-resolution LiDAR topographic data in the San Gabriel Mountains, California (SGM) spanning a great diversity in landscape form and surface character in order to study the behavior of threshold landscapes in detail.

Here we quantify hillslope response to tectonics across a threshold landscape using this 1 m resolution, LiDAR-derived DEM, high resolution (<0.1 m) panoramic photographs, and cosmogenic ^{10}Be-derived catchment averaged erosion rates. We build on extensive previous work to investigate how hillslope bedrock exposure, slope angle distribution, and drainage density vary across a gradient in relief and erosion rate in the SGM that is expressed as a transition from soil mantled to increasingly rocky hillslopes. We describe and calibrate a new method of quantifying rock exposure using high resolution slope measurements; we calculate statistics from hillslope gradient distributions at a range of spatial scales; and we use small (2-3 km^2), representative catchments to compare the extent of fluvial versus colluvial valley networks and the consequent variations in drainage density.

STUDY AREA: SETTING, EROSION RATES, AND ANALYSIS STRATEGY

The San Gabriel Mountains present an excellent landscape for studying the transition from soil-mantled to rocky hillslopes. A large restraining bend in the San Andreas Fault produces a strong W-E gradient in uplift rate, erosion rate, and topographic relief, whereas climate and lithology do not vary much across the 100 km wide range [*DiBiase et al.*, 2010; *Peterson and Wesnousky*, 1994; *Spotila et al.*, 2002]. *DiBiase et al.* [2010] exploited this gradient in tectonic forcing to quantify the topographic controls on erosion rates determined from detrital cosmogenic ^{10}Be concentrations. Catchment erosion rates averaged over millennial timescales range from 35-1100 m/Ma, and correlate with catchment-mean hillslope angle for slopes less than 30º and erosion rates less than ~300 m/Ma. For steeper slopes and more rapid erosion rates, mean hillslope angle (as measured on 30- and 10-meter USGS DEMs) in catchments 1-150 km^2 in size appears to be decoupled from erosion rate, similar to studies of other steep landscapes [*Binnie et al.*, 2007; *Montgomery and Brandon*, 2002; *Norton et al.*, 2010; *Ouimet et al.*, 2009; *Stock et al.*, 2009]. This transition from slope-dependent to effectively slope-independent erosion rates agrees with predictions from non-linear soil transport models [*Roering et al.*, 1999; *Roering et al.*, 2007], and corresponds with the onset of mass wasting and rock exposure on hillslopes [*Heimsath et al.*, in press]. Interestingly, in contrast to predictions of most hillslope evolution models [e.g., *Tucker and Hancock*, 2010 and references within], rock exposure remains patchy and significant soil cover persists throughout the range despite the transition to threshold hillslopes [*Heimsath et* *al.*, in press]. What controls the extent of rock exposure and how does this affect the distribution of local slopes? *Heimsath et al.* [in press] show that soil production rates increase with catchment-averaged erosion rates in the SGM and that this effect plus an expected increase in the frequency of landslides with erosion rate can explain the persistence of significant soil cover at high erosion rates. They also suggested that rock exposure should track with local topographic roughness and that a roughness index based on local curvature increased broadly with erosion rate, as expected if rock exposure is due to the increasing frequency of landslides [*Heimsath et al.*, in press]. We extend this work by developing a more robust metric of rock exposure and performing a systematic analysis of the response of hillslope morphology to differences in erosion rate.

An important aspect of our study is the spatial correspondence of a 500 km^2 LiDAR-derived 1 m resolution DEM with an extensive soil production and catchment-averaged erosion rate data set quantified from cosmogenic ^{10}Be (CRN) concentrations in quartz from saprolite and alluvial sands [*DiBiase et al.*, 2010; *Heimsath et al.*, in press]. We supplement this dataset with 8 additional alluvial sand samples draining catchments ranging from 2-26 km^2 (Table 3.1). We collected and processed these samples according to methods detailed by *DiBiase et al.* [2010]. To determine erosion rates, we implemented a pixel-by-pixel calculation of elevation and latitude production rate scaling factors calibrated by Dunai [2000], using a density of 2.6 g/cm^3 and a sea level, high latitude production rate of 5.1 atoms/g/yr.

To focus our DEM-based topographic analyses further, we selected a set of 20 small catchments, averaging 2-3 km^2 in size (Table 3.2). These catchments lie within both the coverage of our catchment-averaged erosion rates and of the high-resolution LiDAR DEM, are spatially homogeneous (i.e., no major knickpoints or large landslides), and span a wide range of hillslope texture, from low relief and soil mantled to steep and rocky. Many of these catchments coincide directly with detrital CRN sample locations. For catchments with multiple or nested CRN rates, we used the nearest sample, or averaged the erosion rate. We combine field mapping with topographic analyses and this database of catchment-average erosion rates to determine (1) a robust topographic metric for the spatial extent of rock outcrop, (2) how rock exposure varies with erosion rate, (3) how the change in process from soil creep to rapid mass wasting and progressive exposure of rock outcrops affect the distribution of local slope angles, (4) how hillslope length (or drainage density) varies with erosion rate, and (5) how the drainage network is partitioned between fluvial channels and colluvial headwater channels thought to be scoured by debris-flows.

ROCK EXPOSURE

Steep hillslopes in the SGM and elsewhere are typically composed of a patchwork of colluvial soil, scree, and exposed rock. Soils tend to be coarse, thin (<20 cm), and lack distinct horizons, but we adhere to the geomorphic definition of soil as a locally produced, mobile sediment layer [e.g., *Heimsath et al.*, 1997]. In this framework, colluvial soils can include rockfall sources, but are dominated by clasts sourced from below. The emergence of bedrock outcrops signals that erosion locally exceeds soil production, potentially indicating a change in erosion process from steady to stochastic. To quantify how the spatial extent of this indicator changes across erosion rates we focus our mapping efforts on the hillslope distribution of in-place and exposed bedrock (as opposed to transportable rock debris). These exposures tend to blocky, fractured masses that range in scale from 0.1-100 m, but planar bedrock flush with the soil surface is not uncommon. Vertical cliff faces greater than 10 m are rare.

To quantify how bedrock exposure varies with erosion rate, we selected 11 hillslopes that range in scale from 0.1 – 1 km^2, have minimal vegetation (as a result of recent fires, for example), and that span a wide range of rockiness. For each hillslope, we used unobstructed views approximately surface-normal to construct large panoramic images (up to 3 x 10^8 pixels) with 1-10 cm spatial resolution. Using these panoramas, we selected eight 100 m x 100 m patches for detailed mapping of bedrock exposure (Figure 3.1), with the remainder of the imagery used for spot checking our rock exposure metric defined below. These small patches were chosen to span a wide range of surface texture, from mostly soil mantled with occasional tors, to steep, rocky cliff faces and debris chutes. We chose a spatial scale of 100 m to ensure our mapping area was larger than the typical outcrop size (order 10 m), but small enough to allow for detailed and efficient mapping over a range of hillslopes. We mapped directly on the photographs, and projected the bedrock polygons to plan view maps using perspective hillshade surfaces from the 1 m LiDAR DEM (Figure 3.2). We define measured bedrock exposure as the plan-view ratio of mapped bedrock to total area.

We calibrated our maps of rock exposure to a metric based on local slope (measured as the dip of a 3x3 m plane fitted at each point). We define this new metric, the Rock Exposure Index (REI), as the percentage of cells within a given area greater than a critical slope, S_*. For each of our eight calibration patches, we calculated REI for S_* equal to 40, 45, and 50º (Figure 3.3). Measured bedrock exposure increases monotonically with REI for each value of S_*, though the strongest linear correlation is with a critical slope of 45º ($R^2 = 0.99$). Field observations elucidate why $S_* = 45$º is most effective in this landscape; soil-mantled slopes between 40-45º exist but are uncommon and we have not found soil-covered slopes or scree slopes in the SGM with slopes steeper than 45º. On the other hand, bedrock outcrops gentler than 45º do occur, and likely contribute to the deviation of the regressed slope from 1:1 (Figure 3.3), but are uncommon. Field reconnaissance with classified slope maps reveals that nearly all in-place bedrock exposed on hillslopes in the SGM is captured by our metric, and that false positives are minimal – a finding corroborated by the detailed analysis of high resolution panoramic photographs as described above. The robust linear correlation in Figure 3.3 and our extensive field observations give us confidence that REI provides an effective measure of percent rock exposure in the SGM over spatial scales greater than 100m.

SLOPE DISTRIBUTIONS

To compare hillslope morphology at the catchment scale, we used the 20 small catchments that span a range of morphology from low gradient, smooth and soil mantled to steep, rocky and rugged terrain (Figure 3.1, Table 3.2). For each catchment, we generated a slope map from the 1 m LiDAR DEM, and extracted slope histograms normalized by the area analyzed (subset shown in Figure 3.4a). For comparison, we extracted the same information using the freely available 10m USGS NED DEM (Figure 3.4b). While the catchment-mean slopes from both datasets are tightly correlated, Figure 3.4 highlights the inadequacies of the USGS data to accurately capture the details of hillslope distributions. Using the 1 m LiDAR DEM, We determined the mean (S_{mean}), mode (S_{mode}), standard deviation (σ_S), and skewness for each slope distribution, and used the Rock Exposure Index described above to estimate the percentage of outcropping rock for each basin (red filled circles, Figure 3.5). Because S_{mode} is sensitive to binning choice, we visually inspected histograms with a range of bin sizes to choose the smallest bin size that retains a smooth histogram (0.1º, Figure 3.4).We used the Pearson skewness coefficient, defined as skewness = $3\cdot(S_{mean} - S_{mode})/\sigma_S$. We find that for catchments with

S_{mean} less than ~30º, little to no rock is exposed, modal slopes increase with mean slopes, and the skewness of the slope distribution decreases with increasing mean slope. For catchments with S_{mean} greater than 30º, rock exposure and skewness increase strongly with mean slope, while modal slopes increase only slightly. The standard deviation of the slope distribution is weakly correlated with mean slope (Table 3.2, $r^2 = 0.45$).

Plotting mean slope against erosion rate reveals a similar relationship to that quantified by *DiBiase et al.* [2010], though mean slopes continue increasing rather than become invariant above 300 m/Ma (Figure 3.6a). This is likely due primarily to choosing small, representative basins rather than whole catchments varying widely in scale (up to 150 km^2). As discussed below, the higher resolution of the LiDAR DEM used here does not much affect estimates of mean slope. While mean slope increases slowly with erosion rate for steep catchments, rock exposure as measured by REI increases approximately linearly with erosion rate for steep ($S_{mean} > 30º$) catchments in the SGM, though with considerable scatter (Figure 3.6b). Slowly eroding catchments (< 150 m/Ma) are nearly entirely soil mantled (REI < 0.1). The relationship shown in Figure 3.6b is consistent with predictions from a simple landslide model [*Heimsath et al.*, in press] and observations by *Norton et al.* [2010].

We extended the above analysis to the entire landscape within the LiDAR coverage by breaking up the landscape into a 750 m x 750 m square grid (Figure 3.1) and computing the same slope statistics for each block, similar to the methodology used by *Montgomery* [2001], *Wolinsky and Pratson* [2005], and *Korup* [2008] for their coarser scale DEM analyses. We chose a scale of 750 m to mimic the lower end of existing detrital erosion rate catchments [*DiBiase et al.*, 2010], capture full crest-swale hillslopes, and yet reveal patterns and variations in landscape texture. Results from this analysis corroborate results from the 2-3 km^2 catchments, demonstrating that these catchments are indeed representative of landscape morphology within the SGM (gray crosses, Figure 3.5).

DRAINAGE DENSITY

For 9 of the 20 small catchments, we extracted the total valley network, identified the transition from colluvial to fluvial slope-area scaling, and calculated the colluvial, fluvial, and total drainage density. Objectively defining drainage density, especially across varied terrain, remains a fundamental challenge in geomorphology. We found that the most consistent method for mapping channel heads in both soil-mantled and rocky landscapes involved identifying zones where contributing area increased rapidly, as occurs at channel heads and along channel banks and can be directly resolved in high-resolution LiDAR DEMs. We resampled the 1 m LiDAR DEM to 4m, and smoothed the resampled DEM with a 3-cell radius moving average window to remove high-resolution topographic noise that tends to reflect transient processes (e.g., recent tree throw pits). Such smoothing is often necessary for topographic analysis using LiDAR data [e.g., *Roering*, 2008], and it should be noted that even resampled to 10 m, LiDAR topographic data is vastly superior to the 10 m USGS DEM, which is plagued by contour stepping and is essentially an upsampled 30 m dataset. From the smoothed LiDAR DEM, we generated a grid of total contributing area from D_{inf} derived flow directions using the software package TauDEM [*Tarboton*, 1997]. We then made a gradient map of the log of contributing area grid to highlight zones of rapid convergence. Using this map draped over the LiDAR shaded relief image, we hand-selected channel heads using pixels where the logarithm of contributing area increases by 10% or greater (Figure 3.7a). This resulted in 100-150 channel heads for each of the 9 catchments. We defined the channel network as the downstream extent of drainage network below these channel heads. While this methodology is subjective, it agrees with qualitative assessments of landscape dissection (from shaded relief maps and field observation) better than a simple threshold area classification or curvature- and slope-area-based metrics that work in soil-mantled landscapes but not in steep landscapes dominated by planar hillslopes, rugged rock outcrops, and colluvial channels. Although close inspection of the resultant drainage networks suggests that total drainage density is underestimated in steep landscapes, this method provides a sufficient approximation of the total drainage density necessary for evaluating the relative extent of the colluvial and fluvial valley networks.

We used the hand-picked channel heads to extract channel long profiles from the 1 m LiDAR DEM at vertical intervals of 3 m using the freely available Profiler Toolbar for ArcMap and Matlab (http://www.geomorphtools.org). Log-log plots of downstream slope against contributing area show scaling relationships typically observed in mountainous landscapes (Figure 3.7b). Colluvial channel tips tend to have uniform slopes (horizontal line in slope-area space), while reaches downstream of ~10^5 m^2 exhibit concave-up, Flint's law scaling consistent with expectations for fluvial channels [*Whipple and Tucker*, 1999; *Wobus et al.*, 2006]. This transition in channel profile shape is often cited as the topographic signature of the transition from debris-flow or colluvial to fluvial channels [*Montgomery and Foufoula-Georgiou*, 1993; *Stock and Dietrich*, 2003]. While we acknowledge that there is likely a gradual handover in process dominance that blurs the inflection in slope-area scaling [*Stock and Dietrich*, 2003; 2006], we choose the center of this kink to define a discrete scaling transition, as it is easily identifiable in most SGM channels, particularly for short tributaries feeding into larger channels. For each hand-picked channel head, we identified this transition, and measured the average slope of each colluvial channel segment (Figure 3.7b).

From this analysis, we quantify the following metrics for each catchment analyzed: total drainage density, defined as the total channel length divided by catchment area; fluvial drainage density, defined by the extent of the fluvial slope-area scaling; colluvial drainage density, equal to total minus fluvial drainage density; and mean colluvial slope, defined as the average slope of all colluvial channel segments weighted by length (Figure 3.8, Table 3.2). As noted above, because of uncertainties in defining the upper extent of the channel network in steep landscapes, total drainage density and thus colluvial drainage density is likely underestimated slightly.

We find that fluvial drainage density decreases with increasing erosion rate, consistent with predictions by *Howard* [1997] and *Tucker and Bras* [1998] for threshold landscapes (Figure 3.9a). This decrease in fluvial drainage density, however, is offset by an increase in colluvial drainage density, such that the total valley density stays similar across the landscape (Figures 3.9b, c). It should be noted that although the total drainage density is highly sensitive to the choice of channel classification, our interpretation of colluvial channels growing downstream at the expense of the fluvial network is robust (Figure 3.8).

The mean slope of colluvial channels is tightly correlated to, and slightly lower than, the mean catchment slope (Figure 3.10). Whether this is a signature of debris flow processes responding to increased base level fall, or simply a geometric necessity for convergent topography remains unclear. How distinct are the controls on mean hillslope angles and the mean slope of colluvial channels? Combined with the increase of colluvial drainage density, the increase of colluvial channel slopes with catchment averaged erosion rate implies an increase of colluvial relief with erosion rate; the change in fluvial relief with erosion rate depends primarily on the scale of analysis, such that for small catchments fluvial relief actually decreases with increasing erosion rate due to a process transition from fluvial to debris flow incision.

DISCUSSION

LiDAR-derived slope distributions in the SGM vary systematically with mean slope, with notable changes in distribution shape occurring precisely at the point where we begin to see outcropping rock (mean slope ~30º, Figure 3.5c). Below mean slopes of 28º, skewness and mean slope are inversely correlated, similar with findings by *Wolinsky and Pratson* [2005]. For mean slopes greater than 30º, modal slope becomes decoupled from mean slope and hovers between 35 and 37º (Figure 3.5b), which results in a strong positive relationship between skewness and mean slope. *Wolinsky and Pratson* [2005] used a simplified 2D landscape evolution model to argue that the transition from creep to failure dominated catchments is characterized by a decrease in skewness. Our data supports this interesting finding for soil-mantled landscapes with mean slopes less than 30º. Additionally, they found a weak positive relationship between skewness and S_{mean} at high mean slopes, which they attributed to glacial processes. While this may be a signature of glaciated terrain, the inflection point in Figure 3.5 is due not to glacial processes, which are absent in the SGM. Rather, we interpret this inflection as response to an increase in bedrock exposure on hillslopes as landslides become more common [e.g., *Heimsath et al.*, in press]. In the SGM, modal slopes of 36-38º appear to be controlled by the angle-of-repose wedges of loose debris upslope of rocky outcrops, which we observed in the field (and from the 1 m DEM) to have a similar range in slope. Thus, as hillslopes become rockier, mean slopes increase, and slope distributions become skewed increasingly towards higher slopes while the prevalence of loose debris holds modal slopes to values near the angle of repose (Figure 3.5a). The topographic signature of this transition from creep to failure emerges most clearly in 1 m data, where the onset of rocky hillslopes can be discerned clearly (Figure 3.5c). As highlighted by Figure 3.4b, slope distributions derived from 10 m resolution USGS data fail to reproduce important details present in steep catchments, and reinforce the importance of capturing fine scale texture for topographic analysis in mountainous topography.

Why then does mean slope become insensitive to long term erosion rate, as shown in many studies [*Binnie et al.*, 2007; *Burbank et al.*, 1996; *DiBiase et al.*, 2010; *Montgomery and Brandon*, 2002; *Norton et al.*, 2010; *Ouimet et al.*, 2009; *Stock et al.*, 2009]? For example, using 10 m resolution topography, *DiBiase et al.* [2010] argued that in the SGM, hillslopes fail to record changes in erosion rate above rates of ~300 m/Ma. Figure 3.6a suggests, however, that using 1 m LiDAR topography reveals a positive relationship between mean slope and erosion rate for "threshold" catchments. Although using higher resolution topographic data enables more precise measurements of hillslope angle, catchment mean slope depends primarily on the hillslope relief structure, which does not change significantly with measurement scale (as opposed to local measurements of slope and curvature). Rather, the positive relationship is likely due to the selection of small, homogeneous study catchments of similar size in the current analysis – there is a strong linear relationship between mean slope as measured with the LiDAR DEM and USGS 10 m DEM ($r^2 = 0.99$ for catchments shown in Figure 3.4). The robust interrelations among topographic characteristics for these catchments strongly suggest that this positive relationship between mean slope and erosion rate is not an artifact of site selection bias. In contrast to typical assumptions about threshold hillslopes [e.g., *Burbank and Anderson*, 2001], hillslopes in the SGM show systematic variation in morphology and texture with increasing mean slope across the full range of relief and erosion rates (Figure 3.7). *Gabet et al.* [2004] and *Korup* [2008] suggest that local variations in climate and/or rock strength control slope, rock exposure, and the surface expression of steep hillslopes. That is, as slopes steepen to the point where landsliding begins and rock becomes exposed, differences in meso-scale rock strength control the topographic expression of hillslopes, and decouple hillslope morphology from tectonic processes. While spatial variability in rock strength and local climate probably contribute to the significant scatter in the relationship between erosion rate and both REI and mean slope (Figure 3.6), the strong interrelationships observed between mean slope, rock exposure, and slope distributions demonstrates that steepland hillslopes are far more sensitive to tectonic processes than previously thought.

One of the key linkages in the study of the climatic, tectonic, and geomorphic evolution of mountain ranges is the relationship between landscape relief and erosion rate. Total landscape relief for unglaciated terrain can be split into its components consisting of fluvial, colluvial, and hillslope relief [*DiBiase et al.*, 2010; *Whipple et al.*, 1999]. While the fluvial network occupies only a small fraction of the areal extent of a typical mountainous landscape, it can account for more than 80% of the total relief structure – an observation that motivates much research into the details of bedrock river incision, and lies behind the strength of the channel steepness index as a topographic metric of erosion rate [*DiBiase et al.*, 2010; *Ouimet et al.*, 2009]. However, Figure 3.8 implies that the relative contributions to total landscape relief vary with erosion rate as fluvial drainage density decreases. Hillslope relief can be quantified by multiplying mean hillslope length (estimated as one half the inverse of total drainage density and approximately constant in the SGM) by the tangent of mean hillslope angle. Colluvial relief can be determined in a similar fashion using fluvial drainage density, and increases steadily with erosion rate because both the length and slope of colluvial channels increase with E (Figures 3.9b, 3.10). *Lague and Davy* [2003] note a similar increase in colluvial slopes with erosion rate in the Siwalik Hills of Nepal, and *Stock and Dietrich* [2003] note that a significant fraction of catchment relief in the Oregon Coast Range is occupied by colluvial channels. It appears then that partitioning relief into its individual process components becomes important for characterizing landscape response to external forcing. However, in the SGM, the total of hillslope and colluvial relief does not exceed 150 m, while local relief measured over a 5 km diameter window can be 1000 m or greater. Indeed, *DiBiase et al.* [2010] find a strong linear correlation between channel steepness and 5 km local relief in the SGM. Thus, while threshold hillslopes and colluvial channel networks encode tectonic information in their texture, extent, and slopes, it is the fluvial network that governs kilometer scale relief in steep landscapes.

CONCLUSION

Our results suggest that high-resolution LiDAR topography reveals complexity and textural details in threshold hillslopes not evident from coarser elevation data. We use detailed panoramic photographs to calibrate a Rock Exposure Index based on a slope map derived from a 1 m LiDAR-derived DEM. We find that the fraction of slopes greater than 45 degrees closely matches mapped bedrock exposure. While this index likely requires recalibration for use in other landscapes, it highlights the potential for using increasingly numerous LiDAR datasets to map the distribution of soil and bedrock at a previously unattainable scale. While previous studies suggest that hillslopes fail to record tectonic information in steep landscapes, we show strongly correlated, systematic variations in rock exposure, mean slope, catchment slope skewness, and colluvial and fluvial drainage density as catchment averaged erosion rates increase from about 40 to about 1000 m/Ma. We find two distinct trends in hillslope gradient distributions. For mean slopes less than 30º, little rock is exposed, modal slopes track with mean slopes, and catchment slope skewness decreases with increasing mean slope. For mean slopes greater than 30º, rock exposure increases with mean slope, and the prevalence of angle-of-repose debris slopes holds modal slopes at about 37º. As a result, skewness increases as mean slopes steepen up to 45º, which cannot be discerned in similar analysis of 10 m USGS topographic data. Our detailed analysis of the extent of the fluvial and colluvial channel network reveals that colluvial drainage density increases with average erosion rate at the expense of the fluvial network. This keeps total drainage density roughly constant and highlights the need for better quantifying the role of debris flow processes in threshold landscapes.

ACKNOWLEDGEMENTS

This work was supported by funding from the Geomorphology and Land Use Dynamics Program at NSF (EAR-0518998 to AMH, EAR-0724194 to KXW). Laser altimetry was acquired and processed by NCALM with support from ASU and Caltech. Taufique Mahmood helped develop the Rock Exposure Index.

REFERENCES

Binnie, S. A., W. M. Phillips, M. A. Summerfield, and L. K. Fifield (2007), Tectonic uplift, threshold hillslopes, and denudation rates in a developing mountain range, *Geology*, *35*(8), 743-746, doi:10.1130/g23641a.1.

Burbank, D. W., and R. S. Anderson (2001), *Tectonic Geomorphology*, 274 pp., Blackwell, Malden, MA.

Burbank, D. W., J. Leland, E. Fielding, R. S. Anderson, N. Brozovic, M. R. Reid, and C. Duncan (1996), Bedrock incision, rock uplift and threshold hillslopes in the northwestern Himalayas, *Nature*, *379*(6565), 505-510, doi:10.1038/379505a0.

Carson, M. A., and D. J. Petley (1970), The existence of threshold hillslopes in the denudation of the landscape, *Transactions of the Institute of British Geographers*(49), 71-95.

Council, N. R. (2010), *Landscapes on the edge: New horizons for research on Earth's surface*, 163 pp., National Academies Press, Washington, DC.

DiBiase, R. A., K. X. Whipple, A. M. Heimsath, and W. B. Ouimet (2010), Landscape form and millennial erosion rates in the San Gabriel Mountains, CA, *Earth and Planetary Science Letters*, *289*(1-2), 134-144, doi:10.1016/j.epsl.2009.10.036.

Dunai, T. J. (2000), Scaling factors for production rates of in situ produced cosmogenic nuclides: a critical reevaluation, *Earth and Planetary Science Letters*, *176*(1), 157-169, doi:10.1016/s0012-821x(99)00310-6.

Gabet, E. J., B. A. Pratt-Sitaula, and D. W. Burbank (2004), Climatic controls on hillslope angle and relief in the Himalayas, *Geology*, *32*(7), 629-632, doi:10.1130/g20641.1.

Heimsath, A. M., R. A. DiBiase, and K. X. Whipple (in press), Soil production limits and the transition to bedrock dominated landscapes, *Nature Geoscience*, Accepted manuscript: NGS-2011-03-00349B.

Heimsath, A. M., W. E. Dietrich, K. Nishiizumi, and R. C. Finkel (1997), The soil production function and landscape equilibrium, *Nature*, *388*(6640), 358-361, doi:10.1038/41056.

Hilley, G. E., and J. R. Arrowsmith (2008), Geomorphic response to uplift along the Dragon's Back pressure ridge, Carrizo Plain, California, *Geology*, *36*(5), 367-370, doi:10.1130/g24517a.1.

Howard, A. D. (1997), Badland morphology and evolution: Interpretation using a simulation model, *Earth Surface Processes and Landforms*, *22*(3), 211-227.

Korup, O. (2008), Rock type leaves topographic signature in landslide-dominated mountain ranges, *Geophysical Research Letters*, *35*(11), L11402, doi:10.1029/2008gl034157.

Lague, D., and P. Davy (2003), Constraints on the long-term colluvial erosion law by analyzing slope-area relationships at various tectonic uplift rates in the Siwaliks Hills (Nepal), *Journal of Geophysical Research-Solid Earth*, *108*(B1), doi:10.1029/2002jb001893.

Montgomery, D. R. (2001), Slope distributions, threshold hillslopes, and steady-state topography, *American Journal of Science*, *301*(4-5), 432-454, doi:10.2475/ajs.301.4-5.432.

Montgomery, D. R., and E. Foufoula-Georgiou (1993), Channel network source representation using digital elevation models, *Water Resour. Res.*, *29*(12), 3925-3934, doi:10.1029/93wr02463.

Montgomery, D. R., and M. T. Brandon (2002), Topographic controls on erosion rates in tectonically active mountain ranges, *Earth and Planetary Science Letters*, *201*(3-4), 481-489, doi:10.1016/s0012-821x(02)00725-2.

Norton, K. P., F. von Blanckenburg, and P. W. Kubik (2010), Cosmogenic nuclide-derived rates of diffusive and episodic erosion in the glacially sculpted upper Rhone Valley, Swiss Alps, *Earth Surface Processes and Landforms*, *35*(6), 651-662, doi:10.1002/esp.1961.

Ouimet, W. B., K. X. Whipple, and D. E. Granger (2009), Beyond threshold hillslopes: Channel adjustment to base-level fall in tectonically active mountain ranges, *Geology*, *37*(7), 579-582, doi:10.1130/g30013a.1.

Peterson, M. D., and S. G. Wesnousky (1994), Fault slip rates and earthquake histories for active faults in Southern California, *Bulletin of the Seismological Society of America*, *84*(5), 1608-1649.

Roering, J. J. (2008), How well can hillslope evolution models "explain" topography? Simulating soil transport and production with high-resolution topographic data, *Geological Society of America Bulletin*, *120*(9-10), 1248-1262, doi:10.1130/b26283.1.

Roering, J. J., J. W. Kirchner, and W. E. Dietrich (1999), Evidence for nonlinear, diffusive sediment transport on hillslopes and implications for landscape morphology, *Water Resour. Res.*, *35*(3), 853-870, doi:10.1029/1998wr900090.

Roering, J. J., J. T. Perron, and J. W. Kirchner (2007), Functional relationships between denudation and hillslope fonn and relief, *Earth and Planetary Science Letters*, *264*(1-2), 245-258, doi:10.1016/j.epsl.2007.09.035.

Schmidt, K. M., and D. R. Montgomery (1995), Limits to relief, *Science*, *270*(5236), 617-620.

Spotila, J. A., M. A. House, A. E. Blythe, N. A. Niemi, and G. C. Bank (2002), Controls on the erosion and geomorphic evolution of the San Bernardino and San Gabriel Mountains, southern California, *Geological Society of America Special Paper*, *365*, 205-230.

Stock, G. M., K. L. Frankel, T. A. Ehlers, M. Schaller, S. M. Briggs, and R. C. Finkel (2009), Spatial and temporal variations in denudation of the Wasatch Mountains, Utah, USA, *Lithosphere*, *1*(1), 34-40, doi:10.1130/l15.1.

Stock, J., and W. E. Dietrich (2003), Valley incision by debris flows: Evidence of a topographic signature, *Water Resour. Res.*, *39*(4), 1089, doi:10.1029/2001wr001057.

Stock, J. D., and W. E. Dietrich (2006), Erosion of steepland valleys by debris flows, *Geological Society of America Bulletin*, *118*(9-10), 1125-1148, doi:10.1130/b25902.1.

Strahler, A. N. (1950), Equilibrium theory of erosional slopes approached by frequency distribution analysis, *American Journal of Science*, *248*, 673-696.

Tarboton, D. G. (1997), A new method for the determination of flow directions and upslope areas in grid digital elevation models, *Water Resour. Res.*, *33*(2), 309-319, doi:10.1029/96wr03137.

Tucker, G. E., and R. L. Bras (1998), Hillslope processes, drainage density, and landscape morphology, *Water Resour. Res.*, *34*(10), 2751-2764, doi:10.1029/98wr01474.

Tucker, G. E., and G. R. Hancock (2010), Modelling landscape evolution, *Earth Surface Processes and Landforms*, *35*(1), 28-50, doi:10.1002/esp.1952.

Whipple, K. X., and G. E. Tucker (1999), Dynamics of the stream-power river incision model: Implications for height limits of mountain ranges, landscape response timescales, and research needs, *Journal of Geophysical Research-Solid Earth*, *104*(B8), 17661-17674, doi:10.1029/1999jb900120.

Whipple, K. X., E. Kirby, and S. H. Brocklehurst (1999), Geomorphic limits to climate-induced increases in topographic relief, *Nature*, *401*(6748), 39-43, doi:10.1038/43375.

Wobus, C., K. X. Whipple, E. Kirby, N. Snyder, J. Johnson, K. Spyropolou, B. Crosby, and D. Sheehan (2006), Tectonics from topography: Procedures, promise, and pitfalls, *Geological Society of America Special Paper*, *398*, 55-74.

Wolinsky, M. A., and L. F. Pratson (2005), Constraints on landscape evolution from slope histograms, *Geology*, *33*(6), 477-480, doi:10.1130/g21296.1.

FIGURE CAPTIONS

Figure 3.1. Shaded relief map of San Gabriel Mountains, California. Outlines of study catchments are shown as white lines, with labels corresponding to Table 3.2. Bold outlines indicate catchments used for drainage density analysis (Figure 3.8). White diamonds indicate sites where panoramic photos were used to calibrate the Rock Exposure Index. White grid highlights the block sampling scheme used for topographic analysis across the extent of the 1 m LiDAR DEM (dark gray).

Figure 3.2. Example of rock exposure calibration from east slope of Mt. Baden-Powell. Top panel shows high-resolution (1 cm) photograph overlain by three mapping patches (black outlines, 1 hectare each). Purple polygons indicate mapped rock exposure, which is transferred to planview maps using shaded relief images tilted to the same perspective as the photograph (middle panel). The bottom panel highlights pixels with slope greater than 45° (red).

Figure 3.3. Plot of percentage of slopes greater than S_* against percent rock mapped from panoramic photographs. The best linear fit is for $S_* = 45°$, and we use this calibration to define our Rock Exposure Index. Dashed line indicates 1:1 relationship.

Figure 3.4. Slope histograms generated from sample catchments using the 1 m LiDAR DEM (a) and the 10 m USGS DEM (b). Arrows indicate the mean slope for each of the catchments used (from left to right: basin 1, 17, 4, 16, 2, 15). While the mean slope generated from the two datasets is correlated, there are significant differences in histogram shape, including the sign of the skewness for steep catchments.

Figure 3.5. Slope statistics calculated using 2-3 km^2 sample catchments (red circles) and across 750 m x 750 m square grid (gray crosses). Plotted against mean slope are modal slope (a), skewness (b), and Rock Exposure Index (c). Note the inflection at mean slopes of 30° present in all three plots, highlighting the onset of significant rock exposure and the prevalence of angle of repose debris wedges that hold modal slopes near 37°.

Figure 3.6. Plot of mean slope from 1m LiDAR (a) and Rock Exposure Index (b) against detrital CRN erosion rate for the 20 study catchments listed in Table 3.2.

Figure 3.7. Channel network delineation for catchment 16 (Big Rock 3). D_{inf} contributing area shown over LiDAR shaded relief (a); black pixels highlight areas where contributing area increases rapidly (see text for details). White (colluvial) and gray (fluvial) lines show channel network resulting from hand-picked channel heads. Example slope-area plot and long profile (b) shown for bold channel, with star indicating transition from colluvial to fluvial scaling.

Figure 3.8. Shaded relief maps of 9 study catchments used for drainage density analysis. Blue lines indicate channel network with fluvial slope-area scaling and red lines indicate colluvial channels. As erosion rates increase, colluvial drainage density increases at the expense of the fluvial network, while total drainage density remains roughly steady.

Figure 3.9. Plots of drainage density against erosion rate for 9 catchments shown in Figure 3.8. Fluvial drainage density (a) is defined by channels following Flint's law

scaling in slope-area space. Total drainage density (b) is determined from hand-picked channel heads in areas with rapid increase in contributing area (Figure 3.7). Colluvial drainage density (c) is calculated as the difference between total and fluvial drainage density.

Figure 3.10. Mean colluvial slope plotted against catchment-mean slope for the 9 study catchments shown in Figure 3.8. Dashed line indicates 1:1 relationship. Colluvial slope is calculated as the slope of a linear fit to each colluvial channel, and the mean colluvial slope is the average of all such channels for each catchment, weighted by channel length.

Table 3.1. Catchment averaged erosion rates from cosmogenic ^{10}Be concentrations

Sample ID	Easting[a]	Northing[a]	Area (km^2)	$^{10}Be/SiO_2$ (x 10^3 atoms/g)	N(z,I)[b]	Erosion rate (m/Ma)[c]
SG160	429950	3795861	18.8	14.82 ± 2.44	4.16	907 ± 195
SG0706	398469	3783358	17.3	10.79 ± 1.91	2.02	605 ± 137
SG0708	399180	3794240	1.9	18.89 ± 1.99	2.54	435 ± 68
SG0747	406053	3786078	7.3	11.81 ± 3.51	1.97	541 ± 188
SG0748	406129	3785893	7.4	11.77 ± 2.61	1.97	541 ± 147
SG0749	406010	3784661	6.1	10.53 ± 2.83	1.99	611 ± 195
SG0818	391759	3790469	25.5	9.98 ± 1.33	2.19	711 ± 130

[a] UTM coordinates (NAD 27 Datum)

[b] Production rate latitude/elevation scaling factor (Dunai, 2000)

[c] Erosion rates calculated using density of 2.6 g/cm3, attenuation length of 165 g/cm2, and high latitude production rate of 5.1 atoms/g/yr

Table 3.2. Study catchment characteristics

ID	Name	Area (km^2)	CRN sample	E (m/Ma)	S_{mean}	σ_S	S_{mode}	skewness(S)	REI	$S_{\text{colluvial}}$	Total D_d	Fluvial D_d	Colluvial D_d
1	Chilao	2.3	SG128[a]	42 ± 6	16.2	7.5	15.0	0.47	0.1	14.6	11.8	10.5	1.3
2	Big Rock 1	3.8	SG0809[b]	434 ± 59	35.7	8.9	36.8	-0.38	8.2	32.7	8.4	3.5	4.9
3	Big Rock 2	2.5	SG0804[b]	493 ± 111	33.8	9.7	36.4	-0.80	6.8	-	-	-	-
4	Mule Fork	3.8	SGB2[a], SG124[a]	150 ± 50[c]	28.1	9.4	32.2	-1.31	1.7	24.5	11.0	7.9	3.1
5	Little Bear	2.0	SG0818	711 ± 130	36.9	10.1	37.4	-0.13	12.4	-	-	-	-
6	Lucas	2.3	SGB7[a]	253 ± 54	37.5	8.7	38.2	-0.24	11.6	-	-	-	-
7	Millard	2.1	SG0704	668 ± 186	36.1	9.6	37.4	-0.41	10.0	-	-	-	-
8	Santa Anita	2.0	SG0748	541 ± 147	38.0	9.8	39.8	-0.54	16.7	33.1	9.9	5.6	4.3
9	Winter	2.6	SG0749	611 ± 195	39.8	10.3	39.4	0.12	21.3	35.1	9.6	2.7	6.9
10	Upper Eaton	2.3	SG127[a]	736 ± 99	42.0	11.1	38.2	1.01	26.1	36.1	10.1	2.9	7.2
11	Deer Branch	2.3	SG126[a]	591 ± 71	39.6	10.1	39.6	-0.01	20.7	-	-	-	-
12	Harvard Branch	2.0	SG125[a]	465 ± 61	37.8	10.3	38.6	-0.23	16.8	-	-	-	-
13	Upper SF Iron	2.0	SG151[a], SG152[a]	256 ± 180	31.8	8.0	35.2	-1.29	2.5	-	-	-	-
14	North Iron Fork	2.5	SG160	907 ± 195	41.8	10.6	38.0	1.08	24.9	-	-	-	-
15	South Iron Fork	2.1	SG161[a]	1006 ± 191	42.7	10.5	38.4	1.21	28.6	35.5	10.5	3.2	7.3
16	Big Rock 3	3.2	SG0805[b]	343 ± 58	33.0	9.2	35.6	-0.84	5.0	29.8	7.8	3.6	4.2
17	Little Rock 1	2.6	SG131[a]	98 ± 17	20.2	7.7	20.6	-0.15	0.1	18.0	12.2	10.7	1.5
18	Little Rock 2	1.2	SG132[a]	106 ± 10	22.2	7.9	25.0	-1.07	0.1	-	-	-	-
19	Clear	3.0	SGB10[a]	279 ± 23	32.4	12.0	36.2	-0.96	8.3	-	-	-	-
20	Wickiup	1.9	SG0708	435 ± 68	35.6	7.5	37.8	-0.87	4.8	-	-	-	-

Source for CRN data: [a] DiBiase et al., 2010; [b] Heimsath et al., 2011; [c] Poor CRN coverage. Slope measurements are in degrees, drainage density measurements are in units of km^{-1}

Figure 3.1

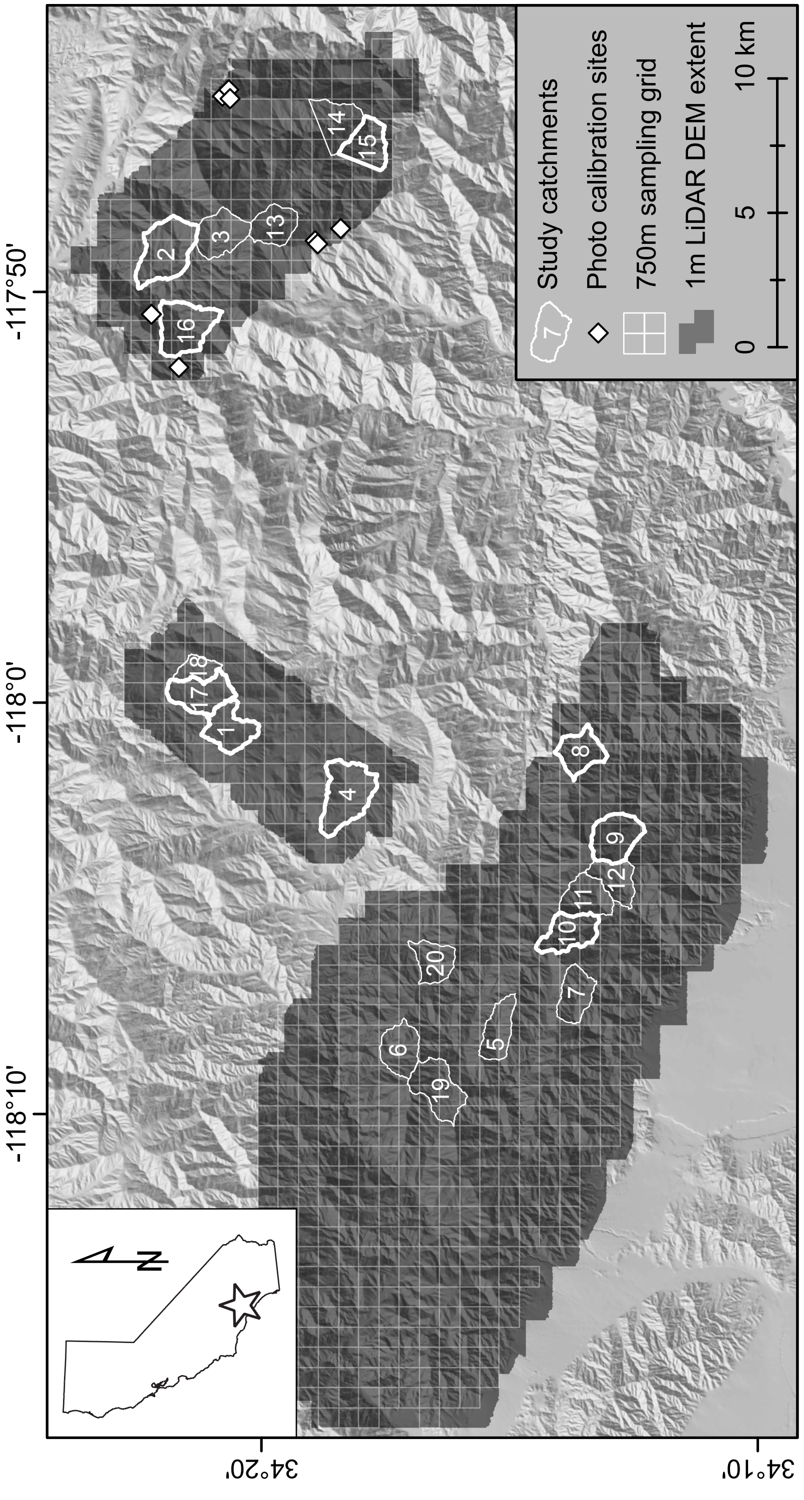
-117°50'
-118°0'
-118°10'
34°20'
34°10'
Study catchments
Photo calibration sites
750m sampling grid
1m LiDAR DEM extent
0
5
10 km
N
1
2
3
4
5
6
7
8
9
10
11
12
13
14
15
16
17
18
19
20

Figure 3.2

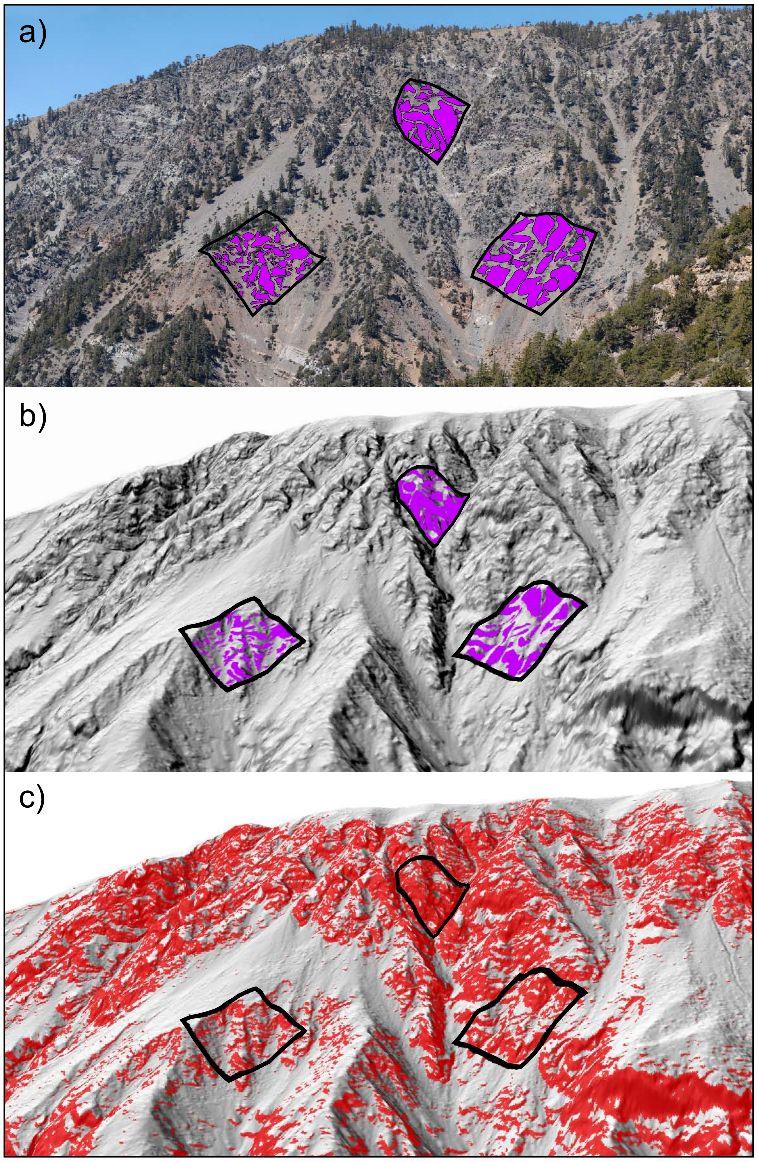

Figure 3.3

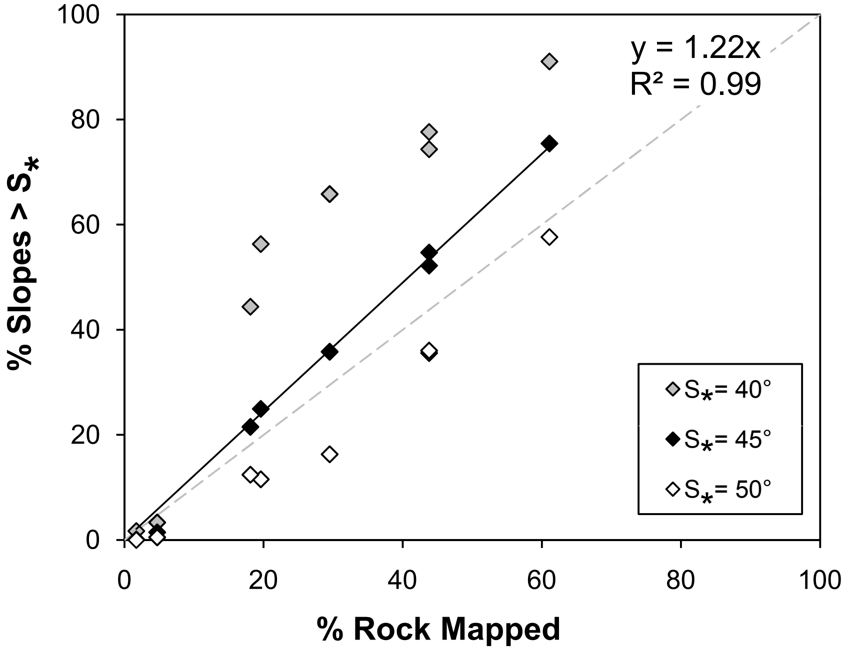

100
80
60
40
20
0
% Slopes > S*
0
20
40
60
80
100
% Rock Mapped
y = 1.22x
R² = 0.99
◇ S* = 40°
◆ S* = 45°
◇ S* = 50°

Figure 3.4

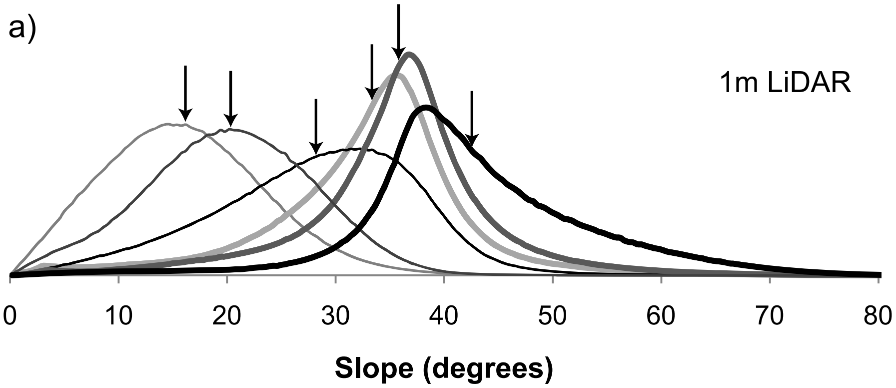
a)
1m LiDAR
0
10
20
30
40
50
60
70
80
Slope (degrees)

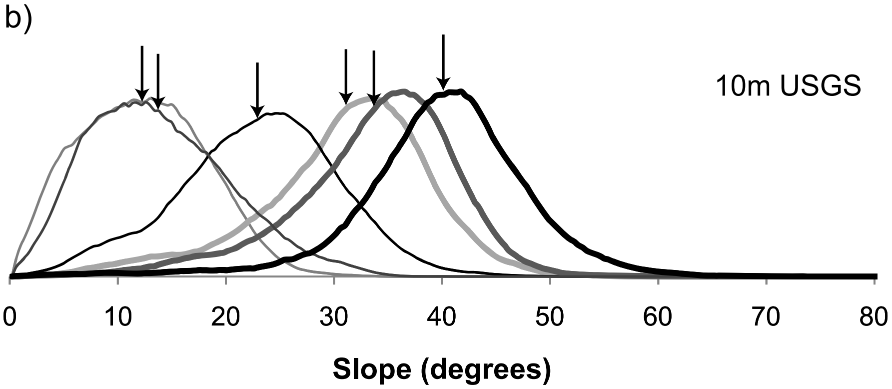
b)
10m USGS
0
10
20
30
40
50
60
70
80
Slope (degrees)

Figure 3.5

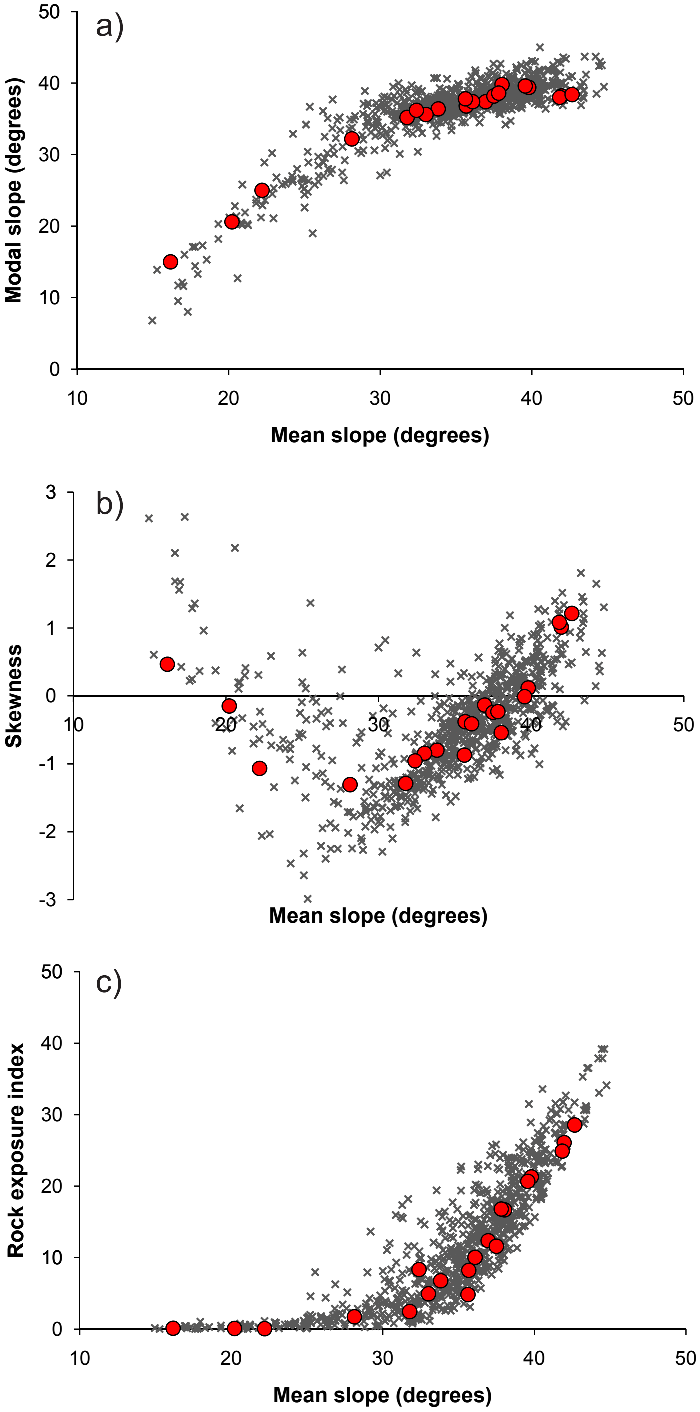
a)
Modal slope (degrees)
0
10
20
30
40
50
Mean slope (degrees)
10
20
30
40
50
b)
Skewness
-3
-2
-1
0
1
2
3
Mean slope (degrees)
10
20
30
40
50
c)
Rock exposure index
0
10
20
30
40
50
Mean slope (degrees)
10
20
30
40
50

Figure 3.6

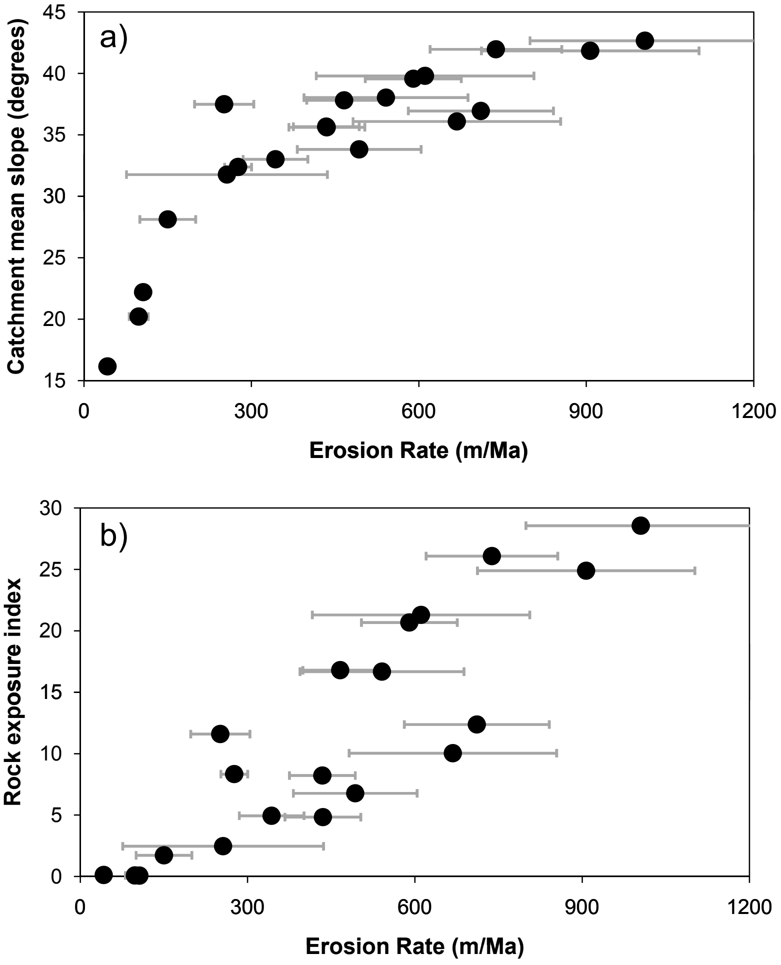
a)
Catchment mean slope (degrees)
45
40
35
30
25
20
15
0
300
600
900
1200
Erosion Rate (m/Ma)
b)
Rock exposure index
30
25
20
15
10
5
0
0
300
600
900
1200
Erosion Rate (m/Ma)

Figure 3.7

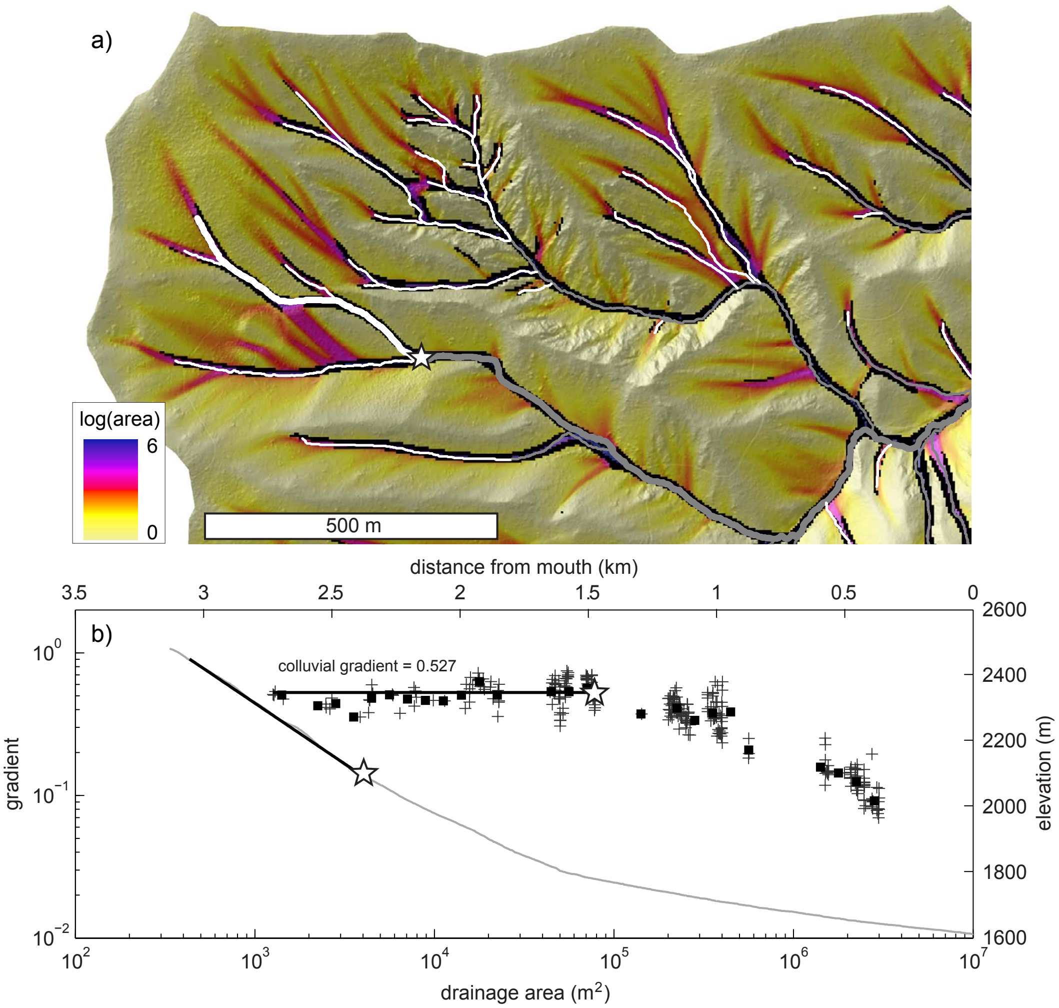
a)
log(area)
6
0
500 m
distance from mouth (km)
3.5
3
2.5
2
1.5
1
0.5
0
b)
colluvial gradient = 0.527
gradient
10^0
10^{-1}
10^{-2}
10^2
10^3
10^4
10^5
10^6
10^7
drainage area (m^2)
elevation (m)
2600
2400
2200
2000
1800
1600

Figure 3.8

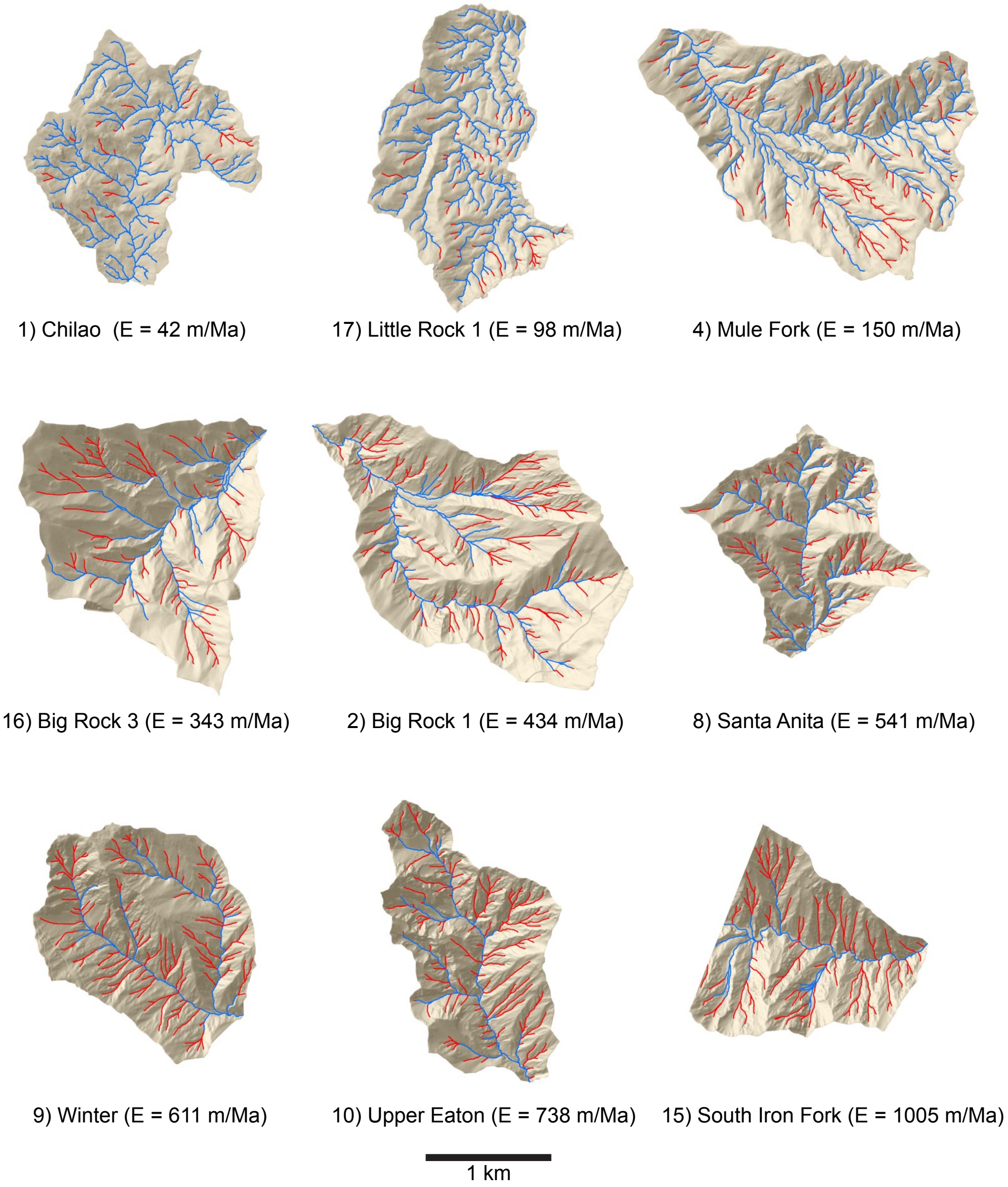

1) Chilao (E = 42 m/Ma)

17) Little Rock 1 (E = 98 m/Ma)

4) Mule Fork (E = 150 m/Ma)

16) Big Rock 3 (E = 343 m/Ma)

2) Big Rock 1 (E = 434 m/Ma)

8) Santa Anita (E = 541 m/Ma)

9) Winter (E = 611 m/Ma)

10) Upper Eaton (E = 738 m/Ma)

15) South Iron Fork (E = 1005 m/Ma)

Figure 3.9

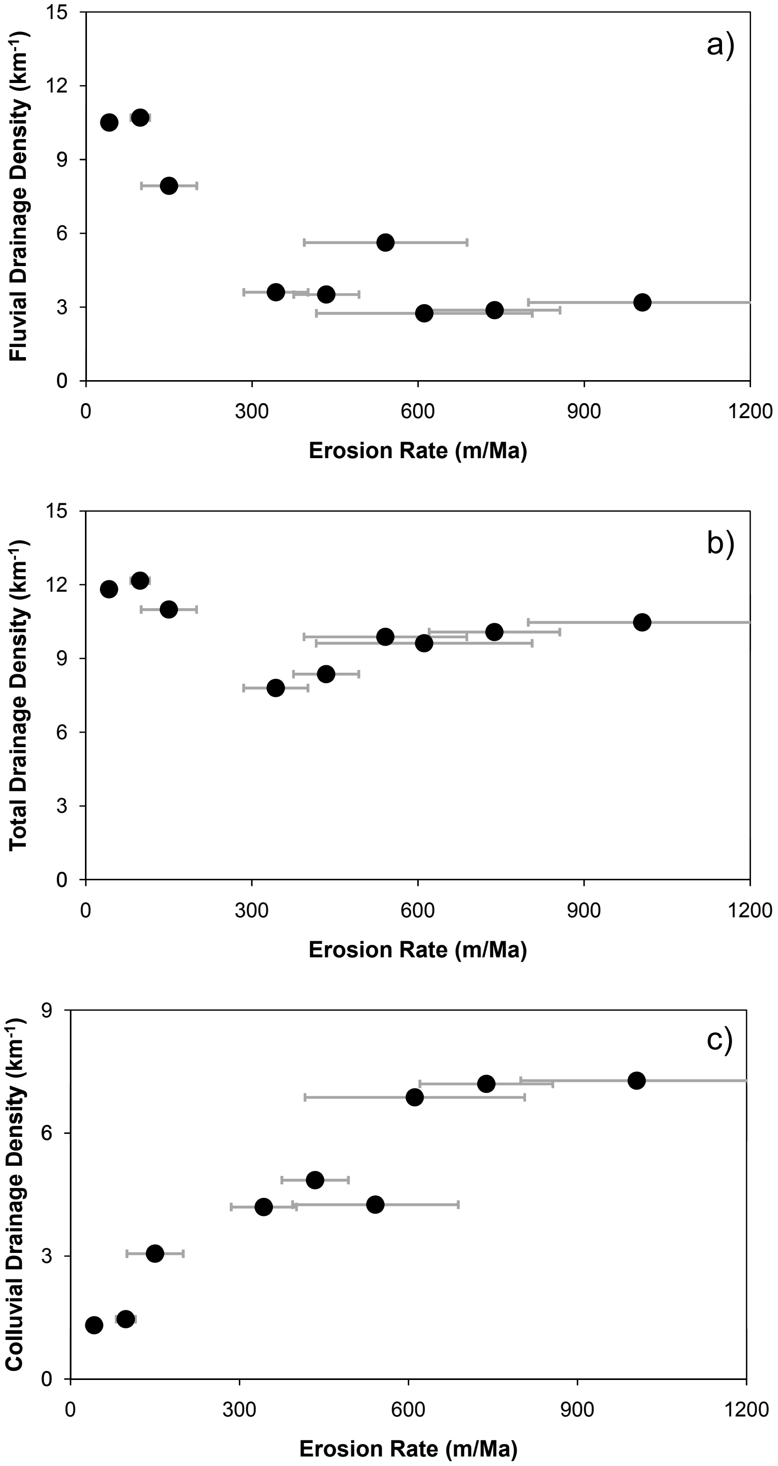

a)
Fluvial Drainage Density (km^{-1})
15
12
9
6
3
0
0
300
600
900
1200
Erosion Rate (m/Ma)
b)
Total Drainage Density (km^{-1})
15
12
9
6
3
0
0
300
600
900
1200
Erosion Rate (m/Ma)
c)
Colluvial Drainage Density (km^{-1})
9
6
3
0
0
300
600
900
1200
Erosion Rate (m/Ma)

Figure 3.10

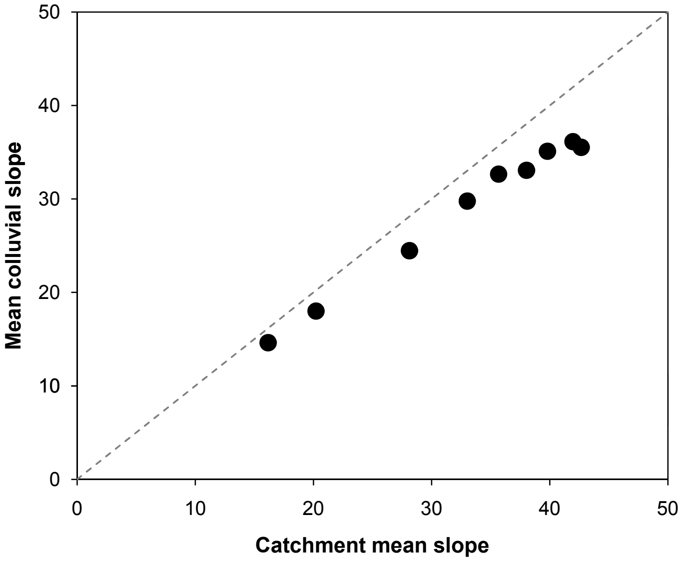

50
40
30
20
10
0
Mean colluvial slope
0
10
20
30
40
50
Catchment mean slope

CHAPTER 4

THE INFLUENCE OF EROSION THRESHOLDS AND RUNOFF VARIABILITY ON THE RELATIONSHIPS AMONG TOPOGRAPHY, CLIMATE, AND EROSION RATE

ABSTRACT

Bedrock river incision occurs only during floods large enough to mobilize sediment and overcome substrate detachment thresholds. New data relating channel steepness and erosion rate provide the opportunity to evaluate the role of thresholds and discharge variability in landscape evolution. We augment an extensive erosion rate data set in the San Gabriel Mountains, CA with analysis of streamflow records and observations of channel width and sediment cover to evaluate the importance of climate and erosion thresholds on incision rates. We find the relationship between channel steepness and erosion rate in the San Gabriel Mountains can be explained using a simple stochastic-threshold incision model where the distribution of large floods follows an inverse power law, suggesting that details of incision mechanics, sediment effects, width adjustment, and debris flows do not significantly influence the steady-state relationship between steepness and erosion rate. Using parameters tuned to this case, we vary climate parameters to explore a range of behavior for the steepness-erosion relationship. Erosion is enhanced by both increases in mean runoff and discharge variability. We explore the implications of an empirical relationship between mean runoff and variability to test whether dry, variable climates can erode more efficiently than wet, stable climates. For channels with high thresholds or low steepness, modeled erosion rate peaks at a mean runoff of 200-400 mm/a. For much of the parameter space tested, erosion rates are predicted to be insensitive to increases in runoff above ~500mm/a, with important implications for the hypothesized influence of climate on tectonics.

INTRODUCTION

Understanding what controls erosion rate in mountainous terrain is critical to the study of a wide range of tectonic and geomorphic problems, such as exploring potential feedbacks between climate and uplift [*Hilley and Strecker*, 2004; *Roe et al.*, 2008; *Stolar et al.*, 2007; *Whipple*, 2009; *Willett*, 2010], determining the role of extreme versus frequent events in shaping the landscape [*Hartshorn et al.*, 2002; *Wolman*, 1960], and distinguishing between climatic and tectonic signals in sedimentary basin deposits [*Armitage et al.*, 2011; *Paola et al.*, 1992]. Bedrock rivers define the relief structure of unglaciated ranges, set the pace of hillslope denudation, and transmit changes in baselevel throughout the landscape. Accordingly, bedrock rivers have been a focus of considerable research over the past decade [e.g., *Cowie et al.*, 2008; *Gasparini et al.*, 2007; *Tucker and Hancock*, 2010; *Whipple*, 2004]. Existing models for bedrock river incision generally predict that erosion rate depends to first order on topographic relief, climate, lithology, and sediment caliber and flux; yet there is a dearth of field data that can be used to evaluate even the relative importance of these factors. For example, it was first recognized over a century ago that sediment in bedrock channels dually influences erosion by both providing tools to erode the bed and cover to protect it [*Gilbert*, 1877]. *Sklar and Dietrich* [1998; 2004] developed a bed-load saltation-abrasion model that accounted for these effects, and much recent work has focused on refining and calibrating the exact formulations for both "tools" and "cover" effects. These adjustments have been primarily theoretical [*Lague*, 2010; *Lamb et al.*, 2008; *Turowski*, 2009], or based on laboratory flume experiments [*Chatanantavet and Parker*, 2008; *Johnson and Whipple*, 2010; *Sklar and Dietrich*, 2001]. In addition, the potential influence of channel narrowing in response to increased incision rate has likewise been the focus of several theoretical treatments [*Finnegan et al.*, 2007; *Finnegan et al.*, 2005; *Stark*, 2006; *Turowski et al.*, 2007; *Turowski et al.*, 2009; *Wobus et al.*, 2006b; *Wobus et al.*, 2008; *Yanites and Tucker*, 2010]. In this regard, theory is far ahead of observation; for example, there have been few field studies of the influence of tools and cover on bedrock incision rates [e.g., *Cowie et al.*, 2008; *Jansen*, 2006; *Jansen et al.*, 2011; *Johnson et al.*, 2009; *Tomkin et al.*, 2003; *Valla et al.*, 2010]. Furthermore, the predicted steady-state channel profiles of detachment-limited and sediment-flux dependent channels mimic those of the simpler, transport-limited case, and only during transient conditions are the differences between these formulations observable [e.g., *Attal et al.*, 2011; *Gasparini et al.*, 2007; *Valla et al.*, 2010]. This result deemphasizes the influence of fully incorporating sediment flux relations into steady-state models. In this paper, we return to work done by *Tucker and Bras* [2000], *Snyder et al.* [2003b], *Tucker* [2004], and *Lague et al.* [2005], and argue that under steady-state conditions and spatially uniform erosion rate, the effects of dynamic width adjustment and sediment cover are subordinate to the role of erosion thresholds and discharge variability in controlling the relation between topography and bedrock channel incision rate. Specifically our field data show no evidence that width and sediment cover differ as a function of erosion rate under steady-state, uniform rock uplift conditions and we demonstrate that a simple stochastic-threshold model [*Lague et al.*, 2005] can explain the observed relationship between channel steepness and erosion rate without appeal to a tools/cover effect or dynamic channel width adjustment.

A number of recent studies attempted to isolate the topographic controls on erosion rates by investigating landscapes where climate and lithology are nearly uniform. *DiBiase et al.* [2010] and *Ouimet et al.* [2009] used cosmogenic ^{10}Be concentrations in active stream sediments to quantify millennial erosion rates for comparison with the channel steepness index, a metric of fluvial relief that normalizes local channel slope for its expected dependence on drainage area [*Wobus et al.*, 2006a]. They found that the channel steepness index increases monotonically with catchment-averaged erosion rate for equilibrium channels (those lacking distinct knickpoints) in the San Gabriel Mountains [*DiBiase et al.*, 2010] and along the eastern margin of the Tibetan plateau [*Ouimet et al.*, 2009]. The channel steepness index emerges as a robust metric of topographic relief that reflects the influence of tectonics, climate, and lithology and that can furthermore be directly tied to bedrock incision models.

While the distinction between specific transport-limited, detachment-limited, and sediment-flux dependent models of fluvial incision is often only expressed during transient landscape response [*Attal et al.*, 2011; *Gasparini et al.*, 2007; *Valla et al.*, 2010; *Whipple and Tucker*, 2002], the relief-erosion rate relationships for steady-state conditions determined in the above studies allows for an examination of first order controls on channel steepness common to all incision models. For example, channel width variation, the presence of erosion thresholds, and water discharge magnitude and variability will all influence the shape of the relationship between relief and landscape-averaged erosion rate predicted by all variants of river incision models. Both *Ouimet et al.* [2009] and *DiBiase et al.* [2010] found a power-law relation between channel steepness and erosion rate:

$$k_s \propto E^{\phi}, \tag{4.1}$$

where k_s is the channel steepness index, E is long-term erosion rate, and $\phi \sim 0.5$. The dimension of k_s depends on the assumed reference concavity, which we fix to 0.45, resulting in units of $m^{0.9}$[*Wobus et al.*, 2006a]. In every studied region, channel steepness increases monotonically with increasing rates of base-level fall, as quantified by either erosion or rock uplift rate [*Cyr et al.*, 2010; *DiBiase et al.*, 2010; *Duvall et al.*, 2004; *Harkins et al.*, 2007; *Kirby and Whipple*, 2001; *Ouimet et al.*, 2009; *Safran et al.*, 2005; *Snyder et al.*, 2003b; *Wobus et al.*, 2006a]. However, the magnitude and shape of this relationship varies widely among different field sites. For example, while a channel steepness index of 60 $m^{0.9}$ is sufficient to erode at 10 mm/a in the Siwalik Hills of Nepal, one tenth that erosion rate requires a channel steepness of 500 $m^{0.9}$ along the eastern margin of the Tibetan plateau [*Ouimet et al.*, 2009; *Wobus et al.*, 2006a]. Furthermore, the shape of this relationship varies; studies have fit data to equation (4.1) with $\phi \sim 0.25$ [*Snyder et al.*, 2003b], $\phi \sim 0.5$ [*DiBiase et al.*, 2010; *Harkins et al.*, 2007; *Ouimet et al.*, 2009], and $\phi \sim 1$ [*Kirby and Whipple*, 2001; *Safran et al.*, 2005; *Wobus et al.*, 2006a]. For the cases where $\phi < 1$, the erosional efficiency of a channel, or its capacity to incise for a given slope, increases with erosion rate (or equivalently, slope).

A non-linear (i.e., $\phi < 1$) relationship between channel steepness and erosion rate may arise for a number of reasons. For example, the relationship between erosion and bed shear stress may be non-linear, as in the case of suspended-load abrasion or plucking [*Whipple et al.*, 2000]; bedrock exposure may change with channel slope, either decreasing available sediment cover or increasing the amount of tools available to abrade the bed [*Sklar and Dietrich*, 2006]; orographic precipitation gradients may intensify rainfall in steeper catchments [*Roe et al.*, 2002]; channels may narrow as they steepen [*Finnegan et al.*, 2005; *Lavé and Avouac*, 2001; *Whittaker et al.*, 2007; *Wobus et al.*, 2006b; *Yanites and Tucker*, 2010]; or an erosion threshold may preferentially retard incision of low gradient channels [*Lague et al.*, 2005; *Snyder et al.*, 2003b; *Tucker*, 2004; *Tucker and Bras*, 2000]. Other factors, including the role of debris flows and varying bed roughness, may also contribute to steep channels becoming more efficient. The relative importance of all the factors listed above on the relation between channel steepness and erosion rate is, however, unclear.

A successful model must include at least thresholds of motion and/or detachment and a representation of the stochastic distribution of floods, as these are known to operate in all channels, whether transport- or detachment-limited [*Lague et al.*, 2005; *Sklar and Dietrich*, 2006; *Snyder et al.*, 2003b; *Tucker*, 2004]. In this contribution, we ask whether a simple model incorporating these factors alone can explain the range of behavior observed in relationships between channel steepness and erosion rate under steady-state and uniform rock uplift conditions. We begin with a review of the theoretical framework of published stochastic-threshold models that predict a non-linear relationship between channel steepness (k_s) and erosion rate (E) consistent with equation (4.1), and then use these models and the erosion rate dataset of *DiBiase et al.* [2010], along with detailed field surveys and discharge records, to explore the controls on ϕ in the San Gabriel Mountains of California. Finally, we combine the model of *Lague et al.* [2005] with an empirical relationship between discharge variability and mean runoff [*Molnar et al.*, 2006] to explore the influence of climate on erosion rate as a function of channel steepness and erosion threshold magnitude.

THEORETICAL FRAMEWORK

Overview of Stream Power Model

We begin by reviewing the formulation of a generalized stream power incision model that incorporates both a threshold term and a stochastic distribution of flood discharges [*Lague et al.*, 2005; *Tucker and Bras*, 2000]. As we will discuss later, graded rivers in the San Gabriel Mountains are actively incising bedrock (at rates from 0.1 – 1 mm/yr), but tend to be mantled with a thin layer of alluvium. Here we follow *Lague et al.*

[2005] in employing a detachment-limited model for simplicity. We acknowledge this as a limitation, but emphasize that at steady state under uniform rock uplift rate conditions the relationship between k_s and E predicted by detachment-limited, transport-limited, and sediment-flux dependent incision models are broadly similar, as shown by *Whipple and Tucker* [2002], *Tucker* [2004], *Sklar and Dietrich* [2006], and *Gasparini et al.* [2007]. In particular, *Tucker* [2004] showed that when the effects of thresholds for detachment or sediment mobilization and a stochastic distribution of floods are incorporated, end member detachment- and transport-limited models predict nearly identical steady-state relationships between k_s and E (see Figures 7a and 7c in [*Tucker*, 2004]); we surmise that steady-state relationships among topography, thresholds, mean runoff, runoff variability, and erosion rate predicted by a detachment-limited model, as used here, will be broadly applicable. Thus, we will adopt the commonly used stream power model of detachment-limited channel incision, which postulates that instantaneous vertical channel incision I is proportional to a power law of bed shear stress τ, commonly approximated as

$$I = k_e(\tau^a - \tau_c^a), \tag{4.2}$$

where k_e and a are parameters that depend on substrate properties and erosion process, respectively [*Howard and Kerby*, 1983; *Lague et al.*, 2005; *Snyder et al.*, 2003b; *Tucker*, 2004]. The threshold term τ_c represents a critical shear stress which must be overcome before erosion occurs. At a minimum, τ_c must be large enough to mobilize detached particles or bed load material, and may be much larger in channels where plucking of fractured blocks is the dominant incision process [*Snyder et al.*, 2003b].

Next we must describe how shear stress depends on water discharge both due to at-a-station variability and downstream increases. A common formulation involves combining a steady, uniform flow approximation for a wide channel (i.e., negligible bank friction) with a frictional resistance relationship (e.g., Manning, Darcy-Weisbach equations), to express bed shear stress as

$$\tau = k_t \left(\frac{Q}{w} \right)^{\alpha} S^{\beta}, \tag{4.3}$$

where k_t is a constant that incorporates gravitational and frictional terms, Q is water discharge, w is channel width, S is water surface slope (usually approximated by the channel bed gradient), and α and β are exponents that depend on the frictional relationship used (for a Manning relation, $\alpha = 3/5$ and $\beta = 7/10$, and for a Darcy-Weisbach relation, $\alpha = \beta = 2/3$; see *Howard* [1994] for full derivation). To close equation (4.3), we must explicitly model how channel width varies across the landscape. In lieu of a more rigorous and direct treatment, bedrock channel width is often modeled using classical hydraulic geometry relations originally developed for alluvial rivers and found to be good descriptors in bedrock rivers as well [e.g., *Montgomery and Gran*, 2001; *Wohl and David*, 2008]

$$w_b = k_w Q_b^{\omega_b}, \tag{4.4a}$$

$$\frac{w}{w_b} = \left(\frac{Q}{Q_b} \right)^{\omega_s}, \tag{4.4b}$$

where the subscript b indicates a reference condition such as mean daily or bankfull flow, and k_w, ω_b, and ω_s are typically empirically derived constants for downstream (equation (4a)) and at-a-station (equation (4.4b)) variations in channel width [*Tucker*, 2004]).

Combining equations (4.3) and (4.4), we can write bed shear stress as:

$$\tau = k_t k_w^{-\alpha} \left(\frac{Q}{Q_b} \right)^{\alpha(1-\omega_s)} Q_b^{\alpha(1-\omega_b)} S^{\beta}, \tag{4.5}$$

with the dependence on water discharge partitioned into at-a-station variation (Q/Q_b term) and downstream variation (Q_b term). Although ω_s is defined in equation (4.4b) as a function of channel cross-sectional geometry alone [e.g., *Turowski et al.*, 2008], it enters the bedrock channel erosion problem through its influence on the exponent on the at-a-station discharge variability term ($\alpha(1-\omega_s)$) after being combined with a resistance relationship that ignores bank friction. We show in *Appendix A* that although ω_s, as defined in equation (4.4b), varies significantly as a function of channel cross-sectional geometry [*Turowski et al.*, 2008], tradeoffs between the increase in width with discharge in channels with gentle banks, and an increase in sidewall friction with discharge in channels with steep banks, conspire to hold the at-a-station discharge exponent ($\alpha(1-\omega_s)$) approximately constant at ~0.5 under a wide range of channel cross-sectional forms (*see Appendix A*). Given that $0.6 < \alpha < 0.7$ holds for standard resistance relationships and the cross-sectional flow model we use in *Appendix A* [*Kean and Smith*, 2004], we implement this constraint in our analyses by holding α fixed at 2/3 and ω_s fixed at 0.25, but acknowledge that this aspect of the problem merits further work.

In many landscapes, it is reasonable to substitute a power-law relationship between a characteristic discharge (such as the mean daily or bankfull) and upstream drainage area A, such that

$$Q_b = R_b A^c, \tag{4.6}$$

where R_b and c are again empirically derived constants. We define this characteristic discharge based solely on streamflow data, rather than channel form, and for our case in the San Gabriel Mountains, we find that $c \sim 1$, for both mean daily discharges (see *section 3.2*) and for decadal maximum flood events [*Lavé and Burbank*, 2004]. Thus R_b can be thought of as a characteristic runoff with dimensions of L/T [*Tucker*, 2004]. We use mean daily discharge as the reference discharge Q_b in all our analyses and thus R_b represents mean daily runoff. Finally, we can use a representation of the channel steepness index consistent with steady-state channels and the stream power river incision model,

$$k_s = SA^{m/n}, \tag{4.7}$$

where $m = \alpha a(1\text{-}\omega_b)$ and $n = \beta a$ to incorporate the topographic variables into a single term. The channel steepness index k_s, can be readily derived from digital elevation models, and for steady state landscapes serves as a scale-independent metric of fluvial relief [*DiBiase et al.*, 2010; *Wobus et al.*, 2006a]. Using equations (4.5) and (4.7), instantaneous channel incision (equation (4.2)) can be written as

$$I = K\left(\frac{Q}{Q_b}\right)^{\gamma} k_s^n - \Psi, \tag{4.8}$$

where $K = k_e k_t^a k_w^{-\alpha a} R_b^m$, $\gamma = \alpha a(1\text{-}\omega_s)$, and $\Psi = k_e \tau_c^a$. Equation (4.8) represents the simplest formulation that, when combined with a probability distribution of flood discharges, allows for the study of climatic influences on fluvial incision as a function of topography. Versions of equation (4.8) are used by *Tucker and Bras* [2000], *Snyder et al.* [2003b], *Tucker* [2004], and *Lague et al.* [2005].

Discharge Variability and Long-term Erosion Rate

For a given channel reach, equation (4.8) predicts a power-law relationship between instantaneous bedrock incision rate and water discharge. A similar power-law relationship is commonly used to model bed-load transport [e.g., *Bagnold*, 1977; *Meyer-*

Peter and Müller, 1948]. *Wolman and Miller* [1960] combined such a relationship with an assumed log-normal distribution of annual peak flows to introduce the concept of an effective discharge that defines channel morphology; small flows do not perform enough work, and large floods are too infrequent. Often the effective discharge in alluvial channels is assumed to be roughly equivalent to the bankfull flood (recurrence interval ~1-2 years). This conceptual framework has transferred to studies of bedrock rivers, where in most studies Q in equation (4.7) is set to a reference discharge Q_b, and τ_c is assumed to be insignificant during such flows. This gives the familiar expression for long-term channel erosion E [*Whipple and Tucker*, 1999],

$$E = K' A^m S^n . \tag{4.9}$$

If using the assumption of $Q = Q_b$, as done in the standard stream power model, the dynamic impact of including the threshold term Ψ becomes absorbed into the constant K'. However, in order to appreciate the influence of the threshold term Ψ, equation (8) must be paired with a model of temporal variability of flood discharge because the fraction of time that flows exceed the threshold is a key factor in long-term erosion [*Lague et al.*, 2005; *Snyder et al.*, 2003b; *Tucker*, 2004].

Tucker and Bras [2000], *Tucker* [2004], and *Lague et al.* [2005] instead define Q as a probability density function $pdf(Q)$, and show that the long-term erosion rate E is given by the product of instantaneous incision rate for a given discharge and the probability of a flood of that magnitude, integrated over the full distribution of floods,

$$E = \int_{Q_c(k_s)}^{Q_m} I(Q, k_s)\, pdf(Q)\, dQ, \tag{4.10}$$

where Q_c is the discharge needed to overcome the threshold shear stress and Q_m is the maximum discharge considered. *Lague et al.* [2005] showed that for most of parameter space (and for all cases considered in this study), the integral in equation (4.10) converges quickly and the choice of Q_m is insignificant. Q_c can be determined by setting I in equation (4.8) to zero and solving for Q. Importantly, Q_c varies with the channel steepness index, k_s (gentler channels require larger flows to overcome erosion thresholds), introducing complexity to the relationship between E and k_s. The nature of the resulting relationship depends on the nature of the probability density function $pdf(Q)$ in equation (4.10). *Tucker and Bras* [2000] and *Tucker* [2004] used the Poisson pulse storm rainfall model of *Eagleson* [1978], along with a simple hydrologic model (spatially uniform Horton overland flow), which together result in an exponential distribution of discharges (Figure 4.1a). In contrast, *Lague et al.* [2005] modeled mean daily discharge following *Crave and Davy* [2001], and define the *pdf* of discharge normalized by the mean daily discharge ($Q/Q_b = Q^*$) as

$$pdf(Q^*) = \frac{k^{k+1}}{\Gamma(k+1)} \exp\left(-\frac{k}{Q^*}\right) Q^{*-(2+k)}, \tag{4.11}$$

where Γ is the gamma function, and k is a variability parameter that varies from 0.1 (high variability) to 3 (low variability). Equation (4.11) is an inverse gamma distribution with a scale parameter k and shape parameter (k+1) [*Evans et al.*, 2000]. Essentially, the inverse gamma distribution combines an exponential tail for low discharges with a power-law distribution of large floods, where the tail of large events is heavy relative to an exponential distribution (Figure 4.1b). To avoid binning issues when comparing actual discharge data (*section 3.2*), we plot the complementary cumulative distribution function (*ccdf*) instead of equation (4.11), which is defined as

$$ccdf(Q^*) = \Gamma(k/Q^*, k+1), \tag{4.12}$$

where $\Gamma(a,x)$ is the regularized gamma function

$$\Gamma(a,x) = \frac{1}{\Gamma(a)} \int_0^x y^{a-1} e^{-y} dy \quad . \tag{4.13}$$

While the Poisson pulse model used by *Tucker and Bras* [2000] and *Tucker* [2004] has been shown to match rainfall data well using independent exponential distributions of storm interval, duration, and intensity, the conversion from rainfall to discharge is of course more complex than represented in the simplified hydrologic model used by *Tucker and Bras* [2000]; adequately modeling runoff distributions based on rainfall distributions requires more sophisticated treatment of catchment-scale infiltration, evapo-transpiration, soil moisture response, non-linear runoff processes, and flood routing through the channel network. Alternatively, stream gage records can be studied directly. *Turcotte and Greene* [1993] suggested that peak flow distributions follow a power-law scaling, where the ratio of the ten-year peak discharge to the one-year peak discharge defines a variability factor that depends on climate. *Malamud and Turcotte* [2006] tested the predictions of a power-law flood scaling and found good agreement with paleo-flood records on the Colorado River in the Grand Canyon. *Molnar et al.* [2006] expanded on the analysis of *Turcotte and Greene* [1993] to incorporate gaging stations across the United States, and analyzed both peak flow records and records of mean daily discharge, finding that both sets of records tend to have power-law tails for the range of climate zones and catchment sizes tested. Indeed, only 3% of the 144 gaging stations analyzed by *Molnar et al.* [2006] exhibited exponential tails. *Lague et al.* [2005] also defined the slope of the power-law tail, expressed as 2 + *k* in equation (4.11), as a climate variability factor analogous to that developed by *Turcotte and Greene* [1993]. Following these studies, we assume that equation (4.11) is broadly applicable for upland catchments, as supported by our own analyses of discharge records in the San Gabriel Mountains (*section 3.2*). Although not intuitively obvious, the difference between an exponential and power-law tail to the discharge probability distribution significantly influences the predicted relation between channel steepness and erosion rate, as developed by *Tucker* [2004] (exponential tail) and *Lague et al.* [2005] (power-law tail) and illustrated below.

APPLICATION: SAN GABRIEL MOUNTAINS

We use the San Gabriel Mountains of California to evaluate the controls on steady-state channel steepness using (1) an extensive dataset of catchment-averaged cosmogenic radionuclide (CRN) derived erosion rates [*DiBiase et al.*, 2010], (2) an analysis of long time series of hydrologic data, and (3) detailed field observations of channel morphology and bed state.

Prior Work

The San Gabriel Mountains (SGM) lie along a large restraining bend in the San Andreas Fault, just north of Los Angeles, California (Figure 4.2). A series of north-dipping thrust faults along the southern range front accommodates most of the convergence, and sets up a strong W-E gradient in uplift rate and topographic relief [*Spotila et al.*, 2002]. Additionally, this gradient in uplift rate has been sustained long enough such that we can investigate a number of moderately sized (~1-100 km^2) catchments developed in similar lithologies and experiencing similar climate forcing that have adjusted to differing rates of relative base level fall. *DiBiase et al.* [2010] measured *in situ* produced cosmogenic ^{10}Be concentrations in active stream sands from 50 basins spanning the range to quantify millennial erosion rates ranging from 35-1100 m/Ma (Figure 4.2). The basins range in size from 0.1-175 km^2, and were chosen to sample a wide range of relief. For each basin larger than 3 km^2, a representative channel steepness index was determined from freely available 10 m resolution digital elevation models following the methodology of *Ouimet et al.* [2009] and *Wobus et al.* [2006a]. Channel steepness ranges from 30-180 m$^{0.9}$, and increases monotonically with erosion rate [*DiBiase et al.*, 2010]. Mean annual precipitation (MAP) varies with elevation from 500 mm/a in the Los Angeles basin to over 1000 mm/a along the range crest, and decreases again to 200 mm/a in the rain shadow to the north; MAP in sampled catchments spans a range of 600-1000 mm/a. The range lithology is composed mainly of crystalline basement rocks and Mesozoic granitic intrusions, and rock type appears to play a minor role, with no measureable difference between end-member cases of anorthosite, schist, and granite expressed in the k_s-E relationship [*DiBiase et al.*, 2010].

Climate and Discharge Records

Streamflow in the San Gabriel Mountains has historically been heavily monitored. While only two basins are actively gaged by the USGS at present (Arroyo Seco and Big Rock Creek), twentieth century records for dozens more can be easily obtained. For this study, we selected 9 gages that have records spanning at least 40 years, and have minimal anthropogenic impact (e.g. dams, diversions) (Table 4.1). Mean daily discharge scales linearly with drainage area across 3 orders of magnitude, corresponding to a mean annual runoff of ~280 mm/a, about 30% of average rainfall as expected for losses to infiltration and evapotranspiration (Figure 4.3).

To test the applicability of the inverse gamma distribution (equations (4.11-4.12)) [*Crave and Davy*, 2001; *Lague et al.*, 2005], we normalized flows by the mean of all daily flows for each respective gage, and generated a rank-frequency plot of all values (equivalent to the *ccdf*) [*Newman*, 2005]. Equation (4.12) fits the SGM discharge data well using a variability factor k ~0.4-0.6 (Figure 4.4) – much better than the best-fit exponential distribution, but not perfectly. As shown in Figure 4.4, there is a slight separation between two groups of gages; small catchments along the southern range front appear to experience slightly more frequent moderate floods ($10 < Q^* < 100$). We emphasize that while the inverse gamma distribution, with only one free parameter (k), cannot capture such subtle differences between individual gages, most of the discharge data lie within $k = 0.5 \pm 0.1$, and we make the assumption that flood distributions across the SGM are similar and adequately described by this range of k. For comparison with the approach of *Tucker* [2004], we also used hourly rainfall station data in the SGM to calibrate the Poisson pulse model of *Eagleson* [1978] similar to *DiBiase et al.* [2010]. We assume spatially uniform Horton overland flow, and scale mean runoff to equal 280 mm/a for direct comparison to discharge data. Specific model parameters are given in Table 4.2.

Channel Width and Sediment Cover Surveys

We conducted field surveys of over 40 km of river channels to produce an extensive dataset detailing the distribution of channel width and sediment cover across the range. Many, but not all of these reaches lie within basins sampled for detrital CRN-derived erosion rates. For the context of this paper, we focus on channel segments that can be considered equilibrated; that is, the long profile lacks prominent knickpoints in or above the surveyed section, and the upstream extent of the drainage network can be fit with a single channel steepness index and concavity [*Wobus et al.*, 2006a]. We characterize channel segments as either low relief (k_s = 30-100) or high relief (k_s = 100-180).

For each of our field surveys, we used a laser rangefinder and electronic data logger to record measurements of bankfull channel width and percent exposed bedrock (estimated visually to the nearest 10%) in the channel bed at intervals of approximately 20-40 m, over channel lengths ranging from 700 m to 4 km. We measured channel width using a laser rangefinder, based on vegetation lines and slope breaks in channel cross sections. We supplemented our surveys with point measurements of channel width taken along streams we did not survey in detail. In order to avoid biasing width measurements toward the high-resolution surveys, we averaged the logarithm of width and drainage area between major tributary junctions for each survey. Figure 4.5 shows the results of our width measurements plotted against upstream drainage area. The widths of both high and low relief channel reaches follow similar scaling with drainage area, and furthermore lie on the same general trend as a world-wide compilation of similar data for bedrock channels [*Whipple*, 2004; *Wohl and David*, 2008]. While some authors argue for channel narrowing as a means to increase erosional efficiency in steep landscapes [*Duvall et al.*, 2004; *Whittaker et al.*, 2007; *Yanites and Tucker*, 2010], this appears to not be the case for graded streams in the San Gabriel Mountains, consistent with earlier findings in the King Range, CA [*Snyder et al.*, 2003a]. As discussed by *Whipple* [2004] and consistent with analysis by *Yanites and Tucker* [2010] and observations by *Whittaker et al.* [2007], channel width response is likely strongest during transient adjustment and where rock uplift is localized along a downstream segment of a river profile [e.g., *Lavé and Avouac*, 2001]. Thus we can rule out channel width as a cause for increasing erosional efficiency with relief for steady-state channels in the San Gabriel Mountains, and possibly in general.

At each survey point, we also estimated the percent of exposed bedrock on the channel bed. As shown in Figure 4.6, bare bedrock channels are rare in the San Gabriel Mountains, and the mean of all reaches, both high and low uplift, is ~4% exposure. Most importantly, while our observations of bed conditions at low flow are unlikely to reflect conditions during floods, we see no trend in percent bed exposure across the range. Additionally, many range front channels grade smoothly into fan deposits, suggesting that the shear stress exponent for detachment-limited incision is similar to that of transport-limited rivers (n~1 for bedload transport [*Meyer-Peter and Müller*, 1948]). Moreover, as shown by Whipple and Tucker (2002), if the shear stress exponent for detachment-limited incision is greater than that for bedload transport ($n > 1$), channels must become increasingly buried in sediment as relief and erosion rate increase – a process that will tend to force channels into a transport-limited condition in which $n \sim 1$ pertains. Because of this tendency and because our observations do not support an increase in the degree of bed cover with erosion rate, we can rule out non-linear bedrock incision processes ($n > 1$) as a means of increasing erosional efficiency as relief increases in the San Gabriel Mountains.

Lastly, while we did not quantify the threshold shear stress in the SGM directly, we can use a Shields criterion to approximate a minimum required shear stress based on that needed to mobilize the alluvial bed material,

$$\tau_c = 0.03(\rho_s - \rho_w)D_{50}, \tag{4.14}$$

where 0.03 is a conservative estimate of the critical Shields stress for initiation of motion in mixed grain-size beds [*Buffington and Montgomery*, 1997], D_{50} is the median grain size, and ρ_s and ρ_w are sediment (~2700 kg/m^3) and water (1000 kg/m^3) densities, respectively. We conducted pebble counts of bed surface material at 44 locations across the SGM, consisting of ~100 grains each. Additionally, we estimated median grain size by eye along each of our channel surveys, with periodic calibration by more detailed point counts. We find that at the reach scale (ca. 100 m), D_{50} varies widely, from 22 – 180 mm (Figure 4.6 inset, gray lines). There is no systematic variation with relief. For simplicity, we assume a D_{50} of 90 mm, corresponding to $\tau_c = 45$ Pa, based on the median of all point counts combined (Figure 4.6 inset, black line), and consistent with the median of all estimated values from channel surveys (not shown).

Comparing Model Predictions and Data in the SGM

Using the above field observations and discharge records as constraints, we tuned the model of *Lague et al.* [2005] (combination of equations (4.8), (4.10), and (4.11)) to fit the relationship between channel steepness and erosion rate quantified in the SGM by *DiBiase et al.* [2010]. While *Tucker* [2004] and *Lague et al.* [2005] provided analytical solutions to end-member cases for exponential and inverse gamma flood distributions, respectively, we opted to numerically integrate equation (4.10) using an adaptive Simpson's method [*Gander and Gautschi*, 2000] in all our analyses to smoothly capture the full range of model behavior. We used a generalized Darcy-Weisbach friction relation ($\alpha = \beta = 2/3$; $k_t = \rho_w g^{2/3} C_f^{1/3}$) with non-dimensional friction coefficient $C_f = 0.01$, following *Tucker* [2004]. As mentioned above, we find no evidence that the degree of rock exposure varies with channel steepness or erosion rate in steady-state channels in the SGM, so we make the assumption that the shear stress exponent is equal to that of common bedload transport formulae [e.g., *Meyer-Peter and Müller*, 1948], giving $n = a\beta = 1$ in equation (4.8).

Assumptions regarding channel width scaling are somewhat more complicated. In order to equate the channel steepness index measured from field data (reference concavity = 0.45) with that in equation (4.8), we must fix the ratio m/n to 0.45, which implies a width-discharge exponent value of 0.55 (ω_b in equation (4.4a)). The regressed value of ω_b from SGM channels is much lower (Figure 4.5), so for internal consistency here we determine k_w by regressing the width data in the SGM using a fixed value of ω_b = 0.55. Although a bit awkward and suggestive that the controls on channel profile concavity in the SGM are not fully understood [*Snyder et al.*, 2003a], these adjustments have little impact because the width scaling holds constant across the landscape (Figure 4.5). Only a systematic change in width-area scaling with channel steepness will influence the shape of the k_s-E relationship. We fix ω_s to 0.25, based on general results from a 2D cross-sectional flow model as mentioned earlier (*Appendix A*; Figures A1, A2). As noted earlier, mean runoff and discharge variability (R_b = 280 mm/a; k = 0.5 ± 0.1) are calibrated against USGS gaging records, and we use field estimates of D_{50} to determine a value of 45 Pa for τ_c.

Given these constraints, there is only one free parameter, k_e, a measure of rock strength, which we tune to fit the model to our data, minimizing the RMS error in erosion rate for each of our CRN data points (black line, Figure 4.7). We also show two fits (dashed lines, Figure 7) reflecting the range of uncertainty in k (0.4-0.6) and the quantity $\alpha(1- \omega_s)$ (0.45-0.55, Figure A2). To highlight the influence of the choice of *pdf(Q)* in equation (4.10), we also fit the *Tucker* [2004] model to the SGM data using a similar approach (gray line, Figure 4.7). We use Poisson rainfall parameters as described above, and hold all other parameters equal to the *Lague et al.* [2005] case except for k_e, which we again vary to minimize RMS error in erosion rate. While both the *Tucker* [2004] and the *Lague et al.* [2005] model capture the rollover of the k_s-E relationship at high erosion rates, the *Tucker* [2004] model deviates from a power law at low erosion rates, precisely where the influence of an erosion threshold is most important (Figure 7 inset).

Discussion of Model Application to the SGM

Whereas the *Lague et al.* [2005] model explains much of the variability in the SGM data, there are two notable deviations. Channels with $k_s < 40$ erode more rapidly than predicted by the model, which by definition assumes that hillslope erosion is set by the channel incision rate (i.e., steady-state) and thus that erosion rate goes to zero for $k_s = 0$. One plausible explanaton is that these slowly eroding, low-relief catchments are not in steady state, but rather in a state of slowly declining relief. Under such a scenario it would be likely that catchment-mean erosion rate would exceed the channel incision rate – hillslope erosion will continue as long as some local relief persists even where channel incision has ceased. A second misfit is noted in that rapidly eroding catchments ($E > 500$ m/Ma) tend to be less steep than predicted (Figure 4.7). Potential reasons for this misfit include an increased influence of debris flows in the high relief landscapes of the SGM, inaccuracies of the detrital CRN method at high erosion rates, changes in bed roughness, or differences in the flood frequency probability distribution not resolved by equation (4.11).

The *Tucker* [2004] model appears to better capture the behavior of rapidly eroding catchments, but at the cost of significant misfit at low erosion rates due to the thinner tail of the exponential flood distribution. Whereas the considerable scatter in the SGM erosion rate data prevents discriminating between the *Tucker* [2004] and *Lague et al.* [2005] models, we note that the power-law tail exhibited by SGM discharge data strongly supports the *Lague et al.* [2005] model. Indeed, it is at low erosion rates where differences in the tail of the flood distribution becomes most important, as the critical flow needed to overcome the erosion threshold, Q_c, increases with decreasing channel steepness because deeper flows are required to exceed the threshold shear stress in channels with gentler slopes. It is therefore quite satisfying that the model that includes the fatter power-law tail to the flood distribution fits the data at low to moderate channel steepness considerably better (Figure 4.7). The ability of this simple model, which includes no treatment of bed cover and dynamic width adjustment, to explain the shape of the k_s-E relationship reinforces our field observations that indicate that these factors are not important in the SGM.

We speculate, but cannot yet definitively demonstrate, that this finding has general implications and is not unique to the SGM – that under steady-state conditions and uniform rock uplift rate in general, the effects of bed cover variations and dynamic width adjustment tend to be negligible compared to the effects of a probability distribution of floods acting in the presence of significant detachment or mobilization thresholds. If true, this implies that much can be learned about the relationships among climate, topography and erosion rate from further study of the behavior of the stochastic-threshold model of *Lague et al.* [2005], which we undertake in the following section.

APPLICATION: CLIMATIC CONTROLS ON THE RELIEF-EROSION RATE RELATIONSHIP

General Model Behavior

The relationship between steady state erosion rate and relief (as quantified by the channel steepness index, k_s) is both a critical input for landscape evolution and coupled climate-landscape-tectonics models, and directly measureable. With the widespread availability of digital elevation models, and an increasing number of studies quantifying catchment-averaged erosion rates using cosmogenic radionuclides, we are able to begin untangling the first-order effects of topography, climate, and rock strength in controlling bedrock incision rate. In the previous section, we showed that a non-linear ($\phi \sim 0.5$; equation (4.1)) relationship between erosion rate and channel steepness in the San Gabriel Mountains could be explained well using the stochastic-threshold model of *Lague et al.* [2005]. Other regions with similar data suggest that ϕ ranges from 0.25 to 1 [*Kirby and Whipple*, 2001; *Ouimet et al.*, 2009; *Snyder et al.*, 2003b; *Wobus et al.*, 2006a]. In this section, we will summarize some of the key points of *Lague et al.* [2005] within the context provided by the San Gabriel Mountains example. We focus here on the controls on the shape of the relationship between channel steepness and erosion rate – differences that are most clearly manifest by the power-law exponent (ϕ) of equation (4.1). The power-law form of the predicted relationship is directly a result of combing a power-law relationship between I and Q^* (equation (4.8)) with a power-law distribution of floods (equation (4.11)). Following a discussion of the controls on the power-law exponent (ϕ), we explore how changing climate mean and variability influence the relationship between channel steepness and erosion rate.

A convenient way to show the variations in the relationship between channel steepness and erosion rate is to plot the power-law exponent, ϕ, against erosion rate normalized by the threshold term Ψ (Figure 4.8). As discussed by *Lague et al.* [2005], there are 3 regimes expressed in Figure 4.8, depending on the relative importance of the threshold parameter Ψ (or equivalently, the return time of the critical discharge, Q^*_c). At high incision rate (or negligible threshold, Regime III), the relation approaches the approximation of equation (4.9), and k_s is proportional to $E^{1/n}$ (equation 1 with $\phi = 1/n$), where n reflects process mechanics [*Whipple et al.*, 2000], for any flood distribution. On the other hand, when the threshold is large compared to the incision rate (Regime I), the exponent ϕ in equation (4.1) is independent of n (or a in equation (4.2) and thus erosion process mechanics), and rather depends primarily on k (discharge variability) and the at-a-station shear stress-discharge exponent, $\alpha(1\text{-}\omega_s)$, in equation (4.5)) according to the following relation [*Lague et al.*, 2005]:

$$\phi = \frac{\alpha(1-\omega_s)}{\beta(1+k)}. \tag{4.15}$$

where β is from the flow resistance relationship and takes values of 7/10 for the Manning relation and 2/3 for the generalized Darcy-Weisbach relation (equation (4.3)). Between the end-member cases of Regime I and III lies a transitional zone (Regime II). The San Gabriel Mountains lie entirely within the threshold-dominated regime, with the critical flow return time [*Lague et al.*, 2005] ranging from 500 days (low relief) to 50 days (high relief) (Figure 4.8). Thus uncertainty in most parameters (especially τ_c) can be subsumed into the high uncertainty in k_e, which we varied to fit the model to the SGM data. The predicted ϕ of 0.5 for the SGM (from equation (4.15)) matches well with a simple error-weighted least squares power-law fit to the erosion rate data, which results in a fitted exponent of 0.48 (95% confidence range = 0.36-0.75; $R^2 = 0.64$).

We use this well-constrained case to fix all parameters except mean runoff (k_q) and climate variability (k) to explore the role of climate alone in controlling incision rates. Figure 4.9a shows the effect of changing mean runoff (R_b) by an order of magnitude in either direction from the SGM case. As R_b does not factor into ϕ or Ψ, the shape of the k_s-E relationship stays the same; however, increasing mean runoff increases erosion rate for a given channel steepness and decreasing mean runoff does the opposite [*Lague et al.*, 2005]. It should also be noted that the influence of changing mean runoff is partially offset by corresponding changes in channel width (i.e., equation (4.4a)). Changing climate variability (k) induces a more complex response. As shown in Figure 4.9b, the power-law exponent in the k_s-E relationship (ϕ) decreases with decreasing variability (large k). Thus the k_s-E relationship becomes increasingly non-linear as discharge variability decreases (large k, Figure 4.9b). Indeed, for an exponential flood distribution tail [*Tucker*, 2004], the k_s-E relationship becomes too strongly non-linear at low channel steepness (in Regime I) to be described by a power-law (Figure 4.7). Additionally, when in the threshold-dominated regime, increasing climate variability, while holding all else equal, increases erosion rate for a given k_s, (Figure 4.9b). The opposite is true for channels in regime III [*Lague et al.*, 2005].

Co-variation of Mean Runoff and Climate Variability

The above analysis indicates that all else equal, wetter and more variable climates increase erosional efficiency, while dry and steady climates are less efficient – a fairly intuitive result and one familiar from previous work [*Lague et al.*, 2005; *Tucker*, 2004]. A more challenging question, and one often postulated by workers interested in global climate change and climate/tectonics feedbacks, is whether dry and variable climates can be more efficient than stable, wet climates [*Molnar*, 2001; *Molnar et al.*, 2006; *Zhang et al.*, 2001]. While *Istanbulluoglu and Bras* [2006] explicitly modeled the catchment-scale response of soil moisture and vegetation cover to changes in rainfall intensity, such field data are scarce, and we focus instead on exploring only the observed relationships between mean runoff and variability from gaged streams. *Turcotte and Greene* [1993] argued that discharge variability was highest in arid environments, and lowest in humid environments. *Molnar et al.* [2006] extended this analysis and found that, at least for gages within the United States, there is a roughly inverse relationship, albeit with much scatter, between mean annual runoff and variability expressed by k ($R_b \sim k^{1.6}$). Using precipitation records compiled by *Hawk* [1992], *Tucker* [2004] and *Istanbulluoglu and Bras* [2006] found a similar relationship between a metric of storm variability and mean annual precipitation across the United States.

Here we extend the analyses of *Lague et al.* [2005] and *Molnar et al.* [2006] to explore quantitatively the competition between the influence of mean runoff and variability on channel incision when the two are inversely related according to the relationship

$$k = \left(\frac{R_b}{B} \right)^C , \tag{4.16}$$

where B and C are empirically derived constants [*Molnar et al.*, 2006]. B and C values of 850 mm/a and 0.625, respectively, describe the central tendency in the discharge data compiled by *Molnar et al.* [2006], but we emphasize that there is significant scatter in the data (B ranges from ~20-1000; C ranges from ~0.5-1.0), which in addition covers only the continental United States and does not apply across all climate zones. Indeed some tropical climates, where heavy rainfall is dominated by tropical cyclones, can be both wet and variable (e.g., Taiwan [*Lague et al.*, 2005]).

Figure 4.9c shows the effect of varying mean annual runoff from 0.03 to 2.8 m (corresponding to a range in k from 0.12 to 2.1 using equation (4.16) with the B and C values given above), while holding all other parameters equal to the SGM case. The crossing of curves at low erosion rates (< 200 m/Ma) represents a transition in climate sensitivity; low-steepness channels are more sensitive to changes in climate variability than mean runoff, while the opposite is true for steep channels (see also Figures 4.9, 4.10). Channels with low steepness require larger floods to overcome thresholds of erosion – floods that can actually be more common in dry, but variable environments (see Figure 4.6 in *Molnar et al.*, [2006]).

Plotting erosion rate against mean runoff highlights this behavior. Figure 4.10a shows the relationship between erosion rate and mean runoff for a range of channel steepness index values, using the parameters in Table 4.2 and values for B and C given above. For channels with low channel steepness ($k_s < 100$), there is a hump in the erosion-runoff relationship between mean runoff (R_b) of 100 and 400 mm/a, indicated by the white diamonds. For channels with high channel steepness ($k_\mathrm{s} \geq 100$) the relationship between erosion and runoff is monotonic (dashed lines), though there is still a significant flattening of the relationship for $R_b > \sim 200$ mm/a. We emphasize that while this peak in erosional efficiency (erosion rate for a given channel steepness) roughly matches that observed by *Langbein and Schumm* [1958], and predicted by *Istanbulluoglu and Bras* [2006], it arises here solely because of trade-offs between variability and mean runoff in bedrock channel incision, factors not considered in these other works.

The existence and location of a peak erosional efficiency depend not only on the channel steepness index, but also on the magnitude of the threshold, τ_c, and the strength of the runoff-variability relationship (controlled by C in equation (4.16)), as shown in Figure 4.10 (b-e). Increasing τ_c has a similar effect on the relationship between erosion and runoff as decreasing channel steepness – by increasing Q^*_c, discharge variability becomes more important, and the peak is enhanced (Figure 4.10c). Conversely, for small τ_c, large floods are less important, and the peak is diminished (Figure 4.10b). Changing C varies the strength of the runoff-variability relationship and thus illustrates the uncertainty associated with the scatter in the data. When C is large, variability increases rapidly with decreasing mean runoff, and the peak in erosional efficiency is enhanced

(Figure 4.10d); when *C* is small, variability and mean runoff are but weakly related and thus the peak is subdued (Figure 4.10e). Naturally, Figures 9a and 9b illustrate the model behavior when R_b and *k* are independent.

The results shown in Figure 4.10 suggest that the relationship between climate and erosion rate is complex, and changes depending on the ratio of channel steepness to the erosion threshold. While *Molnar et al.* [2006] suggested that change to drier, more variable conditions would rarely increase erosion rate, we show here that such a trend is possible over a wide range of conditions (solid lines in Figure 4.10). Furthermore, there is a range of parameter space where changing climate does not influence erosional efficiency – that is, the competing effects of decreased variability and increased runoff are in balance. We emphasize again that the relationship between mean runoff and discharge variability expressed by equation (4.16) only applies to a narrow band of potential climate scenarios (those analyzed by *Molnar et al.* [2006] in the continental US). Even so, Figures 4.9 and 4.10 highlight both the potential implications of co-variance between R_b and *k* and the need for careful site selection when trying to quantify the relationship between climate and erosion rate in the field. These results suggest one plausible explanation for the diversity of published relationships summarized by *Riebe et al.* [2001].

DISCUSSION

Implications for Climate-Tectonic Interactions

The finding that the relationship between channel steepness and erosion rate in the SGM is highly non-linear ($\phi = 0.5$; Figure 4.7) and the model implication that this may be a common circumstance (Figure 8) carry important implications for the strength of the hypothesized influence of climate on rock uplift rates and deformation patterns in compressional orogens [e.g. , *Hilley and Strecker*, 2004; *Whipple*, 2009; *Whipple and Meade*, 2004; *Willett*, 1999]. *Whipple and Meade* [2004] show that steady-state rock uplift rate in a compressional orogen, U, scales with the tectonic accretionary flux (F_a) and coefficient of erosional efficiency (C_e) according to:

$$U \propto F_a^{\frac{p}{p+1}} C_e^{\frac{1}{p+1}} \tag{4.17a}$$

$$p = 0.8/\phi, \tag{4.17b}$$

where the 0.8 arises from the product of the channel concavity index (~0.5) and the inverse of the Hack's law exponent (~1.7). A value of $\phi = 0.5$, as found for the SGM and the eastern margin of the Tibetan Plateau [*Ouimet et al.*, 2009], implies $U \propto F_a^{0.6}\, C_e^{0.4}$ – the weakest dependence of rock uplift rate on erosional efficiency considered to be within the range of likely conditions by *Whipple and Meade* [2004].

The analyses illustrated in Figures 4.9 and 4.10 exacerbate this apparent weakening of theoretical predictions of the strength of the potential influence of precipitation rate on steady state rock uplift. As discussed by *Stolar et al.* [2006], in the standard stream power river incision models (which ignore the threshold-stochastic effects and potential inverse relationship between mean annual runoff and discharge variability emphasized here) the coefficient of erosional efficiency, C, scales approximately with the square root of mean annual runoff. Combined with the above result, this implies that steady state rock uplift rate varies only weakly with mean annual runoff, $U \alpha F_a^{0.6} R_b^{0.2}$. As illustrated in Figure 4.10, when thresholds of erosion and the potential co-variation of discharge variability and mean annual runoff are considered, the relation between erosional efficiency and mean annual runoff can be much weaker as cautioned by *Whipple and Meade* [2006] and *Whipple* [2009]. Although we can only speculate for now, this could be one reason why clear field evidence for a strong coupling between climate and tectonics has been difficult to find [e.g., *Whipple*, 2009]. That said, model predictions also indicate that the strongest influence of climate on tectonics will likely be found where channels are steep (Figure 4.10), where flood discharges are highly variable (Figure 4.8), and where increases in mean annual runoff are not offset by decreases in discharge variability, such as orogens frequently struck by tropical cyclones like the Central Range of Taiwan [*Lague et al.*, 2005]. Moreover, glaciated mountain ranges may be more sensitive to climate changes and tectonics more responsive to glacial erosion [e.g., *Tomkin and Roe*, 2007].

Limitations and Future Research Needs

Whereas the simple stochastic-threshold incision model described above is consistent with channel steepness (k_s) and erosion rate (E) data in the SGM, suggesting that the presence of erosion thresholds and discharge variability may be primarily responsible for the strong non-linearity in the k_s-E relationship (equations 4.1 and 4.15), we cannot yet determine whether climatic effects alone provide a full explanation for the steady-state channels in the SGM, nor whether they can potentially explain differences in the relief-erosion rate relationships observed in other landscapes. There are few studies in the literature that provide the range of relief and erosion rates necessary to evaluate this possibility, and even fewer that also have long-term discharge records and field observations to constrain the parameters listed in Table 4.2. Moreover, the use of decadal to centennial hydrologic records must be used to extrapolate climate conditions over the timescale of erosion rate measurements, which must in turn be long enough to incorporate the influence of large events. Finally, the challenge of quantifying rock strength and erosion thresholds directly makes inter-site comparison difficult. However, given careful site selection, the relationships shown in Figures 4.9 and 4.10 serve as a set of testable hypotheses that have the potential to illuminate the currently cloudy empirical relationships between climate and erosion rate.

In particular, detecting a climatic control on erosion rate (i.e., determining the dependence of erosional efficiency on mean annual runoff and discharge variability) requires a suite of field sites in different climate regimes, each covering a range of relief, but having similar lithology. It is only through the lens of topography that we will be able to resolve the role of mean runoff and discharge variability in controlling erosion rate. An exacting test of the *Lague et al.* [2005] model will require data from field sites chosen to explore independently the roles of mean runoff and runoff variability and their dependences on channel steepness. In addition, there is a need to further explore the controls on k_e and its dependence on substrate properties [e.g., *Sklar and Dietrich*, 2001; *Tressler et al.*, 2010]. Though it is unlikely that this simple model captures the full range of behavior in steady-state channels, the fit to the SGM data suggests that the first-order implications of this model may apply to many landscapes. Of course, under transient conditions, a broader suite of controls (sediment tools and cover, process mechanics, channel width) will likely emerge [e.g., *Attal et al.*, 2008; *Attal et al.*, 2011; *Valla et al.*, 2010] – it is channel evolution during periods of transience that will provide the most exacting tests of channel incision models. Whether or not these transient effects need to be accounted for, however, depends on the time scale of the geologic problem. For example, in million-year, orogen-scale studies of climate-tectonic interactions, an assumption of quasi-steady-state river incision is probably sufficient to develop relationships among climate, rock type, topography, erosion rate, and tectonic style, even when the landscape is changing over long time periods [*Stolar et al.*, 2006; *Whipple and*

Meade, 2006]; the stochastic-threshold model may be sufficient for quantitative analyses at these long time scales as discussed above for steady-state conditions. Conversely, in studies directed at extracting the tectonic or climatic history of a specific field area recorded in landscape morphology or sedimentary records, an appreciation for the rich behavior in fluvial systems during periods of adjustment to changing climatic or tectonic conditions is paramount, and a simple stochastic-threshold model is likely inadequate [*Attal et al.*, 2008; *Crosby et al.*, 2007; *Gasparini et al.*, 2007; *Valla et al.*, 2010].

CONCLUSIONS

We have shown here that a non-linear relationship between channel steepness index and erosion rate in the San Gabriel Mountains, CA can be explained by a simple bedrock incision model that incorporates a stochastic distribution of discharge events coupled with an erosion threshold [*Lague et al.*, 2005], but does not include the complexities of recent modeling efforts regarding dynamic cross sectional evolution [*Turowski et al.*, 2009; *Wobus et al.*, 2006b] or detailed accounting for sediment tools and cover effects [*Lague*, 2010; *Sklar and Dietrich*, 2004]. We constrained the relationship using field observations of channel geometry and bed state, along with an analysis of discharge records from throughout the range. We found that for graded channels, in the SGM at least, possibly in general, the role of sediment tools and cover, channel width adjustment, and changes in incision process appear to play a subordinate role to the influence of erosion thresholds and discharge variability. We showed explicitly that the choice of discharge distribution strongly influences the modeled relationship between channel steepness and erosion rate, particularly for low channel slopes, where the heaviness of the flood distribution tail strongly controls the frequency of erosive events.

Based on parameters calibrated from the SGM, we evaluated the implications of the *Lague et al.* [2005] model for the relationship between channel steepness and erosion rate. Bedrock channels in the SGM lie well within the "threshold dominated" regime of *Lague et al.* [2005], which surprisingly implies that the shape of the k_s-E relationship is governed by discharge variability k and the at-a-station discharge exponent $\alpha(1-\omega_s)$ rather than erosion process, as is almost universally assumed. For threshold dominated channels, erosion is enhanced by increasing mean runoff as well as increasing variability. We imposed an empirical relationship between mean runoff and variability to test if dry, variable climates can be more efficient than wet, stable climates. We extended the analysis of *Molnar et al.* [2006] and found that for channels with a high erosion threshold (or alternatively, low steepness) there exists a peak in erosional efficiency that lies near a mean runoff of 200-400 mm/a, similar to the relationship observed by *Langbein and Schumm* [1958]. Furthermore, for a large range of parameter space (but excluding tropical climates), erosion rate is predicted by this model to be insensitive to increases in runoff above 500 mm/a, suggesting that any climatic influence on tectonics in unglaciated landscapes may be restricted to subhumid or drier climates and climates where higher mean annual runoff is not offset by a decrease in discharge variability. The relationships among channel steepness index, erosion rate, and climate variables developed here thus form a set of critical, testable hypotheses that should be explored further to elucidate the complex relationships among climate, topography, and erosion rate.

ACKNOWLEDGEMENTS

We would like to thank all those involved with the field surveys, including B. Adams, E. DiMaggio, N. Gasparini, B. Guralnik, M. Jungers, J. McDermott, D. Stolar, and J. Walsh. Thanks to M. Rossi and G. Tucker for valuable discussion and feedback. J. Kean provided assistance with cross sectional flow modeling. Excellent and thorough reviews by M. Attal, D. Lague, G. Tucker, and J. Turowski greatly improved the manuscript. Funding for this project was provided by the Geomorphology and Land Use Dynamics program at NSF (EAR-0724194 to KXW).

REFERENCES

Armitage, J. J., R. A. Duller, A. C. Whittaker, and P. A. Allen (2011), Transformation of tectonic and climatic signals from source to sedimentary archive, *Nature Geoscience*, *4*(4), 231-235.

Attal, M., G. E. Tucker, A. C. Whittaker, P. A. Cowie, and G. P. Roberts (2008), Modeling fluvial incision and transient landscape evolution: Influence of dynamic channel adjustment, *Journal of Geophysical Research-Earth Surface*, *113*, F03013, doi:10.1029/2007JF000893.

Attal, M., P. A. Cowie, A. C. Whittaker, D. Hobley, G. E. Tucker, and G. P. Roberts (2011), Testing fluvial erosion models using the transient response of bedrock rivers to tectonic forcing in the Apennines, Italy, *Journal of Geophysical Research-Earth Surface*, *116*, F02005, doi:10.1029/2010JF001875.

Bagnold, R. A. (1977), Bed load transport by natural rivers, *Water Resources Research*, *13*(2), 303-312.

Buffington, J. M., and D. R. Montgomery (1997), A systematic analysis of eight decades of incipient motion studies, with special reference to gravel-bedded rivers, *Water Resources Research*, *33*(8), 1993-2029.

Chatanantavet, P., and G. Parker (2008), Experimental study of bedrock channel alluviation under varied sediment supply and hydraulic conditions, *Water Resources Research*, *44*, W12446, doi:10.1029/2007WR006581.

Cowie, P. A., A. C. Whittaker, M. Attal, G. Roberts, G. E. Tucker, and A. Ganas (2008), New constraints on sediment-flux-dependent river incision: Implications for extracting tectonic signals from river profiles, *Geology*, *36*(7), 535-538.

Crave, A., and P. Davy (2001), A stochastic "precipiton" model for simulating erosion/sedimentation dynamics, *Computers & Geosciences*, *27*(7), 815-827.

Crosby, B. T., K. X. Whipple, N. M. Gasparini, and C. W. Wobus (2007), Formation of fluvial hanging valleys: Theory and simulation, *Journal of Geophysical Research-Earth Surface*, *112*, F03S10, doi:10.1029/2006JF000566.

Cyr, A. J., D. E. Granger, V. Olivetti, and P. Molin (2010), Quantifying rock uplift rates using channel steepness and cosmogenic nuclide-determined erosion rates: Examples from northern and southern Italy, *Lithosphere*, *2*(3), 188-198.

DiBiase, R. A., K. X. Whipple, A. M. Heimsath, and W. B. Ouimet (2010), Landscape form and millennial erosion rates in the San Gabriel Mountains, CA, *Earth and Planetary Science Letters*, *289*(1-2), 134-144.

Duvall, A., E. Kirby, and D. Burbank (2004), Tectonic and lithologic controls on bedrock channel profiles and processes in coastal California, *Journal of Geophysical Research*, *109*, F03002, doi:10.1029/2003JF000086.

Eagleson, P. S. (1978), Climate, soil, and vegetation 2. Distribution of annual precipitation derived from observed storm sequences, *Water Resources Research*, *14*(5), 713-721.

Evans, M., N. Hastings, and B. Peacock (2000), *Statistical Distributions*, 3rd ed., 221 pp., John Wiley & Sons, Inc, New York.

Finnegan, N. J., L. S. Sklar, and T. K. Fuller (2007), Interplay of sediment supply, river incision, and channel morphology revealed by the transient evolution of an experimental bedrock channel, *Journal of Geophysical Research-Earth Surface*, *112*, F03S11, doi:10.1029/2006JF000569.

Finnegan, N. J., G. Roe, D. R. Montgomery, and B. Hallet (2005), Controls on the channel width of rivers: Implications for modeling fluvial incision of bedrock, *Geology*, *33*(3), 229-232.

Gander, W., and W. Gautschi (2000), Adaptive quadrature - Revisited, *BIT*, *40*(1), 84-101, 10.1023/a:1022318402393.

Gasparini, N. M., K. X. Whipple, and R. L. Bras (2007), Predictions of steady state and transient landscape morphology using sediment-flux-dependent river incision models, *Journal of Geophysical Research-Earth Surface*, *112*, F03S09, doi:10.1029/2006JF000567.

Gilbert, G. K. (1877), Report on the Geology of the Henry Mountains, 160 pp, U.S. Geographical and geological survey of the Rocky Mountains Region, Washington, D.C.

Harkins, N., E. Kirby, A. Heimsath, R. Robinson, and U. Reiser (2007), Transient fluvial incision in the headwaters of the Yellow River, northeastern Tibet, China, *Journal of Geophysical Research-Earth Surface*, *112*, F03S04, doi:10.1029/2006JF000570.

Hartshorn, K., N. Hovius, W. B. Dade, and R. L. Slingerland (2002), Climate-driven bedrock incision in an active mountain belt, *Science*, *297*, 2036-2038.

Hawk, K. L. (1992), Climatology of station storm rainfall in the continental United States: parameters of the Bartlett-Lewis and Poisson rectangular pulses models, MS thesis, Massachusetts Institute of Technology, Boston.

Hilley, G. E., and M. R. Strecker (2004), Steady state erosion of critical Coulomb wedges with applications to Taiwan and the Himalaya, *Journal of Geophysical Research-Solid Earth*, *109*, B01411, doi:10.1029/2002JB002284.

Houjou, K., Y. Shimizu, and C. Ishii (1990), Calculation of boundary shear stress in open channel flow, *Journal of Hydroscience and Hydraulic Engineering*, *8*(2), 21-37.

Howard, A. D. (1994), A detachment-limited model of drainage basin evolution, *Water Resources Research*, *30*(7), 2261-2285.

Howard, A. D., and G. Kerby (1983), Channel changes in badlands, *Geological Society of America Bulletin*, *94*(6), 739-752.

Istanbulluoglu, E., and R. L. Bras (2006), On the dynamics of soil moisture, vegetation, and erosion: Implications of climate variability and change, *Water Resources Research*, *42*, W06418, doi:10.1029/2005WR004113.

Jansen, J. D. (2006), Flood magnitude-frequency and lithologic control on bedrock river incision in post-orogenic terrain, *Geomorphology*, *82*(1-2), 39-57.

Jansen, J. D., D. Fabel, P. Bishop, S. Xu, C. Schnabel, and A. T. Codilean (2011), Does decreasing paraglacial sediment supply slow knickpoint retreat?, *Geology*, *39*(6), 543-546.

Johnson, J. P. L., and K. X. Whipple (2010), Evaluating the controls of shear stress, sediment supply, alluvial cover, and channel morphology on experimental bedrock incision rate, *Journal of Geophysical Research-Earth Surface*, *115*, F02018, doi:10.1029/2009JF001335.

Johnson, J. P. L., K. X. Whipple, L. S. Sklar, and T. C. Hanks (2009), Transport slopes, sediment cover, and bedrock channel incision in the Henry Mountains, Utah, *Journal of Geophysical Research-Earth Surface*, *114*, F02014, doi:10.1029/2007JF000862.

Kean, J. W., and J. D. Smith (2004), Flow and boundary shear stress in channels with woody bank vegetation, in *Riparian Vegetation and Fluvial Geomorphology, Water Science and Application 8*, edited by S. J. Bennett and A. Simon, pp. 237-252, AGU, Washington, D.C.

Kirby, E., and K. X. Whipple (2001), Quantifying differential rock-uplift rates via stream profile analysis, *Geology*, *29*(5), 415-418.

Lague, D. (2010), Reduction of long-term bedrock incision efficiency by short-term alluvial cover intermittency, *Journal of Geophysical Research-Earth Surface*, *115*, F02011, doi:10.1029/2008JF001210.

Lague, D., N. Hovius, and P. Davy (2005), Discharge, discharge variability, and the bedrock channel profile, *Journal of Geophysical Research*, *110*, F04006, doi:10.1029/2004JF000259.

Lamb, M. P., W. E. Dietrich, and L. S. Sklar (2008), A model for fluvial bedrock incision by impacting suspended and bed load sediment, *Journal of Geophysical Research-Earth Surface*, *113*, F03025, doi:10.1029/2007JF000915.

Langbein, W. B., and S. A. Schumm (1958), Yield of sediment in relation to mean annual precipitation, *Trans Amer Geophys Union*, *39*(6), 1076-1084.

Lavé, J., and J. P. Avouac (2001), Fluvial incision and tectonic uplift across the Himalayas of central Nepal, *Journal of Geophysical Research-Solid Earth*, *106*(B11), 26561-26591.

Lavé, J., and D. W. Burbank (2004), Denudation processes and rates in the Transverse Ranges, southern California: Erosional response of a transitional landscape to external and anthropogenic forcing, *Journal of Geophysical Research*, *109*, F01006, doi:10.1029/2003JF000023.

Malamud, B. D., and D. L. Turcotte (2006), The applicability of power-law frequency statistics to foods, *Journal of Hydrology*, *322*(1-4), 168-180.

Meyer-Peter, E., and R. Müller (1948), Formulas for bed-load transport, in *Proceedings: Stockholm, Sweden, Second Congress, International Association for Hydraulic Structures Research*, edited, pp. 39-64.

Molnar, P. (2001), Climate change, flooding in arid environments, and erosion rates, *Geology*, *29*(12), 1071-1074.

Molnar, P., R. S. Anderson, G. Kier, and J. Rose (2006), Relationships among probability distributions of stream discharges in floods, climate, bed load transport, and river incision, *Journal of Geophysical Research-Earth Surface*, *111*, F02001, doi:10.1029/2005JF000310.

Montgomery, D. R., and K. B. Gran (2001), Downstream variations in the width of bedrock channels, *Water Resources Research*, *37*(6), 1841-1846, 10.1029/2000wr900393.

Newman, M. E. J. (2005), Power laws, Pareto distributions and Zipf's law, *Contemporary Physics*, *46*(5), 323-351.

Ouimet, W. B., K. X. Whipple, and D. E. Granger (2009), Beyond threshold hillslopes: Channel adjustment to base-level fall in tectonically active mountain ranges, *Geology*, *37*(7), 579-582.

Paola, C., P. L. Heller, and C. L. Angevine (1992), The large-scale dynamics of grain-size variation in alluvial basins, 1: Theory, *Basin Research*, *4*, 73-90.

Riebe, C. S., J. W. Kirchner, D. E. Granger, and R. C. Finkel (2001), Minimal climatic control on erosion rates in the Sierra Nevada, California, *Geology*, *29*(5), 447-450.

Roe, G. H., D. R. Montgomery, and B. Hallet (2002), Effects of orographic precipitation variations on the concavity of steady-state river profiles, *Geology*, *30*(2), 143-146.

Roe, G. H., K. X. Whipple, and J. K. Fletcher (2008), Feedbacks among climate, erosion, and tectonics in a critical wedge orogen, *American Journal of Science*, *308*(7), 815-842.

Safran, E. B., P. R. Bierman, R. Aalto, T. Dunne, K. X. Whipple, and M. Caffee (2005), Erosion rates driven by channel network incision in the Bolivian Andes, *Earth Surface Processes and Landforms*, *30*(8), 1007-1024.

Sklar, L., and W. E. Dietrich (1998), River longitudinal profiles and bedrock incision models: Stream power and the influence of sediment supply, in *Rivers Over Rock: Fluvial Processes in Bedrock Channels*, edited by K. J. Tinkler and E. E. Wohl, pp. 237-260, American Geophysical Union, Washington, D.C.

Sklar, L., and W. E. Dietrich (2001), Sediment and Rock Strength Controls on River Incision Into Bedrock, *Geology*, *29*(12), 1087-1090.

Sklar, L. S., and W. E. Dietrich (2004), A mechanistic model for river incision into bedrock by saltating bed load, *Water Resources Research*, *40*, W06301, doi:10.1029/2003WR002496.

Sklar, L. S., and W. E. Dietrich (2006), The role of sediment in controlling steady-state bedrock channel slope: Implications of the saltation-abrasion incision model, *Geomorphology*, *82*(1-2), 58-83.

Snyder, N. P., K. X. Whipple, G. E. Tucker, and D. J. Merritts (2003a), Channel response to tectonic forcing: field analysis of stream morphology and hydrology in the Mendocino triple junction region, northern California, *Geomorphology*, *53*(1-2), 97-127.

Snyder, N. P., K. X. Whipple, G. E. Tucker, and D. J. Merritts (2003b), Importance of a stochastic distribution of floods and erosion thresholds in the bedrock river incision problem, *Journal of Geophysical Research*, *108*(B2), 2117, doi:10.1029/2001JB001655.

Spotila, J. A., M. A. House, A. E. Blythe, N. A. Niemi, and G. C. Bank (2002), Controls on the erosion and geomorphic evolution of the San Bernardino and San Gabriel Mountains, southern California, *Geological Society of America Special Paper 365*, 205-230.

Stark, C. P. (2006), A self-regulating model of bedrock river channel geometry, *Geophysical Research Letters*, *33*, L04402, doi:10.1029/2005GL023193.

Stolar, D., G. Roe, and S. Willett (2007), Controls on the patterns of topography and erosion rate in a critical orogen, *Journal of Geophysical Research-Earth Surface*, *112*, F04002, doi:10.1029/2006JF000713.

Stolar, D. B., S. D. Willett, and G. H. Roe (2006), Climatic and tectonic forcing of a critical orogen, *Geological Society of America Special Paper 398*, 241-250.

Tomkin, J. H., and G. H. Roe (2007), Climate and tectonic controls on glaciated critical-taper orogens, *Earth and Planetary Science Letters*, *262*(3-4), 385-397.

Tomkin, J. H., M. T. Brandon, F. J. Pazzaglia, J. R. Barbour, and S. D. Willett (2003), Quantitative testing of bedrock incision models for the Clearwater River, NW Washington state, *Journal of Geophysical Research-Solid Earth*, *108*(B6), 2308, doi:10.1029/2001JB000862.

Tressler, C., J. Pederson, and R. Mackley (2010), The hunt for knickzones and their meaning along the Colorado - signatures of transience after integration, bed resistance, or differential uplift?, *Origin and Evolution of the Colorado River System II Workshop: May 24-26, Flagstaff, AZ.*

Tucker, G. E. (2004), Drainage basin sensitivity to tectonic and climatic forcing: Implications of a stochastic model for the role of entrainment and erosion thresholds, *Earth Surface Processes and Landforms*, *29*, 185-205.

Tucker, G. E., and R. L. Bras (2000), A stochastic approach to modeling the role of rainfall variability in drainage basin evolution, *Water Resources Research*, *36*(7), 1953-1964.

Tucker, G. E., and G. R. Hancock (2010), Modelling landscape evolution, *Earth Surface Processes and Landforms*, *35*(1), 28-50.

Turcotte, D. L., and L. Greene (1993), A scale-invariant approach to flood-frequency analysis, *Stochastic Hydrology and Hydraulics*, *7*(1), 33-40.

Turowski, J. M. (2009), Stochastic modeling of the cover effect and bedrock erosion, *Water Resources Research*, *45*, W03422, doi:10.1029/2008WR007262.

Turowski, J. M., D. Lague, and N. Hovius (2007), Cover effect in bedrock abrasion: A new derivation and its implications for the modeling of bedrock channel morphology, *Journal of Geophysical Research-Earth Surface*, *112*, F04006, doi:10.1029/2006JF000697.

Turowski, J. M., D. Lague, and N. Hovius (2009), Response of bedrock channel width to tectonic forcing: Insights from a numerical model, theoretical considerations, and comparison with field data, *Journal of Geophysical Research-Earth Surface*, *114*, F03016, doi:10.1029/2008JF001133.

Turowski, J. M., N. Hovius, A. Wilson, and M. J. Horng (2008), Hydraulic geometry, river sediment and the definition of bedrock channels, *Geomorphology*, *99*(1-4), 26-38.

Valla, P. G., P. A. van der Beek, and D. Lague (2010), Fluvial incision into bedrock: Insights from morphometric analysis and numerical modeling of gorges incising glacial hanging valleys (Western Alps, France), *Journal of Geophysical Research-Earth Surface*, *115*, F02010, doi:10.1029/2008JF001079.

Whipple, K. X. (2004), Bedrock rivers and the geomorphology of active orogens, *Annual Review of Earth and Planetary Sciences*, *32*, 151-185.

Whipple, K. X. (2009), The influence of climate on the tectonic evolution of mountain belts (vol 2, pg 97, 2009), *Nature Geoscience*, *2*(10), 730-730.

Whipple, K. X., and G. E. Tucker (1999), Dynamics of the stream-power river incision model: Implications for height limits of mountain ranges, landscape response timescales, and research needs, *Journal of Geophysical Research-Solid Earth*, *104*(B8), 17661-17674.

Whipple, K. X., and G. E. Tucker (2002), Implications of sediment-flux-dependent river incision models for landscape evolution, *Journal of Geophysical Research-Solid Earth*, *107*(B2), doi:10.1029/2000JB000044.

Whipple, K. X., and B. J. Meade (2004), Controls on the strength of coupling among climate, erosion, and deformation in two-sided, frictional orogenic wedges at steady state, *Journal of Geophysical Research-Earth Surface*, *109*, F01011, doi:10.1029/2003JF000019.

Whipple, K. X., and B. J. Meade (2006), Orogen response to changes in climatic and tectonic forcing, *Earth and Planetary Science Letters*, *243*(1-2), 218-228.

Whipple, K. X., G. S. Hancock, and R. S. Anderson (2000), River incision into bedrock: Mechanics and relative efficacy of plucking, abrasion, and cavitation, *Geological Society of America Bulletin*, *112*(3), 490-503.

Whittaker, A. C., P. A. Cowie, M. Attal, G. E. Tucker, and G. P. Roberts (2007), Contrasting transient and steady-state rivers crossing active normal faults: new field observations from the Central Apennines, Italy, *Basin Research*, *19*(4), 529-556.

Willett, S. D. (1999), Orogeny and orography: The effects of erosion on the structure of mountain belts, *Journal of Geophysical Research-Solid Earth*, *104*(B12), 28957-28981.

Willett, S. D. (2010), Late Neogene Erosion of the Alps: A Climate Driver?, *Annual Review of Earth and Planetary Sciences*, *38*, 411-437.

Wobus, C., K. X. Whipple, E. Kirby, N. Snyder, J. Johnson, K. Spyropolou, B. Crosby, and D. Sheehan (2006a), Tectonics from topography: Procedures, promise, and pitfalls, *Geological Society of America Special Paper 398*, 55-74.

Wobus, C. W., G. E. Tucker, and R. S. Anderson (2006b), Self-formed bedrock channels, *Geophysical Research Letters*, *33*, L18408, doi:10.1029/2006GL027182.

Wobus, C. W., J. W. Kean, G. E. Tucker, and R. S. Anderson (2008), Modeling the evolution of channel shape: Balancing computational efficiency with hydraulic fidelity, *Journal of Geophysical Research-Earth Surface*, *113*, F02004, doi:10.1029/2007JF000914.

Wohl, E., and G. C. L. David (2008), Consistency of scaling relations among bedrock and alluvial channels, *Journal of Geophysical Research-Earth Surface*, *113*, F04013, doi:10.1029/2008JF000989.

Wolman, M. G., and Miller, J. P. (1960), Magnitude and frequency of forces in geomorphic processes, *Journal of Geology*, *68*, 54-74.

Yanites, B. J., and G. E. Tucker (2010), Controls and limits on bedrock channel geometry, *Journal of Geophysical Research-Earth Surface*, *115*, F04019, doi:10.1029/2009JF001601.

Zhang, P. Z., P. Molnar, and W. R. Downs (2001), Increased sedimentation rates and grain sizes 2-4 Myr ago due to the influence of climate change on erosion rates, *Nature*, *410*, 891-897.

FIGURE CAPTIONS

Figure 4.1. Plots of predicted exceedence frequency as a function of non-dimensional daily discharge for the Poisson rainfall model (a) and the inverse gamma distribution discharge model (b). Poisson discharge distribution was calculated using a Monte Carlo approach to model individual storms and assumes simple Horton overland flow with negligible infiltration.

Figure 4.2. Map of San Gabriel Mountains, California, showing elevation over shaded relief. Catchments with detrital CRN erosion rates measured by *DiBiase et al.* [2010] highlighted in blue according to erosion rate. The stream network (drainage area > 2 km^2) is color coded by channel steepness index, which increases with erosion rate from west to east. USGS stream gages listed in Table 1 are shown by numbered circles.

Figure 4.3. Mean daily discharge plotted against drainage area for USGS stream gages listed in Table 4.1, with linear least squares fit forced through origin.

Figure 4.4. Plot of exceedence frequency as a function of non-dimensional daily discharge ($Q^* = Q/Q_b$) for Cucamonga Creek gage, showing inverse gamma distribution with $k = 0.5$. Gray dashed lines show inverse gamma distribution with $k = 0.4$ and $k = 0.6$. Poisson model in gray is generated using parameters calibrated from rainfall station data at Mt. Baldy (Table 4.2). Inset shows Cucamonga Creek discharge distribution (red) in comparison to other gages in Table 4.1 (blue).

Figure 4.5. Bankfull channel width plotted against drainage area for SGM channels, showing the similarity of power-law fits through low relief ($k_s < 100$) and high relief ($k_s \geq 100$) channels. For channels surveyed in detail, we show the log-averaged value of widths measured between major tributary junctions (typically 5-50 measurements), with error bars indicate the inner quartile range. No error bars are shown for individual width measurements (those not associated with detailed surveys).

Figure 4.6. Histogram of bedrock exposure measured in surveys of SGM channels comparing low relief ($k_s < 100$) and high relief ($k_s \geq 100$) channels. Inset plot shows grain size distributions for 44 pebble counts across the range (gray lines), with D_{50} values ranging from ~22-180 mm. Black line indicates the grain size distribution of all pebble count data taken together.

Figure 4.7. Plot of channel steepness index against catchment-average erosion rate for the San Gabriel Mountains (gray and hollow symbols). Erosion rates are derived from ^{10}Be concentrations in stream sands measured by *DiBiase et al.* [2010], with error bars showing 1σ analytical uncertainty in erosion rate and uncertainty in k_s as described by *DiBiase et al.* [2010]. Black line shows best fit of equation (10) through erosion rate data using the inverse gamma distribution (equation (11); parameters given in Table 4.2). Dashed lines show fits reflecting range of plausible ϕ values. Gray line shows similar fit using an exponential discharge distribution [e.g., *Tucker*, 2004]. Hollow symbols indicate two outliers not included in fit calculation. Square symbols indicate repeat measurements from *DiBiase et al.* [2010] that have been combined into single points.

Figure 4.8. Plot of power-law exponent from equation (1) against erosion rate normalized by the threshold term Ψ from equation (7), assuming a constant threshold shear stress (τ_c = 45 Pa). Vertical gray bars separate 3 regimes described by *Lague et al.* [2005]. Regime I (low E/Ψ) is dominated by the threshold term, and the shape of the k_s-E relationship (dictated by ϕ) is controlled by the at-a-station shear stress-discharge exponent, $\alpha(1-\omega_s)$, and discharge variability (k, equation (4.11)). Regime III (high E/Ψ) approaches the effective discharge approximation (equation (4.8)), where ϕ is set by the exponent n in the instantaneous incision rule (equation (4.7)). We use $n = 1$ in all calculations. Regime II is transitional. Gray box shows conditions in the SGM, indicating the range of erosion rates and uncertainty in discharge variability.

Figure 4.9. Plot of channel steepness index against erosion rate showing the influence of (a) changing mean runoff only, (b) changing discharge variability only, and (c) co-varying mean runoff and discharge variability according to the relationship given by equation (4.16). Gray symbols and black line indicate SGM data and fit from Figure 4.7 (R_b = 280 mm/a; k = 0.5).

Figure 4.10. Plot of erosion rate vs. mean runoff as a function of channel steepness index when discharge variability and mean runoff vary according to equation (4.16). Solid lines and diamonds indicate the presence and location of a peak erosional efficiency, while dashed lines indicate a monotonic relationship between erosion rate and mean runoff. A peak in erosional efficiency is enhanced by decreasing channel steepness (a-e), increasing erosion threshold magnitude (c), or strengthening the relationship between mean runoff and discharge variability (d).

Table 4.1. USGS stream gages used in this study

Name	Site #	Latitude	Longitude	Area (km^2)	Q_b (m^3/s)	R_b (mm/a)	Record Length
(1) Arroyo Seco	11098000	34.222	-118.177	41.4	0.28	214	1910 - 2011
(2) Little Santa Anita Creek	11100500	34.187	-118.043	4.8	0.03	179	1916 - 1979
(3) Santa Anita Creek	11100000	34.192	-118.016	25.1	0.19	238	1916 - 1970
(4) Fish Creek	11084500	34.166	-117.923	16.5	0.13	252	1916 - 1979
(5) Rogers Creek	11084000	34.165	-117.906	17.2	0.08	148	1917 - 1962
(6) E.F. San Gabriel River	11080500	34.236	-117.805	219.1	2.01	290	1932 - 1979
(7) Cucamonga Creek	11073470	34.179	-117.628	25.1	0.23	284	1929 - 1975
(8) Day Creek	11067000	34.185	-117.539	11.8	0.12	315	1928 - 1972
(9) Big Rock Creek	10263500	34.421	-117.839	59.3	0.50	265	1923 - 2011

Table 4.2. Model parameters used for fit to SGM erosion rate data

parameter	value	units
k_e	4.3×10^{-12}	$m^{2.5}\,s^{2}\,kg^{-1.5}$
τ_c	45	Pa
k_q	9×10^{-9}	$m\,s^{-1}$
k_w	15	$m^{-0.65}\,s^{0.55}$
k_t	1000	$m^{-7/3}\,s^{-4/3}\,kg$
k	0.5	dimensionless
ω_s	0.25	dimensionless
ω_b	0.55	dimensionless
a	3/2	dimensionless
α	2/3	dimensionless
β	2/3	dimensionless
P [a]	9.94	m/a
T_r [a]	7	h
T_b [a]	238	h

[a] Poisson pulse rainfall parameters [*Tucker*, 2004]

Figure 4.1

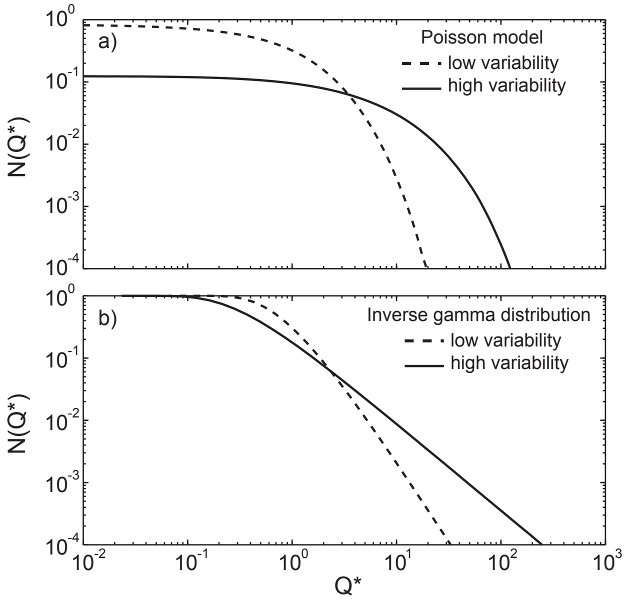
a)
Poisson model
low variability
high variability
N(Q*)
10^0
10^{-1}
10^{-2}
10^{-3}
10^{-4}
b)
Inverse gamma distribution
low variability
high variability
N(Q*)
10^0
10^{-1}
10^{-2}
10^{-3}
10^{-4}
10^{-2}
10^{-1}
10^0
10^1
10^2
10^3
Q*

Figure 4.2

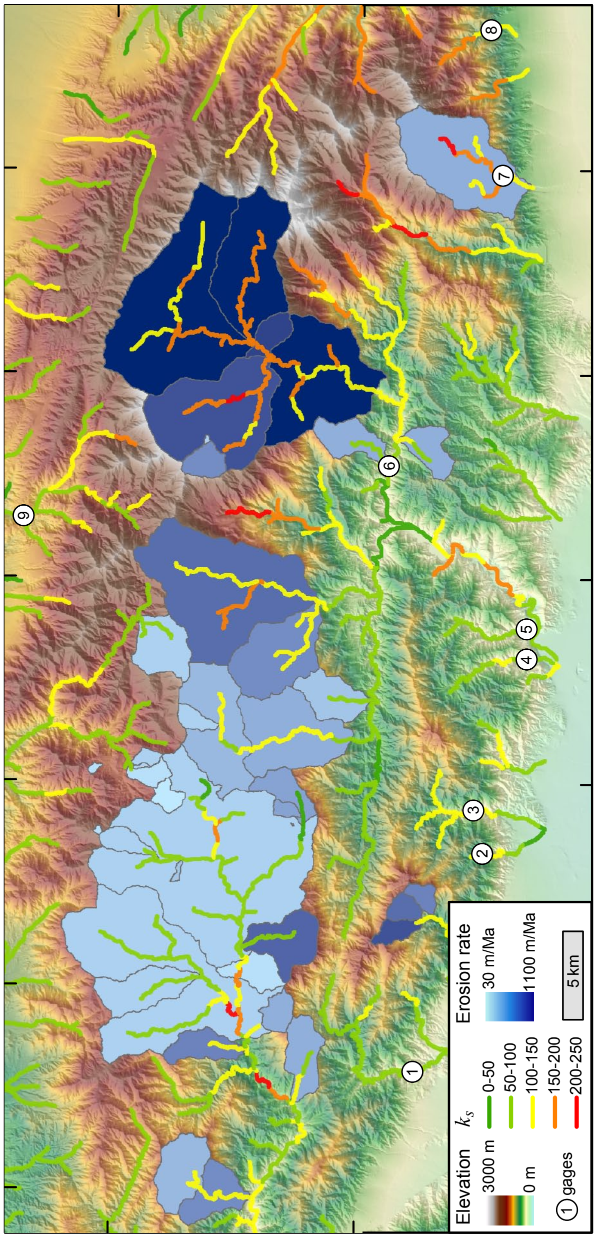
-118°15'
-118°7'30"
-118°0'
-117°52'30"
-117°45'
-117°37'30"
34°22'30"
34°15'
1
2
3
4
5
6
7
8
9
Elevation
3000 m
0 m
1 gages
k_s
0-50
50-100
100-150
150-200
200-250
Erosion rate
30 m/Ma
1100 m/Ma
5 km

Figure 4.3

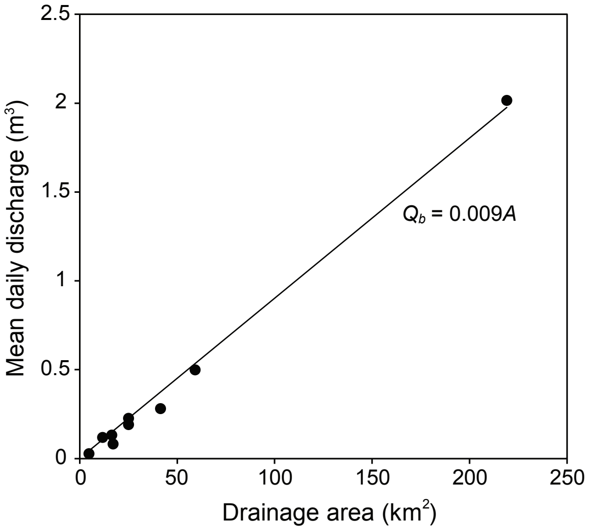
2.5
2
1.5
1
0.5
0
0
50
100
150
200
250
Mean daily discharge (m^3)
Drainage area (km^2)
$Q_b = 0.009A$

Figure 4.4

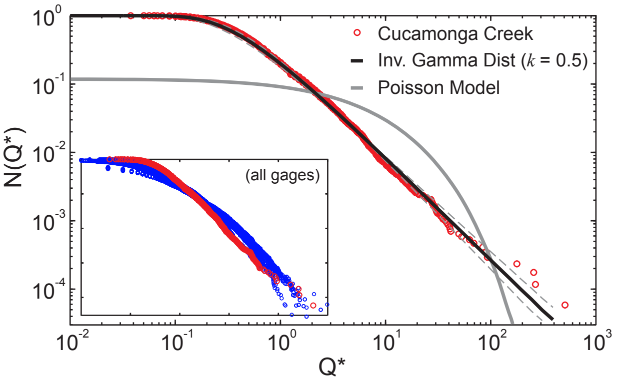
Cucamonga Creek
Inv. Gamma Dist (k = 0.5)
Poisson Model
(all gages)
10^0
10^{-1}
10^{-2}
10^{-3}
10^{-4}
N(Q*)
10^{-2}
10^{-1}
10^0
10^1
10^2
10^3
Q*

Figure 4.5

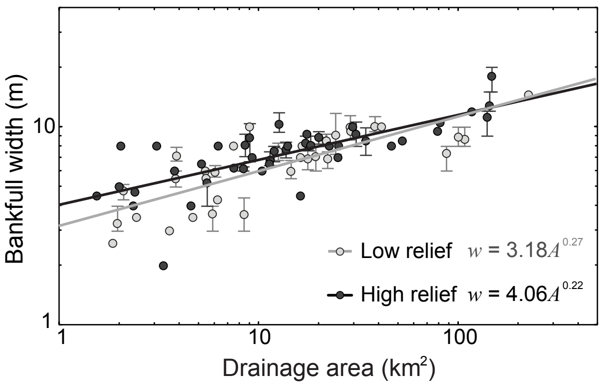
Bankfull width (m)
10
1
1
10
100
Drainage area (km^2)
Low relief $w = 3.18A^{0.27}$
High relief $w = 4.06A^{0.22}$

Figure 4.6

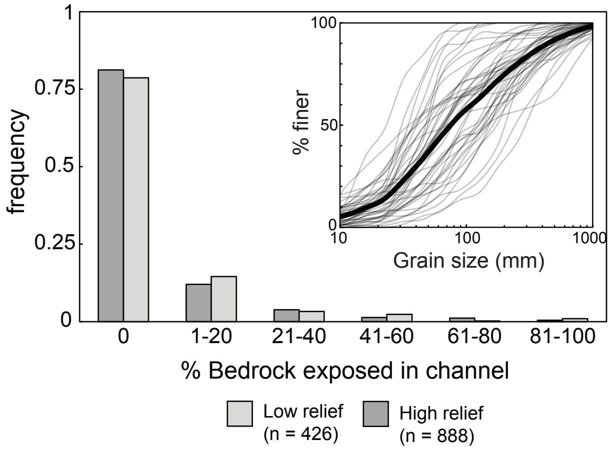

1
0.75
0.5
0.25
0
frequency
0
1-20
21-40
41-60
61-80
81-100
% Bedrock exposed in channel
Low relief (n = 426)
High relief (n = 888)
100
50
0
% finer
10
100
1000
Grain size (mm)

Figure 4.7

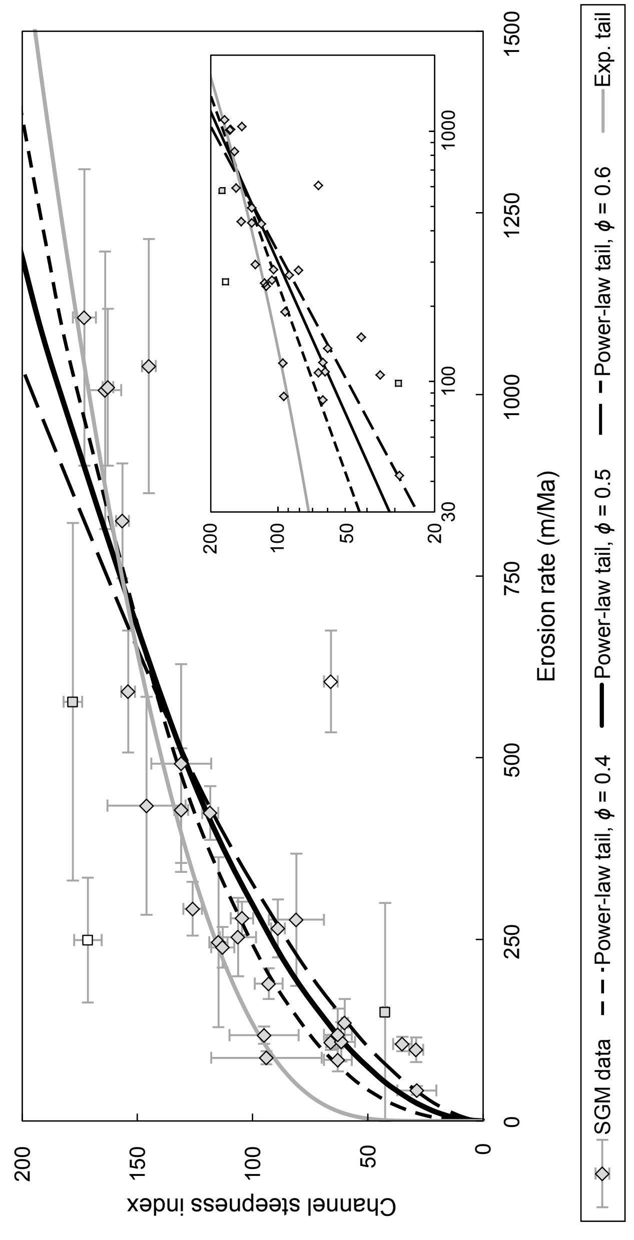

Channel steepness index
0
50
100
150
200
Erosion rate (m/Ma)
0
250
500
750
1000
1250
1500
20
50
100
200
30
100
1000
SGM data
Power-law tail, ϕ = 0.4
Power-law tail, ϕ = 0.5
Power-law tail, ϕ = 0.6
Exp. tail

Figure 4.8

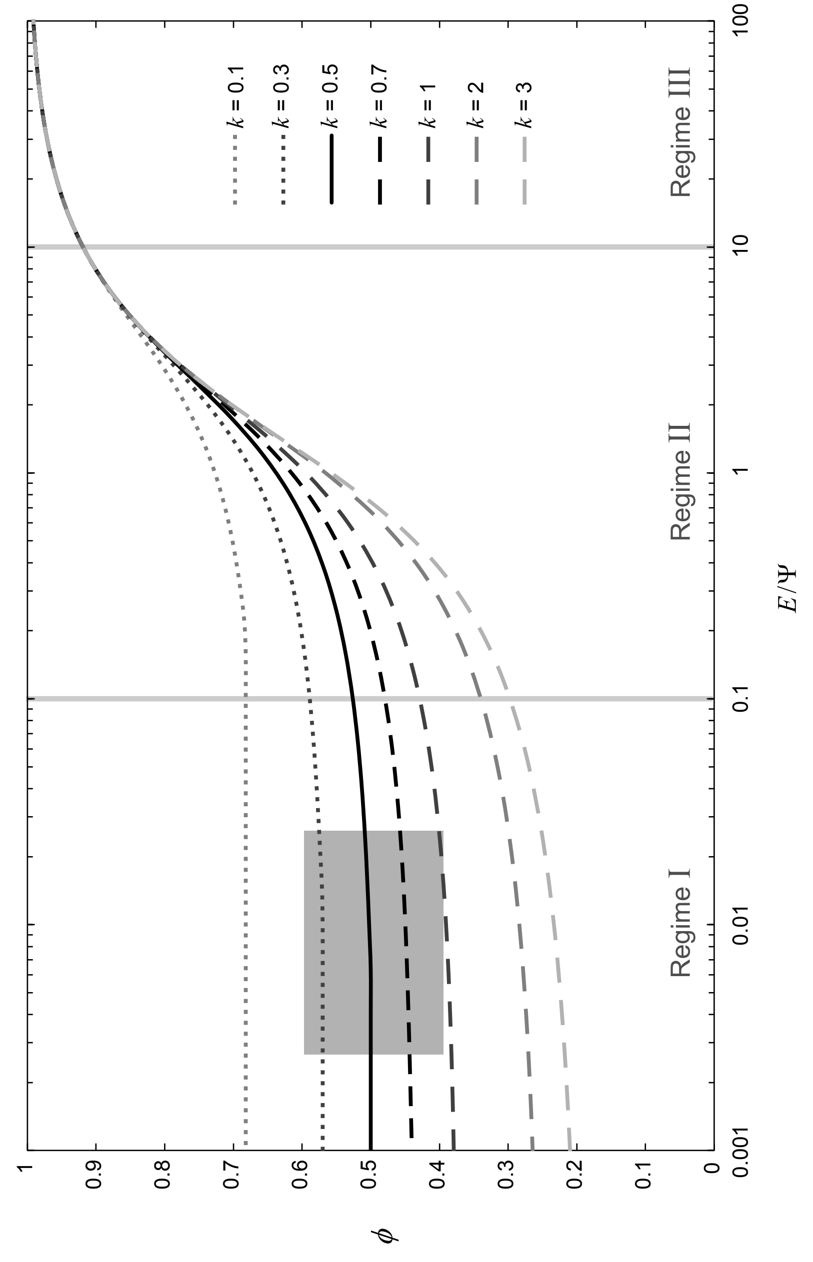
φ
E/Ψ
1
0.9
0.8
0.7
0.6
0.5
0.4
0.3
0.2
0.1
0
0.001
0.01
0.1
1
10
100
Regime I
Regime II
Regime III
k = 0.1
k = 0.3
k = 0.5
k = 0.7
k = 1
k = 2
k = 3

Figure 4.9

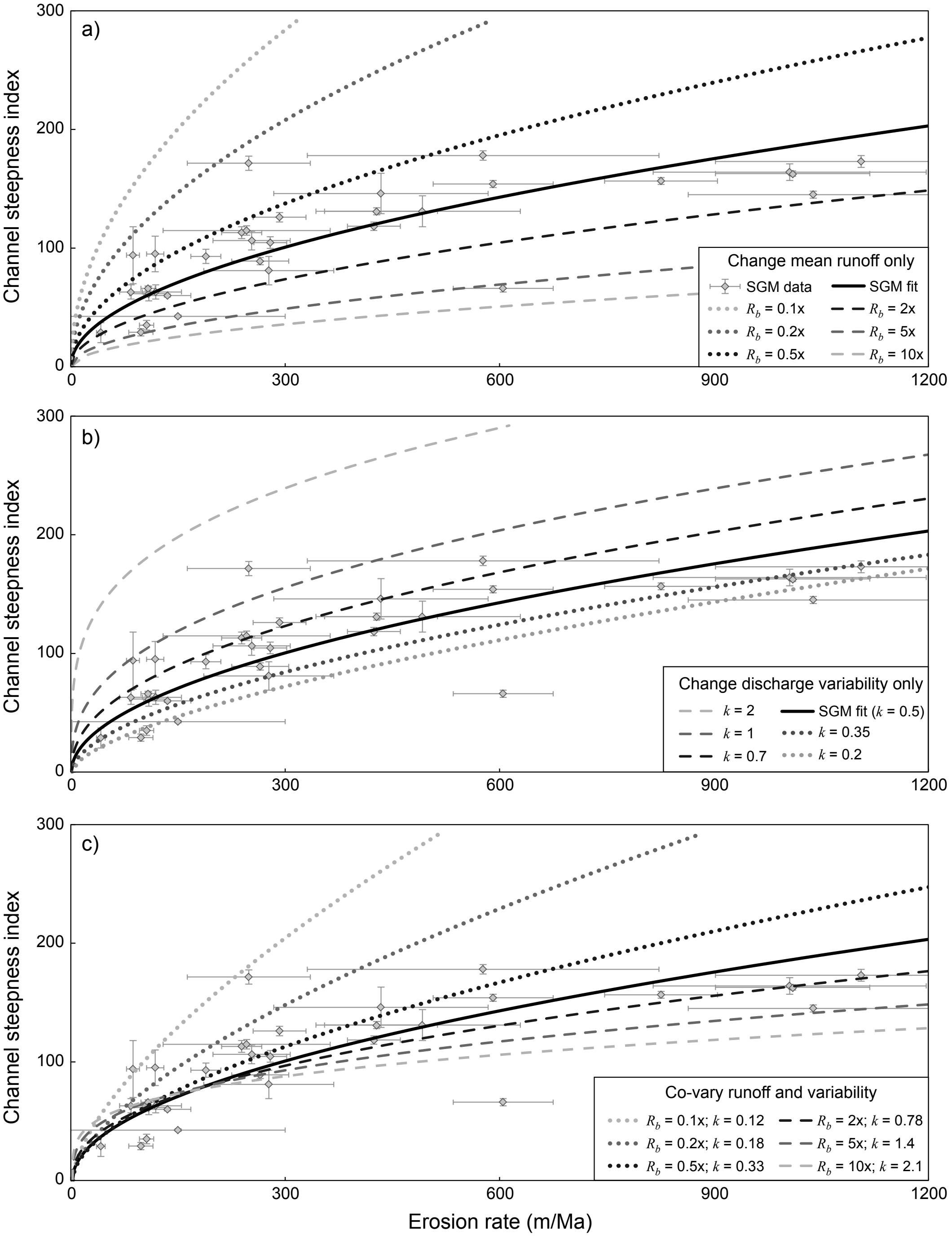
a)
Channel steepness index
300
200
100
0
0
300
600
900
1200
Change mean runoff only
SGM data
SGM fit
R_b = 0.1x
R_b = 2x
R_b = 0.2x
R_b = 5x
R_b = 0.5x
R_b = 10x
b)
Channel steepness index
Change discharge variability only
k = 2
SGM fit (k = 0.5)
k = 1
k = 0.35
k = 0.7
k = 0.2
c)
Channel steepness index
Co-vary runoff and variability
R_b = 0.1x; k = 0.12
R_b = 2x; k = 0.78
R_b = 0.2x; k = 0.18
R_b = 5x; k = 1.4
R_b = 0.5x; k = 0.33
R_b = 10x; k = 2.1
Erosion rate (m/Ma)

Figure 4.10

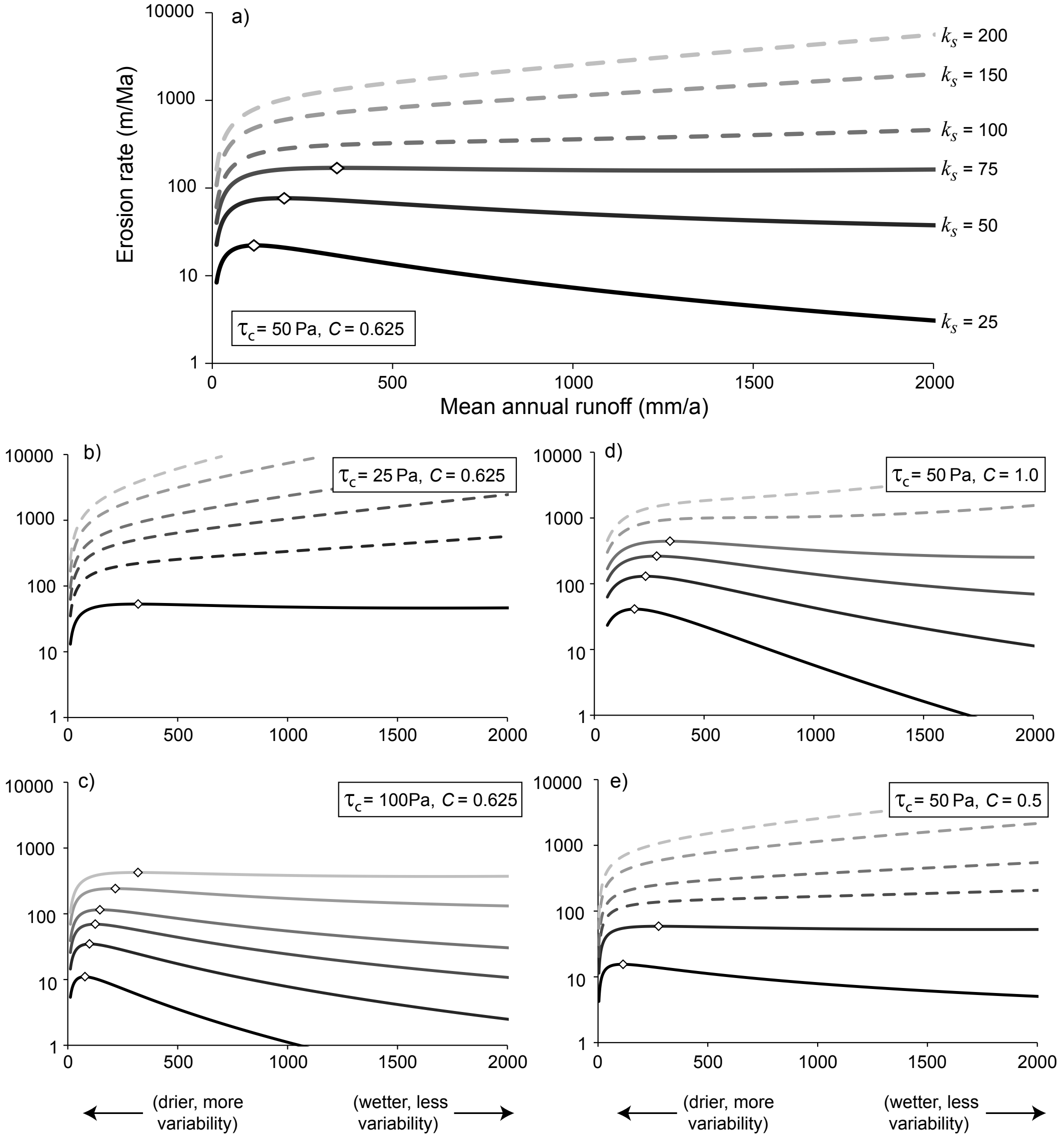
a)
10000
1000
100
10
1
Erosion rate (m/Ma)
0
500
1000
1500
2000
Mean annual runoff (mm/a)
k_s = 200
k_s = 150
k_s = 100
k_s = 75
k_s = 50
k_s = 25
τ_c = 50 Pa, C = 0.625
b)
τ_c = 25 Pa, C = 0.625
d)
τ_c = 50 Pa, C = 1.0
c)
τ_c = 100Pa, C = 0.625
e)
τ_c = 50 Pa, C = 0.5
(drier, more variability)
(wetter, less variability)
(drier, more variability)
(wetter, less variability)

CHAPTER 5

INVESTIGATION OF A TRANSIENT LANDSCAPE IN THE WESTERN SAN GABRIEL MOUNTAINS, CALIFORNIA: IMPLICATIONS FOR KNICKPOINT MIGRATION AND TECTONIC HISTORY

ABSTRACT

Transient landscapes serve an important role in tectonic geomorphology, both by recording the temporal changes of driving climatic or tectonic forces, and by aiding in the discrimination among different surface process models that exhibit otherwise similar behaviors at steady-state. Here we investigate the surface expression of a two-staged transient signal in the 300 km^2 catchment of Big Tujunga Creek in the western San Gabriel Mountains using a combination of DEM analysis, detailed field surveys of stream channels, and an extensive erosion rate dataset.

The upper (earlier) transient in the Big Tujunga catchment has nearly propagated through the entire fluvial network, with only isolated patches of an elevated low-relief weathering surface remaining. The lower transient, however, is characterized by a dramatic inner gorge with over-steepened valley walls and fluvial hanging valleys. In both cases, an increase in the rate of local baselevel fall resulted in the propagation of a wave of incision upstream through the landscape, with discrete knickpoints separating adjusting from relict portions of the landscape. We use a 10 m digital elevation model to identify knickpoints and extract channel long profiles and hillslope angles. Combining erosion rate estimates with elevation differences between projected long profiles allows for the estimation of the timing of increases in baselevel fall rate. We find the age of the upper transient to be ca. 7-9 Ma, which likely corresponds to the initiation of uplift in the San Gabriel Mountains associated with the transfer of slip from the San Gabriel Fault to

the current trace of the San Andreas Fault. The younger transient dates to ca. 0.5-2.5 Ma, which overlaps with estimates of activation of the San Jacinto Fault Zone, whose inception has been linked to increases in rock uplift rate in both the eastern San Gabriel Mountains and in the nearby San Bernardino Mountains.

The lower Big Tujunga Creek transient also affords us the opportunity to investigate the nature of bedrock channel response to temporal forcing in a relatively homogenous lithology (massive crystalline rocks). Supplementing detailed field surveys with 160 km^2 of airborne LiDAR-derived topography (1 m resolution), we mapped channel width, valley width, and the extent of bedrock steps greater than 3 m throughout the channel network. We also mapped the extent of bedrock exposure in 20 km of channels both above and below the main knickpoint. We find, as observed in other landscapes, that channels respond to the transient signal by narrowing and steepening. Additionally, much of the increase in slope (up to 60 percent) tends to be in the form of discrete bedrock steps separating channel reaches that maintain slopes just necessary to transport available sediment. The prevalence of large bedrock steps, as well as the preservation of a continuous strath terrace 60 m above the current channel profile in the lower gorge of Big Tujunga Creek strongly contrasts the channel morphology upstream, suggesting that the style, in addition to the pace, of baselevel fall has changed in the past 1-2 Ma.

INTRODUCTION

Changes in prevailing climatic or tectonic conditions can trigger periods of landscape adjustment that may last thousands to millions of years [e.g., *Hilley and Arrowsmith*, 2008; *Snyder et al.*, 2002; *Whittaker et al.*, 2007]. These transient landscapes serve an important role for tectonic geomorphologists; transient landscapes both record tectonic or climatic history [*Clark et al.*, 2006; *Schoenbohm et al.*, 2004], and provide the most discriminating tests of landscape evolution models that often predict similar steady-state behavior [*Attal et al.*, 2011; *Cowie et al.*, 2008; *Crosby et al.*, 2007]. For example, the preservation of a pervasive low relief surface throughout the eastern Tibetan Plateau above a series of dramatically incised fluvial gorges allows for quantitative estimates of Cenozoic surface uplift when appropriate geochronologic tools are applied [*Clark et al.*, 2006; *Clark et al.*, 2005b; *Ouimet*, 2007]. Furthermore, the nature of the relict landscape gives clues to past climatic and tectonic conditions, and provides valuable constraints to regional tectonic interpretations [e.g., *Harkins et al.*, 2007; *Reinhardt et al.*, 2007a; *Schoenbohm et al.*, 2004]. In addition, transient landscapes are the ultimate test of fluvial incision models. Under steady-state conditions and uniform uplift, the predicted longitudinal profile forms of transport-limited, detachment-limited, and sediment-flux dependent bedrock river models can be similar [*Whipple and Tucker*, 2002]. Following changes in erosional efficiency or the rate of baselevel fall, however, the nature and timing of transient adjustment varies significantly, depending on the processes involved [*Gasparini et al.*, 2007; *Whipple and Tucker*, 2002].

Here we combine stream profile analysis with detailed field surveys and an extensive data set of catchment-averaged erosion rates to investigate a 300 km^2 catchment in the western San Gabriel Mountains, CA which we interpret to reflect a two-staged increase in erosion rate. We use a 10 m digital elevation model (DEM) to generate channel profiles and identify large scale knickpoints; a 1 m LiDAR DEM to map the distribution of strath terrace levels along the mainstem and to identify channel-spanning bedrock steps larger than 3 m in height; and we use detailed field surveys to highlight reductions in valley width and bed sediment cover near and below knickpoints. Additionally, we supplement an already extensive erosion rate dataset with 20 new catchment-averaged erosion rates derived from ^{10}Be concentrations in alluvial sands throughout the San Gabriel Mountains. We use direct and indirect estimates of erosion rates together with projections of relict stream profiles to interpret the tectonic history of the western San Gabriel Mountains and compare the results to independent studies of regional tectonics.

STUDY AREA

The San Gabriel Mountains (SGM) lie in the central Transverse Ranges of southern California (Figure 5.1), bounded by the right-lateral San Andreas Fault (SAF) to the north, and a series of north dipping thrust faults (Sierra Madre Fault Zone – SMFZ, Cucamonga Fault Zone – CFZ) to the south, which accommodate contraction necessitated by a large restraining bend in the SAF. Uplift of the SGM began ca. 5-7 Ma, with the transfer of dextral slip from the San Gabriel Fault to the current trace of the SAF [*Matti and Morton*, 1993]. Vertical components of Holocene slip rates along the SMFZ and CFZ increase from west to east [*Lindvall and Rubin*, 2008; *Peterson and Wesnousky*, 1994], along with topographic relief, decadal sediment flux [*Lavé and Burbank*, 2004], millennial erosion rates [*DiBiase et al.*, 2010], and long-term (million-year timescale) exhumation rates [*Spotila et al.*, 2002]. Combined with the surprising agreement between measures of uplift and erosion spanning decadal, millennial, and million year timescales, these studies suggest that the position of the SGM along the SAF has sustained an E-W gradient in tectonic forcing for at least the past 5 Ma. Palinspastic reconstructions of the Transverse Ranges by *Blythe et al.* [2002] constrained by apatite fission track and (U-Th)/He thermochronology support this interpretation.

In contrast to the strong E-W gradient in tectonic forcing, runoff and lithology do not vary systematically across the SGM. Mean annual precipitation (MAP) varies with elevation, with the highest elevations (2000-3000 m) receiving in excess of 1 m/a (PRISM). The northern flank of the SGM borders the Mojave Desert and lies in a rain shadow (MAP as low as 0.2 m/a). However, the majority of the SGM receives ~0.6-1.0 m/a. Decadal runoff records from throughout the SGM suggest that discharge characteristics are similar across the range with respect to mean daily runoff, decadal maximum runoff, and flood variability [*DiBiase and Whipple*, in review; *Lavé and Burbank*, 2004]. Variations in rock strength are more difficult to quantify. In general, the SGM consist of highly fractured Precambrian and Mesozoic crystalline rock. Extensive decimeter-scale weaknesses tend to minimize differences in lithologic strength among rock types, and while exposed rock is common across the SGM, outcrops tend to be blocky (fractured at the decimeter to meter scale), rather than massive. Overall, there appears to be little dependence of erosion rate on rock strength at the catchment scale [*DiBiase et al.*, 2010], though as detailed below, smaller scale heterogeneities in erosional resistance likely play a crucial role in modulating the retreat rate of knickpoints and the preservation of relict topography.

For this study, we focus on the 300 km^2 watershed of Big Tujunga Creek (BTC), which drains much of the western SGM (black polygon, Figure 1). The lower gorge of BTC is the most dramatic transient feature in the SGM, and features the highest concentration of fluvial hanging valleys and large (>20 m) waterfalls in the range. *Wobus et al.* [2006b] used the concordance of knickpoint elevations along tributaries to BTC as a type example of constant vertical knickpoint migration in response to an increase in uplift rate along a northern strand of the Sierra Madre Fault Zone that merges with the now inactive San Gabriel Fault north of Mount Lukens. We revisit this approach here with the aid of a new 1 m resolution LiDAR DEM flown shortly after the 2009 Station Fire, which burned much of the drainage.

APPROACH AND BACKGROUND

The scope of this study is twofold: we aim to 1) use topographic and geomorphic information to learn about the processes controlling knickpoint migration rates, and 2) use our understanding of topography and erosion rates in the SGM to reconstruct the uplift history of the western SGM using relict stream profiles of Big Tujunga Creek and its tributaries.

Modeling Knickpoint and Waterfall Migration

To avoid confusion in terminology, it is necessary to first emphasize the difference between knickpoints and discrete bedrock steps. We define knickpoints as regional slope breaks in channel long profiles that separate channel segments with differing steepness; in transient landscapes these knickpoints often separate relict from adjusting portions of the landscape [e.g., *Whipple et al.*, in press]. Discrete bedrock steps, or waterfalls, are identified where locally extreme slopes over length scales greater than water flow depth cause flow separation and a general breakdown of the assumptions inherent in fluvial incision models (i.e., steady, uniform flow and low channel slope). Regional knickpoints are often associated with the presence of waterfalls, which complicates attempts to characterize the transient evolution of fluvial systems. For simplicity, we focus on knickpoint and waterfall retreat in generally homogeneous substrates (as opposed to bedded material with a resistant caprock).

The simplest approach to modeling knickpoint migration follows the classical stream power model for detachment-limited bedrock channels, where channel incision can be approximated as a power-law function of slope and drainage area [e.g., *Berlin and Anderson*, 2007; *Bishop et al.*, 2005]. This convenient formulation predicts that knickpoints propagate as kinematic waves whose celerity is a power-law function of upstream drainage area [*Rosenbloom and Anderson*, 1994]. Additionally, if the assumption is made that slope S and drainage area A are related according to Flint's Law:

$$S = k_s A^{-\theta} \tag{5.1}$$

where k_s is the channel steepness index, and θ is the concavity index which does not vary with uplift rate, then the vertical migration rate of knickpoints is constant, and the boundary between relict and adjusting landscapes is predicted to lie along a single topographic contour [*Niemann et al.*, 2001]. The timing of landscape response and the persistence of knickpoints within the fluvial network additionally depends on the presence of erosion thresholds [e.g., *Tucker*, 2004] and the degree of channel narrowing across knickpoints [e.g., *Whittaker et al.*, 2008].

The presence in many rapidly eroding landscapes of fluvial hanging valleys, where waterfalls or dramatic steepenings insulate tributaries from mainstem incision, highlights the shortcomings of the classic stream power model [*Crosby and Whipple*, 2006; *Goode and Burbank*, 2009; *Wobus et al.*, 2006b]. In order to generate runaway steepenings at tributary junctions, bedrock incision models that incorporate a (somewhat counter-intuitive) negative feedback between slope and incision must be invoked. *Crosby et al.* [2007] showed that a sediment-flux dependent incision model where saltation hop length increases with slope [*Sklar and Dietrich*, 2004], thereby limiting incision of oversteepened reaches, is capable of generating fluvial hanging valleys. Using this model, *Crosby et al.* [2007] showed that whether or not hanging valleys form depends on the ratio of tributary to mainstem drainage area and the magnitude of baselevel fall increase, consistent with field observations of hanging valleys in Taiwan [*Wobus et al.*, 2006b].

In contrast to modeling knickpoint migration and transient landscape development within the context of a single erosion law, some authors model waterfall retreat rate directly. Whereas *Crosby et al.* [2007] focused on when and where waterfalls would form, *Lamb et al.* [2007] develop physical scaling relations for waterfall retreat by plunge-pool scour to explain the distributions of large waterfalls in Kohala, Hawaii. Similarly, *Haviv et al.* [2010] developed a physical model for waterfall retreat rate that combined the effects of mass wasting, amplified erosion above the waterfall lip due to flow acceleration [e.g., *Haviv et al.*, 2006], and the deposition and removal of coarse debris below the waterfall. Alternatively, *Crosby and Whipple* [2006] posit a waterfall retreat rate similar to the knickpoint celerity model of *Rosenbloom and Anderson* [1994], but with a critical drainage area, to explain the distribution of waterfalls in the Waipoa River of New Zealand.

The wide range of approaches described above highlights both the interest in characterizing the timing of landscape response to changes in external forcing, and the need for further field observations to constrain fluvial incision models in these discriminating settings. In this study, we start with the simplified premise of constant vertical migration, which has previously been used to explain the distribution of knickpoints in BTC [*Wobus et al.*, 2006b], and use DEM analysis and detailed field surveys to explore the deviations from this case, implications for the preservation of relict landscapes, and for extracting quantitative information about tectonic (or climatic) history from river profiles.

Inferring Tectonic History

Independent of the nature of knickpoint retreat, it is possible to use the present configuration of relict topography in transient landscapes to reconstruct stream profiles and make interpretations about differential uplift and erosion. By projecting stream profiles and either directly measuring or inferring erosion rates for each channel segment, the timing of changes in rates of baselevel fall can be estimated [*Kirby and Whipple*, in review]. In some cases the magnitude of baselevel fall is high enough that relict landscapes act similarly to passive geomorphic markers [*Clark et al.*, 2006]. In other cases, measurements of erosion rates from either low-temperature thermochronometers [*Clark et al.*, 2005a; *Clark et al.*, 2005b] or cosmogenic radionuclides [*Reinhardt et al.*, 2007a] are necessary to constrain the geomorphic evolution of relict landscapes.

In this study, we follow the approach of *Schoenbohm et al.* [2004] and Clark *et al.* [2005a] to reconstruct the timing of uplift history in the SGM. As shown by *DiBiase et al.* [2010] and *Wobus et al.* [2006a], channel segments above and below knickpoints in the SGM follow the scaling relation between slope and area expressed by equation (5.1). Based on this, we can formulate the following relations to estimate the timing of two-staged increase in baselevel fall (Figure 5.2). The time since the most recent increase in baselevel fall (lower-most knickpoint) can be defined as

$$\Delta T_2 = \frac{\Delta Z_{2-3}}{(E_3 - E_2)}, \tag{5.2}$$

where $\Delta Z_{2\text{-}3}$ is the difference in elevation between the current stream and the intermediate projected profile at the location of the baselevel fall (assumed here to be an active fault), and E_3 and E_2 are the erosion rates of the lowermost and intermediate channel segments, respectively (Figure 5.2). The time since the prior increase in baselevel fall (upper-most knickpoint) can be defined using similar notation as:

$$\Delta T_1 = \Delta T_2 + \frac{\Delta Z_{1-2}}{(E_2 - E_1)} . \qquad (5.3)$$

We can then compare these geomorphic estimates of tectonic history to independent reconstructions of fault activity and block motion in the Transverse Ranges [*Blythe et al.*, 2002; *Matti and Morton*, 1993; *Morton and Matti*, 1993].

METHODS

DEM Analysis

We used two data sets for our topographic analysis: a 1 m resolution digital elevation model (DEM) derived from airborne LiDAR (red polygons, Figure 5.3a), and a 10 m DEM derived from the USGS National Elevation Dataset. We extracted channel long profiles from the 10 m DEM using the freely available channel profile toolbar for ArcMap and Matlab (www.geomorphtools.org). Using these channel profiles, we identified knickpoints and fit different channel segments by hand using a reference concavity of 0.45, following *Wobus et al.* [2006a]. We also generated slope maps using the 10 m DEM by calculating the dip of a 3x3 plane fit to each pixel. To quantify the large-scale hillslope response to upstream-propagating baselevel fall, we binned the landscape into 50 m elevation bins and calculated the mean slope of each.

We used the 1 m LiDAR DEM for three tasks: we identified bedrock steps greater than 3 m in channel profiles; we mapped the extent of strath terrace surfaces; and we measured valley width for select channels. For visualization, we generated a slope map from the 1 m DEM as described above (Figure 5.4). By inspection, we identified bedrock steps along all channels draining areas greater than 0.5 km^2. For each identified step, we extracted a short channel profile to determine step height as shown in Figure 5.4a. For surveyed channels that lie within the LiDAR coverage, we calibrated this method based on field observations of channel spanning bedrock steps, giving confidence that these steep sections represent exposed rock rather than steep boulder reaches. We then transferred this map of bedrock steps to the channel long profiles determined earlier to quantify the elevation drop composed of discrete steps compared to that from smoothly graded channels.

We also used this slope map to identify regions of low (< 10°) slope, which tend to correspond to valley flats and terrace surfaces. Terrace surfaces are readily identifiable along the lower reaches of BTC, but are rarely preserved in tributaries or in the upper reaches of the catchment (elevations > 1000 m). We interpret these surfaces to be strath terraces thinly mantled (order 1 m) with alluvium, based on numerous field observations of at least two distinct terrace levels (Figure 5.4c). We then transferred the mapped surfaces to the channel long profiles based on along-stream position.

Channel Surveys

To supplement our DEM analysis, we surveyed ~20 km of 9 channels in the BTC watershed, including the main stem across both major knickpoints, and multiple smaller side tributaries that enter the lower gorge (blue lines, Figure 5.3a). We used a laser range-finder and electronic data logger to geo-locate measurements of bed cover and channel geometry at intervals of 20-50 m. We estimated the percent of bedrock exposed in channel bed and banks to the nearest 10%, and measured bankfull width based on vegetation lines and high flow marks. In reaches with extensive valley flats (> 20 m), we supplemented our field surveys with measurements of valley width from the 1 m LiDAR

DEM (Figure 5.3a). Additionally, we noted all channel-spanning bedrock steps greater than 3 m, and identified strath and fill terrace surfaces where visible from the channel.

Erosion Rates

Detrital cosmogenic radionuclide (CRN) methods have proven to be effective for quantifying catchment-averaged rates of erosion over the intermediate spatial (1-100 km^2) and temporal (10^2-10^5 a) scales critical for identifying and interpreting transient landscapes. However, transient catchments where erosion is highly non-uniform present difficulties when interpreting alluvial CRN concentrations [e.g., *Reinhardt et al.*, 2007b]. Ideally only tributary catchments that have fully adjusted to local baselevel lowering rates (i.e., no knickpoints upstream) would be sampled, but recent increases in baselevel fall preclude this situation. Alternatively, erosion rates can be inferred from adjusted topography, even when relict topography exists upstream (Figure 5.2).

We used a combination of direct and indirect methods to constrain the distribution of erosion rates in the BTC watershed. Because climate and lithology are similar for much of the SGM, we interpret the relations between topography and erosion rate generated from the entire range to be applicable for inferring erosion rate in BTC. We supplement published catchment-averaged erosion rates [*DiBiase et al.*, in review; *DiBiase et al.*, 2010; *Heimsath et al.*, in press] with 20 new measurements of ^{10}Be concentrations in alluvial sands for a total of 80 catchment-averaged erosion rates. We processed the 250-500um sand fraction following methods described by *DiBiase et al.* [2010]. Quartz separation and ^{10}Be isolation was performed at Arizona State University, while ^{10}Be/^{9}Be ratios were measured at PrimeLab (Purdue University). We determined catchment-averaged production rates by calculating pixel-by-pixel elevation and latitude scaling factors [*Dunai*, 2000] from a 10 m DEM. We did not account for topographic shielding, snow cover, or muogenic production, and assume that these factors contribute to an estimated 5% uncertainty in production rates that is added to the 1σ analytical error. For each sample catchment, we also report mean hillslope angle and normalized channel steepness index following *Ouimet et al.* [2009] and *DiBiase et al.* [2010] using the 10 m USGS DEM.

RESULTS

DEM Analysis

Normalized channel steepness index in the BTC watershed ranges from 20-500 $m^{0.9}$, with values greater than ~200 $m^{0.9}$ corresponding to short, oversteepened reaches just below prominent knickpoints (Figure 5.3a). Two prominent knickpoint levels separate three distinct physiographic regions. In the uppermost reaches of the BTC watershed, knickpoints on Chilao Creek (~1550 m asl) and the East Fork of Alder Creek (~1600 m asl) isolate the saprolitic, low relief surface of Chilao Flats (k_{sn} ~ 20 $m^{0.9}$). Knickpoints on major tributaries ranging in elevation from ~930-1030 m mark the limit of a dramatic inner gorge that characterizes lower BTC (Figure 5.3b). Between Chilao Flats and the lower gorge of BTC lies a dissected, soil-mantled landscape with mean k_{sn} equal to 64 $m^{0.9}$. Mean slope binned by elevation reveals a similar story, with slope declining systematically as elevation increases (Figure 5.5). Furthermore, breaks in mean slope at elevations of 1000 m and 1550 m line up approximately with knickpoint elevations along stream channels, and there is a significant difference between the rocky, rugged slopes of the inner gorge of BTC (mean slope = 33°) and the gentle, soil mantled hillslopes of Chilao Flats (mean slope = 23°). Together, the pattern of hillslope gradient and the map-view distribution of knickpoints suggest that transient behavior in BTC can be well characterized by the simple case where knickpoints migrate at a constant vertical rate, resulting in physiographic breaks at 1000 m and 1500 m elevation.

Inspection of the longitudinal profile of the mainstem BTC, however, suggests a more complicated story. In contrast to models that predict smooth transitions between reaches of different steepness (e.g., Figure 5.2), the two knickpoints along BTC lie at the head of significant oversteepenings (Figure 5.6), as seen in many landscapes [*Whipple et al.*, in press]. Furthermore, the majority of the vertical drop on these oversteepenings consist of bedrock steps greater than 3 m in height (bold lines, Figure 5.6). Long profiles of tributaries flowing into the lower gorge of BTC show a similarly complicated story. For example, Lucas Creek and Clear Creek have few or no bedrock steps along their entire length, yet show clear evidence of a knickpoint near 1000 m elevation. In contrast, Fox Creek and Falls Creek drop from their relict reaches to the inner gorge via a series of 10-30 m waterfalls. However, projections of the relict profiles of these tributaries (dotted lines, Figure 5.7) grade smoothly with the reconstructed intermediate reach of BTC (dashed line, figure 5.7). In addition, mapped strath terraces in lower BTC define a profile parallel to and ~50 m higher than the current stream level (thin dashed line, Figure 5.7) and many tributaries are directly hung on this level.

Channel Surveys

Detailed surveys of channels crossing knickpoints reveal trends consistent with observations by *Berlin and Anderson* [2009] and *Haviv et al.* [2006]. Upstream reaches tend to be mantled with alluvium and across knickpoints, valley width decreases dramatically, channels narrow, and sediment cover decreases. Figure 5.8 highlights three examples of such surveys.

Figure 5.8a shows the behavior of Fox Creek, which enters the lower gorge of BTC. The upper reaches of Fox Creek flow through a wide (~75 m), low gradient alluvial valley consisting primarily of anorthosite bedrock. Just over 1 km upstream of the main knickpoint, the bedrock lithology changes to granite, with no obvious change in valley width or channel slope. Approximately 700 m upstream of the main knickpoint, the valley narrows to ~20 m (~2-3 times channel width), channel slope increases slightly, and there is a gradual loss of sediment cover [cf., *Berlin and Anderson*, 2009; *Haviv et al.*, 2006]. The main knickpoint of Fox Creek consists of a series of 7 waterfalls ranging in height from 3-30 m that incise through a dramatic bedrock gorge 5-10 m wide. Below the main knickpoint is a lower gradient (though steeper than the upstream reach) reach with abundant exposed bedrock in the channel bed. Finally, Fox Creek enters BTC via a 20 m waterfall that corresponds to the lowest-observed strath terrace level along the mainstem. While not shown, bankfull channel width stays approximately constant (7 ± 2 m) for the length of the 4 km survey, while drainage area increases from 17 to 24 km^2.

Figure 5.8b shows a similar survey of the mainstem BTC as it crosses its lower knickpoint (Figure 5.6). The upstream reaches are characterized by low slopes and limited bedrock exposure in the channel bed. The lower knickpoint of BTC is characterized by two over-steepened zones separated by a lower gradient reach. Across these steepened zones, valley width and bankfull channel width decrease, while bedrock exposure increases.

Figure 5.8c tells a slightly different story of the upper knickpoint along Chilao Creek. The uppermost reach of the survey flows through a wide (>100 m), flat, alluvial valley, which narrows ~ 1 km upstream of the main knickpoint, similar to Fox Creek. However, while the entire reach downstream of the knickpoint is characterized by a series of 3-20 m bedrock steps, where exposed bedrock in the channel bed is less abundant through this steepened zone than it is just upstream of the knickpoint. Instead, much of this zone is mantled by 1-3 m boulders.

Reconstructing Uplift History

Erosion rates in the SGM range from 30-1100 m/Ma, with the highest rates focused along the southern range front and in the eastern SGM (Figures 5.1 and 5.9, Appendix B). Channel steepness index increases monotonically with erosion rate across the SGM, following a power law relationship described by:

$$k_{sn} \propto E^{\phi}, \tag{5.4}$$

where $\phi \sim 0.5$ [*DiBiase and Whipple*, in review]. DiBiase et al. [in review] argue that this non-linear relationship between channel steepness and erosion rate arises due to the presence of erosion thresholds that preferentially retard the incision of channels with low steepness. It should be emphasized that this relationship only applies to adjusted channel reaches, and should not be used to describe the oversteepened reaches observed immediately downstream of knickpoints.

Using this relationship, we infer three different erosion rates for the distinct physiographic regions of the BTC watershed (Figures 5.3c, 5.6). The uppermost region, Chilao Flats, with a mean k_{sn} of 22 $m^{0.9}$, can be directly measured to have a rate of 45 ± 7 m/Ma, based on two catchment erosion samples (SG128 and SG129) and consistent with local soil production rates [*Heimsath et al.*, in press]. The middle BTC, with a mean k_{sn} of 64 $m^{0.9}$,can be inferred to have a rate of 151 ± 32 m/Ma, based on the average of 10 catchment samples (we ignore two outliers in this analysis, both from Wickiup Canyon – SG0703 and SG0708). For the lower gorge of BTC, none of the detrital CRN samples directly measure the erosion rate of the most recently adjusted topography. Four samples

(SGB7, SGB9, SGB10, and SG0730) reflect erosion rates in transient catchments that average 358 ± 113 m/Ma, but these rates may be biased too high as a result of amplified erosion near knickpoints or too low due to the contribution of sediment from upstream of the knickpoints. Alternatively, based on the normalized channel steepness (80-105 $m^{0.9}$) and mean hillslope angle (33°) measured in the adjusted topography, we can estimate erosion rates for the lower-most BTC to be 230 ± 60 m/Ma.

In addition to erosion rates, we also need to identify the locus of baselevel fall from which we want to calculate the time since initiation. We interpret that active deformation is concentrated along a northern strand of the Sierra Madre Fault System that intercepts BTC at its confluence with Trail Canyon (Figures 5.6 and 5.7). To determine values for $\Delta Z_{1\text{-}2}$ and $\Delta Z_{2\text{-}3}$, we also need to determine the elevations of the projected relict channels at the chosen outlet point (Figure 2). The normalized channel steepness index of the upper reaches of BTC and its tributaries averages 22 ± 2 $m^{0.9}$ (Figure 5.6). Channel steepness values for the intermediate reaches of BTC and its tributaries averages 64 ± 4 $m^{0.9}$. Because the elevations of the projected streams is well constrained relative to the uncertainty in erosion rates, we ignore the errors in ΔZ for our calculations. Furthermore, the exact choice of where the Sierra Madre Fault Zone intersects BTC does not strongly influence values of ΔZ. If we use direct measurements of erosion rate for lower BTC (i.e., 358 ± 113 m/Ma), $\Delta T_1 \sim$ 7-8 Ma and $\Delta T_2 \sim$ 0.5-1.5 Ma following equations (5.2) and (5.3). If we instead infer erosion rates for lower BTC based on the relationship between normalized channel steepness index and erosion rate shown in Figure 5.9 (i.e., 230 ± 60 m/Ma), $\Delta T_1 \sim$ 8-9 Ma and $\Delta T_2 \sim$ 1.5-2.5 Ma.

DISCUSSION

Knickpoint Propagation

What controls the knickpoint migration rate? Analytical solutions to the simple detachment-limited stream power model suggest that knickpoints propagate upstream as a kinematic wave at rate that increases with increasing drainage area [*Rosenbloom and Anderson*, 1994]. Furthermore, for cases where erosion rate increases linearly with channel slope (i.e., $\phi = 1$, equation (5.4)), knickpoint migration rate is expected to be independent of the forcing strength [*Whipple and Tucker*, 1999]. In a recently de-glaciated valley in the French Western Alps, *Valla et al.* [2010] found a strong power-law relationship between the retreat distances of glacially formed hanging valleys and upstream drainage area. *Whittaker et al.* [2008] found that for transient catchments in the Central Apennines of Italy, knickpoint migration rate was additionally a function of the magnitude of throw rate increase on range bounding normal faults. *Whittaker et al.* [2008] used obervations of channel narrowing across knickpoints [*Whittaker et al.*, 2007] to argue that non-linear channel incision (with regard to slope) was responsible for the more rapid retreat rates of steeper convexities or knickzones (defined as the steepened reach below a knickpoint). *Attal et al.* [2011] used the same field setting to test a range of fluvial incision laws closely related to the stream power model, and showed that including an erosion threshold [e.g., *Tucker*, 2004] or modeling slope dependent channel width [e.g., *Finnegan et al.*, 2005] reproduces the observed increase in knickpoint retreat rate with uplift rate.

We find little relationship between drainage area and retreat distance for knickpoints on tributaries draining the lower gorge of BTC (Figure 5.7). For example, Fox Creek (A = 24 km^2) plunges over a series of large waterfalls 2 km from its confluence with BTC. In contrast, the knickpoint on Lucas Creek (A = 4 km^2) has migrated more than 3 km upstream from BTC, and contains few bedrock steps. Furthermore, the location of waterfalls is not confined to near tributary junctions, as described by *Crosby and Whipple* [2006] and *Goode and Burbank* [2009]. Thus alternative models that allow for the formation of fluvial hanging valleys do not appear to be capable for describing the distribution of bedrock steps within BTC [e.g., *Crosby et al.*, 2007].

We make two first-order interpretations based on our observations: (1) knickzones in the BTC characterized by the presence of large (>3 m) bedrock steps stall knickpoint retreat and insulate relict topography from baselevel fall; and (2) the development of these oversteepened reaches is enhanced in areas of limited coarse sediment supply. To elaborate, the longitudinal profile “offsets” seen in Figure 5.6 are likely the result of small scale variations in rock strength that initiate negative feedbacks between slope and erosion rate, such as those present in saltation-abrasion models of bedrock incision [*Lamb et al.*, 2008; *Sklar and Dietrich*, 2004]. This results in a switch in the processes controlling waterfall retreat from fluvial incision to weathering and mass wasting, slowing knickpoint migration as a result. These feedbacks are enhanced in regions with low coarse sediment supply, as observed by *Johnson et al.* [2009] in the Henry Mountains and suggested by the plunge-pool waterfall retreat model of *Lamb et al.* [2007]. We observe this behavior in particular for 3 catchments: Fox Creek, Falls Creek, and Chilao Creek. The headwater lithology of Fox Creek and Falls Creek is dominated by a Precambrian anorthosite body that produces cobbles that rapidly break down into finer material. For example, pebble counts in Fox Creek taken across the lithologic contact to granite (Figure 5.8) reveal a rapid switch in bed material dominance from anorthosite to granite, despite the low areal extent of granite in the catchment. For Chilao Creek, the relict landscape of Chilao Flats consists of deeply weathered granitic surface that contributes a bimodal sediment load of grus and occasional meter-scale boulders to the channel network. Extensive fluting of these large boulders mantling the steep knickzone below the upper knickpoint on Chilao Creek (Figure 5.8) suggests they are relatively immobile, and likely act similar to bedrock. Furthermore, this low relief surface remains only because the upper knickpoint on Chilao Creek has hung up and we speculate that it is incapable of migrating further given the lack of tools (Figure 5.6). While we also observe channel narrowing across these knickzones, it apparently does not enhance incision rates enough to overcome these lithology-initiated negative feedbacks.

Implications for the Tectonic History

By a certain amount of luck then, what we interpret to be a signal of the initial phase of SGM uplift is preserved in the upper knickpoint of BTC. Our estimate of 7-9 Ma overlaps with independent estimates of the timing of SGM uplift (ca. 5-7 Ma) by *Matti and Morton* [1993] and *Blythe et al.* [2002]. In addition to the geomorphic evidence provided by stream profile analysis, the inference that Chilao Flats preserves the pre-uplift surface of the SGM is supported by two additional factors: similarity in relief and weathering extent to the Big Bear Plateau in the nearby San Bernardino Mountains, and old cooling ages (>40 Ma) from low-temperature thermochronometers [*Blythe et al.*, 2000; *Spotila et al.*, 1998]. Traces of this pre-uplift surface have likely been entirely erased in the eastern SGM, due to more rapid rates of uplift and erosion [*DiBiase et al.*, 2010; *Spotila et al.*, 2002]. Assuming a similar W-E gradient in erosion rates (approximately 2-3x) has existed over long time periods [e.g., *Spotila et al.*, 2002], the equivalent surface would lie at elevations greater than 6000 m in the Eastern SGM, whereas the highest peaks currently only reach 3000 m.

The origin of the lower knickpoint is less definitive. As noted earlier, this knickpoint reflects a sustained increase in baselevel fall (~2-3x) ca. 0.5-2.5 Ma. This age corresponds with estimates of the initiation of the right lateral San Jacinto Fault Zone, which range from 1.1 Ma [*Kirby et al.*, 2007; *Lutz et al.*, 2006] to 1.8 Ma [*Blisniuk et al.*, 2010]. However, the influence on the pattern of uplift in the SGM from this transfer of slip from the San Andreas Fault to the San Jacinto Fault is unclear. *Spotila et al.* [1998] interpret young mineral cooling ages as evidence for rapid uplift of the Yucaipa Ridge Block in the San Bernardino Mountains since 1.5 Ma, and attribute the increase to the inception of the San Jacinto Fault, following *Morton and Matti* [1993]. Further work is needed using kinematic models of southern California faults to test whether the transfer of slip from the San Andreas Fault to the San Jacinto Fault results in increased vertical slip rates along the Sierra Madre and Cucamonga thrust systems in the SGM.

This increase in uplift rate was likely not restricted to the Big Tujunga drainage, and we see scattered evidence of transient signals elsewhere in the SGM. In particular, the low relief surface of Copter Flats (Figure 1) is potentially correlative to the middle physiographic zone of BTC. Rough estimates based on detrital CRN erosion rates [*DiBiase et al.*, 2010] and the projection of the upper reaches of the Iron Fork of the San Gabriel River reveal a story consistent with that along BTC. However, projecting these spatially limited surfaces is fraught with difficulty, and a change in vegetation or switch to frost shattering at high elevation may also be important.

CONCLUSIONS

We have described a two-staged transient within Big Tujunga Creek in the San Gabriel Mountains, CA. The upper (earlier) transient in the BTC catchment has nearly propagated through the entire fluvial network, with only isolated patches of an elevated low-relief weathering surface remaining. The lower transient, however, is characterized by a dramatic inner gorge with over-steepened valley walls and fluvial hanging valleys. In both cases, we interpret an increase in the rate of local baselevel fall that resulted in the propagation of a wave of incision upstream through the landscape, with discrete knickpoints separating adjusting from relict portions of the landscape. We used a 10 m digital elevation model identify knickpoints and extract channel long profiles and hillslope angles. Combining erosion rate estimates with elevation differences between projected long profiles allows for the estimation of the timing of increases in baselevel fall. We found the age of the older transient to be ca. 7-9 Ma, which likely corresponds to the initiation of uplift in the SGM associated with the transfer of slip from the San Gabriel Fault to the current trace of the San Andreas Fault. The younger transient dates to ca. 0.5-2.5 Ma, which overlaps with estimates of activation of the San Jacinto Fault Zone, the inception of which has been linked to increases in rock uplift rate in both the eastern San Gabriel Mountains and in the nearby San Bernardino Mountains.

The lower BTC transient also affords us the opportunity to investigate the nature of bedrock channel response to temporal forcing in a relatively homogenous lithology (massive crystalline rocks). Supplementing detailed field surveys with 160 km^2 of airborne LiDAR-derived topography (1 m resolution), we mapped channel width, valley width, and the extent of bedrock steps greater than 3 m throughout the channel network. We also mapped the extent of bedrock exposure in 20 km of channels both above and below the main knickpoint. We found, as shown in other landscapes, that channels respond to the transient signal by narrowing and steepening. Additionally, much of the increase in slope (up to 60 percent) tends to be in the form of discrete bedrock steps separating channel reaches that maintain slopes just necessary to transport available sediment. The prevalence of large bedrock steps, as well as the preservation of a continuous strath terrace 60 m above the current channel profile in lower BTC strongly contrasts the channel morphology upstream, suggesting that the style, in addition to the pace, of baselevel fall has changed in the past 1-2 Ma.

ACKNOWLEDGEMENTS

We would like to thank all those involved with the field surveys, including B. Adams, N.Gasparini, M. Jungers, and D. Stolar. Funding for this project was provided by the Geomorphology and Land Use Dynamics program at NSF (EAR-0724194 to KXW).

REFERENCES

Attal, M., P. A. Cowie, A. C. Whittaker, D. Hobley, G. E. Tucker, and G. P. Roberts (2011), Testing fluvial erosion models using the transient response of bedrock rivers to tectonic forcing in the Apennines, Italy, *Journal of Geophysical Research*, *116*, F02005, doi:10.1029/2010JF001875.

Berlin, M. M., and R. S. Anderson (2007), Modeling of knickpoint retreat on the Roan Plateau, western Colorado, *Journal of Geophysical Research*, *112*, F03S06, doi:10.1029/2006jf000553.

Berlin, M. M., and R. S. Anderson (2009), Steepened channels upstream of knickpoints: Controls on relict landscape response, *Journal of Geophysical Research*, *114*, F03018, doi:10.1029/2008jf001148.

Bishop, P., T. B. Hoey, J. D. Jansen, and I. L. Artza (2005), Knickpoint recession rate and catchment area: the case of uplifted rivers in Eastern Scotland, *Earth Surface Processes and Landforms*, *30*(6), 767-778.

Blisniuk, K., T. Rockwell, L. A. Owen, M. Oskin, C. Lippincott, M. W. Caffee, and J. Dortch (2010), Late Quaternary slip rate gradient defined using high-resolution topography and (10)Be dating of offset landforms on the southern San Jacinto

Fault zone, California, *Journal of Geophysical Research-Solid Earth*, *115*, B08401, doi:10.1029/2009jb006346.

Blythe, A., M. A. House, and J. A. Spotila (2002), Low temperature thermochronology of the San Gabriel and San Bernadino Mountains, southern California: Constraining structural evolution, in *Contributions to Structural Evolution of the Southwestern United States: Geological Society of America Special Paper*, edited by A. P. Barth, pp. 231-250, Boulder, Colorado.

Blythe, A. E., D. W. Burbank, K. A. Farley, and E. J. Fielding (2000), Structural and topographic evolution of the central Transverse Ranges, California, from apatite fission-track, (U-Th)/He and digital elevation model analyses, *Basin Research*, *12*, 97-114.

Clark, M. K., G. Maheo, J. Saleeby, and K. A. Farley (2005a), The non-equilibrium landscape of the southern Sierra Nevada, California, *GSA Today*, *15*(9), 4-10.

Clark, M. K., L. H. Royden, K. X. Whipple, B. C. Burchfiel, X. Zhang, and W. Tang (2006), Use of a regional, relict landscape to measure vertical deformation of the eastern Tibetan Plateau, *Journal of Geophysical Research*, *111*, F03002, doi:10.1029/2005jf000294.

Clark, M. K., M. A. House, L. H. Royden, K. X. Whipple, B. C. Burchfiel, X. Zhang, and W. Tang (2005b), Late Cenozoic uplift of southeastern Tibet, *Geology*, *33*(6), 525-528.

Cowie, P. A., A. C. Whittaker, M. Attal, G. Roberts, G. E. Tucker, and A. Ganas (2008), New constraints on sediment-flux-dependent river incision: Implications for extracting tectonic signals from river profiles, *Geology*, *36*(7), 535-538.

Crosby, B. T., and K. X. Whipple (2006), Knickpoint initiation and distribution within fluvial networks: 236 waterfalls in the Waipaoa River, North Island, New Zealand, *Geomorphology*, *82*(1-2), 16-38.

Crosby, B. T., K. X. Whipple, N. M. Gasparini, and C. W. Wobus (2007), Formation of fluvial hanging valleys: Theory and simulation, *Journal of Geophysical Research*, *112*, F03S10, doi:10.1029/2006JF000566.

DiBiase, R. A., and K. X. Whipple (in review), Discharge variability paper, *submitted to: Journal of Geophysical Research*.

DiBiase, R. A., A. M. Heimsath, and K. X. Whipple (in review), Hillslope response to tectonic forcing in threshold landscapes, *submitted to: Earth Surface Processes and Landforms*.

DiBiase, R. A., K. X. Whipple, A. M. Heimsath, and W. B. Ouimet (2010), Landscape form and millennial erosion rates in the San Gabriel Mountains, CA, *Earth and Planetary Science Letters*, *289*(1-2), 134-144.

Dunai, T. J. (2000), Scaling factors for production rates of in situ produced cosmogenic nuclides: a critical reevaluation, *Earth and Planetary Science Letters*, *176*, 157-169.

Finnegan, N. J., G. Roe, D. R. Montgomery, and B. Hallet (2005), Controls on the channel width of rivers: Implications for modeling fluvial incision of bedrock, *Geology*, *33*(3), 229-232.

Gasparini, N. M., K. X. Whipple, and R. L. Bras (2007), Predictions of steady state and transient landscape morphology using sediment-flux-dependent river incision models, *Journal of Geophysical Research*, *112*, F03S09, doi:10.1029/2006JF000567.

Goode, J. K., and D. W. Burbank (2009), Numerical study of degradation of fluvial hanging valleys due to climate change, *Journal of Geophysical Research*, *114*, F01017, doi:10.1029/2007jf000965.

Harkins, N., E. Kirby, A. Heimsath, R. Robinson, and U. Reiser (2007), Transient fluvial incision in the headwaters of the Yellow River, northeastern Tibet, China, *Journal of Geophysical Research*, *112*, F03S04, doi:10.1029/2006jf000570.

Haviv, I., Y. Enzel, K. X. Whipple, E. Zilberman, J. Stone, A. Matmon, and L. K. Fifield (2006), Amplified erosion above waterfalls and oversteepened bedrock reaches, *Journal of Geophysical Research-Earth Surface*, *111*(F4), F04004, doi:10.1029/2006jf000461.

Haviv, I., Y. Enzel, K. X. Whipple, E. Zilberman, A. Matmon, J. Stone, and K. L. Fifield (2010), Evolution of vertical knickpoints (waterfalls) with resistant caprock: Insights from numerical modeling, *Journal of Geophysical Research*, *115*, F03028, doi:10.1029/2008jf001187.

Heimsath, A. M., R. A. DiBiase, and K. X. Whipple (in press), Soil production limits and the transition to bedrock dominated landscapes, *Nature Geoscience*.

Hilley, G. E., and J. R. Arrowsmith (2008), Geomorphic response to uplift along the Dragon's Back pressure ridge, Carrizo Plain, California, *Geology*, *36*(5), 367-370.

Johnson, J. P. L., K. X. Whipple, L. S. Sklar, and T. C. Hanks (2009), Transport slopes, sediment cover, and bedrock channel incision in the Henry Mountains, Utah, *Journal of Geophysical Research*, *114*, F02014, doi:10.1029/2007JF000862.

Kirby, E., and K. X. Whipple (in review), Expression of active tectonics in erosional landscapes, *Journal of Structural Geology*.

Kirby, S. M., S. U. Janecke, R. J. Dorsey, B. A. Housen, V. E. Langenheim, K. A. McDougall, and A. N. Steely (2007), Pleistocene brawley and ocotillo formations: Evidence for initial strike-slip deformation along the San Felipe and San Jacinto fault zones, southern California, *Journal of Geology*, *115*(1), 42-62.

Lamb, M. P., W. E. Dietrich, and L. S. Sklar (2008), A model for fluvial bedrock incision by impacting suspended and bed load sediment, *Journal of Geophysical Research*, *113*, F03025, doi:10.1029/2007JF000915.

Lamb, M. P., A. D. Howard, W. E. Dietrich, and J. T. Perron (2007), Formation of amphitheater-headed valleys by waterfall erosion after large-scale slumping on Hawai ‘i, *GSA Bulletin*, *119*(7/8), 805-822.

Lavé, J., and D. W. Burbank (2004), Denudation processes and rates in the Transverse Ranges, southern California: Erosional response of a transitional landscape to external and anthropogenic forcing, *Journal of Geophysical Research*, *109*, F01006.

Lindvall, S. C., and C. M. Rubin (2008), Slip rate studies along the Sierra Madre-Cucamonga fault system using geomorphic and cosmogenic surface exposure age constraints: Collaborative research with Central Washington University and William Lettis & Associates, Inc., US Geological Survey final report 03HQGR0084.

Lutz, A. T., R. J. Dorsey, B. A. Housen, and S. U. Janecke (2006), Stratigraphic record of Pleistocene faulting and basin evolution in the Borrego Badlands, San Jacinto fault zone, Southern California, *Geological Society of America Bulletin*, *118*(11-12), 1377-1397.

Matti, J. C., and D. M. Morton (1993), Paleogeographic evolution of the San Andreas fault in southern California: A reconstruction based on a new cross-fault correlation, *Geological Society of America Memoir 178*, 107-159.

Morton, D. M., and J. C. Matti (1993), Extension and contraction within an evolving divergent strike-slip fault complex: The San Andreas and San Jacinto fault zones at their convergence in southern California, *Geological Society of America Memoir 178*, 217-230.

Niemann, J. D., N. M. Gasparini, G. E. Tucker, and R. L. Bras (2001), A quantitative evaluation of Playfair's law and its use in testing long-term stream erosion models, *Earth Surface Processes and Landforms*, *26*(12), 1317-1332.

Ouimet, W. B. (2007), Dissecting the eastern margin of the Tibetan plateau: a study of landslides, erosion, and river incision in a transient landscape, Ph.D. thesis, Massachusetts Institute of Technology.

Ouimet, W. B., K. X. Whipple, and D. E. Granger (2009), Beyond threshold hillslopes: Channel adjustment to base-level fall in tectonically active mountain ranges, *Geology*, *37*(7), 579-582.

Peterson, M. D., and S. G. Wesnousky (1994), Fault slip rates and earthquake histories for active faults in Southern California, *Bulletin of the Seismological Society of America*, *84*(5), 1608-1649.

Reinhardt, L. J., P. Bishop, T. B. Hoey, T. J. Dempster, and D. C. W. Sanderson (2007a), Quantification of the transient response to base-level fall in a small mountain catchment: Sierra Nevada, southern Spain, *Journal of Geophysical Research*, *112*, F03S05, doi:10.1029/2006jf000524.

Reinhardt, L. J., T. B. Hoey, T. T. Barrows, T. J. Dempster, P. Bishop, and L. K. Fifield (2007b), Interpreting erosion rates from cosmogenic radionuclide concentrations measured in rapidly eroding terrain, *Earth Surface Processes and Landforms*, *32*(3), 390-406.

Rosenbloom, N. A., and R. S. Anderson (1994), Hillslope and channel evolution in a marine terraced landscape, Santa Cruz, California, *Journal of Geophysical Research*, *99*(B7), 14013-14029.

Schoenbohm, L. M., K. X. Whipple, B. C. Burchfiel, and L. Chen (2004), Geomorphic constraints on surface uplift, exhumation, and plateau growth in the Red River region, Yunnan Province, China, *Geological Society of America Bulletin*, *116*(7-8), 895-909.

Sklar, L. S., and W. E. Dietrich (2004), A mechanistic model for river incision into bedrock by saltating bed load, *Water Resources Research*, *40*, W06301, doi:10.1029/2003WR002496.

Snyder, N. P., K. X. Whipple, G. E. Tucker, and D. M. Merritts (2002), Interactions between onshore bedrock-channel incision and nearshore wave-base erosion forced by eustacy and tectonics, *Basin Research*, *14*, 105-127.

Spotila, J. A., K. A. Farley, and K. Sieh (1998), Uplift and erosion of the San Bernardino Mountains associated with transpression along the San Andreas fault, California, as constrained by radiogenic helium thermochronometry, *Tectonics*, *17*(3), 360-378.

Spotila, J. A., M. A. House, A. E. Blythe, N. A. Niemi, and G. C. Bank (2002), Controls on the erosion and geomorphic evolution of the San Bernardino and San Gabriel Mountains, southern California, *Geological Society of America Special Paper 365*, 205-230.

Tucker, G. E. (2004), Drainage basin sensitivity to tectonic and climatic forcing: Implications of a stochastic model for the role of entrainment and erosion thresholds, *Earth Surface Processes and Landforms*, *29*, 185-205.

Valla, P. G., P. A. van der Beek, and D. Lague (2010), Fluvial incision into bedrock: Insights from morphometric analysis and numerical modeling of gorges incising glacial hanging valleys (Western Alps, France), *Journal of Geophysical Research*, *115*, F02010, doi:10.1029/2008jf001079.

Whipple, K. X., and G. E. Tucker (1999), Dynamics of the stream-power river incision model: Implications for height limits of mountain ranges, landscape response timescales, and research needs, *Journal of Geophysical Research-Solid Earth*, *104*(B8), 17661-17674.

Whipple, K. X., and G. E. Tucker (2002), Implications of sediment-flux-dependent river incision models for landscape evolution, *Journal of Geophysical Research-Solid Earth*, *107*(B2), doi:10.1029/2000JB000044.

Whipple, K. X., R. A. DiBiase, and B. T. Crosby (in press), Bedrock Rivers, in *Treatise on Fluvial Geomorphology*, edited by E. Wohl.

Whittaker, A. C., P. A. Cowie, M. Attal, G. E. Tucker, and G. P. Roberts (2007), Contrasting transient and steady-state rivers crossing active normal faults: new field observations from the Central Apennines, Italy, *Basin Research*, *19*(4), 529-556.

Whittaker, A. C., M. Attal, P. A. Cowie, G. E. Tucker, and G. Roberts (2008), Decoding temporal and spatial patterns of fault uplift using transient river long profiles, *Geomorphology*, *100*(3-4), 506-526.

Wobus, C., K. X. Whipple, E. Kirby, N. Snyder, J. Johnson, K. Spyropolou, B. Crosby, and D. Sheehan (2006a), Tectonics from topography: Procedures, promise, and pitfalls, *Geological Society of America Special Paper 398*, 55-74.

Wobus, C. W., B. T. Crosby, and K. X. Whipple (2006b), Hanging valleys in fluvial systems: Controls on occurrence and implications for landscape evolution, *Journal of Geophysical Research*, *111*, F02017, doi:10.1029/2005JF000406.

FIGURE CAPTIONS

Figure 5.1. Overview map of San Gabriel Mountains, California, showing local relief measured with a 250 m radius circular window. Black lines indicate quaternary faults (thickness corresponds to activity, http://earthquakes.usgs.gov/regional/qfaults). SAF = San Andreas Fault; SGF = San Gabriel Fault; SMFZ = Sierra Madre Fault Zone; CFZ = Cucamonga Fault Zone. Red outline highlights the catchment draining Big Tujunga Creek. Other labeled regions mentioned in text include LG = Lower Gorge of Big Tujunga Creek; ChF = Chilao Flats; and CoF = Copter Flats.

Figure 5.2. Conceptual diagram of a two-staged increase in baselevel fall, showing longitudinal profiles of the current stream channel (solid line), projections of relict channels (dotted and dashed lines), and the location of knickpoints (circles). Arrows indicate variables used in equations (5.2) and (5.3).

Figure 5.3. Shaded relief map of the Big Tujunga Creek watershed, highlighting (a) the extent of LiDAR coverage (gray hachures), detailed field surveys (blue lines), and Figure 5.4 (star), (b) the distribution of channel steepness index (colored stream network) and knickpoints (circles) relative to elevation breaks at 1000 and 1550 m, and (c) the distribution of hillslope angle relative to the position of knickpoints and elevation breaks

Figure 5.4. Example of mapping morphologic features in the lower gorge of the Big Tujunga using 1 m LiDAR slope map draped over shaded relief. Profile A-A’ (inset) shows a four-staged waterfall along Falls Creek, with bedrock steps shown in red. W_V indicates the definition of valley width used in Figure 5.8. Strath terraces appear as

elevated low slope (< 10°) regions adjacent to the main stem Big Tujunga Creek. Block arrows show the location of photos (b) (left arrow, lower waterfall of Falls Creek) and (c) (right arrow, strath terraces of Big Tujunga Creek).

Figure 5.5. Mean slope of 50 m elevation bins derived from 10 m DEM plotted against elevation for the Big Tujunga Creek catchment. Bars indicate mean slope for elevations 600-1000 m (dark bar, 33°), 1000-1550 m (medium bar, 27°), and 1550-2150 m (light bar, 23°).

Figure 5.6. Channel long profile for the main stem of Big Tujunga Creek (location shown by inset), showing three graded channel segments separated by two knickpoints (circles). Bedrock steps greater than 3 m are highlighted in red. Profile fits using equation (5.1) with reference concavity index of 0.45 are fit to the upper ($k_{sn} = 22$), middle ($k_{sn} = 64$), and lower ($k_{sn} = 80$) reaches of the profile. In contrast to typical predictions (e.g., Figure 5.2), the three channel segments are offset by large oversteepened reaches consisting of numerous bedrock steps.

Figure 5.7. Reconstructed long profiles of tributaries to the lower gorge of Big Tujunga Creek (note x-axis similar to Figure 5.6). Dotted lines show projections of tributary profiles approximately grading to the projected mainstem profile (thick dashed line). Thin dashed line highlights an intermediate level defined by numerous mapped strath terraces 30 m above the current channel (grey circles, Figure 5. 4c). Thick black lines indicate bedrock steps greater than 3 m in height.

Figure 5.8. Results of channel surveys along (a) Fox Creek, (b) Big Tujunga Creek, and (c) Chilao Creek. Surveyed long profiles are shown by black lines. Valley width measured from the 1 m LiDAR DEM (Figure 5.4a) is shown by white circles. Percent bedrock exposure in the channel bed is shown by gray circles. The vertical dashed line in (a) highlights the lithologic contact between granite and anorthosite shown in Figure 5.3b. Black circles in (b) indicate field measurements of channel width averaged over 100 m to highlight reaches where valley width and bankfull channel width are equal (usually corresponding to bedrock lined channels).

Figure 5.9. Plot of channel steepness index against catchment averaged erosion rate for the San Gabriel Mountains. Horizontal error bars indicate 5% uncertainty in production rate added to 1σ analytical uncertainty in erosion rates. Vertical error bars indicate estimated uncertainty in k_{sn} as described by *DiBiase et al.* [2010]. Black line shows fit through erosion rate data using the stochastic threshold model described by *DiBiase et al.* [in review].

Figure 5.1

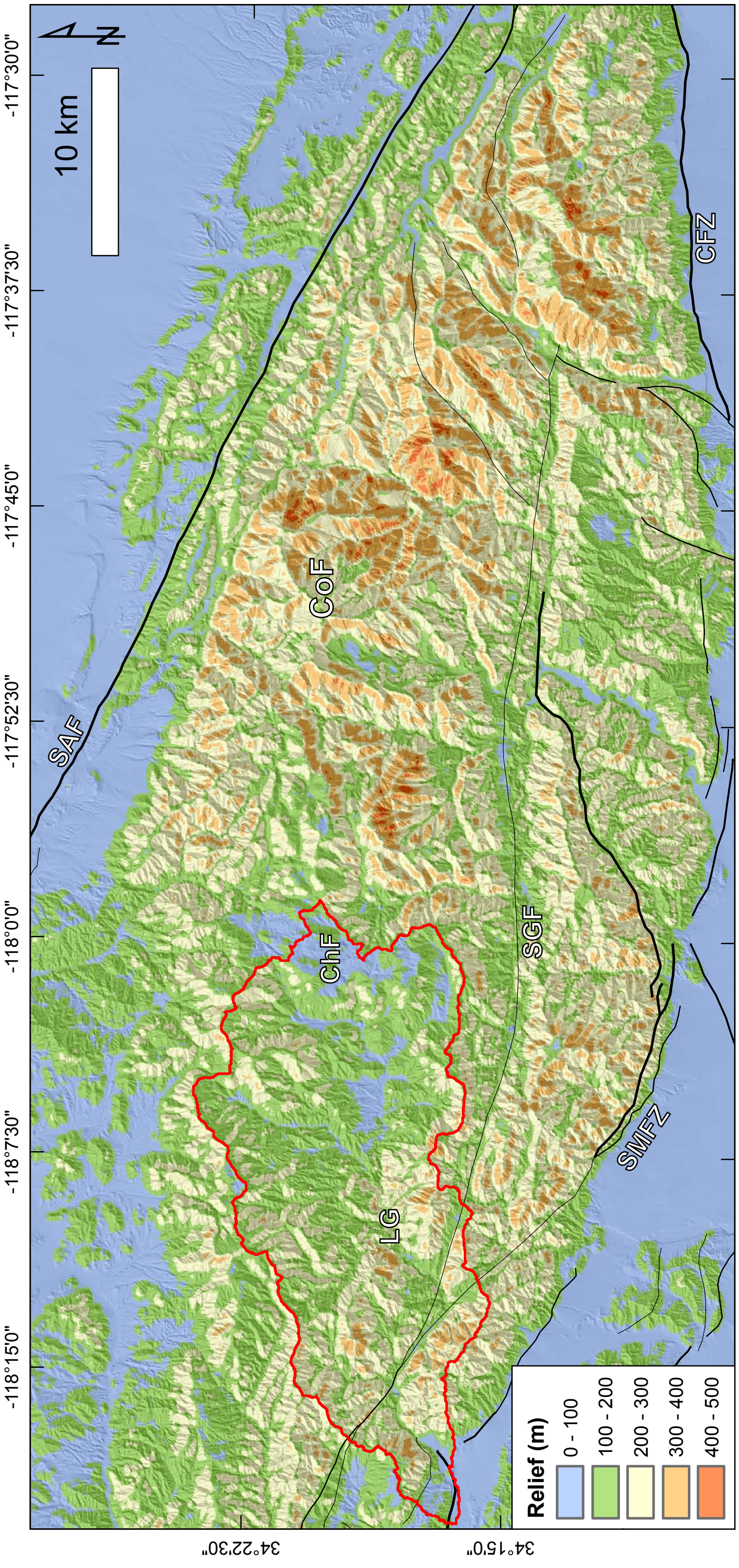
N
10 km
-117°30'0"
-117°37'30"
-117°45'0"
-117°52'30"
-118°0'0"
-118°7'30"
-118°15'0"
34°22'30"
34°15'0"
SAF
CFZ
CoF
ChF
SGF
LG
SMFZ
Relief (m)
0 - 100
100 - 200
200 - 300
300 - 400
400 - 500

Figure 5.2

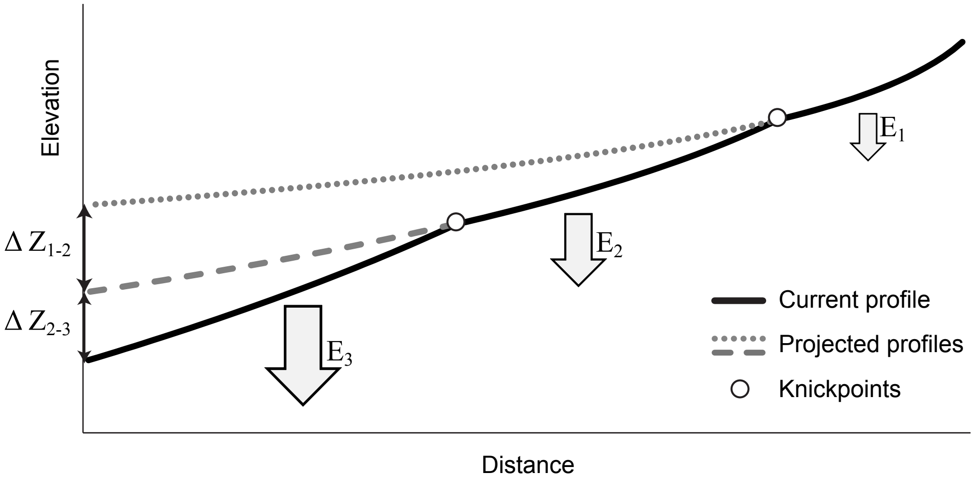
Elevation
Distance
Δ Z1-2
Δ Z2-3
E1
E2
E3
Current profile
Projected profiles
Knickpoints

Figure 5.3

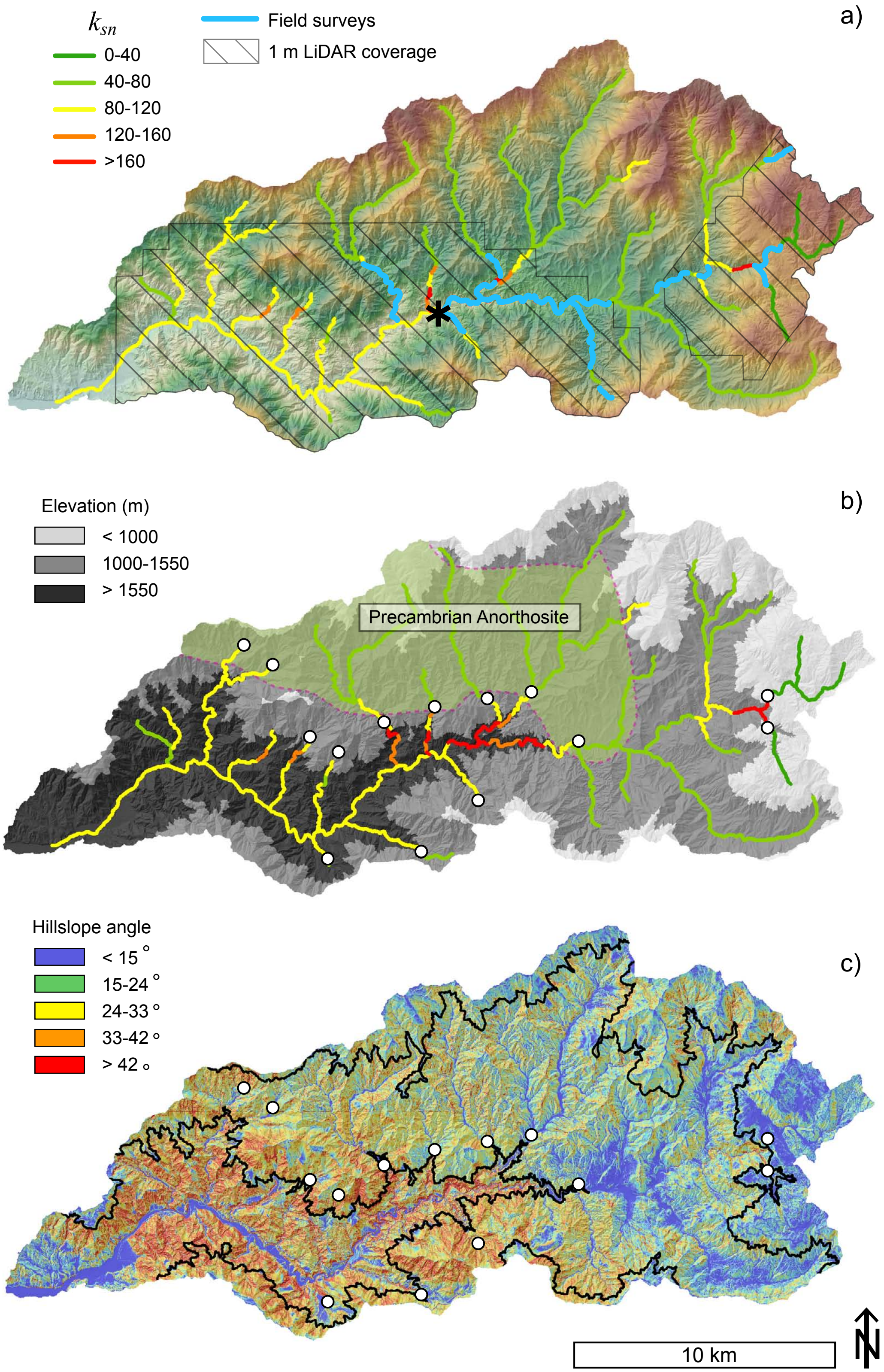

a)
k_{sn}
0-40
40-80
80-120
120-160
>160
Field surveys
1 m LiDAR coverage
b)
Elevation (m)
< 1000
1000-1550
> 1550
Precambrian Anorthosite
Hillslope angle
< 15 °
15-24 °
24-33 °
33-42 °
> 42 °
c)
10 km
N

Figure 5.4

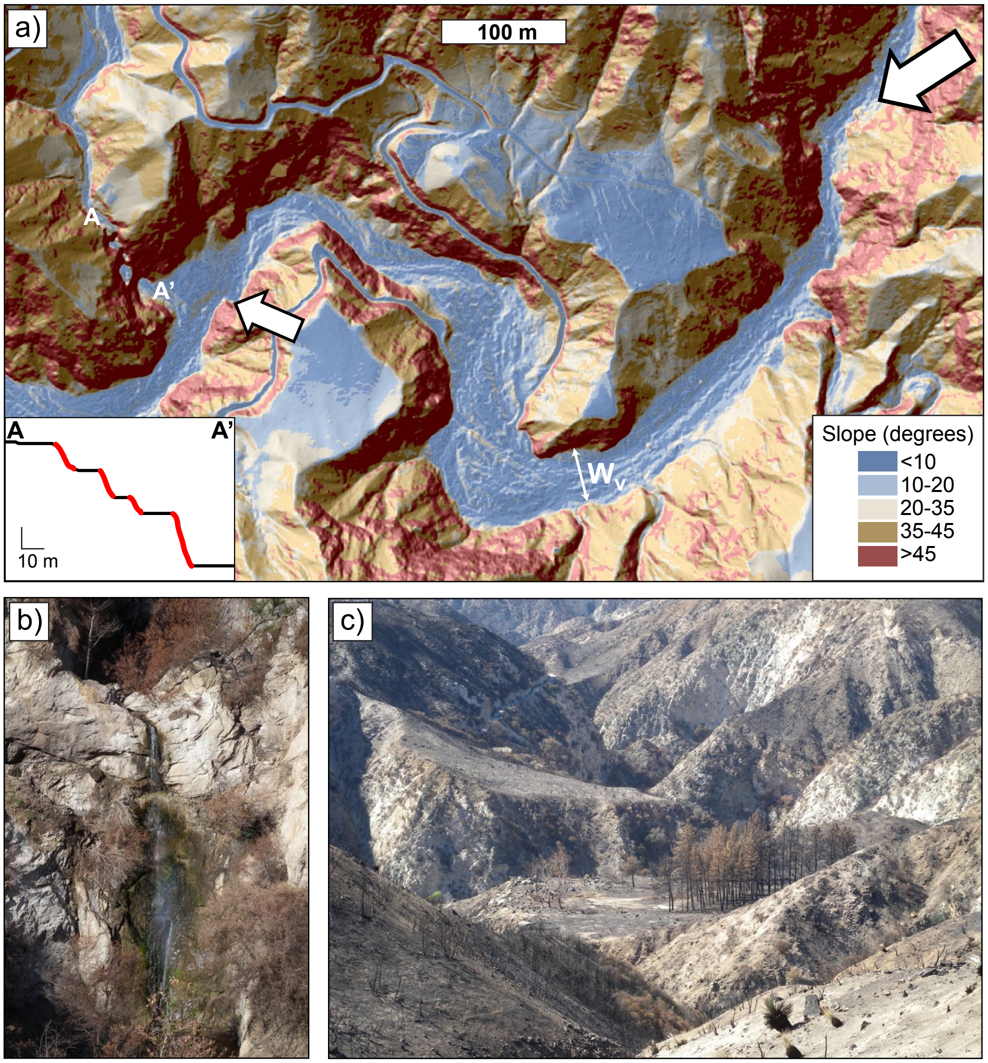

Figure 5.5

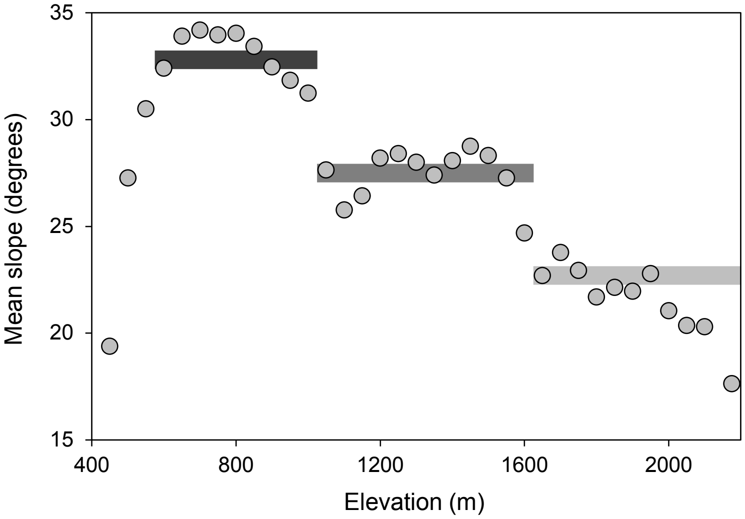
35
30
25
20
15
Mean slope (degrees)
400
800
1200
1600
2000
Elevation (m)

Figure 5.6

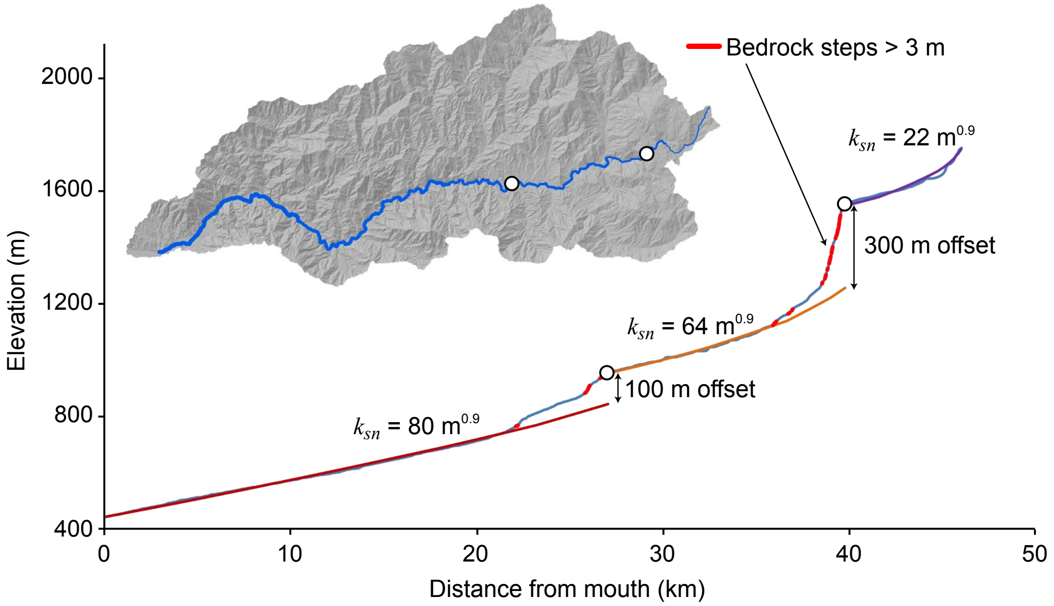
Bedrock steps > 3 m
k_{sn} = 22 m$^{0.9}$
300 m offset
k_{sn} = 64 m$^{0.9}$
100 m offset
k_{sn} = 80 m$^{0.9}$
Elevation (m)
2000
1600
1200
800
400
0
10
20
30
40
50
Distance from mouth (km)

Figure 5.7

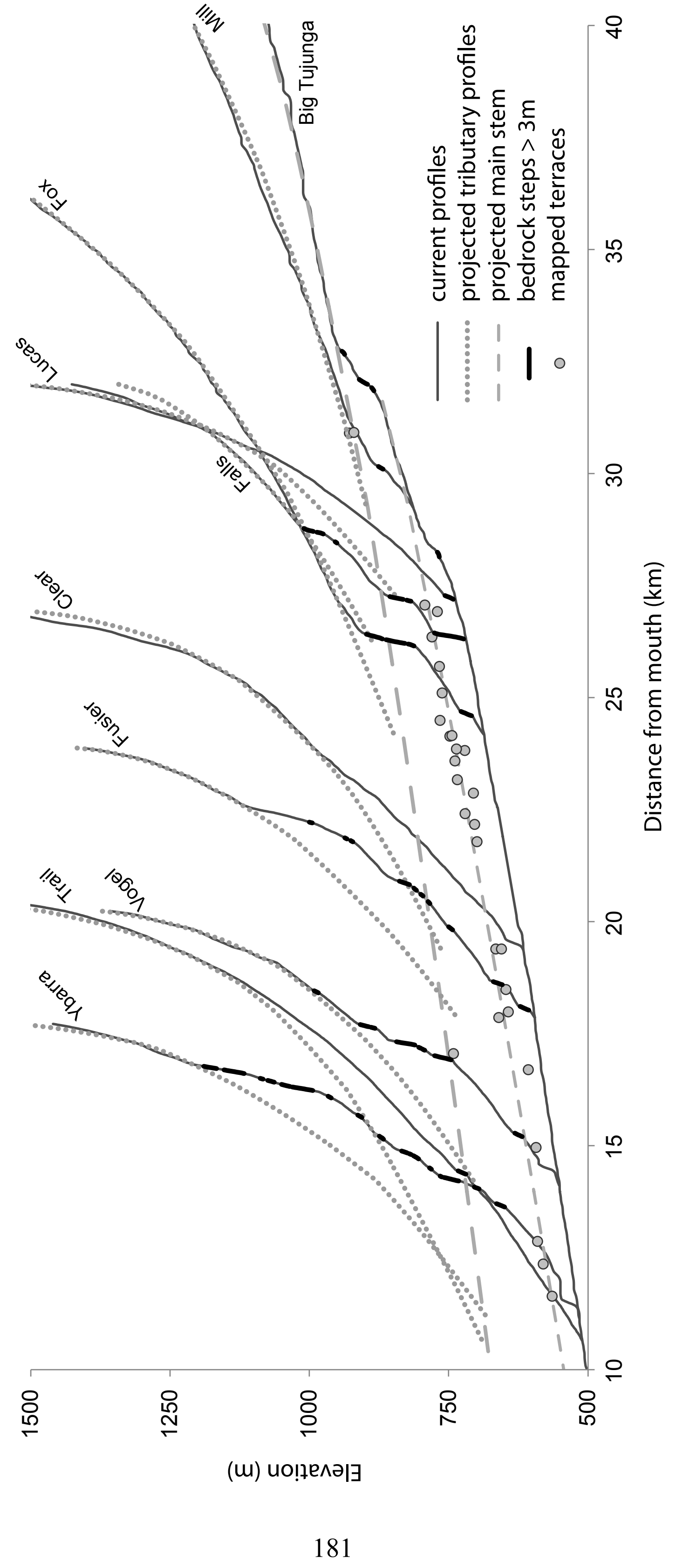
Elevation (m)
1500
1250
1000
750
500
Distance from mouth (km)
10
15
20
25
30
35
40
Ybarra
Trail
Vogel
Fusier
Clear
Lucas
Falls
Fox
Mill
Big Tujunga
current profiles
projected tributary profiles
projected main stem
bedrock steps > 3m
mapped terraces

Figure 5.8

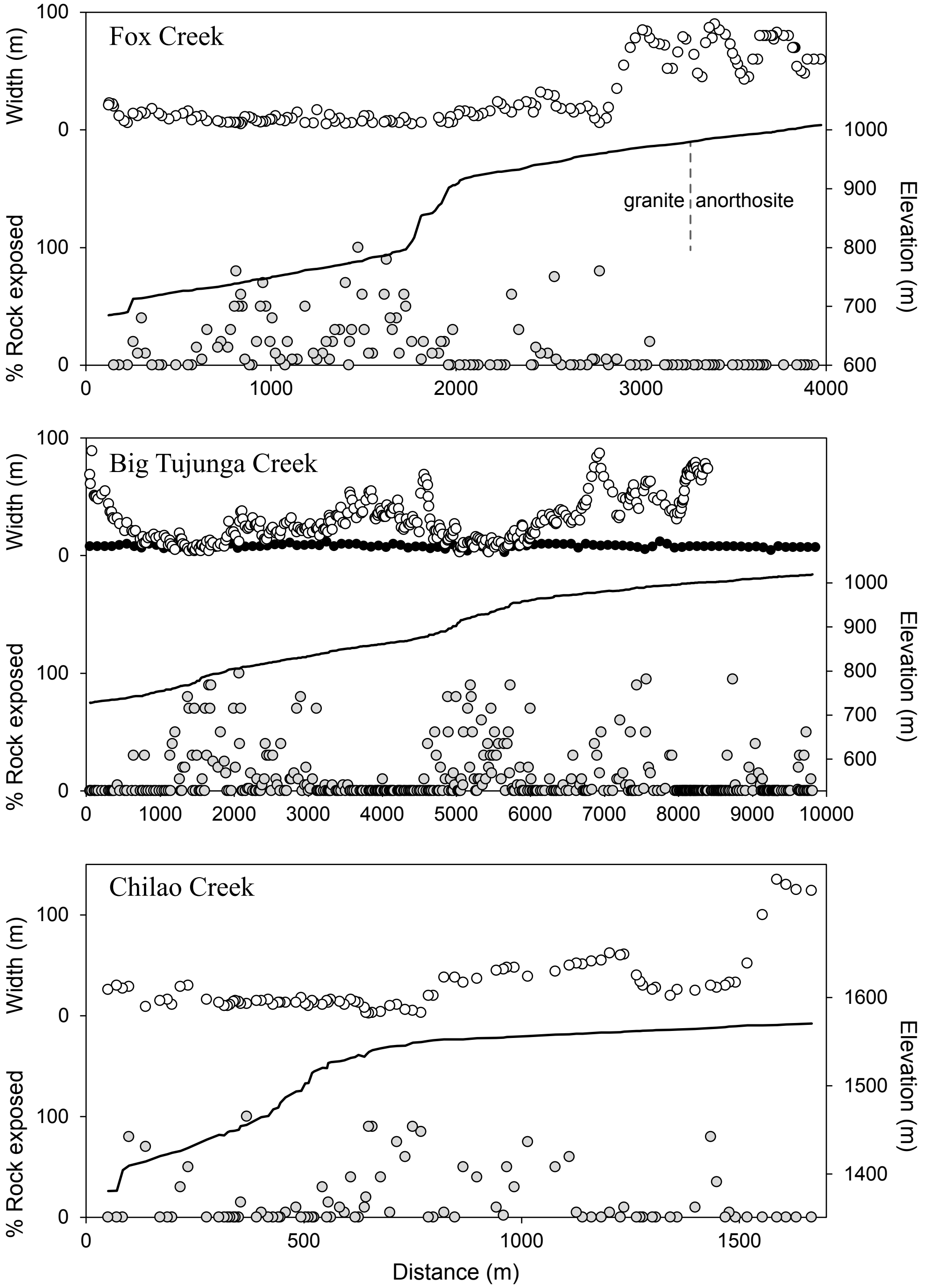

Fox Creek
Width (m)
100
0
% Rock exposed
100
0
granite
anorthosite
Elevation (m)
1000
900
800
700
600
0
1000
2000
3000
4000
Big Tujunga Creek
Width (m)
100
0
% Rock exposed
100
0
Elevation (m)
1000
900
800
700
600
0
1000
2000
3000
4000
5000
6000
7000
8000
9000
10000
Chilao Creek
Width (m)
100
0
% Rock exposed
100
0
Elevation (m)
1600
1500
1400
0
500
1000
1500
Distance (m)

Figure 5.9

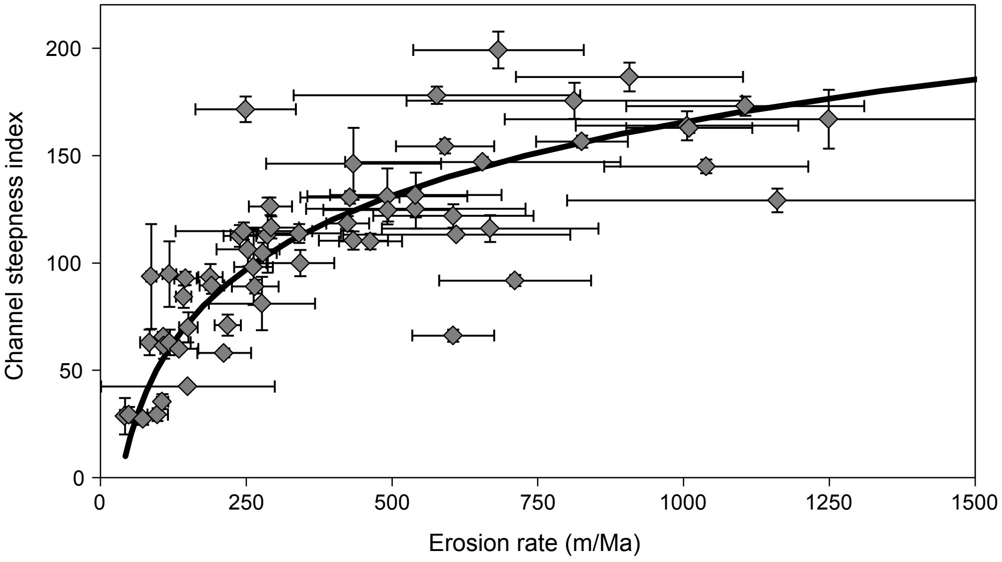
Channel steepness index
0
50
100
150
200
0
250
500
750
1000
1250
1500
Erosion rate (m/Ma)

CHAPTER 6

SYNTHESIS

This study presents a quantitative analysis of the surface processes acting to erode the San Gabriel Mountains of California. Here I summarize the main findings from this research and identify directions for further work.

DISTRIBUTION OF EROSION RATES IN THE SGM

As presented in Chapters 2, 3, and 5, and summarized in Appendix B, we quantified 80 catchment-averaged erosion rates using ^{10}Be concentrations in stream sands from across the San Gabriel Mountains (SGM). These data, in conjunction with nearly 60 point measurements of soil production rates [*Heimsath et al.*, in press], provide one of the most comprehensive collections of long term erosion rates to date, and set the framework for the interpretations described below. Erosion rates in the SGM range from 0.03 to 1.1 mm/a, and generally increase from west to east, with two notable exceptions. First, the lowest erosion rates come from an elevated low relief surface in the central SGM (Chilao Flats, Figure 5.1). As discussed in Chapter 5, we interpreted this surface to be a remnant of pre-uplift SGM topography that remains disconnected from active baselevel fall at the range front. The second exception to the west-east trend in erosion rates occurs in the western front range of the SGM, from Arroyo Seco to Santa Anita Creek. Erosion rates from these catchments rival those measured in the San Gabriel River, but although mean hillslope angle is similar between these regions, the channel steepness index of the front range streams is significantly lower (~100 $m^{0.9}$ vs 175 $m^{0.9}$). We offered two potential explanations for the accelerated erosion rates observed in these catchments. First, increased fire frequency in the 20th century [*Lavé and Burbank*, 2004] may be influencing our erosion rate measurements, even though these rates are averaged over thousands of years. Second, slight differences in the flood frequency distribution (Figure 4.4) may result in erosion thresholds being exceeded more frequently. Nonetheless, Figure 5.9 reflects one of the most robust relationships between topography and erosion rate found to date. The scatter in Figure 5.9 likely reflects differences in rock strength, climatic variables, and inherent variations in stochastic erosion processes. Finally, the erosion rate data from this study suggest that detrital CRN rates in rapidly eroding catchments are less sensitive to issues of mass wasting and fluvial mixing than previously thought. We found no relationship between erosion rate and catchment area in our data (Figure 2.5), and catchments as small as 3 km^2 appear to provide robust estimates of erosion rate, in contrast to predictions based on landslide models by *Niemi et al.* [2005] and *Yanites et al.* [2009].

HILLSLOPE PROCESS AND FORM

Chapter 2 presents a quantitative analysis of the relationship between mean hillslope angle and erosion rate in the SGM using a 10 m digital elevation model (DEM). We found that for catchment-averaged erosion rates below ~0.3 mm/a, mean hillslope angle increases roughly linearly with erosion rate. For basins eroding more rapidly, mean slope stays approximately constant (~36-38°). This relationship is consistent with, but not unique to, the relationship between mean slope and erosion rate predicted by the non-linear hillslope transport model of *Roering et al.* [1999]. We concluded in Chapter 2 that, as found in similar studies of hillslope angle and erosion rate [e.g., *Binnie et al.*, 2007; *Montgomery and Brandon*, 2002; *Ouimet et al.*, 2009], the achievement of threshold slope angles due to limits in rock strength [e.g., *Schmidt and Montgomery,* 1995] appears to decouple hillslope form from erosion rate in steep landscapes.

However, in Chapter 3 we used a LiDAR-derived, high resolution (1 m) DEM to show that hillslopes do indeed preserve signals of tectonic forcing in threshold landscapes. The increase in observation scale afforded by the 1 m DEM (compared to 10- and 30 m DEMs typically used for such analysis), along with a series of high-resolution (1 cm) panoramic field photographs, enabled a closer examination of the transition from soil mantled to rocky landscapes in the SGM. We noticed in the field that areas of locally high slope on the 1 m DEM tended to correspond to rocky outcrops on hillsides. To quantitatively test this, we calibrated a slope-based rock exposure index to independently map bedrock exposure, and found excellent agreement between percent local slopes greater than 45° and percent exposed rock (over scales of ~100 m).

We used 20 small (~3 km^2) catchments where we have both estimates of erosion rate and 1 m LiDAR data to quantitatively evaluate the changes in hillslope texture and form across a gradient in erosion rate from 0.3 – 1.1 mm/a. In contrast to conclusions based on coarser analysis using 10 m topography data and larger basins, we found a monotonic relationship between mean slope and erosion rate, though a kink at ca. 300 m/Ma indicates a decrease in the sensitivity of slope for high erosion rates. Rock exposure, as quantified by the metric described above, increases linearly with erosion rate for catchments eroding more rapidly than ~300 m/Ma. Below this rate, hillslopes tend to be entirely soil mantled. Furthermore, we used slope-area plots and maps of total catchment area to investigate how drainage density varies with erosion rate. We found that as erosion rates increase, the extent of the fluvial network decreases, while colluvial channels extend downstream. This competition acts to keep the total drainage density (and equivalently mean hillslope length) similar across the SGM.

Thus, the above analysis reveals important textural details lost in 10 or 30 m resolution DEMs of steep landscapes, and reinforces the need for process-based studies of threshold hillslopes and colluvial channels.

CHANNEL PROCESS AND FORM

One of the fundamental results from this study is our quantification of the relationship between channel steepness index and erosion rate for steady-state catchments in the SGM. We show in Chapter 2 that the channel steepness index serves as a scale-independent metric of fluvial relief that can furthermore be tied directly to channel incision models [c.f., *Wobus et al.*, 2006]. The relationship between channel steepness and erosion rate is non-linear, approximating a power law with exponent ϕ ~ 0.5 (equation (4.1)) which implies that channels become more efficient as they steepen. We focused on four potential mechanisms that could lead to this form: (1) orographic precipitation gradients may lead to increasing erosional efficiency with relief [e.g., *Roe et al.*, 2002]; (2) channels may narrow as they steepen [e.g., *Finnegan et al.*, 2005]; (3) the mechanics of bedrock incision may be non-linear with shear stress [e.g., *Whipple et al.*, 2000]; or (4) thresholds of erosion preferentially retard the incision of low-slope channels [e.g., *Lague et al.*, 2005; *Tucker*, 2004].

Using detailed channel surveys where we measured channel geometry and bed state, along with analyzing decadal precipitation and stream-flow records, we concluded in Chapter 4 that the first 3 effects are unlikely to be significant enough to generate the observed non-linear relationship between channel steepness and erosion rate. Rather, the nature of the relationship between steady-state channel steepness and erosion rate can be explained using a simple bedrock incision model. This model incorporates both an erosion threshold and a probability distribution function of large floods that follows an inverse power-law scaling [*Lague et al.*, 2005].

Starting from this case, we explored the influence of changing mean runoff and variability on the modeled relationship between channel steepness and erosion rate. For the range of parameter space tested, erosion rates increase with both increasing mean runoff and increasing discharge variability. We used an empirical relationship between discharge mean and variability [*Molnar et al.*, 2006] to test whether dry, variable climates can be more efficient than wet, stable climates. We showed that for channels with a high erosion threshold (or alternatively low steepness) a peak exists in erosional efficiency that lies near a mean runoff of 200-400 mm/a. Furthermore, erosion rates are predicted to be insensitive to increases in runoff above ~500 mm/a.

In Chapter 5, we used the example of Big Tujunga Creek to study the transient behavior of bedrock channels in the SGM responding to what we infer to be increases in rock uplift rate. Detailed channel surveys across knickpoints demonstrated behavior seen in many other landscapes [e.g., *Berlin and Anderson*, 2009; *Crosby and Whipple*, 2006; *Haviv et al.*, 2006]. Just upstream of knickpoints (~10^2 m), channels tend to steepen, sediment cover decreases, and valleys narrow to approximately bankfull channel width (Figure 5.8). In the SGM, as elsewhere, often times knickpoints are characterized not only by a break in regional slope, but also a break in elevation in the form of discrete waterfalls [e.g., *Haviv et al.*, 2010]. Indeed, there are many examples of extensive (up to 300 m of elevation drop) oversteepened zones downstream of knickpoints in Big Tujunga Creek, consisting mainly of bedrock steps larger than 3 m. Furthermore, these oversteepened zones are not constrained to tributary junctions (e.g., hanging valleys), and are not easily reproduced by existing bedrock incision models. Rather, we interpreted that these oversteepenings arise due to local variation in rock strength, and grow and persist due to negative feedbacks between slope and erosion rate present in some sediment-flux dependent incision models [e.g., *Crosby et al.*, 2007]. This interpretation is further supported by the enhancement of these oversteepenings below knickpoints draining relict surfaces with low coarse sediment supply.

TECTONIC IMPLICATIONS

In Chapter 5, we reconstructed relict stream profiles in Big Tujunga Creek and used measures of erosion rate (both direct and inferred) to estimate the timing of a two-staged increase in the rate of baselevel fall. This two-staged increase in baselevel fall, which we attribute to increasing vertical slip rate along the southern range-bounding thrust faults, resulted in the propagation of two waves of knickpoints through Big Tujunga Creek. The upper knickpoints have nearly swept through the landscape, but are retained on two tributaries near elevations of 1550 m, above which lies the relict surface of Chilao Flats. The lower knickpoints separate a predominantly soil-mantled, slowly eroding landscape from a dramatic inner gorge along the main stem of Big Tujunga Creek, with the boundary between the two landscapes lying near the 1000 m elevation contour. Based on our reconstructions, we interpreted the age of the upper knickpoint-forming event to be 7-9 Ma, suggesting that Chilao Flats represents the pre-uplift topography of the SGM. This knickpoint was likely generated by the switch from predominantly strike slip motion along the San Gabriel Fault (~6-12 Ma) to thrust faulting along the Sierra Madre Fault (~7 Ma to present) [*Blythe et al.*, 2002; *Matti and Morton*, 1993]. The younger knickpoint-forming event dates to ca. 1-2 Ma, but the mechanism for a change in uplift pattern is unclear. The age of the younger event was coeval with the estimated initiation age of the right-lateral San Jacinto Fault, which then began accumulating strain formerly accommodated by the San Andreas Fault [e.g., *Blisniuk et al.*, 2010; *Kirby et al.*, 2007]. However, while the initiation of the San Jacinto Fault has been used to explain recent increases in uplift rate of the nearby San Bernardino Mountains [*Spotila et al.*, 1998], the influence of this westward-stepping of strain accumulation on the uplift pattern in the SGM is unclear.

Our results from Chapter 4 have broader implications for the dynamic coupling of climate and tectonics. In particular, we showed that two behaviors emerge from our modeling results that have the potential to greatly weaken the influence of climatically driven increases in rock uplift rate for compressional orogens. First, the prediction of a non-linear relationship between channel steepness and erosion rate ($\phi < 1$, equation (4.1)), along with our observation of $\phi \sim 0.5$ in the SGM, suggests a weaker dependence of rock uplift rate on erosional efficiency than typically assumed [e.g., *Whipple and Meade*, 2004]. Second, and perhaps more importantly, we showed that if increases in mean runoff are offset by decreases in flow variability [e.g., *Molnar et al.*, 2006], then the sensitivity of erosion rate to climate is greatly reduced.

FUTURE WORK

The erosion rate dataset presented above, and used throughout this dissertation, provides a solid foundation for further studies related to surface processes in the SGM. In particular, the gradient in erosion rates, soil production rates, hillslope form, and soil cover enables a test of how chemical denudation varies as a function of physical erosion rate. This relationship has been the focus of a number of recent theoretical treatments [e.g., *Ferrier and Kirchner*, 2008; *Hilley et al.*, 2010], and field studies in soil mantled landscapes [e.g., *Dixon et al.*, 2009; *Riebe et al.*, 2001], but the role of chemical weathering in denuding or weakening steep, rocky landscapes has yet to be tested.

Second, the 2009 Station fire burned much of the range, providing an opportunity to study the influences of fire on soil transport rates, critical hillslope angle, and sediment delivery to channels in an area where long term rates are well constrained. Finally, the tectonic story presented in Chapter 5 can be greatly supplemented by kinematic modeling of southern California faults to test whether the transfer of slip from the San Andreas Fault to the San Jacinto Fault results in increased vertical slip rates along the Sierra Madre and Cucamonga thrust systems. Additionally, although the general thermal history of the SGM was investigated by *Spotila et al.* [1998] and *Blythe et al.* [2000], a series of thermochronologic samples along targeted elevation transects would greatly aid our interpretations of uplift history based on the topographic analysis presented in Chapter 5.

REFERENCES

Berlin, M. M., and R. S. Anderson (2009), Steepened channels upstream of knickpoints: Controls on relict landscape response, *Journal of Geophysical Research*, *114*, F03018, doi:10.1029/2008jf001148.

Binnie, S. A., W. M. Phillips, M. A. Summerfield, and L. K. Fifield (2007), Tectonic uplift, threshold hillslopes, and denudation rates in a developing mountain range, *Geology*, *35*(8), 743.

Blisniuk, K., T. Rockwell, L. A. Owen, M. Oskin, C. Lippincott, M. W. Caffee, and J. Dortch (2010), Late Quaternary slip rate gradient defined using high-resolution topography and (10)Be dating of offset landforms on the southern San Jacinto Fault zone, California, *Journal of Geophysical Research-Solid Earth*, *115*, B08401, doi:10.1029/2009jb006346.

Blythe, A., M. A. House, and J. A. Spotila (2002), Low temperature thermochronology of the San Gabriel and San Bernadino Mountains, southern California: Constraining structural evolution, in *Contributions to Structural Evolution of the Southwestern United States: Geological Society of America Special Paper*, edited by A. P. Barth, pp. 231-250, Boulder, Colorado.

Blythe, A. E., D. W. Burbank, K. A. Farley, and E. J. Fielding (2000), Structural and topographic evolution of the central Transverse Ranges, California, from apatite fission-track, (U-Th)/He and digital elevation model analyses, *Basin Research*, *12*, 97-114.

Crosby, B. T., and K. X. Whipple (2006), Knickpoint initiation and distribution within fluvial networks: 236 waterfalls in the Waipaoa River, North Island, New Zealand, *Geomorphology*, *82*(1-2), 16-38.

Crosby, B. T., K. X. Whipple, N. M. Gasparini, and C. W. Wobus (2007), Formation of fluvial hanging valleys: Theory and simulation, *Journal of Geophysical Research*, *112*, F03S10, doi:10.1029/2006JF000566.

Dixon, J. L., A. M. Heimsath, and R. Amundson (2009), The critical role of climate and saprolite weathering in landscape evolution, *Earth Surface Processes and Landforms*, *34*(11), 1507-1521, 10.1002/esp.1836.

Ferrier, K. L., and J. W. Kirchner (2008), Effects of physical erosion on chemical denudation rates: A numerical modeling study of soil-mantled hillslopes, *Earth and Planetary Science Letters*, *272*(3-4), 591-599, 10.1016/j.epsl.2008.05.024.

Finnegan, N. J., G. Roe, D. R. Montgomery, and B. Hallet (2005), Controls on the channel width of rivers: Implications for modeling fluvial incision of bedrock, *Geology*, *33*(3), 229-232.

Haviv, I., Y. Enzel, K. X. Whipple, E. Zilberman, J. Stone, A. Matmon, and L. K. Fifield (2006), Amplified erosion above waterfalls and oversteepened bedrock reaches, *Journal of Geophysical Research-Earth Surface*, *111*(F4), F04004, doi:10.1029/2006jf000461.

Haviv, I., Y. Enzel, K. X. Whipple, E. Zilberman, A. Matmon, J. Stone, and K. L. Fifield (2010), Evolution of vertical knickpoints (waterfalls) with resistant caprock: Insights from numerical modeling, *Journal of Geophysical Research*, *115*, F03028, doi:10.1029/2008jf001187.

Heimsath, A. M., R. A. DiBiase, and K. X. Whipple (in press), Soil production limits and the transition to bedrock dominated landscapes, *Nature Geoscience*.

Hilley, G. E., C. P. Chamberlain, S. Moon, S. Porder, and S. D. Willett (2010), Competition between erosion and reaction kinetics in controlling silicate-weathering rates, *Earth and Planetary Science Letters*, *293*(1-2), 191-199, 10.1016/j.epsl.2010.01.008.

Kirby, S. M., S. U. Janecke, R. J. Dorsey, B. A. Housen, V. E. Langenheim, K. A. McDougall, and A. N. Steely (2007), Pleistocene brawley and ocotillo formations: Evidence for initial strike-slip deformation along the San Felipe and San Jacinto fault zones, southern California, *Journal of Geology*, *115*(1), 42-62.

Lague, D., N. Hovius, and P. Davy (2005), Discharge, discharge variability, and the bedrock channel profile, *Journal of Geophysical Research*, *110*(F04006), doi:10.1029/2004JF000259.

Lavé, J., and D. W. Burbank (2004), Denudation processes and rates in the Transverse Ranges, southern California: Erosional response of a transitional landscape to external and anthropogenic forcing, *Journal of Geophysical Research*, *109*, F01006.

Matti, J. C., and D. M. Morton (1993), Paleogeographic evolution of the San Andreas fault in southern California: A reconstruction based on a new cross-fault correlation, *Geological Society of America Memoir 178*, 107-159.

Molnar, P., R. S. Anderson, G. Kier, and J. Rose (2006), Relationships among probability distributions of stream discharges in floods, climate, bed load transport, and river incision, *Journal of Geophysical Research-Earth Surface*, *111*, F02001, doi:10.1029/2005JF000310.

Montgomery, D. R., and M. T. Brandon (2002), Topographic controls on erosion rates in tectonically active mountain ranges, *Earth and Planetary Science Letters*, *201*(3-4), 481-489.

Niemi, N. A., M. Oskin, D. W. Burbank, A. J. M. Heimsath, and E. J. Gabet (2005), Effects of bedrock landslides on cosmogenically determined erosion rates, *Earth and Planetary Science Letters*, *237*(3), 480-498.

Ouimet, W. B., K. X. Whipple, and D. E. Granger (2009), Beyond threshold hillslopes: Channel adjustment to base-level fall in tectonically active mountain ranges, *Geology*, *37*(7), 579-582.

Riebe, C. S., J. W. Kirchner, D. E. Granger, and R. C. Finkel (2001), Strong tectonic and weak climatic control of long-term chemical weathering rates, *Geology*, *29*(6), 511-514, 10.1130/0091-7613(2001)029<0511:stawcc>2.0.co;2.

Roe, G. H., D. R. Montgomery, and B. Hallet (2002), Effects of orographic precipitation variations on the concavity of steady-state river profiles, *Geology*, *30*(2), 143-146.

Roering, J. J., J. W. Kirchner, and W. E. Dietrich (1999), Evidence for nonlinear, diffusive sediment transport on hillslopes and implications for landscape morphology, *Water Resources Research, 35*(3), 853-870.

Schmidt, K. M., and D. R. Montgomery (1995), Limits to relief, *Science*, *270*(5236), 617-620.

Spotila, J. A., K. A. Farley, and K. Sieh (1998), Uplift and erosion of the San Bernardino Mountains associated with transpression along the San Andreas fault, California, as constrained by radiogenic helium thermochronometry, *Tectonics*, *17*(3), 360-378.

Tucker, G. E. (2004), Drainage basin sensitivity to tectonic and climatic forcing: Implications of a stochastic model for the role of entrainment and erosion thresholds, *Earth Surface Processes and Landforms*, *29*, 185-205.

Whipple, K. X., and B. J. Meade (2004), Controls on the strength of coupling among climate, erosion, and deformation in two-sided, frictional orogenic wedges at steady state, *Journal of Geophysical Research-Earth Surface*, *109*, F01011, doi:10.1029/2003JF000019.

Whipple, K. X., G. S. Hancock, and R. S. Anderson (2000), River incision into bedrock: Mechanics and relative efficacy of plucking, abrasion, and cavitation, *Geological Society of America Bulletin*, *112*(3), 490-503.

Wobus, C., K. X. Whipple, E. Kirby, N. Snyder, J. Johnson, K. Spyropolou, B. Crosby, and D. Sheehan (2006), Tectonics from topography: Procedures, promise, and pitfalls, *Geological Society of America Special Paper 398*, 55-74.

Yanites, B. J., G. E. Tucker, and R. S. Anderson (2009), Numerical and analytical models of cosmogenic radionuclide dynamics in landslide-dominated drainage basins, *Journal of Geophysical Research*, *114*, F01007, doi:10.1029/2008JF001088.

APPENDIX A

CHAPTER 4 SUPPLEMENTARY:

CROSS-SECTIONAL FLOW MODELING OF AT-A-STATION SHEAR STRESS-DISCHARGE RELATIONSHIP

The standard formulation for bed shear stress (equation (4.3)) combines a steady, uniform flow approximation for a wide channel with a cross-section averaged frictional resistance relationship [e.g. , *Howard*, 1994]. In addition, hydraulic geometry relations are often used to model downstream and at-a-station variations in channel width with water discharge (equations (4.4a, 4.4b)) [e.g. , *Tucker*, 2004]. Taken together, these define the relationship between discharge and bed shear stress (equation (4.5)) used in the stochastic-threshold models of *Tucker* [2004] and *Lague et al.* [2005] and discussed in the text. We argue on the basis of an analysis described below that the at-a-station exponent ($\alpha(1 - \omega_s)$) in equation (4.5) is best considered an effective model parameterization of the combined effects of channel geometry and frictional losses on channel bed and banks – its function in the model is to transform a *pdf* of flood discharges into a *pdf* of bed shear stresses. Thus while the exponent ω_s in equation (4.4b) varies strongly with channel geometry and can be measured in the field [e.g. , *Turowski et al.*, 2008], applying these results to equation (4.5) may not be appropriate due to the influence of frictional losses along channel banks, an effect ignored by the wide channel assumption built into equation (4.3), but that also varies with channel geometry and flow depth. Because it controls how flood magnitude translates into bed shear stress, the at-a-station exponent in equation (4.5) ($\alpha(1 - \omega_s)$) strongly influences the shape of the relationship between channel steepness and erosion rate (equation (4.11)).

To evaluate whether estimates of ω_s using equation (4.4b) provide reasonable approximations of how shear stress varies with discharge in a given cross-section, we used a 2D cross-sectional flow model [*Kean and Smith*, 2004] to measure the relationships among discharge, shear stress, and channel top width for a trapezoidal channel with varying bank angles. *Kean and Smith* [2004] extended the ray-isovel method of *Houjou et al.* [1990] to accommodate a range of cross sectional geometries. We use the simple case of a trapezoidal channel with a fixed basal width of 10 m, and vary bank angle from 20-85°. We fixed slope to 0.001, and z_0 to 0.008 m (for both bed and banks) for all runs. Fixed bed width, slope and roughness are selected because for this analysis only the at-a-station variability of discharge and the resulting bed shear stresses are of interest. Downstream variation in discharge and shear stress is unaffected, and we have confirmed that the effect of channel slope is well captured with the standard exponent, β, in equations (4.3 and 4.5). For each of 4 different bank angles, we ran 4-9 flows of increasing discharge. Flow depth and top width were output from each run, and width-to-depth ratios (w/d) ranged from ~3-30 for each bank angle. In addition, for each run, we measured the average boundary shear stress across the center 70% of the channel bed to minimize corner flow effects and for consistency with a channel incision model based on bed shear stress. We define 3 normalized variables for comparing the results of each geometry – Q^*, W^*, and τ^* – as the discharge, width, and average shear stress normalized by the low flow condition (chosen to have a reasonable width to depth ratio, w/d = 20-30).

Plotting W^* against Q^* enables a literal interpretation of ω_s, though it should be highlighted that the relationship clearly does not follow the power-law scaling described by equation (4.4b). Even so, we can estimate a value of ω_s by fitting a power-law for each geometry to generate a relationship between ω_s and bank angle. Although not entirely accurate, this approach nonetheless captures the general trend of ω_s decreasing to zero as bank angle approaches 90° (Figure A1), generally matching measurements at gage stations on Taiwanese rivers and associated cross-sectional flow analysis by *Turowski et al.* [2008].

We can evaluate the suitability of these estimates of ω_s for application to prediction the discharge-shear stress relationship by comparing data generated by the cross-sectional flow model to the expected relationship between Q^* and τ^* according to equation (5), with ω_s varying as in Figure A1. Figure A2 shows that the results from channel geometries with bank angle ranging from 20-85° follow similar scaling between Q^* and τ^*, in contrast to expectations using equation (4.5) with ω_s varying as a function of channel geometry. The slope of the data in log-log space is ~0.5, which corresponds to a constant, effective ω_s value of ~0.25 for $\alpha = 2/3$ as dictated by the cross-sectional flow model. This suggests geometrical effects and sidewall friction balance each other out approximately to keep the at-a-station exponent ($\alpha(1 - \omega_s)$) constant across a range of channel geometries. Thus to capture this behavior, we use a constant value of $\omega_s = 0.25$ for our analyses, but note that given the importance of the exponent ($\alpha(1 - \omega_s)$) to the k_s-E relationship, this problem deserves greater attention to better parameterize the issue of shear stress and channel width scaling in mountain channels.

REFERENCES

Houjou, K., Y. Shimizu, and C. Ishii (1990), Calculation of boundary shear stress in open channel flow, *Journal of Hydroscience and Hydraulic Engineering*, *8*(2), 21-37.

Howard, A. D. (1994), A detachment-limited model of drainage basin evolution, *Water Resources Research*, *30*(7), 2261-2285.

Kean, J. W., and J. D. Smith (2004), Flow and boundary shear stress in channels with woody bank vegetation, in *Riparian Vegetation and Fluvial Geomorphology, Water Science and Application 8*, edited by S. J. Bennett and A. Simon, pp. 237-252, AGU, Washington, D.C.

Lague, D., N. Hovius, and P. Davy (2005), Discharge, discharge variability, and the bedrock channel profile, *Journal of Geophysical Research*, *110*, F04006, doi:10.1029/2004JF000259.

Tucker, G. E. (2004), Drainage basin sensitivity to tectonic and climatic forcing: Implications of a stochastic model for the role of entrainment and erosion thresholds, *Earth Surface Processes and Landforms*, *29*, 185-205.

Turowski, J. M., N. Hovius, A. Wilson, and M. J. Horng (2008), Hydraulic geometry, river sediment and the definition of bedrock channels, *Geomorphology*, *99*(1-4), 26-38.

FIGURES

Figure A1. Plot of normalized channel width (*W**) against normalized discharge (*Q**) for channel cross-sectional flow model runs with varying bank angle θ. Solid line shows forced fit of equation (4.4b) to the case $\theta = 20°$, resulting in an effective ω_s value of 0.25. Inset shows dependence of effective ω_s on channel bank angle.

Figure A2. Plot of normalized bed shear stress (τ*) against normalized discharge (*Q**) for channel cross-sectional flow model runs with varying bank angle θ. Lines indicate expected relationship between τ* and *Q** assuming no bank friction. Instead, the relationship is similar for all cases, suggesting that the competing effects of channel widening and bank friction are balanced, and that the at-a-station discharge exponent $\alpha(1-\omega_s)$ holds constant near a value of 0.5, corresponding to $\omega_s = 0.25$.

Figure A1

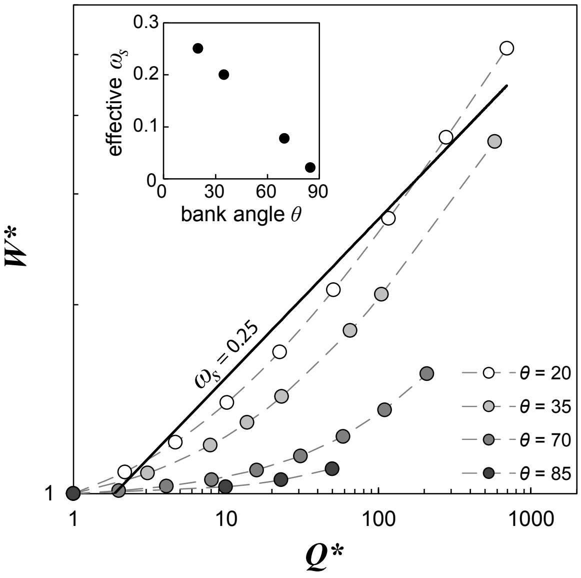
0.3
0.2
0.1
0
effective ω_s
0
30
60
90
bank angle θ
W*
$\omega_s = 0.25$
θ = 20
θ = 35
θ = 70
θ = 85
1
1
10
100
1000
Q*

Figure A2

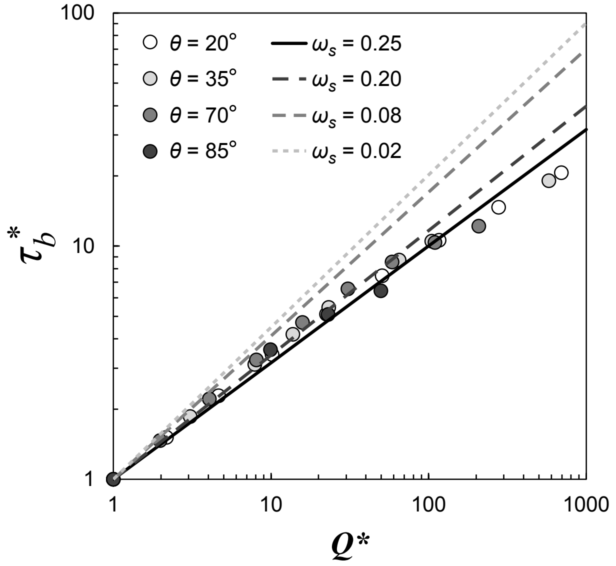

100
10
1
1
10
100
1000
τ_b^*
Q^*
θ = 20°
θ = 35°
θ = 70°
θ = 85°
ω_s = 0.25
ω_s = 0.20
ω_s = 0.08
ω_s = 0.02

APPENDIX B

CHAPTER 5 SUPPLEMENTARY: DETRITAL CRN SAMPLE BASIN LOCATION, MORPHOMETRY AND EROSION RATE DATA

Sample ID	Easting[a]	Northing[a]	Area (km^2)	^{10}Be/SiO$_2$ (x 10^3 atoms/g)	N(z,I)[b]	Erosion rate (m/Ma)[c]	k_{sn}	Mean slope (degrees)	Data source
SGB1	393590	3796490	174.7	73.21 ± 14.60	2.46	109 ± 27	62 ± 6	25.9	*DiBiase et al.,* 2010
SGB2	398070	3796470	102.0	69.03 ± 17.25	2.54	119 ± 36	63 ± 6	24.2	"
SGB3	396850	3797050	106.9	96.74 ± 13.99	2.52	84 ± 16	63 ± 6	24.0	"
SGB4	405576	3793270	6.0	244.33 ± 243.44	2.67	35 ± 37	43 ± 1	21.2	"
SGB5	396964	3799133	9.9	56.53 ± 10.86	2.37	135 ± 33	60 ± 1	27.2	"
SGB6	385052	3799080	9.7	29.39 ± 12.46	2.23	246 ± 117	115 ± 4	33.0	"
SGB7	394360	3795594	3.2	29.16 ± 4.74	2.27	253 ± 54	106 ± 8	34.4	"
SGB9	384501	3796261	17.3	15.33 ± 0.56	2.01	424 ± 37	118 ± 3	33.6	"
SGB10	389930	3793860	7.5	22.56 ± 0.76	1.94	279 ± 23	105 ± 5	32.1	"
SGB11	431950	3795090	82.5	14.82 ± 0.67	3.78	826 ± 79	157 ± 3	34.9	"
SGB12	429900	3789052	148.4	11.07 ± 0.63	3.45	1010 ± 108	163 ± 2	35.3	"
SGB13	431750	3795109	35.0	28.22 ± 1.84	3.80	436 ± 50	178 ± 4	35.2	"
SG116	406050	3793401	1.1	27.15 ± 2.54	2.64	314 ± 45	N/A	22.5	"
SG118	405531	3793280	6.0	33.18 ± 3.35	2.67	265 ± 32	43 ± 1	21.2	"
SG123	403550	3801480	3.2	93.68 ± 3.95	3.14	108 ± 10	66 ± 2	28.4	"
SG124	403580	3800022	0.4	52.55 ± 3.06	2.44	151 ± 16	70 ± 7	24.2	"
SG125	400471	3785950	2.0	16.14 ± 1.32	2.32	465 ± 61	N/A	33.6	"
SG126	400230	3786700	2.3	12.94 ± 0.90	2.36	591 ± 71	N/A	36.4	"
SG127	400100	3786719	2.6	10.26 ± 0.87	2.33	736 ± 99	N/A	39.1	"
SG128	407130	3799908	2.1	250.69 ± 20.68	3.25	42 ± 6	29 ± 8	12.9	"
SG129	406977	3800170	0.14	213.83 ± 57.30	3.24	49 ± 16	29 ± 4	16.0	"
SG130	408940	3804594	0.29	138.47 ± 9.04	3.12	73 ± 8	27 ± 3	25.5	"
SG131	408762	3802978	2.3	102.88 ± 12.70	3.13	98 ± 17	29 ± 3	14.9	"
SG132	409009	3802950	1.1	94.48 ± 4.54	3.10	106 ± 10	35 ± 4	16.8	"
SG136	427489	3798670	0.11	103.09 ± 4.45	4.60	144 ± 13	N/A	24.4	"
SG137	418150	3792511	46.8	15.05 ± 1.40	2.75	591 ± 84	154 ± 3	34.6	"
SG138	417980	3792440	17.9	18.65 ± 2.75	2.47	428 ± 85	131 ± 3	35.7	"

Sample ID	Easting[a]	Northing[a]	Area (km^2)	^{10}Be/SiO$_2$ (x 10^3 atoms/g)	N(z,I)[b]	Erosion rate (m/Ma)[c]	k_{sn}	Mean slope (degrees)	Data source
SG140	412561	3789280	7.7	32.49 ± 1.99	1.89	189 ± 21	93 ± 6	29.9	*DiBiase et al.,* 2010
SG141	410390	3790543	43.1	30.45 ± 2.38	2.74	292 ± 37	126 ± 4	30.2	"
SG150	405510	3793789	0.02	23.82 ± 2.57	2.38	323 ± 51	N/A	13.3	"
SG151	426461	3797780	3.5	34.82 ± 10.27	4.67	434 ± 150	146 ± 17	31.2	"
SG152	426300	3798089	2.1	199.29 ± 9.52	4.85	79 ± 8	N/A	31.4	"
SG157	432789	3796090	25.4	11.68 ± 1.57	3.99	1106 ± 204	173 ± 5	35.0	"
SG158	432614	3796111	53.2	11.68 ± 1.39	3.75	1039 ± 175	145 ± 3	34.4	"
SG159	431831	3795020	35.0	17.15 ± 1.67	3.80	717 ± 106	178 ± 4	35.2	"
SG161	429939	3795791	11.6	12.03 ± 1.69	3.74	1006 ± 191	164 ± 7	36.0	"
SG162	441441	3780431	28.0	33.69 ± 4.63	2.91	279 ± 52	172 ± 6	35.9	"
SG163	441440	3780432	28.0	43.13 ± 2.83	2.91	218 ± 25	172 ± 6	35.9	"
SG204	408889	3802380	0.08	16.00 ± 2.18	3.05	617 ± 115	N/A	10.2	"
SG205	408780	3802535	0.12	89.34 ± 5.77	3.03	110 ± 13	N/A	10.6	"
SG206	427120	3787967	5.4	18.56 ± 5.21	1.59	277 ± 91	81 ± 12	32.2	"
SG207	425810	3788950	6.5	23.04 ± 2.33	1.89	265 ± 40	89 ± 3	35.1	"
SG0701	408768	3802844	0.19	81.27 ± 3.49	2.99	119 ± 11	N/A	10.3	"
SG0702	405524	3804763	0.18	167.58 ± 8.31	4.03	78 ± 8	N/A	20.8	"
SG0703	398617	3796775	9.9	12.54 ± 0.83	2.34	605 ± 70	66 ± 3	30.1	"
SG0728	417222	3802455	9.1	110.91 ± 6.08	4.05	118 ± 12	95 ± 15	24.6	"
SG0729	416848	3802226	5.3	155.05 ± 7.65	4.16	87 ± 9	94 ± 24	23.9	"
SG0730	393010	3706541	5.7	11.55 ± 2.64	1.76	492 ± 137	131 ± 13	31.5	"
SG0740	411172	3798020	2.1	78.64 ± 4.28	3.58	147 ± 15	N/A	24.4	"
SG0743	409731	3796134	22.0	42.70 ± 2.89	3.16	239 ± 28	113 ± 5	27.8	"
SG0803	423170	3803520	11.4	46.34 ± 5.21	4.20	293 ± 48	117 ± 5	32.1	*Heimsath et al.,* in press
SG0804	423141	3803270	8.1	28.51 ± 5.01	4.35	493 ± 111	125 ± 5	32.2	"
SG0805	422929	3803230	3.1	36.66 ± 4.39	3.88	343 ± 58	100 ± 6	32.0	"
SG0809	424195	3805030	18.5	29.97 ± 2.61	4.02	434 ± 59	110 ± 4	33.3	"
SG0704	394872	3786754	5.1	9.82 ± 2.23	2.03	668 ± 186	116 ± 6	34.9	*DiBiase et al.,* in review
SG0706	398469	3783358	17.3	10.79 ± 1.91	2.02	605 ± 137	122 ± 5	34.8	"

Sample ID	Easting[a]	Northing[a]	Area (km^2)	^{10}Be/SiO$_2$ (x 10^3 atoms/g)	N(z,I)[b]	Erosion rate (m/Ma)[c]	k_{sn}	Mean slope (degrees)	Data source
SG0708	399180	3794240	1.9	18.89 ± 1.99	2.54	435 ± 68	N/A	32.3	*DiBiase et al.*, in review
SG0747	406053	3786078	7.3	11.81 ± 3.51	1.97	541 ± 188	125 ± 9	32.1	"
SG0748	406129	3785893	7.4	11.77 ± 2.61	1.97	541 ± 147	132 ± 10	32.2	"
SG0749	406010	3784661	6.1	10.53 ± 2.83	1.99	611 ± 195	113 ± 2	35.2	"
SG0818	391759	3790469	25.5	9.98 ± 1.33	2.19	711 ± 130	92 ± 3	33.0	"
SG160	429950	3795861	18.8	14.82 ± 2.44	4.16	907 ± 195	187 ± 7	35.0	"
SG119	405250	3793499	0.85	24.63 ± 2.40	2.62	344 ± 51	N/A	24.2	*this study*
SG139	417912	3792062	65.0	13.16 ± 4.08	2.67	656 ± 236	147 ± 2	34.6	"
SG0705	398588	3784339	16.3	5.77 ± 1.50	2.07	1161 ± 360	129 ± 5	35.0	"
SG0707	442807	3782897	16.4	15.85 ± 2.60	3.34	682 ± 146	199 ± 9	36.2	"
SG0710	400409	3797980	6.4	36.46 ± 6.09	2.39	212 ± 46	58 ± 2	24.4	"
SG0726	417208	3802620	16.7	91.48 ± 3.84	4.03	143 ± 13	84 ± 5	26.1	"
SG0727	417314	3802530	7.6	59.57 ± 3.17	4.02	218 ± 23	71 ± 5	29.1	"
SG0736	410972	3798694	0.09	78.81 ± 4.24	3.34	137 ± 14	N/A	20.7	"
SG0737	410974	3799003	0.01	40.46 ± 3.07	3.45	276 ± 35	N/A	18.3	"
SG0739	411160	3798132	2.0	32.62 ± 2.17	3.61	358 ± 42	N/A	24.2	"
SG0750	393278	3798368	3.6	5.32 ± 5.16	2.18	1325 ± 1350	N/A	28.7	"
SG0751	438092	3781496	4.8	24.07 ± 4.13	2.13	287 ± 63	113 ± 18	32.7	"
SG0752	437690	3795990	9.4	5.40 ± 2.01	5.20	3112 ± 1316	165 ± 8	32.7	"
SG0802	419200	3795860	14.1	11.91 ± 3.62	2.99	813 ± 288	176 ± 8	33.2	"
SG0806	446719	3789070	3.4	32.45 ± 2.16	4.64	463 ± 54	110 ± 4	32.3	"
SG0808	454050	3788170	14.9	7.59 ± 30.00	2.93	1249 ± 556	167 ± 14	34.3	"
SG0812	417780	3809090	4.7	57.86 ± 3.49	3.42	191 ± 21	90 ± 4	33.8	"
SG0813	411520	3807541	41.7	80.63 ± 6.71	3.63	146 ± 19	93 ± 3	31.4	"
SG0817	410840	3806230	2.5	35.91 ± 2.74	2.91	262 ± 33	98 ± 18	33.6	"
SG0819	410389	3794829	25.8	28.95 ± 4.65	3.05	341 ± 72	114 ± 4	27.7	"

[a] UTM coordinates (NAD 27 Datum)

[b] Production rate latitude/elevation scaling factor [*Dunai*, 2000]

[c] Erosion rates calculated using density of 2.6 g/cm3, attenuation length of 165 g/cm2, and high latitude production rate of 5.1 atoms/g/yr

APPENDIX C

CHANNEL SURVEY METHODS AND DATA

Over the course of four summers (2007-2010), I surveyed approximately 60 km of stream channels throughout the San Gabriel Mountains. This appendix provides both a brief summary of the field methods, as well as a data table containing all of the observations.

Because of poor GPS satellite coverage in these canyons, I used a laser rangefinder and electronic data-logger to geo-locate observations of channel bed state and geometry. At each surveyed point, I recorded measurements of bankfull width, valley width, the percent of rock exposed in the channel bed and banks, and the median grain size (D_{50}) of the surface bed material. I measured bankfull channel width using a laser rangefinder, based on vegetation lines and slope breaks in channel cross sections. For incised reaches, I measured valley width using a laser rangefinder. In reaches with extensive valley flats (> 20 m), I supplemented our field surveys with measurements of valley width from the 1 m LiDAR DEM where applicable (see Chapter 5).

For each point, I estimated the percent of bedrock exposed in channel bed and banks to the nearest 10%. For example, channel reaches incised entirely into bedrock were assigned a bank rock exposure of 100%, while those confined only on one bank by rock were assigned a bank rock exposure of 50%. All observations were made at low flow conditions. I estimated D50 by eye, intermittently calibrating these observations with more detailed point counts (50 total point counts, see Chapter 4 for details). For early surveys, grain size estimates were made qualitatively (e.g., gravel, cobble, boulder); in later surveys I switched to estimating grain size to the nearest ½ phi size. For ease of comparison, I converted qualitative survey results to numeric using the following conversion: sand = 2 mm; pea gravel = 11 mm; fine gravel = 22 mm; coarse gravel = 45 mm; cobble = 90 mm; small boulder = 256 mm; medium boulder = 512 mm; large boulder =1024 mm. These converted estimates, which should be interpreted with caution, are marked in the data table by a star. In particular, the range of clast sizes covered by the “cobble” classification is quite large.

The table below also includes location information and contributing area (calculated from a 10 m DEM) for each point.

Station ID	Easting[a]	Northing[a]	Area (km^2)	Bankfull Width (m)	Valley Width (m)	% Rock (bed)	% Rock (bank)	D$_{50}$
efork-1	429238	3787648	150.5			0	0	
efork-3	429234	3787717	150.5	15	15	0	0	90 *
efork-4	429207	3787788	150.5	15	15	0	40	45 *
efork-5	429208	3787827	150.5			0	0	45 *
efork-5	429209	3787866	150.4			0	0	45 *
efork-7	429217	3787910	150.4	15	30	0	10	45 *
efork-7	429219	3787953	150.4	15	30	0	10	45 *
efork-9	429239	3787988	150.4	13	30	0	0	45 *
efork-9	429257	3788003	150.3	13	30	0	0	45 *
efork-11	429272	3788033	150.3	11	20	0	20	45 *
efork-12	429287	3788085	150.3	17	40	0	50	45 *
efork-12	429297	3788154	150.2	17	40	0	50	45 *
efork-14	429306	3788208	150.2	20	25	0	25	45 *
efork-14	429348	3788259	150.2	20	25	0	25	45 *
efork-16	429424	3788257	150.2	20	50	0	5	45 *
efork-17	429436	3788264	150.2			0	50	45 *
efork-18	429440	3788295	150.2	22	70	0	10	45 *
efork-18	429420	3788336	150.1	22	70	0	10	45 *
efork-20	429412	3788393	150.0	40	90	0	15	45 *
efork-20	429403	3788448	149.9	40	90	0	15	45 *
efork-22	429383	3788495	149.8	15	150	0	0	45 *
efork-22	429417	3788552	149.3	15	150	0	0	45 *
efork-24	429454	3788567	149.3		90	0	0	45 *
efork-24	429523	3788559	149.3		90	0	0	45 *
efork-25	429564	3788577	149.2			0	0	
efork-27	429601	3788613	149.2	15	90	0	5	45 *
efork-27	429619	3788644	149.2	15	90	0	5	45 *
efork-29	429580	3788699	149.2	15	75	0	0	45 *
efork-29	429561	3788770	149.1	15	75	0	0	45 *
efork-30	429558	3788787	149.0			0	0	
efork-31	429579	3788814	148.9			0	0	
efork-32	429610	3788861	148.9			0	0	
efork-34	429642	3788879	148.8	20	70	0	5	45 *
efork-34	429693	3788865	148.7	20	70	0	5	45 *
efork-35	429742	3788860	148.7			0	0	
efork-37	429791	3788877	148.7	15	80	0	0	45 *
efork-37	429826	3788878	148.7	15	80	0	0	45 *
efork-38	429860	3788911	148.7			0	0	
efork-39	429899	3788944	148.4			0	0	
efork-40	429904	3788949	148.4			0	0	
efork-42	429905	3789027	148.4	30		0	80	45 *
efork-42	429907	3789087	148.4	30		0	80	45 *
efork-44	429921	3789129	148.4			0	0	45 *
efork-44	429937	3789190	148.4			0	0	45 *
efork-45	429964	3789226	148.3			0	0	
efork-46	429979	3789228	147.8			0	0	
efork-48	430016	3789277	147.7			0	0	45 *
efork-49	430050	3789349	147.7	15	25	0	0	90 *
efork-50	430078	3789427	147.7			0	0	90 *
efork2-0	430049	3789595	146.3			0	0	90 *
efork2-1	430040	3789658	146.2	12	20	5	50	45 *
efork2-1	430048	3789681	146.1	12	20	5	50	45 *
efork2-3	430068	3789703	146.0	12	25	0	50	90 *
efork2-3	430095	3789731	146.0	12	25	0	50	90 *
efork2-5	430106	3789743	145.9	15	45	0	50	90 *
efork2-5	430110	3789771	145.9	15	45	0	50	90 *
efork2-7	430101	3789805	145.9	13	35	0	0	90 *
efork2-8	430100	3789832	145.9			5	50	90 *
efork2-9	430125	3789862	145.9	15	25	0	0	90 *
efork2-10	430169	3789889	145.9	15	15	0	50	90 *
efork2-10	430176	3789924	145.9	15	15	0	50	90 *
efork2-11	430174	3789934	145.9			0	0	
efork2-14	430176	3789974	145.8	9	30	0	40	90 *
efork2-15	430183	3790022	145.8	9	24	0	50	90 *
efork2-16	430186	3790045	145.8			0	50	90 *
efork2-16	430183	3790065	145.7			0	50	90 *

Station ID	Easting[a]	Northing[a]	Area (km^2)	Bankfull Width (m)	Valley Width (m)	% Rock (bed)	% Rock (bank)	D_{50}
efork2-18	430175	3790090	145.6	15	40	2	40	90 *
efork2-18	430159	3790109	145.5	15	40	2	40	90 *
efork2-19	430134	3790153	145.5			0	0	
efork2-20	430125	3790178	145.4			0	0	
efork2-22	430134	3790218	145.3			0	0	90 *
efork2-23	430156	3790248	145.3			0	0	90 *
efork2-23	430192	3790279	145.2			0	0	90 *
efork2-24	430197	3790314	145.2			0	0	
efork2-25	430194	3790369	145.1			0	0	
efork2-26	430189	3790393	145.1			0	0	
efork2-27	430177	3790421	145.1			0	0	
efork2-28	430172	3790431	145.1			0	0	
efork2-30	430151	3790439	145.1	12	40	0	50	90 *
efork2-30	430138	3790436	145.1	12	40	0	50	90 *
efork2-31	430123	3790449	145.1			0	0	
efork2-32	430115	3790468	145.1			0	0	
efork2-34	430120	3790501	142.3			0	0	90 *
efork2-34	430151	3790528	142.3			0	0	90 *
efork2-35	430158	3790533	142.3			0	0	
efork2-36	430179	3790562	142.3			0	0	
efork2-38	430198	3790596	142.2	12	25	5	0	90 *
efork2-39	430230	3790627	142.2	9	50	0	50	90 *
efork2-39	430243	3790636	142.2	9	50	0	50	90 *
efork2-41	430268	3790627	142.2			0	0	90 *
efork2-43	430316	3790621	142.2	12	30	0	10	45 *
efork2-43	430359	3790632	142.2	12	30	0	10	45 *
efork2-44	430381	3790641	142.2			0	0	
efork2-46	430400	3790657	142.1	12	60	5	0	45 *
efork2-47	430427	3790671	142.1	12		0	15	45 *
efork2-47	430428	3790712	142.1	12		0	15	45 *
efork2-48	430415	3790761	141.6			0	0	
efork2-50	430415	3790785	141.6			0	0	45 *
efork2-52	430423	3790814	141.6			0	0	45 *
efork2-52	430444	3790833	141.6			0	0	45 *
efork2-53	430468	3790834	141.6			0	0	
efork2-54	430491	3790816	141.5			0	0	
efork2-56	430533	3790808	141.5	13	50	0	0	90 *
efork2-56	430571	3790804	141.1	13	50	0	0	90 *
efork2-57	430623	3790802	141.0			0	0	
efork2-58	430684	3790809	140.9			0	0	
efork2-59	430760	3790816	140.9			0	0	
efork2-60	430780	3790825	140.8			0	0	
efork2-62	430830	3790866	140.7	10	35	0	0	90 *
efork2-62	430857	3790900	140.7	10	35	0	0	90 *
efork2-64	430878	3790911	140.6			0	0	90 *
sf-litroc-43	407558	3803086	0.3	2		2	5	45 *
sf-litroc-44	407576	3803099	0.3	1.5		4	10	45 *
sf-litroc-45	407596	3803113	0.3	1.5		30	15	45 *
sf-litroc-45	407608	3803134	0.3			0	0	
sf-litroc-47	407611	3803145	0.3			0	0	45 *
sf-litroc-47	407616	3803148	0.3			0	0	
sf-litroc-48	407626	3803170	0.3			0	0	
sf-litroc-49	407635	3803169	0.3			0	0	
sf-litroc-50	407647	3803166	0.3			0	0	
sf-litroc-51	407652	3803170	0.3			0	0	
sf-litroc-52	407683	3803164	0.3			0	0	
sf-litroc-53	407694	3803163	0.3			0	0	
sf-litroc-54	407717	3803161	0.3			0	0	
sf-litroc-55	407726	3803166	0.3			0	0	
sf-litroc-56	407732	3803164	0.3			0	0	
sf-litroc-57	407745	3803153	0.3			0	0	
sf-litroc-58	407759	3803164	0.3			0	0	
sf-litroc-60	407770	3803179	0.3			0	0	45 *
sf-litroc-60	407775	3803185	0.3			0	0	
sf-litroc-61	407775	3803200	0.9			0	0	
sf-litroc-63	407781	3803203	0.9	1.5		0	0	2 *

Station ID	Easting[a]	Northing[a]	Area (km^2)	Bankfull Width (m)	Valley Width (m)	% Rock (bed)	% Rock (bank)	D_{50}
sf-litroc-64	407799	3803208	0.9	2		0	0	22 *
sf-litroc-65	407803	3803207	0.9	2		100	50	1024 *
sf-litroc-66	407814	3803212	0.9	2		0	0	11 *
sf-litroc-67	407826	3803233	0.9	1.5		0	5	45 *
sf-litroc-68	407841	3803246	0.9			0	10	45 *
sf-litroc-68	407851	3803247	0.9			0	0	
sf-litroc-70	407867	3803248	0.9	2.5		15	40	11 *
sf-litroc-71	407872	3803259	0.9			0	5	45 *
sf-litroc-71	407886	3803266	0.9			0	0	
sf-litroc-72	407900	3803270	0.9			0	0	
sf-litroc-73	407920	3803289	0.9			0	0	
sf-litroc-74	407926	3803308	0.9			0	0	
sf-litroc-75	407924	3803319	0.9			0	0	
sf-litroc-76	407921	3803325	1.9			0	0	
sf-litroc-77	407928	3803339	1.9			0	0	
sf-litroc-78	407936	3803347	1.9			0	0	
sf-litroc-80	407938	3803362	1.9			0	0	45 *
sf-litroc-80	407970	3803366	1.9			0	0	
sf-litroc-81	407980	3803369	2.0			0	0	
sf-litroc-82	407989	3803377	2.0			0	0	
sf-litroc-83	408000	3803382	2.0			0	0	
sf-litroc-84	408008	3803389	2.0			0	0	
sf-litroc-85	408014	3803389	2.0			0	0	
sf-litroc-87	408020	3803384	2.0	2		20	40	22 *
sf-litroc-88	408028	3803379	2.0			30	50	90 *
sf-litroc-89	408049	3803378	2.0	3		0	0	45 *
sf-litroc-89	408066	3803387	2.0			0	0	
sf-litroc-90	408071	3803392	2.0			0	0	
sf-litroc-92	408101	3803386	2.0	4		3	5	45 *
sf-litroc-92	408117	3803379	2.0			0	0	
sf-litroc-93	408126	3803381	2.0			0	0	
sf-litroc-95	408150	3803404	2.0	3		0	0	90 *
sf-litroc-95	408151	3803413	2.0			0	0	
sf-litroc-97	408172	3803449	2.0	3		0	0	90 *
sf-litroc-98	408204	3803472	2.0	3		0	0	45 *
sf-litroc-99	408244	3803501	2.0	4		1	0	45 *
sf-litroc-100	408285	3803498	2.0	5	50	0	0	45 *
sf-litroc-100	408314	3803487	2.0			0	0	
sf-litroc-102	408333	3803486	2.0			0	0	45 *
sf-litroc-102	408357	3803475	3.0			0	0	
sf-litroc-104	408367	3803486	3.1			0	0	45 *
sf-litroc-105	408397	3803431	3.1	5	70	0	0	90 *
sf-litroc-105	408448	3803417	3.2			0	0	
sf-litroc-107	408504	3803421	3.2	3	50	0	0	45 *
sf-litroc-108	408558	3803409	3.2	3	50	15	0	45 *
sf-litroc-109	408599	3803398	3.2			0	0	45 *
sf-litroc-109	408626	3803388	3.2			0	0	
sf-litroc-111	408645	3803382	3.3	3	35	0	0	45 *
sf-litroc-111	408650	3803371	3.3			0	0	
sf-litroc-112	408674	3803357	3.3			0	0	
sf-litroc-113	408722	3803341	3.3			0	0	
sf-litroc-115	408749	3803328	3.3	3	40	0	0	45 *
sf-litroc-115	408788	3803328	3.3			0	0	
sf-litroc-116	408797	3803331	3.4			0	0	
sf-litroc-118	408823	3803306	3.4	2	40	0	0	45 *
sf-litroc-118	408845	3803301	3.4			0	0	
sf-litroc-120	408852	3803289	3.4			0	0	45 *
sf-litroc-120	408859	3803292	3.4			0	0	
sf-litroc-121	408866	3803289	3.4			0	0	
sf-litroc-122	408869	3803288	3.4			0	0	
sf-litroc-124	408867	3803269	3.5			0	0	45 *
sf-litroc-124	408895	3803275	3.5			0	0	
sf-litroc-125	408902	3803271	3.5			0	0	
sf-litroc-126	408910	3803252	3.5			0	0	
sf-litroc-127	408920	3803242	3.5			0	0	
sf-litroc-129	408922	3803237	3.5			0	0	45 *

Station ID	Easting[a]	Northing[a]	Area (km^2)	Bankfull Width (m)	Valley Width (m)	% Rock (bed)	% Rock (bank)	D$_{50}$
sf-litroc-129	408941	3803229	3.5			0	0	
sf-litroc-130	408962	3803223	3.5			0	0	
sf-litroc-132	408977	3803225	3.5	1	50	0	5	11 *
sf-litroc-132	408986	3803229	3.5			0	0	
sf-litroc-133	409000	3803225	3.5			0	0	
sf-litroc-134	409006	3803224	3.5			0	0	
sf-litroc-135	409010	3803227	3.5			0	0	
sf-litroc-136	409018	3803227	3.5			0	0	
sf-litroc-137	409035	3803214	3.5			0	0	
sf-litroc-138	409047	3803206	3.6			0	0	
sf-litroc-139	409065	3803197	3.6			0	0	
sf-litroc-140	409074	3803200	3.6			0	0	
sf-litroc-141	409081	3803201	3.6			0	0	
sf-litroc-142	409094	3803200	3.6			0	0	
sf-litroc-143	409106	3803203	3.6			0	0	
sf-litroc-144	409115	3803204	3.6			0	0	
sf-litroc-146	409122	3803203	3.6			0	0	11 *
sf-litroc-146	409133	3803190	3.6			0	0	
sf-litroc-148	409129	3803184	3.6			0	0	11 *
sf-litroc-149	409165	3803182	3.6	3		10	0	2 *
sf-litroc-149	409185	3803177	7.9			0	0	
sf-litroc-150	409189	3803178	7.9			0	0	
sf-litroc-152	409197	3803190	7.9			0	0	2 *
sf-litroc-152	409224	3803154	7.9			0	0	
sf-litroc-154	409222	3803140	7.9	5	40	10	5	45 *
sf-litroc-155	409256	3803117	7.9	5	30	70	10	90 *
sf-litroc-156	409289	3803114	7.9	3	30	10	0	45 *
sf-litroc-156	409317	3803122	7.9			0	0	
sf-litroc-157	409326	3803133	7.9			0	0	
sf-litroc-158	409333	3803149	7.9			0	0	
sf-litroc-160	409340	3803158	7.9			10	10	45 *
sf-litroc-161	409344	3803164	7.9	2	5	0	0	90 *
sf-litroc-162	409358	3803188	7.9	3	3	80	70	256 *
sf-litroc-163	409371	3803203	8.0	3	3	20	10	2 *
sf-litroc-164	409372	3803210	8.0			5	0	90 *
sf-litroc-165	409391	3803238	8.0	4	4	30	30	90 *
sf-litroc-166	409406	3803245	8.0	4	4	20	40	45 *
sf-litroc-167	409421	3803252	8.0	4	4	50	50	256 *
sf-litroc-167	409440	3803259	8.0			0	0	
sf-litroc-169	409447	3803263	8.0	3	3	5	90	256 *
sf-litroc-170	409452	3803266	8.0	3	3	20	80	256 *
sf-litroc-171	409456	3803268	8.0	4	4	0	40	11 *
sf-litroc-172	409463	3803274	8.0	4	4	0	0	2 *
sf-litroc-173	409477	3803277	8.1	4	4	0	40	2 *
sf-litroc-174	409484	3803275	8.1	4	4	0	50	45 *
sf-litroc-175	409504	3803275	8.1	3	10	0	50	90 *
sf-litroc-176	409563	3803299	8.1	5	10	30	10	90 *
middle_alder-37	406513	3802436	0.4			0	0	
middle_alder-38	406506	3802432	0.4			0	0	
middle_alder-40	406497	3802437	0.4			0	0	45 *
middle_alder-40	406489	3802449	0.4			0	0	
middle_alder-41	406481	3802457	0.4			0	0	
middle_alder-42	406477	3802464	0.4			0	0	
middle_alder-43	406473	3802464	0.4			0	0	
middle_alder-45	406449	3802472	0.4			0	2	45 *
middle_alder-45	406436	3802466	0.5			0	0	
middle_alder-47	406431	3802460	0.5	4		0	0	45 *
middle_alder-47	406422	3802455	0.5			0	0	
middle_alder-49	406411	3802445	0.5			0	0	45 *
middle_alder-49	406405	3802436	0.5			0	0	
middle_alder-51	406390	3802417	0.5			0	0	45 *
middle_alder-52	406364	3802397	0.5			0	0	
middle_alder-52	406350	3802374	0.5			0	0	
middle_alder-53	406341	3802363	0.5			0	0	
middle_alder-54	406337	3802353	0.5			0	0	
middle_alder-55	406329	3802339	0.5			0	0	

Station ID	Easting[a]	Northing[a]	Area (km^2)	Bankfull Width (m)	Valley Width (m)	% Rock (bed)	% Rock (bank)	D_{50}
middle_alder-56	406326	3802340	0.5			0	0	
middle_alder-58	406319	3802340	0.5			0	0	45 *
middle_alder-58	406306	3802329	0.5			0	0	
middle_alder-59	406299	3802323	0.5			0	0	
middle_alder-61	406292	3802309	0.5	3	20	5	0	45 *
middle_alder-62	406283	3802304	0.5	2		0	40	45 *
middle_alder-63	406272	3802291	0.5	3	3	0	0	45 *
middle_alder-64	406269	3802286	0.5			0	0	45 *
middle_alder-64	406263	3802282	0.5			0	0	
middle_alder-65	406257	3802281	0.5			0	0	
middle_alder-67	406253	3802273	0.5	0.4		0	0	45 *
middle_alder-67	406247	3802267	0.5			0	0	
middle_alder-68	406240	3802264	0.5			0	0	
middle_alder-70	406235	3802265	0.5	2	2	20	50	45 *
middle_alder-71	406231	3802265	0.6	2	8	20	40	45 *
middle_alder-71	406228	3802263	0.6			0	0	
middle_alder-72	406221	3802264	0.6			0	0	
middle_alder-73	406218	3802264	0.6			0	0	
middle_alder-74	406214	3802268	0.6			0	0	
middle_alder-75	406209	3802268	0.6			0	0	
middle_alder-77	406203	3802265	0.6			5	5	45 *
middle_alder-78	406200	3802266	0.6	1		0	0	45 *
middle_alder-78	406194	3802266	0.6			0	0	
middle_alder-80	406191	3802267	0.6			0	0	45 *
middle_alder-81	406184	3802268	0.6			0	0	45 *
middle_alder-81	406181	3802267	0.6			0	0	
middle_alder-82	406175	3802268	0.6			0	0	
middle_alder-83	406168	3802267	0.6			0	0	
chilao-1	406435	3798883	8.0			0	0	
chilao-2	406420	3798851	8.0			0	0	
chilao-4	406408	3798831	8.0	3		0	0	45 *
chilao-4	406391	3798818	8.0			0	0	
chilao-5	406359	3798811	8.0			0	0	
chilao-7	406331	3798791	8.0	4		0	0	2 *
chilao-8	406305	3798782	8.7	3.5		0	0	90 *
chilao-9	406292	3798790	8.7	2		5	0	45 *
chilao-10	406286	3798796	8.7	2.5		0	0	45 *
chilao-11	406268	3798804	8.8	3		35	15	90 *
chilao-12	406258	3798814	8.8	2		80	5	2 *
chilao-13	406235	3798841	8.8	4		10	0	90 *
chilao-14	406212	3798875	8.8	4		0	0	2 *
chilao-15	406198	3798884	8.8	2.5		0	0	90 *
chilao-16	406165	3798885	8.8	3.5		0	0	45 *
chilao-16	406161	3798879	8.8			0	0	
chilao-17	406139	3798876	8.8			0	0	
chilao-19	406139	3798870	8.8	2		0	0	45 *
chilao-19	406131	3798868	8.8			0	0	
chilao-21	406102	3798873	8.8	3		10	5	2 *
chilao-22	406094	3798874	10.0	2		0	0	90 *
chilao-23	406071	3798882	10.0	3		5	10	22 *
chilao-24	406052	3798876	10.1	3.5		0	25	22 *
chilao-25	406036	3798862	10.1	1.5		0	0	90 *
chilao-26	406019	3798849	10.1	1.5		0	0	90 *
chilao-27	406021	3798835	10.1	2		5	5	90 *
chilao-28	406015	3798820	10.1	3.5		60	50	90 *
chilao-29	406021	3798788	10.1	4		50	30	2 *
chilao-30	405959	3798775	10.1	5		75	45	2 *
chilao-31	405928	3798772	10.1	4	4	30	50	2 *
chilao-32	405912	3798766	10.1	2		50	50	45 *
chilao-33	405904	3798766	10.1	2.5	10	2	0	45 *
chilao-34	405895	3798753	10.1	3.5		10	0	45 *
chilao-35	405876	3798713	10.2	5	20	40	30	2 *
chilao-36	405884	3798682	10.2	3		50	40	2 *
chilao-37	405895	3798666	10.2	3.5		0	5	22 *
chilao-38	405897	3798641	10.2	3		5	0	2 *
chilao-39	405898	3798616	10.2	2.5		0	0	90 *

Station ID	Easting[a]	Northing[a]	Area (km^2)	Bankfull Width (m)	Valley Width (m)	% Rock (bed)	% Rock (bank)	D_{50}
chilao-39	405894	3798607	10.2			0	0	
chilao-41	405880	3798597	10.2	3		85	100	90 *
chilao-42	405875	3798579	10.2	5	5	90	100	90 *
chilao-43	405865	3798564	10.2	5	5	60	100	2 *
chilao-44	405874	3798547	10.2	3.5	4	75	60	2 *
chilao-45	405885	3798536	10.2	4	4	5	10	256 *
chilao-46	405890	3798515	10.2	4	4	40	50	256 *
chilao-47	405893	3798496	10.2	3		90	100	256 *
chilao-48	405886	3798492	10.2	2.5		90	100	11 *
chilao-49	405882	3798487	10.2	3		20	100	1024 *
chilao-50	405883	3798483	10.2	2.5		10	100	1024 *
chilao-51	405886	3798470	10.2	4		0	100	2 *
chilao-52	405887	3798462	10.2	8	8	0	30	512 *
chilao-53	405885	3798452	10.3	4	8	40	50	1024 *
chilao-54	405890	3798438	10.3	5	5	5	10	1024 *
chilao-55	405891	3798428	10.3	6	6	10	20	512 *
chilao-55	405887	3798407	10.3			0	0	
chilao-57	405892	3798404	10.3	6	6	15	0	512 *
chilao-58	405892	3798400	10.3			0	0	512 *
chilao-59	405897	3798391	10.3	8	8	30	80	1024 *
chilao-59	405887	3798375	10.3			0	0	
chilao-61	405883	3798373	10.3			0	0	1024 *
chilao-62	405876	3798367	10.3			0	0	1024 *
chilao-63	405881	3798361	10.3			0	0	1024 *
chilao-64	405888	3798356	10.3			0	0	1024 *
chilao-65	405895	3798347	10.3	5		10	70	256 *
chilao-66	405893	3798322	10.3			5	10	1024 *
chilao-67	405883	3798315	10.3			0	0	1024 *
chilao-68	405881	3798312	10.3			0	0	1024 *
chilao-69	405878	3798300	10.3			0	0	1024 *
chilao-70	405868	3798297	10.3			0	0	1024 *
chilao-71	405865	3798281	10.3	6	15	5	20	512 *
chilao-72	405854	3798281	10.3			0	0	512 *
chilao-73	405833	3798271	10.4	10	10	100	100	
chilao-74	405821	3798266	10.4	8	8	15	50	512 *
chilao-75	405816	3798265	10.4			0	0	512 *
chilao-76	405808	3798264	10.4	5	5	0	50	256 *
chilao-76	405805	3798266	10.4			0	0	
chilao-77	405801	3798273	10.4			0	0	
chilao-79	405796	3798274	10.4			0	0	256 *
chilao-80	405790	3798279	10.4			0	0	256 *
chilao-81	405784	3798268	10.4			0	0	256 *
chilao-82	405757	3798259	10.4	20	20	0	20	1024 *
chilao-83	405727	3798228	10.5	10		50	0	1024 *
chilao-84	405712	3798220	10.5	6	6	30	0	512 *
chilao-84	405693	3798223	10.5			0	0	
chilao-86	405688	3798232	10.5	6	6	0	30	256 *
chilao-86	405675	3798242	10.5			0	0	
chilao-88	405642	3798249	10.5	5	5	70	30	1024 *
chilao-89	405611	3798227	10.5	8		80	40	11 *
chilao-90	405598	3798220	10.6			0	0	11 *
chilao-91	405586	3798215	10.6			0	0	11 *
chilao-93	405571	3798202	5.3	12		0	50	512 *
chilao-94	405624	3798173	5.3	12		0	100	1024 *
chilao-95	405619	3798156	5.3	12	12	0	100	1024 *
chilao-95	405645	3798141	5.3			0	0	
chilao-97	405670	3798100	5.3	10	10	0	100	1024 *
chilao-98	405681	3798087	5.3	7	7	0	100	1024 *
chilao-99	405698	3798049	5.3	10		0	100	512 *
chilao-100	405718	3798036	5.3	12	12	0	100	512 *
chilao-101	405732	3798029	5.2	7	7	0	50	512 *
chilao-102	405743	3798024	5.2	5	5	0	50	2 *
chilao-103	405760	3797985	5.2	5	5	0	70	1024 *
chilao-104	405770	3797945	5.2	8	8	70	40	1024 *
chilao-105	405783	3797936	5.2	7	7	0	30	256 *
chilao-106	405803	3797931	5.2	7	7	0	5	256 *

Station ID	Easting[a]	Northing[a]	Area (km^2)	Bankfull Width (m)	Valley Width (m)	% Rock (bed)	% Rock (bank)	D_{50}
chilao-107	405819	3797918	5.2	7	7	0	30	90 *
chilao-108	405830	3797903	5.2	7	7	20	100	256 *
chilao-109	405838	3797887	5.2	3	3	0	70	11 *
chilao-110	405840	3797866	5.2	4	4	40	100	512 *
chilao-111	405841	3797854	5.2	5	5	100	100	
chilao-112	405847	3797821	5.2	10	10	25	90	256 *
chilao-113	405851	3797815	5.2	10	10	0	70	256 *
chilao-114	405857	3797793	5.1	10	10	5	50	1024 *
chilao-115	405861	3797767	5.1	10	10	0	50	1024 *
chilao-116	405866	3797738	5.1	8	8	0	30	1024 *
chilao-117	405879	3797691	5.1	7	7	5	0	90 *
chilao-118	405880	3797683	5.1	4	15	0	0	90 *
chilao-119	405860	3797642	5.1	4	20	2	0	90 *
chilao-119	405878	3797613	5.1			0	0	
chilao-121	405885	3797609	5.0			0	0	2 *
chilao-122	405890	3797597	5.0	3	10	0	0	45 *
chilao-123	405910	3797585	5.0	3	10	0	0	2 *
chilao-124	405922	3797561	5.0	3	15	0	0	2 *
chilao-125	405923	3797532	5.0	2.5	15	40	25	2 *
chilao-126	405921	3797520	5.0	2		0	0	90 *
chilao-127	405923	3797510	5.0			0	0	90 *
wickiup-1	398416	3796882	9.7			0	0	
wickiup-3	398427	3796855	9.7	5		5	0	90 *
wickiup-3	398435	3796848	9.7			0	0	
wickiup-4	398450	3796841	9.7			0	0	
wickiup-6	398461	3796828	9.7	4		30	30	90 *
wickiup-7	398459	3796801	9.7	4.5		0	0	90 *
wickiup-8	398478	3796784	9.7	4		0	0	45 *
wickiup-8	398508	3796772	9.7			0	0	
wickiup-9	398527	3796774	9.7			0	0	
wickiup-11	398544	3796794	9.6	6	40	0	0	45 *
wickiup-12	398581	3796796	9.6	5	40	0	0	45 *
wickiup-12	398618	3796778	9.6			0	0	
wickiup-13	398631	3796765	9.6			0	0	
wickiup-14	398650	3796747	9.6			0	0	
wickiup-16	398660	3796727	9.6	4	30	0	0	45 *
wickiup-17	398658	3796713	9.6			0	0	45 *
wickiup-18	398691	3796695	9.6	5	25	0	5	90 *
wickiup-19	398713	3796693	9.6	5	30	2	20	90 *
wickiup-19	398740	3796710	9.6			0	0	
wickiup-21	398756	3796701	9.6			0	0	90 *
wickiup-21	398762	3796689	9.6			0	0	
wickiup-22	398759	3796672	9.6			0	0	
wickiup-23	398743	3796656	9.6			0	0	
wickiup-25	398725	3796648	9.6	5	40	2	4	45 *
wickiup-25	398718	3796639	9.6			0	0	
wickiup-27	398717	3796610	9.5	4	6	0	0	45 *
wickiup-27	398719	3796589	9.5			0	0	
wickiup-29	398739	3796572	9.5	4		3	0	45 *
wickiup-29	398747	3796565	9.5			0	0	
wickiup-30	398749	3796538	9.5			0	0	
wickiup-32	398750	3796520	9.5	3	40	0	0	45 *
wickiup-32	398771	3796493	9.5			0	0	
wickiup-33	398790	3796488	9.5			0	0	
wickiup-34	398807	3796483	9.5			0	0	
wickiup-36	398828	3796472	9.5	3		0	15	90 *
wickiup-36	398831	3796452	9.5			0	0	
wickiup-38	398831	3796407	9.5			0	0	90 *
wickiup-38	398838	3796372	9.5			0	0	
wickiup-40	398843	3796357	9.4	5		0	0	45 *
wickiup-40	398844	3796339	9.4			0	0	
wickiup-42	398852	3796316	9.1	5		1	10	45 *
wickiup-43	398863	3796298	9.1	5		0	0	90 *
wickiup-44	398872	3796277	9.1	4.5		0	50	90 *
wickiup-45	398892	3796254	9.1	5	8	0	40	45 *
wickiup-46	398898	3796222	8.9	5	10	0	0	90 *

Station ID	Easting[a]	Northing[a]	Area (km^2)	Bankfull Width (m)	Valley Width (m)	% Rock (bed)	% Rock (bank)	D_{50}
wickiup-46	398890	3796202	8.9			0	0	
wickiup-47	398896	3796189	8.9			0	0	
wickiup-49	398911	3796174	8.9	7	40	0	0	45 *
wickiup-49	398914	3796153	8.8			0	0	
wickiup-51	398906	3796114	8.8	5		0	0	45 *
wickiup-51	398919	3796078	8.8			0	0	
wickiup-53	398927	3796063	8.8	4		0	0	45 *
wickiup-54	398967	3796027	8.8	4	12	20	15	512 *
wickiup-54	398986	3796016	8.8			0	0	
wickiup-56	399009	3796004	8.8	3	12	20	40	90 *
wickiup-57	399038	3795994	8.8	3.5	10	5	40	45 *
wickiup-58	399052	3795986	8.7	4	35	15	30	90 *
wickiup-59	399058	3795986	8.7	3.5	25	0	0	45 *
wickiup-60	399078	3795983	8.7	3	15	3	0	45 *
wickiup-61	399098	3795982	8.7			10	40	90 *
wickiup-62	399103	3795966	8.7	3.5		0	0	90 *
wickiup-63	399083	3795923	8.7	2		15	15	90 *
wickiup-64	399088	3795901	8.6	2.5		50	100	1024 *
wickiup-65	399101	3795895	8.6			0	0	1024 *
wickiup-66	399118	3795887	8.5	2	20	30	40	45 *
wickiup-67	399136	3795873	8.5	3	15	0	0	45 *
wickiup-67	399171	3795857	8.5			0	0	
wickiup-69	399190	3795833	8.4	3		10	30	90 *
wickiup-70	399193	3795816	8.4	3.5		0	0	90 *
wickiup-70	399196	3795787	8.4			0	0	
wickiup-71	399197	3795793	8.4			0	0	
wickiup-73	399190	3795775	8.1	2.5		10	10	90 *
wickiup-74	399170	3795757	8.1	3		0	0	90 *
wickiup-74	399163	3795716	8.1			0	0	
wickiup-75	399168	3795703	8.1			0	0	
wickiup-77	399214	3795693	8.0	4		2	0	90 *
wickiup-78	399236	3795683	8.0	2.5		50	50	90 *
wickiup-79	399254	3795658	8.0	3.5		0	0	90 *
wickiup-80	399271	3795607	8.0	3.5		10	20	90 *
wickiup-81	399282	3795571	8.0	2.5		50	80	45 *
wickiup-82	399280	3795556	8.0	4		30	50	90 *
wickiup-83	399268	3795543	8.0	4		50	50	90 *
wickiup-84	399251	3795529	7.9	3.5		0	0	90 *
wickiup-85	399239	3795507	7.9	5		0	30	90 *
wickiup-86	399221	3795490	7.9	3		0	10	90 *
wickiup-87	399213	3795484	7.9	3		80	80	256 *
wickiup-88	399188	3795475	7.9	3		0	40	90 *
wickiup-89	399167	3795466	7.9	2.5		5	15	90 *
wickiup-90	399157	3795445	7.9	3		0	0	90 *
wickiup-90	399161	3795424	7.8			0	0	
wickiup-91	399172	3795404	7.8			0	0	
wickiup-92	399177	3795396	7.8			0	0	
wickiup-93	399177	3795378	7.8			0	0	
wickiup-95	399166	3795366	7.8	3		0	0	90 *
wickiup-96	399137	3795350	7.8	3.5		0	5	90 *
wickiup-96	399145	3795313	7.7			0	0	
wickiup-98	399155	3795303	7.7	4		0	0	90 *
wickiup-98	399179	3795289	7.7			0	0	
wickiup-100	399206	3795283	7.7	4		0	0	90 *
wickiup-101	399225	3795283	7.7	4		0	2	45 *
wickiup-102	399253	3795288	7.7	5		0	0	45 *
wickiup-102	399273	3795287	7.7			0	0	
wickiup-103	399283	3795286	7.7			0	0	
wickiup-105	399304	3795272	7.7	4		0	0	45 *
wickiup-106	399318	3795257	7.7	4		5	5	90 *
wickiup-107	399325	3795221	7.6	4		0	0	90 *
wickiup-108	399306	3795200	7.6	4		2	0	45 *
wickiup-109	399279	3795181	7.6	3		50	50	90 *
wickiup-110	399268	3795166	7.6	4		0	0	45 *
wickiup-110	399251	3795133	7.6			0	0	
wickiup-112	399235	3795104	7.6	3		2	0	45 *

Station ID	Easting[a]	Northing[a]	Area (km^2)	Bankfull Width (m)	Valley Width (m)	% Rock (bed)	% Rock (bank)	D$_{50}$
wickiup-113	399228	3795088	7.6	3		30	50	11 *
wickiup-114	399210	3795069	7.6	3		2	5	45 *
wickiup-114	399203	3795060	7.3			0	0	
wickiup-116	399184	3795051	7.3			0	0	45 *
wickiup-117	399197	3795047	7.3			0	0	45 *
wickiup-118	399208	3795026	7.3			0	0	45 *
wickiup-119	399220	3795026	7.3	1		0	0	11 *
wickiup-119	399222	3795018	7.3			0	0	
wickiup-121	399221	3795013	7.3			0	0	11 *
wickiup-122	399222	3795021	7.3			0	0	11 *
wickiup-123	399220	3795026	7.3			0	0	11 *
wickiup-124	399208	3795026	7.3			0	0	11 *
wickiup-125	399197	3795047	7.3			0	0	11 *
wickiup-126	399185	3795052	6.0	2.5		20	20	45 *
wickiup-126	399178	3795040	6.0			0	0	
wickiup-128	399180	3795030	6.0	4		0	0	90 *
wickiup-128	399184	3795022	6.0			0	0	
wickiup-129	399188	3795007	6.0			0	0	
wickiup-130	399189	3794993	6.0			0	0	
wickiup-132	399193	3794967	6.0	4		0	0	90 *
wickiup-132	399201	3794955	6.0			0	0	
wickiup-133	399209	3794942	6.0			0	0	
wickiup-135	399216	3794934	6.0	4		0	0	90 *
wickiup-136	399233	3794922	6.0	4		0	0	90 *
wickiup-136	399244	3794903	6.0			0	0	
wickiup-137	399246	3794901	5.9			0	0	
wickiup-138	399260	3794892	5.9			0	0	
wickiup-139	399268	3794886	5.9			0	0	
wickiup-141	399270	3794865	5.9	5		0	0	90 *
wickiup-141	399272	3794856	5.9			0	0	
wickiup-142	399279	3794837	5.9			0	0	
wickiup-143	399283	3794826	5.9			0	0	
wickiup-145	399286	3794819	5.9			0	0	90 *
wickiup-145	399291	3794814	5.9			0	0	
wickiup-147	399290	3794806	5.9	2.5		10	40	90 *
wickiup-148	399281	3794793	5.8	3		0	0	45 *
wickiup-148	399278	3794789	5.8			0	0	
wickiup-150	399278	3794764	5.8	4		0	0	90 *
wickiup-151	399284	3794744	5.8	4		0	20	45 *
wickiup-152	399287	3794720	5.8	4		5	2	90 *
wickiup-152	399291	3794696	5.8			0	0	
wickiup-154	399291	3794663	4.9	3		0	0	90 *
wickiup-154	399276	3794626	4.9			0	0	
wickiup-156	399247	3794604	4.9	4		0	0	90 *
wickiup-157	399220	3794583	4.9	3		0	2	90 *
wickiup-157	399218	3794571	4.9			0	0	*
wickiup-158	399223	3794554	4.9			0	0	*
wickiup-160	399221	3794536	4.9	2.5		0	0	90 *
wickiup-160	399209	3794518	4.9			0	0	
wickiup-161	399208	3794492	4.9			0	0	
wickiup-162	399217	3794467	4.8			0	0	
wickiup-164	399218	3794456	4.8			0	0	90 *
endofwikiup-0	399209	3794449	4.8			0	0	90 *
endofwikiup-1	399209	3794449	4.8			0	0	90 *
mill-1	395431	3797568	55.0			0	0	
mill-3	395419	3797554	55.0	3.5	8	2	0	22 *
mill-4	395417	3797530	55.0	3.5	5	5	40	22 *
mill-5	395427	3797507	55.0	4	4	0	10	22 *
mill-6	395434	3797493	55.0	3	3	10	80	22 *
mill-7	395438	3797477	55.0	3	3	20	50	11 *
mill-8	395412	3797465	55.1	3	3	80	100	11 *
mill-9	395395	3797459	55.1	3	3	50	100	11 *
mill-10	395384	3797442	55.1	3.5		0	5	90 *
mill-11	395367	3797423	55.1	4	4	0	50	45 *
mill-12	395362	3797410	55.1	2.5		70	100	90 *
mill-13	395361	3797398	55.1	3	3	60	100	90 *

Station ID	Easting[a]	Northing[a]	Area (km^2)	Bankfull Width (m)	Valley Width (m)	% Rock (bed)	% Rock (bank)	D_{50}
mill-14	395342	3797391	55.1	3		10	50	90 *
mill-15	395324	3797392	55.1	3.5	5	10	0	90 *
mill-16	395306	3797403	55.1	5	5	5	50	90 *
mill-17	395286	3797425	55.1	4	4	50	100	22 *
mill-18	395267	3797442	55.1	3.5	4	25	60	11 *
mill-19	395257	3797452	55.1	2	4	10	60	90 *
mill-20	395233	3797458	55.3	3		80	80	2 *
mill-21	395216	3797464	55.3	3	3	50	50	45 *
mill-22	395195	3797472	55.3	3.5	4	20	30	45 *
mill-23	395189	3797486	55.3	3	3	15	60	90 *
mill-24	395188	3797503	55.3	4	4	5	40	45 *
mill-25	395179	3797509	55.3	3.5	4	80	90	45 *
mill-26	395160	3797513	55.3	5	5	0	70	45 *
mill-27	395140	3797525	55.3	3	3	30	50	90 *
mill-28	395125	3797534	55.3	3		5	50	90 *
mill-29	395114	3797535	55.4	5	5	0	40	2 *
mill-29	395102	3797523	55.4			0	0	
mill-31	395096	3797517	55.4			0	0	2 *
mill-32	395091	3797517	55.4			0	0	2 *
mill-33	395085	3797526	55.4			0	0	2 *
mill-34	395071	3797521	55.4	5	5	0	50	256 *
mill-35	395068	3797515	55.4			0	0	256 *
mill-36	395064	3797508	55.4	3.5	4	0	100	512 *
mill-37	395044	3797500	55.4	3	3	0	100	2 *
mill-38	395035	3797490	55.4	4		0	100	45 *
mill-39	395036	3797475	55.4	1	1	100	100	
mill-40	395037	3797459	55.8	3	3	0	100	90 *
mill-41	395033	3797443	55.8	3.5	4	40	100	11 *
mill-42	395023	3797429	55.8	3	3	20	100	11 *
mill-43	395017	3797419	55.8	3	3	60	70	90 *
mill-44	394998	3797413	55.8			0	0	90 *
mill-45	394988	3797401	55.8	4	4	0	50	256 *
mill-46	394977	3797399	55.8	2.5	3	50	59	256 *
mill-47	394958	3797392	55.8	5	7	5	80	256 *
mill-48	394940	3797371	55.8	4	8	0	40	22 *
mill-48	394923	3797374	55.8			0	0	
mill-50	394915	3797374	55.8	5	10	0	0	512 *
mill-51	394904	3797349	55.8	10	12	5	30	90 *
mill-52	394884	3797335	55.8	6	10	5	20	90 *
mill-53	394884	3797324	55.8	5	8	0	20	90 *
mill-54	394859	3797277	55.9	5	5	5	30	45 *
mill-55	394853	3797265	55.9	5	5	0	5	90 *
mill-56	394834	3797252	55.9	5	5	2	0	90 *
mill-56	394826	3797234	55.9			0	0	
mill-58	394825	3797225	55.9	5	5	2	0	256 *
mill-59	394821	3797222	55.9	4		100	0	
mill-60	394806	3797183	55.9	4	10	0	50	11 *
mill-61	394805	3797174	55.9	5	12	0	0	90 *
mill-62	394796	3797167	55.9			0	0	90 *
mill-63	394808	3797142	55.9	7	7	0	40	11 *
mill-64	394845	3797134	56.0	6	10	5	0	90 *
mill-64	394850	3797136	56.0			0	0	
mill-66	394860	3797125	56.0			0	0	256 *
mill-67	394891	3797122	56.0	3	3	90	100	90 *
mill2-0	394891	3797122	56.0	3	3	90	100	90 *
mill2-1	394905	3797114	56.0			70	50	90 *
mill2-2	394904	3797095	56.0	5	5	0	30	22 *
mill2-2	394896	3797076	56.0			0	0	
mill2-3	394896	3797073	56.0			0	0	
mill2-5	394904	3797056	56.0			10	40	2 *
mill2-6	394910	3797041	56.0	3	3	10	40	90 *
mill2-7	394933	3797030	56.0	4	6	0	10	90 *
mill2-8	394947	3797021	56.0	4	5	5	15	90 *
mill2-9	394953	3797008	56.0	4	5	5	60	2 *
mill2-10	394948	3796991	56.0	5	5	10	15	256 *
mill2-11	394958	3796982	56.0	5	5	2	2	90 *

Station ID	Easting[a]	Northing[a]	Area (km^2)	Bankfull Width (m)	Valley Width (m)	% Rock (bed)	% Rock (bank)	D_{50}
mill2-12	394956	3796973	56.0	2.5	5	30	50	45 *
mill2-13	394950	3796967	56.0	2.5	3	10	50	45 *
mill2-13	394938	3796959	56.0			0	0	
mill2-15	394919	3796958	56.0	3	7	0	0	2 *
mill2-16	394909	3796954	56.0	3	8	0	50	2 *
mill2-17	394902	3796952	56.0	3	8	0	50	2 *
mill2-17	394895	3796954	56.0			0	0	
mill2-19	394886	3796945	56.0	6	10	0	0	256 *
mill2-20	394887	3796928	56.0	6	10	0	0	90 *
mill2-21	394887	3796914	56.0	4	10	15	50	90 *
mill2-22	394877	3796895	56.0	5	8	5	50	45 *
mill2-23	394871	3796889	56.1	5	8	0	5	45 *
mill2-24	394872	3796866	56.1	4	4	80	100	2 *
mill2-25	394881	3796846	56.1	6		5	0	11 *
mill2-25	394879	3796840	56.1			0	0	
mill2-27	394883	3796834	167.5			0	0	11 *
mill2-28	394867	3796820	167.5	8		0	5	256 *
mill2-29	394837	3796811	167.5			10	50	256 *
mill2-30	394828	3796810	167.5	8		0	0	256 *
mill2-30	394815	3796804	167.5			0	0	
mill2-32	394783	3796801	167.5	8	8	0	35	90 *
mill2-33	394754	3796804	167.5			15	30	90 *
mill2-34	394735	3796802	167.6			2	5	90 *
mill2-35	394717	3796807	167.6	7	15	2	50	2 *
mill2-35	394693	3796828	167.6			0	0	
mill2-37	394660	3796841	167.6	8		0	0	22 *
mill2-37	394656	3796848	167.6			0	0	
mill2-39	394637	3796846	167.6	4	15	70	50	256 *
mill2-40	394634	3796830	167.6	7		40	50	45 *
mill2-41	394637	3796824	167.6	7	7	100	100	
mill2-42	394612	3796781	167.6	7	7	20	100	45 *
mill2-43	394595	3796764	168.0			70	40	45 *
mill2-44	394567	3796754	168.0	10	12	0	50	45 *
mill2-44	394535	3796753	168.0			0	0	
mill2-46	394520	3796774	168.0		10	0	50	512 *
mill2-47	394518	3796789	168.0			15	50	256 *
mill2-48	394531	3796804	168.1	8	8	25	50	256 *
mill2-49	394510	3796852	168.1			50	100	2 *
mill2-50	394493	3796880	168.1			20	100	22 *
mill2-51	394427	3796901	168.1			25	100	45 *
mill2-52	394400	3796910	168.1			90	100	45 *
mill2-53	394385	3796908	168.1	8	8	70	100	45 *
mill2-54	394372	3796917	168.1	4	4	90	100	90 *
mill2-55	394347	3796920	168.2	9	9	30	100	90 *
mill2-56	394324	3796919	168.2	6	6	70	100	90 *
mill2-56	394321	3796914	168.2			0	0	
mill2-58	394290	3796909	168.2	8		10	100	22 *
mill2-58	394277	3796906	168.2			0	0	
mill2-60	394271	3796899	168.2			0	0	22 *
mill2-61	394259	3796883	168.3			0	0	22 *
mill2-62	394238	3796860	168.3	7		30	100	22 *
mill2-62	394218	3796864	168.3			0	0	
mill2-64	394211	3796873	168.3	4	4	70	100	45 *
mill2-64	394195	3796887	168.3			0	0	
mill2-66	394186	3796890	168.4	5	5	30	100	256 *
mill2-67	394186	3796931	168.4	4	4	70	100	256 *
mill2-68	394169	3796941	168.4	4	4	80	100	45 *
mill2-69	394139	3796920	168.4	8	8	20	100	11 *
mill2-70	394111	3796924	168.4	8	8	20	100	45 *
mill2-70	394099	3796930	168.4			0	0	
mill2-71	394082	3796931	168.4			0	0	
mill2-73	394072	3796944	168.4	8	8	10	60	90 *
mill2-74	394021	3796972	168.4	5	5	50	75	90 *
mill2-75	393988	3796992	169.0	7	7	40	100	90 *
mill2-76	393983	3797013	169.0			0	0	90 *
mill2-77	393975	3797013	169.0	6	6	30	100	90 *

Station ID	Easting^a	Northing^a	Area (km^2)	Bankfull Width (m)	Valley Width (m)	% Rock (bed)	% Rock (bank)	D_{50}
mill2-77	393954	3797023	169.0			0	0	
mill2-79	393922	3797021	169.1	6	6	0	100	11 *
mill2-80	393898	3797018	169.1		5	0	100	256 *
mill2-80	393869	3797017	169.1			0	0	
mill2-81	393831	3797018	169.5			0	0	
mill2-82	393789	3797002	169.6			0	0	
mill2-84	393786	3796973	169.6	9	9	0	100	256 *
mill2-84	393774	3796935	169.6			0	0	
mill2-86	393756	3796902	169.6	10	10	0	80	256 *
mill2-86	393750	3796876	169.6			0	0	
mill2-88	393747	3796856	169.6	6	6	30	100	512 *
mill2-88	393733	3796841	169.7			0	0	
mill2-90	393727	3796835	169.7	6	6	0	100	512 *
mill2-91	393702	3796829	169.7	7	7	0	100	11 *
mill2-92	393692	3796765	169.7	8	8	0	100	11 *
mill2-93	393679	3796737	169.7	8	12	30	15	90 *
mill2-93	393663	3796727	169.7			0	0	
mill2-95	393624	3796672	169.8	10	15	0	0	90 *
mill2-96	393619	3796644	169.9		12	0	10	90 *
mill2-97	393617	3796575	169.9		15	0	40	11 *
mill2-98	393604	3796544	169.9		20	5	50	11 *
mill2-99	393574	3796513	174.3			0	0	11 *
mill2-99	393561	3796501	174.3			0	0	
mill2-100	393555	3796488	174.3			0	0	
mill2-101	393541	3796470	174.3			0	0	
mill2-103	393528	3796459	174.3	8	20	0	0	90 *
mill2-103	393493	3796424	174.3			0	0	
mill2-104	393458	3796398	174.3			0	0	
mill2-105	393414	3796373	174.4			0	0	
mill2-106	393390	3796364	174.4			0	0	
mill2-107	393372	3796368	174.5			0	0	
mill2-108	393364	3796367	174.5			0	0	
mill2-109	393332	3796377	174.5			0	0	
mill2-111	393326	3796397	174.5	8	30	0	0	90 *
mill2-112	393323	3796402	174.5			0	0	90 *
tujunga-1	396819	3797079	106.5			0	0	
tujunga-3	396812	3797101	106.7			80	100	2 *
tujunga-4	396794	3797096	106.7	15	15	5	50	2 *
tujunga-5	396778	3797098	106.8	10	10	15	50	2 *
tujunga-6	396772	3797098	106.8			0	0	2 *
tujunga-7	396755	3797107	106.8	10	10	0	100	1024 *
tujunga-8	396742	3797101	106.8	10	10	10	100	256 *
tujunga-9	396734	3797082	106.8	8	10	0	50	11 *
tujunga-10	396726	3797075	106.8	6	8	50	50	45 *
tujunga-11	396727	3797067	106.8	5	5	80	100	2 *
tujunga-12	396702	3797047	106.8	5	5	10	100	11 *
tujunga-13	396673	3797026	106.9	10	10	0	70	11 *
tujunga-14	396663	3797000	106.9	8	8	20	70	45 *
tujunga-15	396663	3796983	106.9	8	8	0	50	256 *
tujunga-15	396660	3796976	106.9			0	0	
tujunga-17	396647	3796964	106.9	8	8	0	100	256 *
tujunga-18	396643	3796952	106.9	5	8	30	70	256 *
tujunga-19	396628	3796936	106.9	7	8	50	20	11 *
tujunga-20	396620	3796922	106.9	7	7	0	30	512 *
tujunga-21	396605	3796899	106.9	6	6	0	90	11 *
tujunga-22	396594	3796880	107.0	6	10	0	5	11 *
tujunga-22	396581	3796888	107.0			0	0	
tujunga-24	396574	3796886	107.0	6		0	5	256 *
tujunga-25	396565	3796889	107.0	5		40	50	90 *
tujunga-26	396548	3796898	107.0	6		0	15	256 *
tujunga-27	396528	3796921	107.0	7		10	50	256 *
tujunga-28	396521	3796925	107.0	8		0	50	45 *
tujunga-29	396505	3796956	107.0	8		0	50	2 *
tujunga-30	396494	3796971	107.1	9		0	5	11 *
tujunga-31	396483	3796998	107.1	10	25	0	0	11 *
tujunga-32	396473	3797037	107.2	6	25	0	0	45 *

Station ID	Easting[a]	Northing[a]	Area (km^2)	Bankfull Width (m)	Valley Width (m)	% Rock (bed)	% Rock (bank)	D_{50}
tujunga-33	396462	3797054	107.2	7	20	0	0	11 *
tujunga-34	396443	3797058	107.2	7	10	0	0	90 *
tujunga-35	396430	3797067	107.2	6	8	0	50	11 *
tujunga-35	396410	3797055	107.2			0	0	
tujunga-37	396385	3797046	107.3	6	6	0	30	11 *
tujunga-38	396367	3797032	107.3	7	7	0	20	11 *
tujunga-38	396361	3797020	107.3			0	0	
tujunga-40	396332	3797002	107.4	9	9	0	5	2 *
tujunga-40	396325	3796988	107.4			0	0	
tujunga-41	396321	3796981	107.4			0	0	
tujunga-42	396312	3796976	107.4			0	0	
tujunga-44	396305	3796966	107.4	9	12	0	0	22 *
tujunga-45	396261	3796940	107.5	10	15	0	0	90 *
tujunga-45	396251	3796927	107.5			0	0	
tujunga-46	396239	3796922	107.5			0	0	
tujunga-48	396222	3796917	107.5	10	20	0	0	11 *
tujunga-48	396209	3796913	107.5			0	0	
tujunga-50	396179	3796897	107.5	8	20	0	0	45 *
tujunga-50	396163	3796888	107.5			0	0	
tujunga-52	396155	3796883	107.5			0	0	90 *
tujunga-53	396141	3796881	107.6			0	0	90 *
tujunga-54	396123	3796881	107.6	6	15	10	40	11 *
tujunga-55	396108	3796882	107.6			0	10	90 *
tujunga-56	396089	3796881	107.6	9	15	0	0	11 *
tujunga-57	396071	3796886	107.6			0	0	45 *
tujunga-58	396061	3796889	107.6			0	0	11 *
tujunga-59	396055	3796885	107.6			0	0	11 *
tujunga-60	396042	3796897	107.6	8	8	0	0	11 *
tujunga-60	396027	3796902	107.6			0	0	
tujunga-62	395999	3796900	107.6	8		0	0	11 *
tujunga-62	395978	3796903	107.6			0	0	
tujunga-64	395963	3796897	107.7	6	30	0	0	22 *
tujunga-65	395950	3796893	107.7	8		0	0	90 *
tujunga-66	395911	3796886	107.7	9		0	30	2 *
tujunga-67	395885	3796850	107.7			0	20	2 *
tujunga-68	395871	3796845	108.1	8	20	0	0	22 *
tujunga-69	395854	3796834	108.1	8	30	0	0	90 *
tujunga-70	395806	3796816	108.1	10	25	0	0	256 *
tujunga-71	395776	3796806	108.1			0	0	11 *
tujunga-72	395755	3796793	108.1	12	15	0	0	45 *
tujunga-73	395734	3796790	108.1	8		0	0	45 *
tujunga-74	395725	3796789	108.2			0	0	90 *
tujunga-75	395699	3796803	108.2	10	10	5	50	2 *
tujunga-76	395687	3796834	108.2	9	9	0	10	90 *
tujunga-77	395678	3796862	108.2	10	20	5	0	45 *
tujunga-78	395665	3796891	108.2			0	0	90 *
tujunga-79	395668	3796919	109.8			0	0	90 *
tujunga-80	395655	3796924	109.8			0	0	90 *
tujunga-81	395657	3796944	109.8	8	40	0	40	90 *
tujunga-82	395682	3796992	109.8	8	25	5	40	2 *
tujunga-83	395675	3797011	109.8			0	0	45 *
tujunga-84	395670	3797018	109.8	10	12	0	0	45 *
tujunga-85	395662	3797028	109.8	12	15	0	0	256 *
tujunga-86	395656	3797029	109.8	12	20	0	0	1024 *
tujunga-87	395646	3797031	109.8	12	20	0	0	256 *
tujunga-88	395616	3797038	109.8			0	25	11 *
tujunga-89	395611	3797033	109.8	12	20	5	0	90 *
tujunga-90	395592	3797041	109.9	12	15	0	0	90 *
tujunga-90	395556	3797050	109.9			0	0	
tujunga-92	395540	3797045	109.9			0	0	90 *
tujunga-93	395521	3797044	109.9	10	10	0	0	45 *
tujunga-94	395507	3797041	109.9	6	15	0	0	45 *
tujunga-95	395498	3797039	110.0		15	70	50	45 *
tujunga-96	395447	3797036	110.0	10	10	10	2	90 *
tujunga-97	395416	3797025	110.0	10	10	2	20	90 *
tujunga-98	395409	3797001	110.0	8	12	0	40	2 *

Station ID	Easting[a]	Northing[a]	Area (km^2)	Bankfull Width (m)	Valley Width (m)	% Rock (bed)	% Rock (bank)	D$_{50}$
tujunga-99	395409	3796984	110.0	10	10	5	10	2 *
tujunga-100	395401	3796969	110.0	8	8	20	0	256 *
tujunga-101	395396	3796954	110.0	8	8	5	50	90 *
tujunga-102	395367	3796934	110.0	10	10	0	50	11 *
tujunga-103	395355	3796920	110.1	7	7	80	60	90 *
tujunga-104	395324	3796902	110.1	8	12	10	5	90 *
tujunga-105	395306	3796892	110.1	8	12	70	10	90 *
tujunga-106	395272	3796889	110.1	12	12	15	50	22 *
tujunga-107	395238	3796896	110.1	10	15	10	5	22 *
tujunga-108	395221	3796898	110.1			10	0	90 *
tujunga-109	395178	3796917	110.1	12	12	0	0	11 *
tujunga-110	395151	3796933	110.1	10	18	0	0	90 *
tujunga-111	395110	3796956	110.2	8	15	40	40	90 *
tujunga-112	395097	3796956	110.2	10	10	0	2	512 *
tujunga-113	395067	3796939	110.2	10	15	5	30	90 *
tujunga-114	395053	3796931	110.2	8	18	10	15	256 *
tujunga-115	395006	3796921	110.2	10	20	30	50	90 *
tujunga-116	394991	3796916	110.2	10	15	0	50	256 *
tujunga-117	394960	3796910	110.2	10	12	30	2	2 *
tujunga-118	394934	3796894	110.2		6	30	60	90 *
tujunga-119	394921	3796876	110.2	8	8	40	30	256 *
tujunga-120	394911	3796869	110.2	6	6	10	100	256 *
tujunga-121	394900	3796841	110.2	8	8	5	70	2 *
tujunga-122	394882	3796825	110.2			0	50	22 *
tujunga-123	394869	3796815	110.2	6	6	30	50	22 *
uppertuj3-1	397647	3796879	101.9			0	0	
uppertuj3-2	397625	3796900	101.9			0	0	
uppertuj3-4	397609	3796920	101.9	10		10	5	256 *
uppertuj3-5	397579	3796974	101.9	10		0	40	2 *
uppertuj3-6	397558	3797001	101.9			0	0	11 *
uppertuj3-7	397536	3796991	101.9	10		0	40	11 *
uppertuj3-8	397529	3796948	102.0	10		0	0	90 *
uppertuj3-9	397518	3796937	102.0			0	0	90 *
uppertuj3-10	397515	3796920	102.5			0	15	90 *
uppertuj3-10	397509	3796899	102.5			0	0	
uppertuj3-12	397497	3796891	102.5			0	50	90 *
uppertuj3-13	397481	3796893	102.5	8	8	10	50	45 *
uppertuj3-14	397472	3796897	102.5	10	10	70	50	11 *
uppertuj3-14	397466	3796899	102.5			0	0	
uppertuj3-16	397448	3796893	102.5	8	8	20	15	11 *
uppertuj3-17	397448	3796886	102.5			0	0	
uppertuj3-18	397409	3796852	102.5	9	9	0	100	11 *
uppertuj3-19	397394	3796842	102.5	8	15	0	50	11 *
uppertuj3-19	397390	3796834	102.5			0	0	
uppertuj3-21	397382	3796819	102.5			5	50	90 *
uppertuj3-22	397378	3796809	102.5	5	5	20	100	11 *
uppertuj3-23	397373	3796805	102.5	7	7	0	100	11 *
uppertuj3-24	397341	3796804	104.6	10		5	50	2 *
uppertuj3-25	397318	3796831	104.6	10	12	0	60	2 *
uppertuj3-25	397301	3796839	104.7			0	0	
uppertuj3-27	397291	3796845	104.7	10	15	2	40	2 *
uppertuj3-28	397263	3796853	104.7	8	8	90	100	2 *
uppertuj3-29	397256	3796855	104.7	8	8	15	100	1024 *
uppertuj3-30	397244	3796863	104.7	4	4	50	100	256 *
uppertuj3-31	397228	3796874	104.7	2	2	40	100	1024 *
uppertuj3-32	397206	3796879	104.7	5	5	0	100	11 *
uppertuj3-33	397187	3796882	104.7	2.5	3	40	100	512 *
uppertuj3-34	397148	3796886	104.7	2	2	10	0	11 *
uppertuj3-35	397115	3796880	106.3	7	7	40	100	2 *
uppertuj3-36	397086	3796881	106.3	8	6	30	100	256 *
uppertuj3-37	397068	3796896	106.3	8	8	50	100	2 *
uppertuj3-38	397051	3796912	106.3	10	10	30	100	2 *
uppertuj3-39	397044	3796929	106.3	8		15	100	2 *
uppertuj3-40	397039	3796937	106.3	5	8	70	50	90 *
uppertuj3-41	397044	3796945	106.3	5	10	30	100	11 *
uppertuj3-42	397056	3796961	106.3	5	5	20	70	90 *

Station ID	Easting[a]	Northing[a]	Area (km^2)	Bankfull Width (m)	Valley Width (m)	% Rock (bed)	% Rock (bank)	D_{50}
uppertuj3-43	397064	3796970	106.3	3	3	40	100	
uppertuj3-44	397085	3796992	106.3	4	4	10	100	11 *
uppertuj3-45	397100	3797012	106.3	10	10	30	100	11 *
uppertuj3-46	397104	3797030	106.3	8	8	5	100	45 *
uppertuj3-47	397099	3797043	106.3	8	8	60	30	256 *
uppertuj3-48	397084	3797057	106.4	8	8	10	10	11 *
uppertuj3-49	397060	3797056	106.4	8	8	10	50	22 *
uppertuj3-50	397043	3797052	106.4	10	12	0	0	256 *
uppertuj3-51	397029	3797051	106.4			0	0	256 *
uppertuj3-52	397011	3797057	106.4	6	6	10	100	512 *
uppertuj3-53	396986	3797049	106.4	8	8	50	100	11 *
uppertuj3-54	396968	3797048	106.4	6	6	80	100	11 *
uppertuj3-55	396960	3797048	106.4	3	3	90	100	11 *
uppertuj3-56	396960	3797040	106.5	3	3	20	100	256 *
uppertuj3-57	396929	3797043	106.5	6		70	80	11 *
uppertuj3-58	396873	3797038	106.5	8	8	50	100	45 *
uppertuj3-59	396865	3797037	106.5	5	5	5	100	256 *
uppertuj3-60	396847	3797052	106.5	7	7	10	100	2 *
uppertuj3-61	396840	3797053	106.5			0	0	2 *
uppertuj3-61	396831	3797064	106.5			0	0	
uppertuj3-62	396829	3797079	106.5			0	0	
upper_big_tuj-1	397642	3796876	101.9			0	0	
upper_big_tuj-3	397659	3796862	101.8	10	10	0	0	22 *
upper_big_tuj-3	397663	3796858	101.8			0	0	
upper_big_tuj-4	397668	3796856	101.8			0	0	
upper_big_tuj-6	397691	3796832	101.8	10	10	0	0	2 *
upper_big_tuj-7	397711	3796816	101.8	8	12	0	0	11 *
upper_big_tuj-8	397732	3796795	101.8	9		10	0	11 *
upper_big_tuj-9	397757	3796765	101.8	12	25	2	5	11 *
upper_big_tuj-10	397778	3796734	101.8	8		2	5	11 *
upper_big_tuj-11	397790	3796703	101.8	10	25	5	5	90 *
upper_big_tuj-12	397798	3796682	101.8	10	20	20	5	45 *
upper_big_tuj-13	397801	3796638	101.8	10	12	0	0	11 *
upper_big_tuj-14	397805	3796626	101.7	7	20	10	10	90 *
upper_big_tuj-15	397813	3796603	101.7	6	25	0	0	90 *
upper_big_tuj-15	397815	3796600	101.7			0	0	
upper_big_tuj-17	397814	3796599	101.7			0	0	90 *
upper_big_tuj-18	397810	3796588	101.7	11	40	0	0	11 *
upper_big_tuj-18	397811	3796587	101.7			0	0	
upper_big_tuj-19	397812	3796586	101.7			0	0	
upper_big_tuj-20	397811	3796584	101.7			0	0	
upper_big_tuj-21	397813	3796578	101.7			0	0	
upper_big_tuj-22	397824	3796575	101.7			0	0	
upper_big_tuj-23	397826	3796572	101.7			0	0	
upper_big_tuj-25	397860	3796543	101.7			0	0	11 *
bigt_2-1	397647	3796880	101.7			0	0	
bigt_2-2	397666	3796863	101.7			0	0	
bigt_2-3	397673	3796860	101.7			0	0	
bigt_2-5	397696	3796836	101.7	10		0	0	11 *
bigt_2-6	397714	3796820	101.7	10	20	0	0	11 *
bigt_2-7	397737	3796798	101.7	10		5	2	11 *
bigt_2-8	397762	3796768	101.7	9	25	0	2	2 *
bigt_2-8	397783	3796737	101.6			0	0	
bigt_2-10	397796	3796704	101.6	10	20	10	5	90 *
bigt_2-11	397802	3796684	101.6	10	15	30	10	45 *
bigt_2-11	397806	3796641	101.6			0	0	
bigt_2-13	397817	3796593	101.6	7	15	5	2	90 *
bigt_2-14	397824	3796570	101.6	6	25	10	2	90 *
bigt_2-15	397829	3796552	101.6			0	0	90 *
bigt_2-15	397828	3796532	101.6			0	0	
bigt_2-16	397835	3796520	101.6			0	0	
bigt_2-17	397839	3796503	101.6			0	0	
bigt_2-19	397853	3796485	101.6			0	0	90 *
bigt_2-20	397886	3796451	101.6	10		1	0	11 *
bigt_2-21	397916	3796435	101.6	10		40	20	11 *
bigt_2-22	397947	3796425	101.6	7		30	50	90 *

Station ID	Easting[a]	Northing[a]	Area (km^2)	Bankfull Width (m)	Valley Width (m)	% Rock (bed)	% Rock (bank)	D$_{50}$
bigt_2-23	397984	3796417	101.6	9		15	40	90 *
bigt_2-24	397998	3796405	101.5	4		50	60	11 *
bigt_2-25	398035	3796409	101.5	12		0	0	90 *
bigt_2-26	398084	3796456	101.5	10		0	0	90 *
bigt_2-27	398096	3796505	101.4	6		0	0	45 *
bigt_2-28	398094	3796564	101.3	10		10	20	11 *
bigt_2-29	398086	3796590	101.3	10		10	75	11 *
bigt_2-30	398085	3796602	101.3	4	20	60	90	90 *
bigt_2-31	398070	3796641	101.2	10		15	15	11 *
bigt_2-32	398055	3796674	101.2	11		5	0	90 *
bigt_2-33	398046	3796712	101.2			0	0	11 *
bigt_2-34	398048	3796729	101.2			5	2	90 *
bigt_2-35	398043	3796735	101.2			50	50	90 *
bigt_2-36	398050	3796745	101.2			0	0	90 *
bigt_2-36	398059	3796750	101.2			0	0	
bigt_2-37	398061	3796761	101.2			0	0	
bigt_2-39	398067	3796767	101.2	8		0	0	11 *
bigt_2-40	398090	3796781	100.4	6		0	0	90 *
bigt_2-41	398106	3796784	100.3			90	40	11 *
bigt_2-42	398130	3796774	100.3	14		0	0	11 *
bigt_2-43	398180	3796729	100.3	10		2	5	11 *
bigt_2-44	398200	3796710	100.3	2		50	80	11 *
bigt_2-45	398205	3796707	100.3	2		95	100	11 *
bigt_2-46	398237	3796698	100.3	7		20	40	45 *
bigt_2-47	398259	3796699	100.3	7		15	0	45 *
bigt_2-48	398278	3796740	100.3	8		0	0	90 *
bigt_2-49	398281	3796793	100.2	12		0	15	11 *
bigt_2-49	398313	3796838	100.2			0	0	
bigt_2-51	398356	3796860	100.2	10		2	2	90 *
bigt_2-52	398414	3796878	90.5	10		30	25	22 *
bigt_2-53	398441	3796891	90.5	8		30	10	90 *
bigt_2-53	398470	3796919	90.5			0	0	
bigt_2-55	398488	3796935	90.5	5		0	5	90 *
bigt_2-56	398496	3796946	90.5			0	5	90 *
bigt_2-57	398510	3796964	90.5	7		0	2	90 *
bigt_2-57	398509	3796977	90.5			0	0	
bigt_2-59	398517	3796990	90.5			0	0	90 *
bigt_2-59	398527	3796988	90.5			0	0	
bigt_2-60	398536	3796990	90.5			0	0	
bigt_2-61	398542	3796993	90.5			0	0	
bigt_2-62	398551	3797002	90.5			0	0	
bigt_2-63	398562	3797006	90.5			0	0	
bigt_2-64	398568	3797009	90.4			0	0	
bigt_2-65	398576	3797014	90.4			0	0	
bigt_2-67	398585	3797018	90.4			0	0	90 *
bigt_2-68	398588	3797022	90.4			0	0	90 *
bigt_2-69	398604	3797031	90.4			0	0	45 *
bigt_2-69	398618	3797032	90.4			0	0	
bigt_2-70	398626	3797035	90.4			0	0	
bigt_2-71	398630	3797034	90.4			0	0	
bigt_2-72	398636	3797032	90.4			0	0	
bigt_2-73	398655	3797031	89.7			0	0	
bigt_2-74	398665	3797029	89.7			0	0	
bigt_2-75	398672	3797028	89.7			0	0	
bigt_2-76	398683	3797025	89.7			0	0	
bigt_2-77	398690	3797023	89.7			0	0	
bigt_2-78	398703	3797021	89.7			0	0	
bigt_2-79	398715	3797018	89.7			0	0	
bigt_2-80	398729	3797012	89.7			0	0	
bigt_2-81	398745	3797001	89.7			0	0	
bigt_2-82	398760	3796992	89.7			0	0	
bigt_2-83	398775	3796988	89.7			0	0	
bigt_2-85	398783	3796979	88.6			0	0	45 *
bigt_2-85	398808	3796962	88.6			0	0	
bigt_2-86	398815	3796948	88.5			0	0	
bigt_2-88	398824	3796934	88.5			0	0	45 *

Station ID	Easting[a]	Northing[a]	Area (km^2)	Bankfull Width (m)	Valley Width (m)	% Rock (bed)	% Rock (bank)	D_{50}
bigt_2-89	398857	3796900	88.5	8		0	0	22 *
bigt_2-89	398866	3796891	88.5			0	0	
bigt_2-90	398879	3796875	88.5			0	0	
bigt_2-91	398886	3796870	88.5			0	0	
bigt_2-92	398897	3796855	88.5			0	0	
bigt_2-93	398905	3796846	88.4			0	0	
bigt_2-94	398917	3796832	88.4			0	0	
bigt_2-96	398922	3796825	88.4			0	0	45 *
bigt_2-97	398923	3796819	88.4			0	0	45 *
bigt_2-98	398937	3796810	88.4			0	0	45 *
bigt_2-98	398942	3796806	88.4			0	0	
bigt_2-99	398946	3796805	88.4			0	0	
bigt_2-100	398958	3796794	88.4			0	0	
bigt_2-101	398975	3796787	88.4			0	0	
bigt_2-102	398994	3796774	88.4			0	0	
bigt_2-104	399001	3796767	88.4			0	0	45 *
bigt_2-105	399015	3796760	88.4	8		30	0	90 *
bigt_2-106	399024	3796755	88.4	8		0	15	90 *
bigt_2-106	399039	3796742	88.4			0	0	
bigt_2-107	399043	3796737	88.4			0	0	
bigt_2-109	399067	3796728	88.3			0	0	90 *
bigt_2-110	399077	3796722	88.3	8		95	100	90 *
bigt_2-111	399090	3796717	88.3	8		0	2	90 *
bigt_2-112	399112	3796716	88.3	8		5	15	90 *
bigt_2-113	399124	3796722	88.3			0	0	90 *
bigt_2-114	399137	3796724	88.3			0	0	90 *
bigt_2-115	399154	3796746	88.3	7		0	0	90 *
bigt_2-116	399166	3796782	88.2	8		0	0	90 *
bigt_2-117	399187	3796821	88.2			0	0	90 *
bigt_2-118	399219	3796855	88.2	8		20	40	22 *
bigt_2-119	399248	3796872	85.9	6		10	10	90 *
bigt_2-120	399267	3796879	85.9	7		0	0	90 *
bigt_2-121	399300	3796876	85.9	8		40	30	90 *
bigt_2-122	399343	3796881	85.9	8		15	5	11 *
bigt_2-123	399368	3796875	85.9	6		5	0	45 *
bigt_2-124	399377	3796877	85.9	8		0	0	45 *
bigt_2-125	399393	3796877	85.9	6		10	5	90 *
bigt_2-125	399397	3796877	85.8			0	0	
bigt_2-126	399408	3796879	85.8			0	0	
bigt_2-127	399417	3796880	85.8			0	0	
bigt_2-129	399430	3796881	85.8	6		0	0	45 *
bigt_2-130	399448	3796894	85.8	8		0	0	90 *
bigt_2-130	399464	3796898	85.7			0	0	*
bigt_2-132	399471	3796899	85.7	5		0	0	90 *
bigt_2-132	399477	3796897	85.7			0	0	
bigt_2-133	399486	3796895	85.7			0	0	
bigt_2-134	399512	3796886	85.7			0	0	
bigt_2-135	399526	3796882	85.7			0	0	
bigt_2-137	399535	3796875	85.7	4		0	0	22 *
bigt_2-137	399541	3796871	85.7			0	0	
bigt_2-138	399549	3796864	85.7			0	0	
bigt_2-139	399555	3796860	85.7			0	0	
bigt_2-140	399567	3796854	85.7			0	0	
bigt_2-141	399574	3796850	85.7			0	0	
bigt_2-142	399578	3796849	85.7			0	0	
bigt_2-143	399579	3796847	85.7			0	0	
bigt_2-145	399578	3796842	85.7			0	0	22 *
bigt_2-146	399575	3796832	85.6			0	0	22 *
bigt_2-147	399609	3796809	85.6			0	0	11 *
bigt_2-148	399634	3796799	85.6			0	0	45 *
bigt_2-149	399663	3796783	85.6			0	0	90 *
bigt_2-150	399689	3796773	85.6			0	5	45 *
bigt_2-150	399696	3796769	85.6			0	0	
bigt_2-151	399712	3796758	85.6			0	0	
bigt_2-153	399812	3796738	85.6	8		1	10	11 *
bigt_2-154	399817	3796734	85.6			20	30	11 *

Station ID	Easting[a]	Northing[a]	Area (km^2)	Bankfull Width (m)	Valley Width (m)	% Rock (bed)	% Rock (bank)	D_{50}
bigt_2-155	399825	3796735	85.6			0	0	90 *
bigt_2-156	399835	3796735	85.6			30	40	90 *
bigt_2-157	399837	3796741	85.6			0	0	90 *
bigt_2-158	399854	3796743	85.6			0	0	90 *
bigt_2-159	399878	3796759	85.5			0	0	11 *
bigt_2-160	399886	3796761	85.5	6		30	5	11 *
bigt_2-161	399895	3796769	77.9			0	0	11 *
bigt_2-162	399907	3796778	77.8			50	5	11 *
bigt_2-163	399912	3796784	77.8			0	0	45 *
bigt_2-163	399924	3796792	77.8			0	0	
bigt_2-164	399939	3796802	77.8			0	0	
bigt_2-166	399960	3796814	77.7			10	80	45 *
bigt_2-167	399964	3796819	77.7			0	0	90 *
bigt_2-167	399975	3796826	77.7			0	0	
clby-0	395656	3792780	1.6	5.0	5	0	0	
clby-1	395634	3792787	1.6	4.9	5	0	100	
clby-2	395622	3792788	1.6	4.5	5	0	100	
clby-3	395611	3792774	1.6	4.0	4	0	100	
clby-4	395606	3792757	1.6	4.2	4	5	60	128
clby-5	395595	3792741	1.6	5.1	5	0	50	
clby-6	395587	3792723	1.6		5	10	50	
clby-7	395571	3792729	1.6	3.9	4	10	80	
clby-8	395564	3792726	1.6		4	20	100	
clby-9	395552	3792709	1.6	4.2	4	0	70	
clby-10	395542	3792689	1.7		6	10	50	
clby-11	395551	3792681	1.7		6	0	0	
clby-12	395551	3792666	1.7	5.6	7	10	20	
clby-13	395543	3792655	1.7	4.5	5	5	40	
clby-14	395531	3792651	1.7	4.0	4	5	50	128
clby-15	395516	3792653	1.7	4.3	4	20	50	
clby-16	395509	3792643	1.7	5.0	5	0	0	180
clby-17	395518	3792627	1.7	4.9	6	0	30	180
clby-18	395513	3792614	1.7	5.0	6	0	0	180
clby-19	395503	3792605	1.7	5.0	6	0	20	180
clby-20	395495	3792592	1.7	4.5	6	0	50	90
clby-21	395484	3792581	2.6	4.6	8	0	0	90
clby-22	395472	3792592	2.6	5.9	8	0	0	
clby-23	395461	3792602	2.6	4.9	12	0	0	90
clby-24	395449	3792600	2.6		8	0	30	
clby-25	395439	3792589	2.6	4.3	5	0	0	
clby-26	395426	3792574	2.6	4.4	5	5	0	
clby-27	395417	3792569	2.6	3.9	5	30	30	180
clby-28	395404	3792564	2.6	5.0	5	10	20	
clby-29	395390	3792561	2.6	5.0	5	10	80	
clby-30	395376	3792553	2.6	4.0	4	0	70	
clby-31	395362	3792543	2.7	5.0	8	10	20	
clby-32	395341	3792538	2.7	5.4	5	20	60	
clby-33	395326	3792536	2.7	5.3	10	0	0	
clby-34	395312	3792535	2.7	5.3	13	0	0	128
clby-35	395304	3792527	2.7	5.7	11	0	0	
clby-36	395286	3792526	2.7	5.3	7	60	0	
clby-37	395264	3792523	2.7	4.9	7	10	0	
clby-38	395255	3792540	2.7	5.8	8	30	30	
clby-39	395240	3792550	2.7		13	0	0	
clby-40	395224	3792545	2.7		8	0	0	
clby-41	395200	3792540	2.7		9	0	0	
switz-0	393756	3791135	12.1		8	0	0	
switz-1	393766	3791120	12.1	6.6	9	0	70	256
switz-2	393786	3791114	12.1	6.2	10	0	50	256
switz-3	393818	3791114	12.1	7.0	13	5	30	180
switz-4	393839	3791115	12.1	5.7	9	10	40	
switz-5	393863	3791128	12.1		9	0	20	128
switz-6	393887	3791132	12.1	5.6	9	0	50	180
switz-7	393910	3791113	12.1	7.0	7	0	50	180
switz-8	393926	3791092	12.1	7.4	8	10	20	
switz-9	393948	3791063	12.2	6.8	9	20	50	4

Station ID	Easting[a]	Northing[a]	Area (km^2)	Bankfull Width (m)	Valley Width (m)	% Rock (bed)	% Rock (bank)	D_{50}
switz-10	393944	3791020	12.2	7.5	8	30	80	180
switz-11	393940	3791011	12.3	5.9	6	95	100	
switz-12	393937	3790987	12.3	10.6	11	50	100	
switz-13	393933	3790954	12.3	7.2	8	5	30	180
switz-14	393939	3790934	12.3	8.0	12	0	0	180
switz-15	393975	3790930	12.3	6.8	12	0	20	
switz-16	393981	3790916	12.3	6.8	18	0	30	180
switz-17	393962	3790890	12.3	7.6	15	0	20	128
switz-18	393949	3790877	12.3	7.5	17	0	0	180
switz-19	393968	3790843	12.3	8.2	12	0	20	180
switz-20	394006	3790835	12.3	8.2	13	0	0	
switz-21	394044	3790812	12.3	8.7	15	0	0	128
switz-22	394067	3790792	12.4	7.1	12	0	0	
switz-23	394094	3790783	12.4	8.8	22	0	0	90
switz-24	394113	3790807	12.4		37	0	0	
switz-25	394148	3790838	12.4		39	0	0	180
switz-26	394179	3790855	12.4	8.4	20	0	0	128
switz-27	394202	3790834	12.4	8.0	31	0	0	128
switz-29	394195	3790809	12.4		25	0	0	
switz-30	394198	3790790	12.4	6.8	15	0	0	180
switz-31	394217	3790781	12.4	7.3	9	0	50	
switz-32	394238	3790770	12.4		11	0	0	
switz-33	394253	3790748	12.4	7.0	20	0	0	128
switz-34	394241	3790740	12.4	5.8	16	30	50	
switz-35	394226	3790728	12.4	10.4	9	20	75	
switz-36	394198	3790700	12.4	7.3	13	10	30	180
switz-37	394180	3790676	12.4	6.5	16	0	20	180
switz-38	394156	3790676	12.4	6.5	12	30	50	
switz-39	394148	3790673	12.5	5.1	7	90	100	
switz-40	394131	3790656	12.5	10.6	11	20	100	
switz-41	394125	3790645	12.5	10.0	11	30	100	
switz-42	394166	3790621	12.5	6.9	9	0	10	256
switz-43	394181	3790618	12.5	9.1	9	20	100	
switz-44	394205	3790613	12.5	6.8	7	30	100	
switz-45	394210	3790604	12.5	6.2	7	0	50	180
switz-46	394211	3790575	12.5	6.6	7	0	40	180
switz-47	394225	3790546	12.5	6.4	7	20	70	
switz-48	394224	3790540	12.5	6.3	7	100	100	
switz-49	394220	3790523	15.0		10	0	0	
switz-50	394210	3790506	15.0	7.3	14	0	0	256
switz-51	394202	3790444	15.0	8.3	12	0	30	180
switz-52	394199	3790421	15.0	7.8	10	0	0	
switz-53	394205	3790390	15.0	8.1	9	0	50	
bearcyn-0	395337	3789437	5.5		23	0	0	
bearcyn-1	395302	3789451	5.5	6.2	24	0	30	64
bearcyn-2	395292	3789473	5.5	7.3	14	0	0	
bearcyn-3	395283	3789505	5.6	7.0	13	30	50	
bearcyn-4	395285	3789525	5.6	6.5	12	5	10	
bearcyn-5	395272	3789550	5.6	6.0	13	0	0	180
bearcyn-6	395258	3789563	5.6	6.1	14	5	60	64
bearcyn-7	395223	3789563	5.6	5.7	10	0	0	128
bearcyn-8	395193	3789583	5.6	6.5	14	0	20	64
bearcyn-9	395174	3789596	5.6		22	0	0	
bearcyn-10	395159	3789617	5.7	7.5	57	0	10	128
bearcyn-11	395166	3789660	5.7	7.1	35	0	0	
bearcyn-12	395184	3789688	5.7		27	0	0	
bearcyn-13	395181	3789705	5.7		42	0	0	
bearcyn-14	395179	3789722	5.7	7.2	42	0	0	
bearcyn-15	395163	3789729	5.7	6.9	40	0	0	
bearcyn-16	395140	3789716	5.7	5.9	34	0	30	128
bearcyn-17	395122	3789701	5.7	5.8	23	0	0	64
bearcyn-18	395108	3789708	5.7	6.2	21	0	0	64
bearcyn-19	395093	3789729	5.7		20	0	0	
bearcyn-20	395092	3789755	5.8	5.6	16	0	0	
bearcyn-21	395074	3789761	5.8	6.7	15	0	0	128
bearcyn-22	395068	3789751	5.8	6.0	6	30	50	

Station ID	Easting[a]	Northing[a]	Area (km^2)	Bankfull Width (m)	Valley Width (m)	% Rock (bed)	% Rock (bank)	D_{50}
bearcyn-23	395059	3789739	5.8	6.5	7	10	10	128
bearcyn-24	395036	3789739	5.8	5.0	6	0	30	128
bearcyn-25	395016	3789753	5.8	5.0	9	0	30	128
bearcyn-26	395007	3789765	5.8	5.7	8	0	0	
bearcyn-27	394987	3789757	5.8	5.8	6	10	60	
bearcyn-28	394984	3789742	5.8	5.7	12	0	50	
bearcyn-29	394986	3789698	5.8	6.3	12	0	0	
bearcyn-30	394972	3789678	5.8	5.7	11	0	0	128
bearcyn-31	394946	3789683	5.8	5.1	7	0	50	
bearcyn-32	394933	3789695	5.8	5.7	6	0	50	128
bearcyn-33	394899	3789708	5.8	5.6	6	0	50	128
bearcyn-34	394882	3789716	5.9		8	0	0	
bearcyn-35	394862	3789715	5.9	5.7	9	0	45	128
bearcyn-36	394832	3789726	5.9	5.0	8	0	30	128
bearcyn-37	394815	3789741	5.9	4.7	8	0	20	128
bearcyn-38	394795	3789760	5.9	5.0	7	0	10	128
bearcyn-39	394789	3789775	5.9		7	0	0	
bearcyn-40	394787	3789785	5.9		6	0	0	
bearcyn-41	394785	3789811	6.0		7	0	0	
bearcyn-42	394769	3789843	6.0	5.1	8	0	20	90
bearcyn-43	394756	3789865	6.0	5.4	7	0	5	128
bearcyn-44	394746	3789885	6.3	6.0	17	0	0	128
bearcyn-45	394729	3789915	6.3		13	0	0	180
bearcyn-46	394744	3789939	6.3		12	0	0	128
bearcyn-47	394752	3789949	6.3		23	0	0	
bearcyn-48	394749	3789971	6.3	6.4	18	0	0	128
bearcyn-49	394738	3789985	6.3	5.4	16	0	0	360
bearcyn-50	394718	3790000	6.4	5.7	10	0	0	180
bearcyn-51	394693	3790011	6.4	5.7	10	0	10	
bearcyn-52	394678	3790015	6.4		16	0	0	
bearcyn-53	394670	3790029	6.4	6.2	15	0	0	90
bearcyn-54	394686	3790072	6.4	5.5	10	0	0	90
bearcyn-55	394695	3790091	6.4	6.1	13	5	10	128
bearcyn-56	394692	3790109	6.4		21	0	0	
bearcyn-57	394671	3790112	6.5	5.9	19	0	0	180
bearcyn-58	394614	3790120	6.5	6.0	11	0	20	64
bearcyn-59	394594	3790143	6.5	6.5	12	0	0	128
bearcyn-60	394593	3790161	6.5		12	0	0	
bearcyn-61	394609	3790169	6.5	6.0	15	5	5	128
bearcyn-62	394613	3790183	6.7		13	0	5	
bearcyn-63	394592	3790228	6.7	6.5	15	0	30	128
bearcyn-64	394582	3790244	6.7		15	0	0	700
bearcyn-65	394565	3790258	6.7	6.5	13	0	0	
bearcyn-66	394532	3790259	6.7		18	0	0	
bearcyn-67	394496	3790260	6.7		17	0	0	
bearcyn-68	394470	3790264	6.7		12	0	0	
bearcyn-69	394422	3790267	6.8	5.6	9	0	10	
bearcyn-70	394404	3790309	6.8	7.4	13	0	0	128
bearcyn-71	394390	3790324	6.8	6.0	13	0	50	
bearcyn-72	394375	3790315	6.8	6.1	10	0	50	2
bearcyn-73	394367	3790290	6.8	6.0	10	0	5	180
bearcyn-74	394313	3790319	6.8	7.1	8	0	10	90
bearcyn-75	394301	3790317	6.8	4.4	6	0	50	
bearcyn-76	394285	3790301	6.8	5.8	6	0	30	180
bearcyn-77	394268	3790288	6.8	4.9	7	0	30	
bearcyn-78	394260	3790294	6.8		8	0	0	
bearcyn-79	394251	3790322	6.8	6.0	6	0	50	128
bearcyn-80	394230	3790364	6.8	5.5	6	0	60	128
bearcyn-81	394207	3790390	6.8	5.0	7	0	0	
bigrock_1	423611	3804438	17.6	8.0		0	0	32
bigrock_2	423677	3804534	17.7	8.0		0	0	32
bigrock_3	423748	3804616	17.8	8.0		0	0	22
bigrock_4	423845	3804789	18.1	8.0		0	0	22
bigrock_5	423909	3804878	18.3	8.0		0	0	
bigrock_6	423997	3804994	18.4	9.0		0	0	32
bigrock_7	424200	3805039	18.5	9.0		0	0	22

Station ID	Easting[a]	Northing[a]	Area (km^2)	Bankfull Width (m)	Valley Width (m)	% Rock (bed)	% Rock (bank)	D$_{50}$
bigrock_8	424204	3805299	19.4	9.0		0	0	22
bigrock_9	424281	3805429	19.8	6.0		0	0	32
devils_a_1	410281	3794733	25.9	8.0		0	0	
devils_a_2	410377	3794830	25.8	9.0		0	0	
devils_a_3	410379	3794982	25.7	9.0		0	0	
devils_a_4	410261	3795190	25.5	10.0		0	0	
devils_a_5	410250	3795209	25.5	9.0		0	0	
devils_a_6	410245	3795266	25.3	14.0		0	0	
devils_a_7	410115	3795469	24.0	9.0		0	0	
devils_a_8	410117	3795540	24.0			0	0	
devils_a_9	409873	3795859	23.5	9.0		0	0	
devils_a_10	409871	3796017	22.0	9.0		0	0	
devils_a_11	409813	3796085	22.0	9.0		0	0	
devils_a_12	409774	3796112	22.0	9.0		0	0	
devils_a_13	409767	3796217	21.9	9.0		0	0	
devils_a_14	409812	3796478	21.6	11.0		0	0	
devils_a_15	409763	3796782	20.3			0	0	
devils_a_16	409646	3796776	20.2	11.0		0	0	
upperlrc-0	416016	3803349	22.6	9.5		0	0	
upperlrc-1	416036	3803352	22.6	8.7	10	20	5	8
upperlrc-2	416050	3803353	22.6	7.2	10	80	80	11
upperlrc-3	416069	3803354	22.6	8.0	10	20	10	11
upperlrc-4	416104	3803357	22.6	8.4	9	5	0	64
upperlrc-5	416118	3803355	22.6			0	0	
upperlrc-6	416145	3803354	22.6	8.5	19	50	10	2
upperlrc-7	416171	3803350	22.6	10.5	11	25	25	2
upperlrc-8	416188	3803333	22.5	8.9	18	5	5	180
upperlrc-9	416206	3803320	22.5	8.0	18	0	0	45
upperlrc-10	416228	3803299	22.5	8.0	25	5	50	2
upperlrc-11	416274	3803316	22.5	8.0	23	0	0	64
upperlrc-12	416304	3803328	22.5	7.5		0	50	128
upperlrc-13	416316	3803319	21.6	6.4		15	50	128
upperlrc-14	416324	3803300	21.6	7.8	12	0	0	180
upperlrc-15	416337	3803269	21.6	8.1		40	50	64
upperlrc-16	416359	3803268	21.5	8.0		10	10	45
upperlrc-17	416376	3803283	21.5	9.5	15	5	5	45
upperlrc-18	416407	3803278	21.5	10.5	30	0	0	90
upperlrc-19	416420	3803280	21.5			0	0	45
upperlrc-20	416433	3803264	21.5			0	0	
upperlrc-21	416443	3803249	21.4	8.5		0	0	
upperlrc-22	416448	3803227	21.4	8.9		0	0	32
upperlrc-23	416455	3803199	21.4			10	10	16
upperlrc-24	416460	3803172	21.4	11.0		0	0	64
littlerk-0	413224	3807250	37.9			0	0	
littlerk-1	413207	3807258	37.9	7.8	8	0	50	90
littlerk-2	413192	3807263	37.9	9.6	12	0	50	360
littlerk-3	413182	3807278	38.0	11.5	12	25	50	32
littlerk-4	413171	3807290	38.0	10.7	11	5	30	16
littlerk-5	413165	3807302	38.0	10.7	11	0	20	16
littlerk-6	413156	3807311	38.0	11.5	12	70	20	1000
littlerk-7	413134	3807308	38.0	9.9		70	75	128
littlerk-8	413102	3807303	38.0	11.9	16	50	50	90
littlerk-9	413088	3807313	38.0	10.0	13	10	70	32
littlerk-10	413085	3807322	38.0	9.5	9	5	100	32
littlerk-11	413074	3807329	38.0	9.8	10	0	100	180
littlerk-12	413046	3807345	38.0	6.0	6	40	100	256
littlerk-13	413033	3807349	38.0	8.8	9	70	80	128
littlerk-14	413001	3807356	38.0	10.0	12	15	100	22
littlerk-15	412985	3807361	38.0	9.1	10	20	60	64
littlerk-16	412968	3807353	38.0	10.6	12	0	20	22
littlerk-17	412953	3807345	38.0	9.9	15	0	0	90
littlerk-18	412932	3807345	38.0	12.0	14	0	25	11
littlerk-19	412914	3807352	38.1	13.2	16	0	0	32
littlerk-20	412898	3807360	38.2	12.8	17	0	20	11
littlerk-21	412889	3807362	38.3	11.9	12	0	0	11
littlerk-22	412879	3807368	38.4	12.0	15	0	30	22

Station ID	Easting[a]	Northing[a]	Area (km^2)	Bankfull Width (m)	Valley Width (m)	% Rock (bed)	% Rock (bank)	D$_{50}$
littlerk-23	412844	3807387	38.6	9.5	10	10	30	11
littlerk-24	412829	3807389	38.6	11.4	11	0	90	45
littlerk-25	412819	3807384	38.6	11.5	12	0	80	64
littlerk-26	412804	3807392	38.6	11.5	12	0	90	45
littlerk-27	412778	3807414	38.6	10.2	11	0	60	16
littlerk-28	412760	3807436	38.6	9.5	10	5	75	22
littlerk-29	412750	3807447	38.7	10.5	11	0	75	256
littlerk-30	412739	3807469	38.7	10.3	15	5	50	32
littlerk-31	412733	3807479	38.7	11.1	13	0	25	22
littlerk-32	412713	3807486	38.7	12.5	13	0	90	45
littlerk-33	412700	3807485	38.7	9.7	10	0	25	32
littlerk-34	412685	3807480	38.7	8.5	10	0	70	8
littlerk-35	412674	3807480	38.7	9.4	10	15	20	180
littlerk-36	412652	3807479	38.7	9.9	15	30	50	32
littlerk-37	412632	3807473	38.7	8.1	8	30	60	45
littlerk-38	412602	3807473	38.7	7.3	7	5	95	16
littlerk-39	412576	3807462	38.7	10.1	10	10	75	32
littlerk-40	412561	3807440	38.7	6.5	8	25	40	90
littlerk-41	412541	3807418	39.4	9.7	12	5	15	22
littlerk-42	412511	3807395	39.4	9.8	11	0	0	45
littlerk-43	412488	3807395	39.4	7.5	10	0	50	45
littlerk-44	412476	3807404	39.4	11.3	11	0	50	32
littlerk-45	412453	3807407	39.4	12.5	20	0	0	45
littlerk-46	412432	3807408	39.4	12.7	18	0	25	32
littlerk-47	412397	3807415	39.5	10.0	20	0	0	32
littlerk-48	412373	3807418	39.5	10.0	15	0	30	32
littlerk-49	412355	3807418	39.5	10.0	10	0	0	32
littlerk-50	412341	3807420	39.5	10.0	12	0	30	32
littlerk-51	412324	3807430	39.5	10.0	20	0	0	45
littlerk-52	412293	3807439	39.5	9.7	20	0	40	32
littlerk-53	412281	3807447	39.5	10.0		0	0	32
littlerk-54	412266	3807465	39.5	11.3	18	0	0	45
littlerk-55	412236	3807483	39.6	10.8	17	0	20	16
littlerk-56	412207	3807502	39.6	10.0		0	35	16
littlerk-57	412181	3807505	39.6	8.8	32	0	50	4
littlerk-58	412159	3807495	39.6	8.9	25	0	0	32
littlerk-59	412130	3807491	39.7	10.6	25	0	0	16
arroyo-0	393054	3790026	24.4		9	0	0	
arroyo-1	393041	3790045	24.4	8.4	14	70	50	
arroyo-2	393025	3790059	24.4	7.5	11	60	60	
arroyo-3	393004	3790070	24.4	7.0	8	10	100	90
arroyo-4	392986	3790078	24.4	6.8	7	0	75	
arroyo-5	392976	3790081	24.4	7.0	11	10	50	180
arroyo-6	392964	3790076	24.4	8.4	10	5	50	90
arroyo-7	392952	3790063	24.4	7.1	7	5	75	90
arroyo-8	392937	3790044	24.4	6.4	6	0	100	11
arroyo-9	392920	3790021	24.4	6.4	6	0	100	11
arroyo-10	392890	3790030	24.4	6.5	10	0	50	22
arroyo-11	392884	3790038	24.4	7.0	15	0	50	16
arroyo-12	392885	3790049	24.4	10.0	18	0	20	256
arroyo-13	392878	3790056	24.4	12.0	12	0	10	128
arroyo-14	392871	3790078	24.4		10	0	0	
arroyo-15	392863	3790093	24.5	7.6	9	10	50	90
arroyo-16	392856	3790106	24.5	6.8	8	10	50	
arroyo-17	392846	3790113	24.5	7.3	10	40	40	22
arroyo-18	392834	3790125	24.5	8.7	12	5	10	90
arroyo-19	392820	3790129	24.5	8.0	10	0	0	64
arroyo-20	392796	3790135	24.5	7.0	9	0	50	
arroyo-21	392786	3790121	24.5	7.4	9	0	30	180
arroyo-22	392768	3790101	24.5	8.0	12	0	50	45
arroyo-23	392766	3790089	24.5		11	0	0	
arroyo-24	392770	3790069	24.5	9.0	9	0	90	32
arroyo-25	392774	3790032	24.5	7.7	11	5	0	90
arroyo-26	392785	3790012	24.5	7.9	12	0	0	64
arroyo-27	392813	3789988	24.5	7.8	9	0	60	32
arroyo-28	392814	3789973	24.5	9.9	12	0	40	90

Station ID	Easting[a]	Northing[a]	Area (km^2)	Bankfull Width (m)	Valley Width (m)	% Rock (bed)	% Rock (bank)	D$_{50}$
arroyo-29	392803	3789958	24.5	7.0	7	20	50	
arroyo-30	392780	3789957	24.5	7.0	8	0	40	64
arroyo-31	392766	3789952	24.5	10.0	15	0	0	45
arroyo-32	392748	3789949	24.5	10.0	17	0	10	64
arroyo-33	392738	3789950	24.5		14	0	0	
arroyo-34	392728	3789945	24.5		21	0	0	
arroyo-35	392721	3789949	24.5		26	0	0	
arroyo-36	392715	3789945	24.6	12.0	27	0	0	32
arroyo-37	392688	3789939	24.6	12.3	33	0	0	128
arroyo-38	392663	3789937	24.6	12.5	33	0	0	128
arroyo-39	392640	3789935	24.6	10.5	24	0	30	64
arroyo-40	392627	3789926	24.6	12.5	13	0	0	90
arroyo-41	392620	3789913	24.6		13	0	0	
arroyo-42	392627	3789893	24.6		17	0	5	64
arroyo-43	392620	3789870	24.6	10.4	23	0	0	32
arroyo-44	392580	3789861	24.6	12.0	15	0	0	90
arroyo-45	392550	3789878	24.6	13.0	25	0	0	45
arroyo-46	392536	3789914	24.6	12.0	28	0	0	45
arroyo-47	392525	3789934	24.6	8.6	25	0	40	64
arroyo-48	392504	3789953	24.6	11.7	25	0	0	90
arroyo-49	392494	3789964	24.7	11.7	25	0	50	45
arroyo-50	392477	3789970	24.7		40	10	50	64
arroyo-51	392454	3789949	24.8		40	5	50	90
arroyo-52	392410	3789927	24.8	10.5	36	0	0	64
arroyo-53	392373	3789921	24.9	14.0	33	0	0	64
arroyo-54	392349	3789947	24.9	14.6	27	0	0	64
arroyo-55	392345	3789981	25.0		22	0	0	
arroyo-56	392319	3790011	25.0	10.0	13	0	40	64
arroyo-57	392303	3790024	25.0	11.4	18	0	20	45
arroyo-58	392283	3790037	25.0	11.0	20	0	0	64
arroyo-59	392249	3790045	25.1	12.1	25	0	25	45
arroyo-60	392217	3790054	25.1	8.0	30	0	0	90
arroyo-61	392188	3790054	25.1	7.9	28	0	0	90
devils-0	410397	3794148	31.0	6.5	7	0	0	
devils-1	410391	3794157	31.0	8.5		100	100	
devils-2	410388	3794160	31.0			10	50	2000
devils-3	410379	3794165	31.0			0	0	
devils-4	410370	3794172	31.0			10	0	45
devils-5	410357	3794197	30.9	9.0	16	0	0	128
devils-6	410347	3794208	30.9	7.9	15	0	0	90
devils-7	410349	3794223	30.9	11.2	15	5	25	90
devils-8	410347	3794242	30.9	12.3	12	40	90	90
devils-9	410350	3794260	30.9	8.5		50	100	8
devils-10	410346	3794270	29.1	8.7		10	100	180
devils-11	410342	3794277	29.0			0	0	
devils-12	410339	3794301	29.0	11.3	12	30	25	5
devils-13	410329	3794324	29.0	9.0	12	10	50	256
devils-14	410324	3794342	29.0	8.0		10	20	5
devils-15	410313	3794361	29.0			0	0	
devils-16	410301	3794370	29.0	12.9	13	40	20	64
devils-17	410296	3794375	29.0	10.5	11	95	80	
devils-18	410291	3794389	29.0	9.4	12	60	50	32
devils-19	410286	3794394	29.0			0	0	
devils-20	410278	3794405	29.0	9.8		35	80	32
devils-21	410282	3794423	28.9			0	0	
devils-22	410280	3794426	28.9	10.0		20	50	3000
devils-23	410281	3794441	28.9	8.5		5	0	256
devils-24	410270	3794458	28.9	9.5	15	0	0	128
devils-25	410268	3794469	28.9	10.0		0	20	1000
devils-26	410253	3794495	28.9	8.3	15	40	50	256
devils-27	410250	3794508	28.9	9.0	15	5	40	64
devils-28	410250	3794517	28.9			0	0	
devils-29	410236	3794547	28.9	10.1	10	25	60	90
devils-30	410226	3794578	28.9	11.8	15	10	50	180
devils-31	410216	3794602	28.9	11.0	15	0	20	64
devils-32	410226	3794623	28.8	13.5	20	0	0	720

Station ID	Easting[a]	Northing[a]	Area (km^2)	Bankfull Width (m)	Valley Width (m)	% Rock (bed)	% Rock (bank)	D$_{50}$
devils-33	410229	3794637	28.8	15.4	20	0	0	32
devils-34	410239	3794648	28.8	14.4	17	0	0	90
devils-35	410247	3794660	28.8			0	0	128
devils-36	410253	3794673	26.0	11.7	18	0	0	90
devils-37	410267	3794697	25.9	8.9		0	50	180
devils-38	410273	3794710	25.9	9.6		0	0	180
devils-39	410275	3794723	25.9			0	0	
nfmill-0	395354	3798546	14.4			0	0	
nfmill-1	395364	3798541	14.4	5.0	29	0	0	64
nfmill-2	395374	3798543	14.4	5.0	26	0	0	64
nfmill-3	395391	3798539	14.4	5.4	24	0	0	64
nfmill-4	395403	3798527	14.4	5.5	22	0	0	4
nfmill-5	395410	3798525	14.4		25	0	0	
nfmill-6	395419	3798527	14.5	6.0	27	0	0	90
nfmill-7	395439	3798514	14.5	6.0	29	0	0	32
nfmill-8	395449	3798510	14.5		31	0	25	64
nfmill-9	395454	3798495	14.5	5.0	30	85	50	
nfmill-10	395461	3798480	14.5	6.0	26	0	0	45
nfmill-11	395467	3798467	14.5	5.5	28	0	0	8
nfmill-12	395478	3798463	14.5		28	0	0	45
nfmill-13	395488	3798460	14.5		27	0	0	45
nfmill-14	395496	3798453	14.5	5.5	19	0	0	45
nfmill-15	395508	3798446	14.5	5.2	20	0	0	22
nfmill-16	395527	3798436	14.5	5.5	20	0	0	45
nfmill-17	395544	3798424	14.5	5.1	22	0	0	45
nfmill-18	395561	3798415	14.6	5.0	23	0	0	180
nfmill-19	395571	3798413	14.6		22	0	0	32
nfmill-20	395586	3798408	14.6	5.6	21	0	0	45
nfmill-21	395604	3798401	14.6	5.5	15	5	5	45
nfmill-22	395623	3798386	14.6	6.0	19	5	40	64
nfmill-23	395629	3798373	14.6	6.0	21	0	0	180
nfmill-24	395627	3798368	14.6		21	0	0	256
nfmill-25	395617	3798362	14.6	5.0	18	50	50	180
nfmill-26	395605	3798342	14.6	5.0	19	20	0	32
nfmill-27	395626	3798326	14.6	6.0	18	0	0	45
nfmill-28	395629	3798320	14.6		19	0	0	
nfmill-29	395648	3798316	14.6	5.5	17	0	0	64
nfmill-30	395658	3798305	14.6	6.0	18	40	50	90
nfmill-31	395659	3798293	14.6	6.0	20	5	10	
nfmill-32	395656	3798282	14.6		23	5	0	22
nfmill-33	395645	3798269	14.6	6.9	11	0	0	64
nfmill-34	395635	3798259	14.6	6.4	10	0	0	90
nfmill-35	395618	3798249	14.6	6.9	10	5	30	16
nfmill-36	395606	3798245	14.6	6.0	10	0	0	45
nfmill-37	395595	3798250	14.6		9	0	0	
nfmill-38	395583	3798249	14.7		10	5	20	64
nfmill-39	395574	3798248	14.7	5.5	8	0	0	45
nfmill-40	395569	3798239	14.7		15	0	0	
nfmill-41	395568	3798227	14.7	6.8	16	0	0	180
nfmill-42	395579	3798218	14.7	6.5	15	0	0	64
nfmill-43	395594	3798209	14.7		15	0	0	45
nfmill-44	395599	3798209	14.7		15	0	0	
nfmill-45	395613	3798195	14.7	7.1	8	5	50	45
nfmill-46	395625	3798186	14.7	6.3	8	0	0	45
nfmill-47	395638	3798175	14.7	7.0	7	40	50	360
nfmill-48	395645	3798164	14.8	7.0	10	0	0	45
nfmill-49	395653	3798153	14.8	7.0	12	0	0	64
nfmill-50	395664	3798143	14.8	7.0	10	0	0	45
nfmill-51	395678	3798133	14.8		14	0	0	
nfmill-52	395688	3798124	14.8		18	0	0	45
nfmill-53	395698	3798115	14.9	5.0	13	75	50	
nfmill-54	395703	3798109	14.9	6.0	12	85	60	
nfmill-55	395700	3798096	14.9		14	0	0	45
nfmill-56	395694	3798094	14.9		15	0	0	90
nfmill-57	395688	3798092	14.9		18	0	0	180
nfmill-58	395685	3798087	14.9		18	0	0	

Station ID	Easting[a]	Northing[a]	Area (km^2)	Bankfull Width (m)	Valley Width (m)	% Rock (bed)	% Rock (bank)	D_{50}
nfmill-59	395687	3798077	14.9	5.5	12	80	50	
nfmill-60	395680	3798067	14.9	6.1	10	25	75	45
nfmill-61	395668	3798061	14.9		8	0	0	
nfmill-62	395664	3798059	14.9	6.2	6	0	80	22
nfmill-63	395663	3798053	14.9	6.7	7	50	100	22
nfmill-64	395658	3798036	14.9	6.5	7	25	100	45
nfmill-65	395663	3798021	14.9	7.0	12	0	0	128
nfmill-66	395672	3798009	14.9	7.0	14	0	10	45
nfmill-67	395690	3797995	14.9		12	0	0	
nfmill-68	395693	3797990	15.0	6.8	12	0	30	45
nfmill-69	395719	3797985	15.0		17	0	0	64
nfmill-70	395726	3797982	15.0		18	0	0	
nfmill-71	395746	3797970	15.0	7.0	20	0	0	64
nfmill-72	395760	3797963	15.0		21	0	0	
nfmill-73	395766	3797960	15.0		23	0	0	
nfmill-74	395769	3797952	15.0		22	0	0	
nfmill-75	395765	3797943	15.0		23	0	0	
upeaton-0	399718	3785093	12.5	5.4	5	0	0	
upeaton-1	399730	3785094	12.5	6.6	13	15	50	180
upeaton-2	399735	3785070	12.5	7.2	13	5	0	180
upeaton-3	399752	3785054	12.5	7.5	20	20	70	180
upeaton-4	399766	3785052	12.5	7.0	18	5	70	128
upeaton-5	399788	3785061	12.5	7.1	11	0	50	256
upeaton-6	399809	3785073	12.5	6.2	9	0	50	180
upeaton-7	399831	3785080	12.5	7.7	9	25	50	180
upeaton-8	399849	3785090	12.4	6.7	9	0	50	180
upeaton-9	399858	3785102	12.4	7.7	9	15	50	180
upeaton-10	399874	3785136	12.4	6.4	9	0	50	90
upeaton-11	399875	3785145	12.4	7.0	10	0	50	360
upeaton-12	399867	3785165	12.4	7.6	8	0	30	128
upeaton-13	399857	3785171	12.0	5.8	23	0	35	90
upeaton-14	399825	3785167	12.0	6.9	23	0	0	180
upeaton-15	399799	3785170	12.0	8.1	13	0	0	180
upeaton-16	399788	3785173	12.0	8.0	12	60	50	256
upeaton-17	399769	3785180	12.0	6.7	9	10	50	180
upeaton-18	399766	3785200	12.0	10.1	15	25	20	180
upeaton-19	399783	3785222	12.0	6.8	10	20	50	180
upeaton-20	399794	3785225	12.0	6.0	6	20	100	64
upeaton-21	399800	3785235	12.0	6.5	7	45	50	256
upeaton-22	399817	3785238	12.0	8.0	10	0	30	180
upeaton-23	399845	3785248	12.0	7.6	20	10	10	180
upeaton-24	399867	3785268	11.9	8.1	14	5	30	180
upeaton-25	399867	3785286	11.9	7.8	11	90	100	
upeaton-26	399863	3785295	11.9	11.0	11	10	30	180
upeaton-27	399855	3785306	11.9	8.0	8	5	40	180
upeaton-28	399843	3785320	11.9	7.8	8	50	100	256
upeaton-29	399844	3785339	11.9	8.1	8	20	60	180
upeaton-30	399848	3785345	11.9	8.0	10	10	40	256
upeaton-31	399865	3785352	11.9	9.0	12	10	50	256
upeaton-32	399869	3785357	11.9	6.8	14	80	75	180
upeaton-33	399880	3785366	11.9	9.0	15	30	50	180
upeaton-34	399886	3785376	11.9	6.6	10	0	50	128
upeaton-35	399890	3785389	11.9	7.8	10	75	0	360
upeaton-36	399903	3785408	11.9	7.3	9	60	50	180
upeaton-37	399920	3785421	11.9	8.1	18	5	25	360
upeaton-38	399936	3785421	11.9	7.5	22	70	50	
upeaton-39	399956	3785429	11.9		45	0	10	256
upeaton-40	399964	3785440	11.9	7.9	52	0	0	256
upeaton-41	399974	3785454	11.9	14.5	42	0	9	256
upeaton-42	399986	3785462	11.9		34	0	0	
upeaton-43	400007	3785467	11.9		40	0	0	
upeaton-44	400030	3785497	11.9	9.3	40	0	0	180
upeaton-45	400039	3785522	11.9	7.9	16	35	25	256
upeaton-46	400052	3785530	11.9	7.5	18	15	50	360
upeaton-47	400072	3785534	11.9	6.7	18	10	50	256
upeaton-48	400083	3785529	11.8		20	0	0	

Station ID	Easting[a]	Northing[a]	Area (km^2)	Bankfull Width (m)	Valley Width (m)	% Rock (bed)	% Rock (bank)	D$_{50}$
upeaton-49	400094	3785518	8.8	7.4	34	0	0	256
upeaton-50	400105	3785502	8.8	6.3	38	0	50	256
upeaton-51	400118	3785500	8.8	9.0	36	0	20	256
upeaton-52	400123	3785481	8.8		40	0	0	360
upeaton-53	400153	3785479	8.8	9.9	44	0	0	180
upeaton-54	400171	3785469	8.8	8.7	52	30	40	8
upeaton-55	400189	3785488	8.8		49	90	50	64
upeaton-56	400180	3785530	7.4	8.1	48	0	0	
midcuca-0	442053	3782249	17.7			0	0	
midcuca-1	442066	3782250	17.7	9.0		0	0	256
midcuca-2	442083	3782252	17.7			0	0	
midcuca-3	442098	3782259	17.7	8.0		5	50	
midcuca-4	442109	3782274	17.7	9.0		10	30	
midcuca-5	442125	3782296	17.7	10.0		0	25	128
midcuca-6	442141	3782334	17.7	9.0	60	0	45	45
midcuca-7	442150	3782353	17.3	7.0		0	50	
midcuca-8	442159	3782374	17.3			0	40	
midcuca-9	442170	3782398	17.3	8.0	45	0	50	
midcuca-10	442185	3782425	17.3	8.0	20	0	50	
midcuca-11	442204	3782437	17.3			0	25	
midcuca-12	442214	3782444	17.2			0	0	
midcuca-13	442231	3782469	17.2	10.0	20	0	15	
midcuca-14	442240	3782484	17.2			0	50	128
midcuca-15	442257	3782495	17.2			0	0	
midcuca-16	442282	3782518	17.2	9.0	10	0	50	128
midcuca-17	442306	3782541	17.2	8.0	8	0	100	128
midcuca-18	442335	3782550	17.2	6.0	10	10	60	
midcuca-19	442355	3782577	17.2	8.0	15	0	20	
midcuca-20	442371	3782615	17.2			15	50	32
midcuca-21	442393	3782635	17.1	8.0	8	10	90	90
midcuca-22	442408	3782645	17.1	8.0	8	0	100	128
midcuca-23	442413	3782663	16.8			0	0	
midcuca-24	442421	3782673	16.8			80	100	
midcuca-25	442433	3782681	16.8			0	0	
ice-0	443329	3789686	4.6	2.0	35	0	0	128
ice-1	443321	3789680	4.7			0	0	
ice-2	443308	3789680	4.7			0	0	
ice-3	443296	3789681	4.7			0	0	
ice-4	443288	3789678	5.5			0	0	
ice-5	443284	3789675	5.5			0	0	90
ice-6	443275	3789675	5.6	3.0	20	0	0	
ice-7	443253	3789688	5.6	4.0	10	0	0	180
ice-8	443227	3789696	5.6	4.0	12	0	0	64
ice-9	443224	3789697	5.6			0	0	
ice-10	443191	3789688	5.6	6.0	25	0	0	32
ice-11	443184	3789688	5.6	6.0	35	0	0	
ice-12	443160	3789698	5.6			0	0	
ice-13	443129	3789704	5.6			0	0	
ice-14	443123	3789702	5.6			0	0	
ice-15	443111	3789704	5.6		31	0	0	
ice-16	443086	3789700	5.6	5.3	20	0	0	
ice-17	443074	3789701	5.6			0	0	
ice-18	443071	3789690	5.6			0	0	
ice-19	443053	3789678	5.6	6.0	35	0	0	45
ice-20	443036	3789676	5.6	6.0	35	0	0	
ice-21	443014	3789674	5.6			0	0	
ice-22	442986	3789670	5.7	6.0	30	0	0	
ice-23	442959	3789666	5.7			0	0	
ice-24	442934	3789685	5.7	8.0		0	0	
ice-25	442923	3789685	6.0			0	0	
ice-26	442906	3789689	6.0			0	0	
ice-27	442880	3789691	6.0			0	0	
ice-28	442870	3789682	6.0			0	0	
ice-29	442851	3789674	6.0			0	0	
ice-30	442839	3789669	6.0			0	0	
ice-31	442833	3789667	6.0			0	0	

Station ID	Easting[a]	Northing[a]	Area (km^2)	Bankfull Width (m)	Valley Width (m)	% Rock (bed)	% Rock (bank)	D$_{50}$
ice-32	442822	3789655	6.1			0	0	
ice-33	442803	3789652	6.1			0	0	
ice-34	442779	3789633	6.1	5.0		0	0	
ice-35	442765	3789633	6.1			0	0	
ice-36	442760	3789636	6.1			0	0	
ice-37	442752	3789636	6.1			0	0	
ice-38	442746	3789635	6.1			0	0	
ice-39	442722	3789637	6.2			0	0	
ice-40	442695	3789639	8.5	6.0		0	0	
ice-41	442673	3789632	8.5	6.3		0	0	
mflytle-0	447671	3790203	12.2			0	0	
mflytle-1	447682	3790199	12.2	9.0	45	0	50	45
mflytle-2	447705	3790204	12.2	8.6	45	0	25	64
mflytle-3	447719	3790200	12.2	9.8	45	0	0	22
mflytle-4	447754	3790190	12.2	10.6	35	0	0	45
mflytle-5	447767	3790188	12.2	8.2	25	0	0	256
mflytle-6	447775	3790156	12.2	9.6		0	0	23
mflytle-7	447817	3790151	12.3	12.0	34	0	25	23
mflytle-8	447858	3790151	12.3	9.6	25	0	0	45
mflytle-9	447889	3790138	12.3	9.4	22	0	0	64
mflytle-10	447918	3790127	12.3	7.2	20	0	0	45
mflytle-11	447961	3790134	12.4	7.9	26	0	0	32
mflytle-12	447996	3790146	12.5	12.9	50	0	0	32
mflytle-13	448013	3790136	12.5	12.0	50	0	0	32
mflytle-14	448028	3790155	12.5	10.5	60	0	0	128
mflytle-15	448051	3790164	12.5	7.8		0	0	64
mflynew-15	448051	3790164	12.5			0	0	
mflynew-16	448094	3790166	12.5			0	0	
mflynew-17	448096	3790163	12.5	9.3		0	0	45
mflynew-18	448122	3790162	12.5			0	0	
mflynew-19	448145	3790166	12.5	12.1		0	0	45
mflynew-20	448179	3790165	12.5	10.6	15	0	0	32
mflynew-21	448209	3790173	13.1	12.1	15	0	0	45
mflynew-22	448233	3790174	13.1	10.3	12	0	0	32
mflynew-23	448266	3790162	13.2	13.0	40	0	0	32
mflynew-24	448289	3790164	13.2	11.5	40	0	0	23
mflynew-25	448311	3790147	13.2	11.6	48	0	0	45
mflynew-26	448337	3790150	13.2	9.2		0	20	45
mflynew-27	448347	3790158	13.2			0	15	32
mflynew-28	448382	3790163	13.2	12.5	51	0	0	45
mflynew-29	448410	3790163	13.2	10.9	50	0	0	64
mflynew-30	448428	3790157	13.2	11.6	50	0	0	45
mflynew-31	448458	3790152	13.5	10.5	68	0	0	32
mflynew-32	448476	3790158	13.5	10.0	58	0	0	45
mflynew-33	448490	3790179	13.6	10.0	58	0	0	45
mflynew-34	448517	3790172	13.6	10.5	45	0	0	32
mflynew-35	448564	3790174	13.6	11.3	55	0	0	32
mflynew-36	448572	3790153	13.6	12.2	56	0	0	32
sflytle-0	451536	3787588	8.0			0	0	
sflytle-1	451553	3787599	8.0	4.6	100	0	30	
sflytle-2	451569	3787609	8.0	8.1	120	10	50	
sflytle-3	451582	3787619	8.0	5.6		40	70	16
sflytle-4	451597	3787629	8.0	5.4		40	80	11
sflytle-5	451608	3787649	8.1	8.5	86	0	40	45
sflytle-6	451606	3787664	8.1	11.5	85	0	0	45
sflytle-7	451625	3787695	9.0	15.3	80	0	0	64
sflytle-8	451642	3787726	9.1	14.5	95	0	0	
sflytle-9	451676	3787748	9.1	22.0	100	0	0	64
sflytle-10	451737	3787776	9.1	16.3	82	0	0	64
sflytle-11	451765	3787760	9.1	14.4	62	0	0	64
sflytle-12	451781	3787732	9.1	10.2	50	0	0	45
sflytle-13	451788	3787725	9.3			0	0	
sflytle-14	451783	3787717	9.3	9.5	45	0	0	45
sflytle-15	451796	3787712	9.4	9.1	57	0	0	64
sflytle-16	451810	3787708	9.4	9.4	55	0	0	45
sflytle-17	451835	3787719	9.4	10.4	65	0	0	45

Station ID	Easting[a]	Northing[a]	Area (km^2)	Bankfull Width (m)	Valley Width (m)	% Rock (bed)	% Rock (bank)	D_{50}
sflytle-18	451843	3787727	9.4			0	0	
sflytle-19	451852	3787719	9.4			0	0	
sflytle-20	451883	3787722	9.5	6.4	64	0	0	45
sflytle-21	451904	3787714	9.5	7.1	69	0	0	45
sflytle-22	451934	3787718	9.5	6.7	71	0	0	45
sflytle-23	451956	3787716	9.5	7.0	70	0	50	45
sflytle-24	451978	3787724	9.5	8.3	68	0	50	45
sflytle-25	452000	3787720	9.7	9.1	61	0	0	45
sflytle-26	452016	3787713	9.8	6.5	63	0	0	45
sflytle-27	452035	3787709	9.8	7.7	65	0	30	45
sflytle-28	452055	3787701	9.8	7.8	71	0	45	45
sflytle-29	452063	3787694	9.8	6.3	75	50	50	32
sflytle-30	452085	3787689	9.8		84	0	20	45
sflytle-31	452101	3787680	9.8	8.1	81	0	50	45
sflytle-32	452116	3787688	9.8			0	0	
millard-0	396051	3787619	2.8		17	0	0	
millard-1	396031	3787611	2.8	9.5	18	0	0	512
millard-2	396013	3787602	2.8		12	0	0	
millard-3	396002	3787581	2.8	8.3	8	0	100	
millard-4	396012	3787568	2.8	8.0	10	0	30	
millard-5	396040	3787563	2.9	8.0	15	0	20	180
millard-6	396046	3787543	2.9	8.0	12	0	0	180
millard-7	396049	3787528	2.9		15	5	50	
millard-8	396054	3787521	3.0		20	0	25	
millard-9	396054	3787506	3.0		20	0	30	720
millard-10	396054	3787491	3.0	9.0	20	0	0	512
millard-11	396043	3787485	3.0		26	0	0	
millard-12	396029	3787478	3.0		18	0	0	
millard-13	396015	3787477	3.0		15	0	0	
millard-14	396001	3787479	3.0	10.5	13	0	20	180
millard-15	395979	3787461	3.0	8.5	9	0	10	
millard-16	395958	3787448	3.0		13	0	0	
millard-17	395966	3787430	3.0	8.5	12	0	30	45
millard-18	395974	3787422	3.0		12	0	0	
millard-19	395968	3787415	3.0		13	0	0	
millard-20	395952	3787411	3.3		13	0	0	
millard-21	395936	3787427	3.3	8.3	14	0	40	
millard-22	395917	3787433	3.3	7.1	18	0	0	
millard-23	395900	3787425	3.3	7.7	18	0	0	
millard-24	395889	3787407	3.3		40	0	0	360
millard-25	395877	3787392	3.3		40	0	0	
millard-26	395869	3787374	3.3	7.0	40	0	0	
millard-27	395852	3787369	3.3		40	0	0	64
millard-28	395845	3787355	3.4		40	0	0	
millard-29	395846	3787341	3.4		28	0	0	
millard-30	395827	3787330	3.4		30	0	0	
millard-31	395818	3787325	3.4		28	0	0	
millard-32	395814	3787314	3.4		29	0	0	
millard-33	395801	3787307	3.4		25	0	0	
millard-34	395799	3787305	3.4		25	0	0	
millard-35	395794	3787293	3.4		25	0	0	
millard-36	395790	3787285	3.4	7.6	25	0	0	64
millard-37	395779	3787276	3.4		25	0	0	
millard-38	395777	3787259	3.4		25	0	0	
millard-39	395773	3787239	3.4	7.3	28	0	10	256
millard-40	395763	3787225	3.5		22	0	0	
millard-41	395760	3787210	3.5	7.3	14	0	0	
millard-42	395738	3787198	3.5		12	0	0	
millard-43	395732	3787183	3.5		17	0	0	
millard-44	395738	3787164	3.5		19	0	0	
millard-45	395749	3787153	3.5	8.0	18	0	50	
millard-46	395750	3787143	3.5		18	0	0	
millard-47	395749	3787119	3.5		14	0	0	
millard-48	395746	3787103	3.5		12	0	0	
millard-49	395743	3787092	3.5		14	5	50	
millard-50	395747	3787083	3.5		13	0	50	1000

Station ID	Easting[a]	Northing[a]	Area (km^2)	Bankfull Width (m)	Valley Width (m)	% Rock (bed)	% Rock (bank)	D_{50}
millard-51	395747	3787069	3.5		15	0	100	360
millard-52	395736	3787060	3.5			0	0	
millard-53	395725	3787048	3.5		7	0	0	
millard-54	395719	3787038	3.5		10	0	0	
millard-55	395710	3787036	3.5	7.5	9	0	0	
millard-56	395706	3787028	3.5		17	0	0	
millard-57	395698	3787019	3.5	7.5	20	0	0	
millard-58	395702	3787003	3.5		21	0	0	
millard-59	395716	3786994	3.5		21	0	0	
millard-60	395714	3786978	3.5		24	0	0	
millard-61	395713	3786965	3.6		14	0	0	
millard-62	395713	3786950	3.6	7.7	19	0	30	256
millard-63	395699	3786939	3.8		14	0	0	
millard-64	395689	3786925	3.8	6.6	15	0	30	
millard-65	395668	3786907	3.8	7.0	20	0	50	
millard-66	395652	3786892	3.8	7.3	21	0	0	128
millard-67	395630	3786881	3.8		20	0	0	
millard-68	395615	3786865	3.8		14	0	0	
millard-69	395606	3786855	3.8		13	0	0	
millard-70	395597	3786840	3.8		16	0	0	
millard-71	395581	3786819	3.9		20	0	0	
millard-72	395572	3786836	3.9		21	0	0	
millard-73	395573	3786853	3.9		15	0	0	
millard-74	395579	3786875	3.9	8.0	13	0	40	90
millard-75	395576	3786889	3.9	7.0	14	50	50	
millard-76	395564	3786921	3.9	6.8	13	0	10	
millard-77	395545	3786939	3.9		12	0	50	
millard-78	395530	3786946	3.9	7.0	7	0	70	
millard-79	395516	3786946	3.9		8	20	20	
millard-80	395494	3786930	3.9	6.2	8	80	50	
millard-81	395483	3786909	3.9	6.8	8	5	40	
millard-82	395476	3786886	3.9	6.5	10	0	0	
millard-83	395460	3786868	3.9	7.0	10	30	0	180
millard-84	395439	3786883	4.0	6.1	7	60	80	
millard-85	395423	3786896	4.0	6.5	8	10	60	
millard-86	395401	3786922	4.0	6.5	11	70	100	
millard-87	395375	3786931	4.0	7.2	15	0	0	
millard-88	395363	3786951	4.0		17	0	0	
millard-89	395351	3786961	4.0		17	0	50	
millard-90	395339	3786962	4.0		13	0	0	
millard-91	395324	3786962	4.0	7.4	11	0	30	
millard-92	395300	3786964	4.0		14	0	0	
millard-93	395293	3786955	4.9		18	0	0	
millard-94	395279	3786952	4.9		18	0	0	
millard-95	395268	3786941	4.9		18	0	50	
millard-96	395262	3786926	4.9	7.9	18	0	0	
millard-97	395244	3786900	4.9	7.3	18	0	0	45
millard-98	395231	3786910	4.9		22	0	0	
millard-99	395224	3786931	5.0		20	0	0	
millard-100	395217	3786953	5.0		13	0	0	
millard-101	395207	3786965	5.0	7.9	14	0	0	
millard-102	395192	3786963	5.0		14	0	0	
millard-103	395182	3786958	5.0	7.5	15	0	0	
millard-104	395173	3786946	5.0	6.8	15	50	0	
millard-105	395166	3786926	5.0	6.8	14	10	30	
millard-106	395160	3786903	5.0		14	0	0	
millard-107	395146	3786886	5.0		14	0	0	
millard-108	395124	3786888	5.0	7.0	7	0	50	
millard-109	395103	3786893	5.0		12	0	0	
millard-110	395073	3786882	5.0	6.7	8	20	20	
millard-111	395048	3786871	5.0	7.2	9	0	50	180
millard-112	395036	3786860	5.0	7.2	13	10	30	
millard-113	395016	3786856	5.1	5.3	10	10	50	
millard-114	395002	3786864	5.1	5.0	11	30	50	
millard-115	394992	3786896	5.1	6.2	9	0	30	
millard-116	394970	3786885	5.1		7	0	0	

Station ID	Easting[a]	Northing[a]	Area (km^2)	Bankfull Width (m)	Valley Width (m)	% Rock (bed)	% Rock (bank)	D_{50}
millard-117	394955	3786868	5.1	5.0	7	10	50	64
millard-118	394939	3786852	5.1	5.1	12	0	50	
millard-119	394916	3786843	5.1	5.9	10	0	50	
lucas-1	394264	3795755	3.5		15	0	0	
lucas-2	394250	3795755	3.5	5.2	14	10	30	
lucas-3	394232	3795745	3.5	4.6	15	0	20	64
lucas-4	394214	3795751	3.5		14	0	0	
lucas-5	394202	3795765	3.5	5.4	14	0	0	45
lucas-6	394189	3795782	3.5		16	0	0	
lucas-7	394168	3795792	3.7	4.0	20	0	0	64
lucas-8	394153	3795811	3.7		18	0	0	
lucas-9	394140	3795819	3.7	4.9	14	0	0	128
lucas-10	394137	3795829	3.7	4.5	14	25	40	500
lucas-11	394130	3795850	3.7	6.7	14	0	10	128
lucas-12	394130	3795864	3.7	5.0	12	0	20	90
lucas-13	394141	3795870	3.7		13	0	0	
lucas-14	394152	3795880	3.7		10	0	40	2
lucas-15	394152	3795895	3.7	8.0	9	10	40	2
lucas-16	394153	3795913	3.7	4.1	5	10	40	4
lucas-17	394145	3795930	3.7	4.0	11	20	0	32
lucas-18	394135	3795934	3.7	4.5	14	0	0	
lucas-19	394122	3795934	3.9	5.0	12	0	0	
lucas-20	394108	3795944	3.9	6.1	10	10	20	45
lucas-21	394096	3795946	3.9	5.9	11	5	0	45
lucas-22	394076	3795934	3.9	5.5	12	0	0	64
lucas-23	394061	3795938	3.9	4.0	10	0	50	32
lucas-24	394047	3795949	3.9	6.0	12	0	0	
lucas-25	394046	3795968	3.9	6.0	15	5	10	64
lucas-26	394051	3795975	3.9	6.0	12	5	10	45
lucas-27	394065	3796007	3.9	6.0	10	20	15	32
lucas-28	394066	3796027	3.9	6.0	9	10	0	90
lucas-29	394059	3796047	3.9	5.4	12	0	40	4
lucas-30	394039	3796054	3.9	5.8	12	0	50	45
lucas-31	394021	3796054	3.9	5.5	9	0	40	45
lucas-32	394017	3796067	3.9	6.0	6	0	50	64
lucas-33	394019	3796081	3.9		12	0	0	
lucas-34	394002	3796099	3.9		15	0	0	
lucas-35	393989	3796111	4.0		15	0	0	
lucas-36	393976	3796116	4.0		15	0	0	
lucas-37	393945	3796093	4.0	7.4	20	0	10	45
lucas-38	393933	3796115	4.0	8.0	15	0	10	45
lucas-39	393929	3796145	4.0	5.6	10	0	0	45
lucas-40	393933	3796161	4.1		14	0	0	
lucas-41	393927	3796183	4.1	6.0	20	0	0	180
lucas-42	393911	3796200	4.1	5.0	15	0	0	4
lucas-43	393910	3796233	4.1		15	0	0	
lucas-44	393889	3796236	4.1	5.0	20	0	10	32
lucas-45	393859	3796251	4.1	6.0	20	0	5	64
lucas-46	393833	3796256	4.1	6.1	20	0	0	45
lucas-47	393817	3796287	4.1	5.6	10	0	25	64
lucas-48	393807	3796305	4.1		13	0	0	
lucas-49	393789	3796307	4.1		15	0	20	32
lucas-50	393764	3796304	4.1	6.0	15	0	0	90
lucas-51	393754	3796314	4.1	5.5	15	0	0	64
lucas-52	393747	3796333	4.1		16	5	0	
lucas-53	393769	3796343	4.1		9	5	0	90
lucas-54	393774	3796360	4.1	5.0	16	0	50	
lucas-55	393761	3796376	4.1		17	0	0	
lucas-56	393754	3796381	4.1		9	0	0	
lucas-57	393748	3796375	4.2	4.0	4	30	30	
lucas-58	393736	3796372	4.2	4.3	4	30	80	
lucas-59	393729	3796369	4.2	5.0	5	15	75	4
lucas-60	393726	3796361	4.2	5.0	5	5	60	
lucas-61	393714	3796343	4.2	5.3	5	10	40	128
lucas-62	393699	3796342	4.3	4.4	10	0	50	90
lucas-63	393675	3796342	4.3	3.5	10	15	70	2

Station ID	Easting[a]	Northing[a]	Area (km^2)	Bankfull Width (m)	Valley Width (m)	% Rock (bed)	% Rock (bank)	D$_{50}$
lucas-64	393671	3796358	4.3	5.8	12	40	10	64
lucas-65	393684	3796372	4.3	3.5	4	60	80	2
lucas-66	393695	3796381	4.3	4.5	5	20	100	4
lucas-67	393701	3796398	4.3	5.4	6	20	80	4
lucas-68	393723	3796417	4.3		6	30	30	90
lucas-69	393727	3796433	4.3	6.3	8	0	0	32
lucas-70	393721	3796447	4.3	6.0	8	0	0	64
lucas-71	393696	3796443	4.4	6.0	9	0	0	180
lucas-72	393694	3796418	4.4	5.5	9	10	25	128
lucas-73	393683	3796414	4.4		14	0	0	
lucas-74	393674	3796420	4.4		10	0	0	
lucas-75	393660	3796415	4.4	4.0	8	30	50	64
lucas-76	393645	3796406	4.4	5.5	10	0	0	45
lucas-77	393633	3796404	4.4	5.0	8	0	30	90
lucas-78	393626	3796414	4.4		11	5	30	128
lucas-79	393627	3796430	4.4	4.0	12	0	50	4
lucas-80	393630	3796436	4.4		12	0	0	
lucas-81	393633	3796448	4.4		10	0	0	180
lucas-82	393638	3796456	4.4		8	0	0	90
lucas-83	393633	3796473	4.4		6	70	80	2
lucas-84	393629	3796493	4.4	5.0	5	0	0	
eatonB-0	399413	3785180	12.7	5.9	6	0	0	
eatonB-1	399389	3785173	12.8	8.8	9	10	80	
eatonB-2	399375	3785174	12.8		9	0	0	
eatonB-3	399366	3785181	12.8		10	10	80	128
eatonB-4	399356	3785195	12.8		15	0	0	256
eatonB-5	399343	3785204	12.8	9.5	15	5	0	
eatonB-6	399325	3785194	13.2	8.5	12	0	50	256
eatonB-7	399326	3785188	13.2		12	0	0	
eatonB-8	399297	3785163	13.2	8.0	16	0	30	180
eatonB-9	399289	3785142	13.2	8.8	16	0	5	256
eatonB-10	399302	3785118	13.2	8.0	15	0	30	180
eatonB-11	399307	3785100	13.2	7.0	15	0	0	128
eatonB-12	399309	3785088	13.2	8.0	22	0	0	180
eatonB-13	399302	3785072	13.2	7.0	22	0	20	128
eatonB-14	399277	3785061	13.2	8.0	20	50	50	90
eatonB-15	399266	3785054	13.2	7.3	14	0	0	256
eatonB-16	399269	3785017	13.7	7.5	11	0	50	180
eatonB-17	399268	3784994	13.7	8.0	15	0	5	256
eatonB-18	399261	3784986	13.7		14	0	0	512
eatonB-19	399253	3784981	13.7		23	0	0	
eatonB-20	399243	3784975	13.7		17	0	25	180
eatonB-21	399221	3784964	13.7	8.0	20	5	0	360
eatonB-22	399219	3784949	13.7	9.9	30	0	5	180
eatonB-23	399237	3784915	13.7	7.0	24	0	30	256
eatonB-24	399259	3784915	13.7	7.8	15	0	10	180
eatonC-0	399273	3784912	13.7		22	0	0	
eatonC-1	399287	3784907	13.7	7.0	22	0	50	11
eatonC-2	399295	3784901	13.7		22	0	0	
eatonC-3	399298	3784892	13.7		15	0	0	
eatonC-4	399295	3784887	13.7		16	0	0	512
eatonC-5	399301	3784883	13.7		16	10	50	360
eatonC-6	399308	3784871	13.7	7.0	16	0	20	90
eatonC-7	399305	3784853	13.7	8.0	10	0	20	180
eatonC-8	399298	3784840	13.7	10.0	14	0	50	2
eatonC-9	399304	3784833	13.8		15	0	0	
eatonC-10	399301	3784828	13.8		15	0	5	256
eatonC-11	399299	3784819	13.8	8.0	16	20	20	180
eatonC-12	399295	3784802	13.8	8.2	16	0	5	180
eatonC-13	399289	3784768	14.7	8.6	15	0	0	180
eatonC-14	399274	3784742	14.7	8.7	18	0	0	180
eatonC-15	399263	3784719	14.7		30	0	0	
eatonC-16	399235	3784701	14.7	11.6	33	0	0	90
eatonC-17	399227	3784693	14.7		35	0	0	
eatonC-18	399227	3784680	14.7		36	0	0	360
eatonC-19	399216	3784662	14.7	7.0	45	15	0	128

Station ID	Easting[a]	Northing[a]	Area (km^2)	Bankfull Width (m)	Valley Width (m)	% Rock (bed)	% Rock (bank)	D$_{50}$
eatonC-20	399190	3784642	14.7	6.9	10	0	30	256
eatonC-21	399173	3784635	14.7	7.0	12	0	0	256
eatonC-22	399173	3784624	14.7	7.0	12	0	40	64
eatonC-23	399184	3784605	14.7	6.0	15	0	30	180
eatonC-24	399189	3784589	14.7	6.3	17	0	40	180
eatonC-25	399181	3784569	14.8	7.0	15	0	30	90
eatonC-26	399180	3784545	14.8	6.6	15	0	0	256
eatonC-27	399153	3784551	14.9	6.5	10	0	40	180
foxck-0	390599	3798244	17.7		60	0	0	
foxck-1	390617	3798222	17.7	5.6	60	0	0	64
foxck-2	390652	3798210	17.7	8.0	60	0	0	64
foxck-3	390686	3798224	17.7	6.3	48	0	30	64
foxck-4	390699	3798229	17.7		50	0	0	64
foxck-5	390716	3798220	17.8	7.6	54	0	0	90
foxck-6	390738	3798212	17.8		70	0	0	
foxck-7	390745	3798206	17.8		70	0	0	
foxck-8	390748	3798204	17.8		70	0	0	
foxck-9	390752	3798202	17.8		70	0	0	
foxck-10	390757	3798203	17.8		80	0	0	
foxck-11	390780	3798204	17.8		80	0	0	90
foxck-12	390803	3798193	17.8		83	0	0	
foxck-13	390825	3798164	17.8		77	0	0	45
foxck-14	390828	3798148	17.8		80	0	0	
foxck-15	390834	3798144	17.8		80	0	0	
foxck-16	390840	3798139	17.8	7.0	80	0	30	64
foxck-17	390864	3798127	17.9	7.1	80	0	25	64
foxck-18	390878	3798124	19.3		80	0	0	
foxck-19	390888	3798118	19.3	7.7	60	0	0	64
foxck-20	390899	3798112	19.3	7.0	60	0	30	64
foxck-21	390923	3798111	19.3		45	0	0	
foxck-22	390946	3798111	19.3		43	0	0	
foxck-23	390970	3798118	19.3		50	0	0	
foxck-24	390981	3798121	19.3		48	0	0	
foxck-25	390990	3798122	19.4		56	0	0	64
foxck-26	391001	3798113	19.4		60	0	0	
foxck-27	391013	3798109	19.4	6.0	65	0	0	64
foxck-28	391029	3798104	19.4		73	0	0	
foxck-29	391040	3798103	19.5		81	0	0	
foxck-30	391050	3798078	19.5	8.5	85	0	0	128
foxck-31	391061	3798048	19.5	8.2	90	0	0	90
foxck-32	391077	3798029	19.6	8.0	78	0	0	5
foxck-33	391073	3798017	19.6	8.0	87	0	0	128
foxck-34	391074	3798000	19.6		74	0	0	
foxck-35	391086	3797985	19.6		45	0	0	
foxck-36	391103	3797975	19.7	8.0	48	0	0	128
foxck-37	391126	3797968	19.7	6.0	64	0	0	180
foxck-38	391129	3797949	19.7	6.9	77	0	0	180
foxck-39	391156	3797914	19.7	9.4	79	0	0	128
foxck-40	391167	3797904	19.7	7.0	66	0	0	180
foxck-41	391193	3797892	19.7	6.0	52	0	0	180
foxck-42	391221	3797887	19.7	6.0	52	0	0	180
foxck-43	391250	3797889	19.7	5.3	72	0	0	
foxck-44	391263	3797892	22.1		73	0	0	
foxck-45	391300	3797897	22.1		74	0	0	
foxck-46	391329	3797895	22.1		78	20	10	5
foxck-47	391344	3797878	22.1	7.0	84	0	0	5
foxck-48	391344	3797861	22.1	10.0	85	0	0	64
foxck-49	391343	3797838	22.1	7.9	78	0	0	64
foxck-50	391360	3797804	22.1	8.0	70	0	0	128
foxck-51	391344	3797782	22.2		55	0	0	
foxck-52	391351	3797747	22.2	7.5	35	5	10	
foxck-53	391337	3797713	22.2	7.1	19	0	0	180
foxck-54	391295	3797694	22.2	6.2	10	5	5	180
foxck-55	391298	3797684	22.2	6.0	6	80	100	8
foxck-56	391327	3797662	22.3	5.5	10	5	20	128
foxck-57	391350	3797648	22.3	6.5	16	5	0	180

Station ID	Easting[a]	Northing[a]	Area (km^2)	Bankfull Width (m)	Valley Width (m)	% Rock (bed)	% Rock (bank)	D$_{50}$
foxck-58	391357	3797638	22.3	6.0	20	0	0	180
foxck-59	391359	3797610	22.3	6.2	18	0	5	180
foxck-60	391373	3797576	22.3	6.0	15	0	5	180
foxck-61	391408	3797580	22.4	6.9	18	0	0	256
foxck-62	391425	3797576	22.4	6.5	18	0	0	360
foxck-63	391483	3797597	22.4	6.2	20	5	20	256
foxck-64	391510	3797589	22.4	7.5	29	75	75	180
foxck-65	391518	3797587	22.4	7.5	30	10	10	180
foxck-66	391540	3797558	22.5	6.5	32	10	10	128
foxck-67	391568	3797531	22.5	6.4	20	15	10	180
foxck-68	391586	3797512	22.5	6.2	15	0	0	180
foxck-69	391586	3797500	22.5		23	0	0	
foxck-70	391593	3797492	22.5		24	0	0	
foxck-71	391597	3797465	22.6	7.1	21	30	50	256
foxck-72	391560	3797449	22.6	7.0	15	60	60	256
foxck-73	391521	3797446	22.6	6.6	18	0	0	180
foxck-74	391486	3797448	22.6	8.3	22	0	0	180
foxck-75	391488	3797426	22.6	7.0	24	0	25	180
foxck-76	391490	3797407	22.7	8.0	16	0	0	128
foxck-77	391502	3797359	22.7		14	0	0	
foxck-78	391502	3797322	22.7	7.1	12	0	0	256
foxck-79	391492	3797296	22.7	6.4	12	0	25	128
foxck-80	391473	3797286	22.7		15	0	0	
foxck-81	391472	3797267	22.7		16	0	0	360
foxck-82	391494	3797247	22.7	7.7	16	0	10	
fox2-0	391506	3797229	22.7		13	0	10	
fox2-1	391524	3797226	22.7	6.8	7	30	100	2
fox2-2	391531	3797218	22.7	11.2	11	0	100	8
fox2-3	391538	3797208	22.7	6.0	6	0	80	360
fox4-0	391545	3797194	22.7	7.0	7	20	100	1000
fox4-1	391562	3797192	22.7	10.0	10	10	100	90
fox4-2	391574	3797200	22.7		8	0	100	
fox4-3	391580	3797219	22.7		9	10	100	2
fox4-4	391587	3797232	22.7		7	0	100	
fox4-5	391603	3797236	22.7		7	20	100	128
fox4-6	391634	3797251	22.7	6.4	6	5	100	180
fox4-7	391641	3797258	22.7		8	0	100	
fox4-8	391639	3797263	22.7		6	0	100	
fox4-9	391663	3797277	22.7	5.0	5	20	100	180
fox4-10	391673	3797282	22.7	8.0	8	50	100	90
fox4-11	391693	3797290	22.7	8.0	8	60	100	180
fox4-12	391707	3797290	22.7	10.4	10	10	100	
fox4-13	391729	3797301	22.8	6.0	6	40	100	
fox4-14	391744	3797295	22.8	6.5	7	30	70	180
fox4-15	391766	3797300	22.8	8.0	8	40	70	64
fox4-16	391776	3797297	22.8	7.5	8	90	100	
fox4-17	391797	3797293	22.8	6.5	7	60	100	16
fox4-18	391803	3797283	22.8	6.1	6	10	100	90
fox4-19	391849	3797233	22.8	7.5	12	10	30	180
fox4-20	391863	3797220	22.8		12	30	30	
fox4-21	391866	3797195	22.8	7.3	7	60	100	2
fox4-22	391874	3797186	22.8		11	100	100	
fox4-23	391876	3797164	22.9	6.1	6	30	50	2
fox4-24	391901	3797142	22.9	7.0	7	20	30	180
fox4-25	391911	3797134	22.9		14	0	0	180
fox4-26	391913	3797132	22.9		14	0	0	
fox4-27	391914	3797124	22.9	5.5	6	70	100	
fox4-28	391915	3797114	23.0	5.9	10	30	50	180
fox4-29	391914	3797083	23.0	6.0	7	30	70	90
fox4-30	391908	3797058	23.0	7.0	10	20	20	2
fox4-31	391907	3797045	23.0	5.0	13	5	100	2
fox4-32	391892	3797039	23.1		5	20	100	
fox4-33	391875	3797033	23.1		11	10	50	
fox4-34	391856	3797034	23.2	7.0	17	5	50	180
fox4-35	391825	3797030	23.2	5.8	6	10	50	32
fox4-36	391805	3797030	23.2	6.0	6	50	75	128

Station ID	Easting[a]	Northing[a]	Area (km^2)	Bankfull Width (m)	Valley Width (m)	% Rock (bed)	% Rock (bank)	D$_{50}$
fox4-37	391769	3797008	23.3	8.0	15	5	0	64
fox4-38	391782	3796969	23.3	7.0	10	5	40	256
fox4-39	391783	3796941	23.4	7.5	11	20	20	256
fox4-40	391777	3796917	23.4	7.5	8	0	0	256
fox4-41	391776	3796904	23.4	7.5	9	5	50	16
fox4-42	391756	3796887	23.5		12	10	50	2
fox4-43	391731	3796889	23.5	5.8	9	40	50	4
fox4-44	391712	3796887	23.6	7.0	9	20	25	180
fox4-45	391700	3796887	23.6	6.5	7	50	100	8
fox4-46	391689	3796867	23.6	7.0	7	70	50	180
fox4-47	391700	3796854	23.7		7	50	100	
fox4-48	391706	3796844	23.7	7.1	8	20	40	
fox4-49	391700	3796824	23.8	7.0	10	0	50	2
fox4-50	391690	3796802	23.8		11	0	50	
fox4-51	391677	3796794	23.8		11	5	20	180
fox4-52	391676	3796769	23.8	6.3	6	50	100	128
fox4-53	391675	3796755	23.9	5.0	5	60	80	180
fox4-54	391671	3796748	23.9	6.3	6	50	100	2
fox4-55	391675	3796737	23.9	6.0	6	80	100	256
fox4-56	391676	3796722	23.9	6.3	6	50	100	90
fox4-57	391681	3796716	24.0	6.5	7	30	100	180
fox4-58	391702	3796712	24.0	6.4	6	15	100	2
fox4-59	391714	3796703	24.0	6.5	7	20	50	90
fox4-60	391710	3796666	24.0	7.4	8	15	50	64
fox4-61	391707	3796649	24.0	7.5	8	30	30	
fox4-62	391734	3796594	24.0	8.0	12	5	30	
fox4-63	391739	3796566	24.1		11	15	10	
fox4-64	391727	3796540	24.1	8.0	9	0	30	
fox4-65	391714	3796518	24.1	8.0	16	0	10	180
fox4-66	391702	3796503	24.2		14	0	0	
fox4-67	391674	3796498	24.2	9.5	12	0	0	90
fox4-68	391671	3796454	24.2		9	0	0	
fox4-69	391635	3796442	24.2	8.5	12	0	20	90
fox4-70	391597	3796443	24.3	8.1	14	0	0	180
fox4-71	391585	3796431	24.3	8.0	18	0	40	64
fox4-72	391579	3796394	24.3	8.0	14	10	30	256
fox4-73	391568	3796360	24.4	8.0	15	40	40	8
fox4-74	391572	3796340	24.4	8.0	12	10	10	180
fox4-75	391590	3796332	24.4		14	20	50	
fox4-76	391613	3796323	24.5	5.5	6	0	100	
fox4-77	391631	3796299	24.5	7.5	8	20	100	
fox4-78	391649	3796298	24.5	9.8	12	0	0	256
fox4-79	391676	3796295	24.5	8.0	20	0	0	180
fox4-80	391695	3796271	24.6		22	0	0	
fox4-81	391699	3796266	24.6		23	0	0	
fox4-82	391707	3796260	24.6		23	0	0	
fox4-83	391712	3796256	24.6		21	0	0	
sfiron-0	429617	3795730	11.4			0	0	
sfiron-1	429625	3795729	11.4	5.7	8	10	50	
sfiron-2	429636	3795731	11.4	6.0	6	20	100	
sfiron-3	429654	3795715	11.4	6.3	6	10	50	
sfiron-4	429674	3795701	11.4	5.8	6	30	100	
sfiron-5	429684	3795687	11.4	7.1	8	0	40	
sfiron-6	429700	3795675	11.4	7.1	8	10	50	
sfiron-7	429739	3795687	11.4	7.9	13	0	30	
sfiron-8	429746	3795684	11.4	7.6	11	10	20	
sfiron-9	429758	3795688	11.4	5.9	6	10	5	
sfiron-10	429770	3795707	11.5	7.9	8	60	90	
sfiron-11	429789	3795714	11.5	7.8	9	10	10	
sfiron-12	429796	3795721	11.5	7.3		0	50	
sfiron-13	429808	3795716	11.5	6.5		10	40	
sfiron-14	429823	3795731	11.5	7.1		5	60	
sfiron-15	429842	3795749	11.5		14	0	50	
sfiron-16	429862	3795746	11.5	7.6		0	0	
sfiron-17	429882	3795758	11.5	6.7		5	40	
sfiron-18	429894	3795757	11.5	6.8		10	60	

Station ID	Easting[a]	Northing[a]	Area (km^2)	Bankfull Width (m)	Valley Width (m)	% Rock (bed)	% Rock (bank)	D$_{50}$
sfiron-19	429914	3795784	11.5			0	10	
sfiron-20	429929	3795806	11.5	6.9	18	5	0	
sfiron-21	429940	3795813	11.5	6.5	11	0	0	
sfiron-22	429953	3795824	11.6	7.0		0	0	
nfiron-0	429500	3796921	17.3			0	0	
nfiron-1	429517	3796908	17.4	7.8		0	0	
nfiron-2	429535	3796882	17.5			0	0	
nfiron-3	429559	3796866	17.5	8.7		0	0	
nfiron-4	429568	3796846	17.6	7.0		0	0	
nfiron-5	429569	3796830	17.7			0	0	
nfiron-6	429593	3796813	17.7	7.8		10	50	
nfiron-7	429626	3796797	17.8	8.9		0	0	
nfiron-8	429644	3796765	17.8	7.7		0	0	
nfiron-9	429643	3796740	17.8	8.1		0	0	
nfiron-10	429670	3796702	17.8	8.1		0	0	
nfiron-11	429677	3796674	17.8	7.0		0	0	
nfiron-12	429687	3796662	17.8	8.4		0	0	
nfiron-13	429710	3796650	17.8	8.0		0	0	
nfiron-14	429727	3796638	17.8	8.1		0	0	
nfiron-15	429740	3796624	17.8	8.0		5	20	
nfiron-16	429749	3796598	17.9	8.1		0	0	
nfiron-17	429745	3796566	17.9	7.5		0	0	
nfiron-18	429744	3796546	18.0	8.1		0	15	
nfiron-19	429751	3796521	18.0	7.5		0	50	
nfiron-20	429753	3796508	18.0			0	0	
nfiron-21	429757	3796491	18.1	7.7		0	0	
nfiron-22	429764	3796468	18.1	8.6		0	0	
nfiron-23	429769	3796457	18.2			0	0	
nfiron-24	429771	3796449	18.2	6.9		0	0	
nfiron-25	429786	3796429	18.2	7.2		0	0	
nfiron-26	429809	3796417	18.3	10.2		0	0	
nfiron-27	429824	3796404	18.3	7.9		0	0	
nfiron-28	429833	3796385	18.3			0	0	
nfiron-29	429833	3796377	18.3	8.9		0	0	
nfiron-30	429857	3796359	18.4	7.7		0	0	
nfiron-31	429849	3796347	18.4	7.7		0	0	
nfiron-32	429846	3796332	18.4	8.5		0	0	
nfiron-33	429853	3796304	18.4	8.0		0	25	
nfiron-34	429866	3796278	18.5	8.3		0	30	
nfiron-35	429884	3796258	18.5	9.2		0	10	
nfiron-36	429891	3796213	18.5	7.0		0	50	
nfiron-37	429905	3796178	18.6	6.7		0	50	
iron-0	429955	3795819	30.4			0	0	
iron-1	429967	3795827	30.4			0	0	
iron-2	429988	3795824	30.4	7.0		0	0	
iron-3	429994	3795813	30.4	8.6		0	50	
iron-4	430005	3795794	30.4			0	50	
iron-5	430009	3795764	30.4	8.4		0	5	
iron-6	430017	3795747	30.4	9.0		0	0	
iron-7	430027	3795733	30.4	10.7		0	0	
iron-8	430039	3795710	30.4	9.3		0	0	
iron-9	430054	3795688	30.4	11.6		0	0	
iron-10	430081	3795663	30.5	8.8		0	5	
iron-11	430093	3795639	30.5	11.1		0	30	
iron-12	430106	3795621	30.5	9.2		15	25	
iron-13	430109	3795612	30.5	9.0		0	0	
iron-14	430126	3795604	30.5	9.3		0	0	
iron-15	430138	3795596	30.6			0	0	
iron-16	430138	3795577	30.6			0	0	
iron-17	430156	3795555	30.6	10.0		5	5	
iron-18	430199	3795541	30.6	9.1		0	0	
iron-19	430214	3795533	30.7	8.0		0	25	
iron-20	430223	3795524	30.7	9.5		0	0	
iron-21	430240	3795514	30.7	10.7		20	50	
iron-22	430255	3795512	30.7	12.3		95	50	
iron-23	430270	3795500	30.7	7.1		0	50	

Station ID	Easting[a]	Northing[a]	Area (km^2)	Bankfull Width (m)	Valley Width (m)	% Rock (bed)	% Rock (bank)	D_{50}
iron-24	430274	3795501	30.7			0	0	
iron-25	430275	3795486	30.8	13.1		0	0	
iron-26	430298	3795480	30.8	7.9		5	10	
iron-27	430332	3795453	30.8	8.6		0	30	
iron-28	430348	3795420	30.8	8.0		5	50	
iron-29	430330	3795394	30.8	9.8		0	15	
iron-30	430328	3795379	30.8	10.2		0	5	
iron-31	430328	3795360	30.8	9.7		0	50	
iron-32	430331	3795339	30.9	10.3		20	40	
iron-33	430345	3795321	30.9	10.4		15	50	
iron-34	430378	3795325	30.9	7.9		0	50	
iron-35	430395	3795330	30.9	11.5		0	0	
iron-36	430413	3795337	30.9	10.6		0	0	
iron-37	430436	3795354	30.9	11.0		0	0	
iron-38	430451	3795374	30.9	11.7		0	50	
iron-39	430461	3795388	30.9	11.2		0	50	
iron-40	430485	3795394	31.0	9.4		0	50	
iron-41	430503	3795405	31.0	10.9		0	0	
iron-42	430518	3795411	31.0	12.2		0	0	
iron-43	430539	3795406	31.0			0	10	
iron-44	430552	3795407	31.1			0	0	
iron-45	430558	3795405	31.1			0	0	
iron-46	430575	3795407	31.1			5	50	
iron-47	430578	3795411	31.1			0	30	
iron-48	430589	3795416	31.1			0	0	
iron-49	430595	3795416	31.1			0	0	
iron-50	430612	3795407	31.1	8.1		10	0	
iron-51	430609	3795386	31.2	7.4		40	80	
iron-52	430610	3795373	31.2	8.5		0	50	
iron-53	430624	3795353	31.2	12.6		0	0	
iron-54	430630	3795357	31.2			0	0	
iron-55	430636	3795347	31.2	11.8		0	50	
iron-56	430639	3795334	31.2	8.6		60	50	
iron-57	430649	3795312	31.2	15.0	15	10	60	
iron-58	430658	3795307	31.2			5	50	
iron-59	430664	3795294	31.2	8.6		0	40	
iron-60	430677	3795280	31.2	8.5		0	0	
iron-61	430697	3795264	31.2	9.3		30	60	
iron-62	430705	3795264	31.3	10.5		20	0	
iron-63	430718	3795243	31.3	8.6		20	80	
iron-64	430722	3795226	31.3	9.5		0	40	
iron-65	430729	3795209	31.3	9.5		20	60	
iron-66	430731	3795205	31.3			0	0	
iron-67	430741	3795189	31.3	7.3		10	100	
iron-68	430748	3795189	31.3			10	50	
iron-69	430762	3795176	31.4	8.1		20	100	
iron-70	430798	3795158	31.4	5.0		30	100	
iron-71	430808	3795153	31.5	11.7		0	60	
iron-72	430826	3795165	31.5	9.6		30	30	
iron-73	430852	3795168	31.6	7.0		40	100	
iron-74	430879	3795163	31.7	8.7		5	90	
iron-75	430907	3795181	31.7	9.7		0	20	
iron-76	430938	3795206	31.7	7.0		20	60	
iron-77	430953	3795219	31.7	9.0		0	50	
iron-78	430960	3795239	31.8	12.7		0	80	
iron-79	430969	3795246	31.8	13.7		5	60	
iron-80	431012	3795286	31.8	8.0		5	80	
iron-81	431022	3795294	31.8	7.5		0	50	
iron-82	431030	3795327	31.8	7.2		50	70	
iron-83	431012	3795376	31.9	7.5		60	100	
iron-84	430999	3795406	31.9	7.0		50	100	
iron-85	431001	3795446	31.9	11.3		10	50	
iron-86	431021	3795493	31.9	9.3		5	50	
iron-87	431053	3795500	31.9	9.1		0	50	
iron-88	431105	3795492	32.0	9.2		0	0	
iron-89	431142	3795468	32.0	5.8		90	70	

Station ID	Easting[a]	Northing[a]	Area (km^2)	Bankfull Width (m)	Valley Width (m)	% Rock (bed)	% Rock (bank)	D$_{50}$
iron-90	431157	3795464	32.0	9.1		20	40	
iron-91	431170	3795451	32.0	8.8		15	20	
iron-92	431192	3795469	32.0	7.8		10	90	
iron-93	431215	3795509	32.0	7.5		0	0	
iron-94	431243	3795561	34.5	7.5		5	90	
iron-95	431261	3795565	34.5	6.2		10	100	
iron-96	431275	3795562	34.5			0	60	
iron-97	431296	3795534	34.6	7.3		10	75	
iron-98	431319	3795521	34.6	7.2		5	100	
iron-99	431348	3795525	34.6	7.3		20	100	
iron-100	431364	3795536	34.6	5.7		10	80	
iron-101	431399	3795532	34.6	6.8		20	100	
iron-102	431424	3795500	34.6	6.9		20	70	
iron-103	431445	3795480	34.7	9.2		0	0	
iron-104	431454	3795469	34.7	8.7		0	20	
iron-105	431481	3795454	34.7	8.4		0	50	
iron-106	431501	3795436	34.7			0	50	
iron-107	431526	3795423	34.7	9.0		0	0	
iron-108	431544	3795411	34.7	9.5		15	50	
iron-109	431557	3795402	34.7	10.3		0	30	
iron-110	431574	3795405	34.7			0	0	
iron-111	431585	3795402	34.7	9.9		0	10	
iron-112	431610	3795397	34.8	8.9		0	10	
iron-113	431636	3795395	34.8	9.0		0	0	
iron-114	431664	3795380	34.8	10.5		0	0	
iron-115	431683	3795366	34.8	11.4		0	0	
iron-116	431684	3795348	34.8			0	0	
iron-117	431685	3795328	34.8	11.5		0	0	
iron-118	431710	3795292	34.9	10.4		0	0	
iron-119	431708	3795264	34.9	10.6		0	0	
iron-120	431684	3795248	34.9	11.0		0	20	
iron-121	431668	3795222	35.0	9.0		0	50	
iron-122	431667	3795199	35.0	9.5		0	0	
iron-123	431666	3795182	35.0	9.7		0	20	
iron-124	431684	3795161	35.0	9.7		0	30	
iron-125	431701	3795150	35.0	9.0		0	0	
iron-126	431720	3795136	35.0	8.5		0	0	
iron-127	431725	3795130	35.0			0	0	
iron-128	431749	3795116	35.0	5.9		0	100	
iron-129	431770	3795112	35.0	8.2		0	0	
iron-130	431777	3795111	35.0			0	0	
iron-131	431787	3795102	35.0	11.6		30	50	
iron-132	431798	3795090	35.0	6.6		0	50	
iron-133	431797	3795057	35.0			0	50	
iron-134	431807	3795042	35.0	9.0		0	0	
iron-135	431832	3795014	35.0	7.0		0	50	
iron-136	431844	3794999	35.0	6.0		0	60	
fish-0	434503	3796840	19.9	8.2		0	100	
fish-1	434468	3796818	19.9	6.7		0	50	
fish-2	434442	3796809	19.9	9.1		0	25	
fish-3	434425	3796825	20.0	9.1		0	10	
fish-4	434412	3796832	20.0	8.6		0	5	
fish-5	434392	3796831	20.0	9.5		0	15	
fish-6	434365	3796841	20.0	8.4		0	0	
fish-7	434351	3796849	20.0	8.9		0	5	
fish-8	434338	3796858	20.0	8.9		0	0	
fish-9	434327	3796842	20.1	7.5		0	20	
fish-10	434334	3796816	20.1	8.0		0	15	
fish-11	434328	3796800	20.1	13.7		0	0	
fish-12	434310	3796781	20.1	8.3		0	50	
fish-13	434261	3796769	20.1	9.9		0	70	
fish-14	434228	3796782	20.1	9.9		0	50	

[a] UTM coordinates (NAD 27 Datum)

*converted from qualitative measurement (see text)

APPENDIX D

STATEMENT OF PERMISSION FROM CO-AUTHORS

Chapters 2-5 were prepared independently for publication with help from Kelin X Whipple (Chapters 2-5), Arjun M. Heimsath (Chapters 2, 3, 5), and William B. Ouimet (Chapter 2). These co-authors have acknowledged and granted permission for the use of this work in the context of this dissertation.